# The use of Cosmic-Rays in Detecting Illicit Nuclear Materials


**Timothy Benjamin Blackwell**

Department of Physics and Astronomy

University of Sheffield

This dissertation is submitted for the degree of

*Doctor of Philosophy*

05/05/2015

# Declaration

I hereby declare that except where specific reference is made to the work of others, the contents of this dissertation are original and have not been submitted in whole or in part for consideration for any other degree or qualification in this, or any other University. This dissertation is the result of my own work and includes nothing which is the outcome of work done in collaboration, except where specifically indicated in the text.

Timothy Benjamin Blackwell
05/05/2015

# Acknowledgements

This thesis could not have been completed without the tremendous support of many people. Firstly I would like to express special appreciation and thanks to my academic supervisor, Dr Vitaly A. Kudryavtsev for his expertise, understanding and encouragement. I have enjoyed our many discussions concerning my research topic throughout the PhD journey. I would also like to thank my viva examiners, Professor Lee Thompson and Dr Chris Steer, for the time you have taken out of your schedules, so that I may take this next step in my career. Thanks must also be given to Professor Francis Liven, Professor Neil Hyatt and the rest of the Nuclear FiRST DTC team, for the initial opportunity to pursue postgraduate research. Appreciation is also given to the University of Sheffield, the HEP group and EPRSC for providing me with the facilities and funding, during this work.

Many thanks to my friends and family for there continuous support throughout this process. In particular, recognition must be given to James Gibson for his willingness to listen to my questions and his ability to solve just about any of them. Other close friends I would like to mention are Chris Shaw, Chris Martyn, David Slack and James Gould. Thank you for listening, offering me advice, and supporting me through this entire process.

I want to thank my parents, brother and nephews for always being there for me. Their love and support mean very much to me. Finally my greatest appreciation must be saved for my girlfriend, Rachel. Her continuous love, caring and patience throughout the many months it has taken to complete this work, is what has kept me going.

# Abstract

Muon tomography represents a new type of imaging technique that can be used in detecting high-$Z$ materials (such as shielded HEU). As muons pass through materials, they continuously lose energy via ionisation and can stop within a material. Upon stopping secondary processes can occur, which result in the production of excess neutrons and $\gamma$-rays. Due to their high energies most muons can pass through large depths of different materials. These muons will also undergo multiple scattering. Previous radiographic methods that looks to differentiate high-$Z$ materials from low-$Z$ clutter tend to be based on multiple scattering of muons only.

Presented is the development of two new types of analysis algorithm, which makes use of the different interactions cosmic-ray muons undergo when passing through a material. The first algorithm developed makes use of the multiple Coulomb scattering that a muon will undergo. This involves using a novel density based clustering approach that ascertains regions of high-$Z$ material placed within an inspected volume. The capability of this new type of algorithm has been tested under realistic scenarios. These scenarios involve placing shielded HEU in cargo containers filled with a variety of different clutter. The algorithm has been shown to be efficient in detecting shielded HEU amongst low-$Z$ clutter, but struggles upon the introduction of blocks of aluminium, or materials with densities higher than this.

Whereas previous radiographic methods were based on multiple scattering of muons only, the second developed algorithm uses muon absorption on nuclei to enhance the detection capabilities of the scattering technique. In particular, the goal is to improve on the distinction between high-density materials and low-density clutter. Muons will more readily lose energy in higher density materials. Therefore multiple muon disappearances within a localised volume may signal the presence of high-density materials. Muons that disappear have their track evaluated using a 3D line extrapolation algorithm, which is in turn used to construct a 3D tomographic image of the inspected volume. The

ability to differentiate between materials using the 3D line extrapolation algorithm is established.

The technique of muon disappearance has been applied to identifying shielded HEU in realistic scenarios. Despite being capable of identifying shielded HEU in otherwise empty cargo containers, multiple additional regions (due to the lorry and container itself) were misclassified as possible threat materials. This makes accurate detection systems that solely use this technique for shielded HEU unlikely. However, since the build-up of nuclear materials was apparent, we have demonstrated how this technique can be used as a supplementary technique to help enhance muon scattering tomography capabilities. This is done through first identifying 'areas of interest' using muon scattering tomography before confirming whether they are threats or other materials with the muon disappearance algorithm. It is concluded that while muon disappearance can slightly enhance the capabilities of muon scattering tomography, muon scattering still remains the most efficient method for detection of nuclear materials.

# Contents

# List of Figures

# List of Tables

# Chapter 1

# Introduction

## 1.1 Introduction

Current passive technologies in place at international borders involve the use of polyvinyl toluene scintillator (PVT) $\gamma$-ray detectors and pressurised $^3$He-based neutron counters, to detect the naturally occurring radioactive signatures emitted by nuclear materials. While effective under some circumstances these systems struggle to detect nuclear materials (in particular highly enriched uranium (HEU)) upon the introduction of shielding.

Generated in outer space, cosmic-rays interact with the Earth's upper atmosphere producing a variety of secondary particles. These secondary particles include short-lived pions, which decay to produce muons. Muons represent a natural and free source of inspecting radiation with a flux at sea level of $\approx$170 m$^{-2}$ s$^{-1}$.

Muon scattering tomography (MST) represents a new type of imaging technique that has shown promise in both simulation and experimental studies in discriminating high-$Z$ shielding materials from low-$Z$ background clutter [1–5]. As muons pass through matter they undergo multiple Coulomb scattering. The degree of observed scattering is dependent on the $Z$ of the material. Due to their intrinsically high energies (average energy of 3-4 GeV at sea level) they can pass through any shielding present and hence be used to probe an object of unknown composition.

Muons undergo energy loss via electromagnetic interactions and can stop within the material they are passing through. Individual muons can be tracked as they enter a

volume to be inspected, with any tracks belonging to muons that disappear being easily identifiable. The rate of muon disappearance in the air surrounding a target (due to muon decay) will remain fairly constant, independent of the target material. High-density materials, such as HEU and its shielding components are more likely to cause a muon to stop than low-density materials. Therefore the disappearance of multiple muons within a particular volume represents a strong signature for high density and nuclear materials, which can distinguish them from lower density clutter.

Using these interactions the capability to discriminate different materials is investigated. The development and performance of a new type of analysis algorithm for MST, and the development of a new analysis algorithm for muon disappearance tomography is presented, under a variety of different scenarios. The capability of the two techniques when used in conjunction with one another is also described. The advantages of using muons to interrogate a volume are that they naturally occur, therefore no excess dose will be delivered to the target. This limits potential dangers involved and allow inspection to be performed while the cargo operators remain within their vehicle.

Other particles produced via primary cosmic-ray interaction with the atmosphere include cosmic-ray neutrons. A discussion into whether cosmic-ray neutrons can be used to aid the detection of shielded HEU is presented. Upon interaction with a target material, cosmic-ray neutrons will cause multiple secondary neutrons and $\gamma$-rays to be produced. The number of excess secondaries is dependent on the density and atomic weight of the material. Higher density materials (such as HEU and shielding components) will produce more secondaries than lower density materials (such as clutter). For these systems 'clutter' is defined as any material or commercial good that may be transported in cargo containers. Through measuring the gross count rate of neutrons or $\gamma$-rays over a defined time interval, the observation of an elevated rate may infer the presence of nuclear materials.

## 1.2 Thesis Outline

Chapter 2 introduces background information on the topics to be discussed. A description of passive detection methods currently in use at ports and the inherent limitations of this system is given. Other techniques that have been investigated to solve the issues of passive detection, along with their inherent problems are also presented. The production of cosmic-ray muons and a description of the cosmic-ray muon spectrum are given. The physics behind muons interactions with materials is summarised. A review is given of the previous work that has been done into using cosmic-ray muons as a probe for information, along with prior attempts that have looked to use these cosmic-rays to detect hidden nuclear material. This chapter concludes with a description of the cosmic-ray neutron spectrum and neutron interactions with matter.

Chapter 3 introduces the concept of muon scattering tomography along with introducing initial simulation conditions, the Point of Closest Approach (PoCA) algorithm and parameters involved in volume reconstruction. Initial numerical tests for discriminating different density materials from one another are presented.

Chapter 4 introduces the concept of using stopping muons for material segregation. Individual muons can be tracked as they enter a volume to be inspected, with any tracks belonging to muons that disappear easily identifiable. The rate of muon disappearance in the air surrounding a target will remain fairly constant, independent of the target material. High-density materials, such as HEU and its shielding components are more likely to cause a muon to stop than low-density materials. Therefore the disappearance of multiple muons within a particular volume represents a strong signature for high density and nuclear materials. Detailed GEANT4 simulations are presented that demonstrate the capability of using muon disappearance to distinguish between different density materials.

Chapter 5 discusses the capability of using cosmic-ray muons to detect shielded HEU in empty cargo containers. Using muon scattering tomography the dependence of the detector capability to detect high-Z targets in empty cargo containers, on spatial resolution has been studied. A number of different resolutions representative of gaseous and scintillator detectors are tested. The development of a new secondary analysis algorithm that is applied to the reconstructed PoCA points is also presented. Using this secondary

algorithm the effect of other parameters, such as the distance between detectors and the number of detectors per set, on detecting shielded HEU is presented. Finally, the capability of both muon scattering tomography and muon disappearance tomography in conjunction with one another, to correctly detect five shielded HEU targets in empty cargo containers is presented.

Chapter 6 analyses the feasibility of using cosmic-ray muons to correctly detect shielded HEU when placed in a cargo container, filled with different levels of clutter. Two types of clutter scenario are considered. Ones where shielded HEU is surrounded by low-$Z$ clutter and ones where shielded HEU is surrounded by medium-$Z$ clutter. The ability to detect shielded HEU in each of these scenarios is considered using muon scattering tomography, muon disappearance tomography and the two techniques in conjunction with one another.

In addition to muons, cosmic-ray neutrons also cascade down upon the Earths surface. Chapter 7 discusses whether these neutrons can be used as an additional source of information to detect shielded HEU in empty cargo containers.

This thesis will conclude in Chapter 8 with a summary of the material presented. Any supportive material will be delivered in separate Appendices.

# Chapter 2

# Background

This chapter introduces the justification behind the work along with any relevant theory. Section 2.1 gives a discussion into the current systems in place at borders for detecting radioactive materials, along with the limitations of these systems. Section 2.2 presents other techniques that have been investigated to solve the issues with current systems in place, along with their inherent problems. Section 2.3 discusses the physics processes upon which passive and active interrogation techniques are based. This includes a brief description of radioactive decay, spontaneous fission and induced fission. In section 2.4 a discussion into cosmic rays and how they are produced is given, in particular cosmic-ray muons and cosmic-ray neutrons. The theory behind muon interactions with matter is presented in section 2.5 and neutron interactions with matter is presented in section 2.6. Finally, sections 2.7 and 2.8 give a review of the previous work done using cosmic rays as a probe for information, along with prior attempts that have looked to use these cosmic rays to detect 'hidden' nuclear material.

## 2.1 Passive Interrogation

Nuclear material refers to the metals uranium, plutonium, and thorium, in any form, according to the International Atomic Energy Agency (IAEA). These elements are radioactive and undergo radioactive decay as well as spontaneous fission, resulting in the emission of multiple neutrons and $\gamma$-rays. The detection of these signatures is the principle behind passive detection systems. The ability to detect illicit nuclear materials, in particular highly enriched uranium (HEU) is an important, yet challenging issue of concern in securing nuclear materials that are attempted to be smuggled into a country. A large percentage of goods imported and exported from the UK (and other countries)

are contained within shipped cargo containers, meaning efficient scanning techniques of these containers is of the utmost importance. Current systems in place are passive detection methods that involve using radiation portal monitors (RPMs) installed at international borders. An example of this type of system is given in Fig. 2.1. The majority of RPMs consist of multiple polyvinyl toluene (PVT) scintillators, due to their low cost and large coverage area. Because of their low resolution, isotope identification is difficult to measure. For neutron detection multiple pressurised $^3$He neutron detectors are placed around the cargo to be inspected [6]. Detection of both neutrons and $\gamma$-rays is based on observing a significant increase in the total amount of counts measured above the background. The main advantages of these systems over active interrogation techniques are:

- Due to there being no irradiating source the system becomes simpler to deploy.
- Since there is not an irradiating source no intense radiation dose is delivered to the target.


Fig. 2.1 *Example display of a radiation portal monitor employed at an international border crossing [7].*

During the decay process, a radionuclide will usually undergo $\alpha$ or $\beta$ decay resulting in the formation of a decay product, with this decay product often left in an excited state. The emission of a $\gamma$-ray allows this newly formed excited nucleus to lose energy and reach a lower (normally ground), more stable state. If the emitted $\gamma$-ray has high enough energy, it is able to penetrate through any surrounding fissionable materials and shielding. In addition to undergoing $\alpha$ and $\beta$ decay, ultra-heavy radionuclides can also spontaneously fission resulting in the production of two (sometimes more) daughter nuclides, 2-3 neutrons and multiple photons. These signatures are of interest when detecting nuclear material via passive methods. A description of each of these radioactive processes is given in section 2.3.

Gamma-rays and neutrons will also be present in the background. Gamma-rays are produced from radionuclides within the soil, such as the $\gamma$-rays emitted when $^{238}$U, $^{232}$Th and $^{40}$K undergo radioactive decay. Neutrons are also naturally present in the surrounding environment, as they are produced by radioactive contaminants and the interaction of cosmic rays in the upper atmosphere. These cosmic-ray neutrons reach the surface with a continuous flux of $\approx 30$ neutrons $s^{-1}$ $m^{-2}$ [8]. Large intensity variations of the neutron background can occur aboard large ships where, due to the high volume of material (particularly iron and lead), high-energy neutrons can produce multiple secondary neutrons with MeV energies via spallation [9].

Current RPM gross count algorithms attempt to detect an elevated rate of $\gamma$-rays or neutrons above the background. The total amount of background $\gamma$-rays and neutrons detected by the RPMs is continuously measured, while no vehicle is present. Over a certain time interval the probability of detecting those $\gamma$-rays or neutrons present in the background will remain constant, since their arrival times are random. Upon the introduction of a vehicle to be inspected, the total amount of $\gamma$-rays and neutrons over a specific time interval is measured. The measured amount when a vehicle occupies the inspected volume is compared to the average background rate over the same time interval [10]. If nuclear material is present, then $\gamma$-rays and neutrons produced by nuclear materials will be detected in addition to the background. Therefore measuring an increased rate of $\gamma$-rays or neutrons over a defined time period will provide an unambiguous signature of nuclear material [11]. Given the average background rate, the threshold that the number of counts must be above for detection to be made is given by

Eq. (2.1):

$$T = B + k\sqrt{B} \tag{2.1}$$

where $T$ is the gross count threshold, $B$ is the background count rate and $k$ is the sigma level. A high detection efficiency with a low false alarm rate is required, therefore $k$ = 4 is often used.

There are a number of issues with passive detection techniques. Although an elevated rate of $\gamma$-rays can be detected if the nuclear material is unshielded, these signatures are both low in intensity and in energy. Therefore a sufficient amount of high-$Z$ materials placed around any nuclear materials present, can attenuate the number of $\gamma$-rays to below the threshold required for detection to be made. This makes detection of shielded nuclear materials for security applications in short time periods, with low false positives, problematic for passive techniques. While emitted neutrons will have no problem overcoming high-$Z$ shielding, this method of detection is limited to certain radionuclides ($^{238}$U and some Pu isotopes) where the specific activity for spontaneous fission is high. For radionuclides where this is not the case ($^{235}$U) a sufficient increased rate of neutrons will not be produced, hence detectors will struggle to measure elevated levels of neutrons above the background.

A secondary concern with passive techniques is the lack of information that can be gathered upon an alarm. Many cargo containers will house materials that naturally undergo radioactive decay (fertiliser, cat litter, etc), as these materials can contain trace amounts of uranium, thorium or potassium. Therefore if the cargo possesses sufficient quantities of these materials, the amount of $\gamma$-rays detected may be above the alarm threshold, resulting in a false alarm.

Finally the technique of using gross counts over time to detect nuclear materials is sensitive to baseline suppression [12]. Baseline suppression occurs when placing a vehicle to be inspected between the radiation portal monitors. The presence of a vehicle acts to absorb a number of the background $\gamma$-rays and therefore reduce the number detected. Therefore the background count of $\gamma$-rays measured while a vehicle occupies the inspected region is lower than when no vehicles are present. This effect raises the detection threshold, meaning sources that would have caused an alarm no longer do.

A final consideration to be discussed is whether detectors with greater energy resolution

can be used to enhance passive interrogation techniques when detecting unshielded nuclear materials. Each radioactive isotope has a well described $\gamma$-ray spectrum that is distinguishable from each other and from background signals. Through measuring these emitted $\gamma$-rays the identity and quantity of certain radionuclides can be determined. Fig 2.2 displays a comparison of the natural background $\gamma$-ray spectra for plastic (PVT), sodium iodide (NaI), cadmium zinc telluride (CZT) and high purity germanium (HPGe) $\gamma$-ray detectors, in the energy range 30 keV to 3000 keV [13]. It is clearly evident from Fig. 2.2 that given a high energy resolution and efficiency, individual $\gamma$-ray peaks are able to be identified.

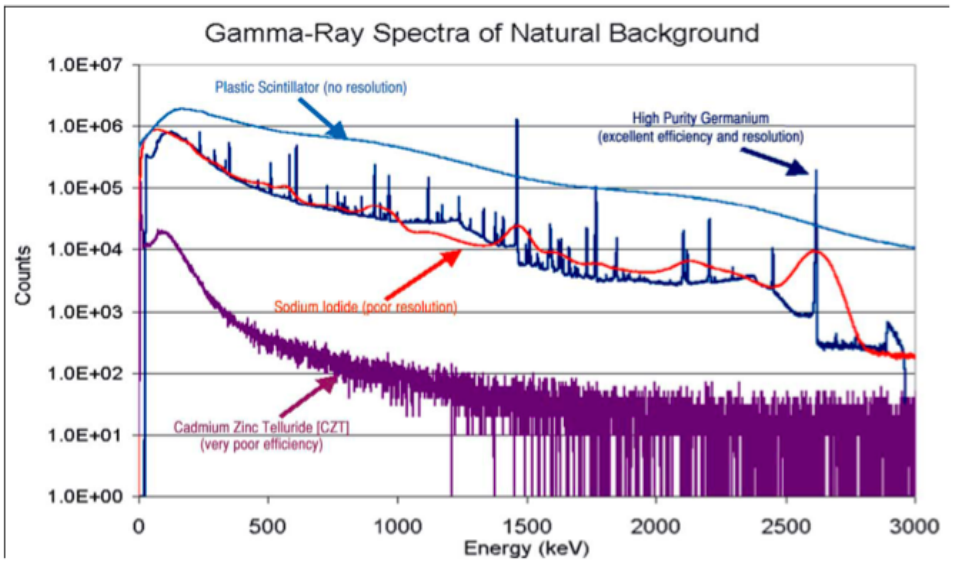


Fig. 2.2 *A comparison of the natural background $\gamma$-ray spectra for plastic (PVT), sodium iodide (NaI), cadmium zinc telluride (CZT) and high purity germanium (HPGe) $\gamma$-ray detectors, in the energy range 30 keV to 3000 keV [13].*

The effect shielding has on the ability to detect HEU is shown in Fig. 2.3 [14]. The unique signatures of HEU observed on its $\gamma$-ray spectra are its 185 keV peak, produced when $^{235}$U undergoes radioactive decay and its 2614 keV peak, produced if the sample contains $^{232}$U as a contaminant. However, due to the low energy of emitted 185 keV $\gamma$-rays, they are readily attenuated by shielding down to background levels meaning it is not useful for detecting shielded HEU. The 2614 keV peak is also problematic since it requires the contamination of the sample with $^{232}$U. Despite being highly penetrating, the 2614 keV $\gamma$-ray is also present in background radiation as it is emitted from $^{208}$Tl,

which is a daughter product of the $^{232}$Th series. Therefore any signatures which could be detected, may end up being hidden by the high background [14]. The decay chain of $^{232}$Th is displayed in Fig. 2.4. $^{232}$U will undergo $\alpha$ decay to $^{228}$Th, at which point it will move through the same decay sequence given in Fig. 2.4 (from $^{228}$Th). Therefore both isotopes will result in the emission of the 2614 keV peak.

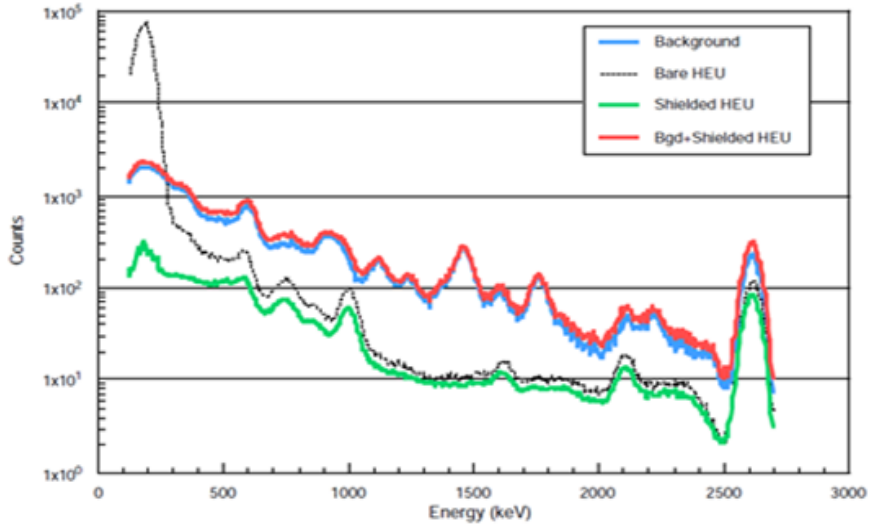


Fig. 2.3 *Computer synthesised sodium iodide $\gamma$-ray pulse-height spectra from a 1 kg source of HEU and background radiation using COG code from LLNL [14].*

A secondary technique has been developed to help detection capabilities, which involves actively interrogating the cargo with either neutron or photon beams in an attempt to induce fission in any special nuclear material (SNM) present. This type of technique is known as active interrogation.

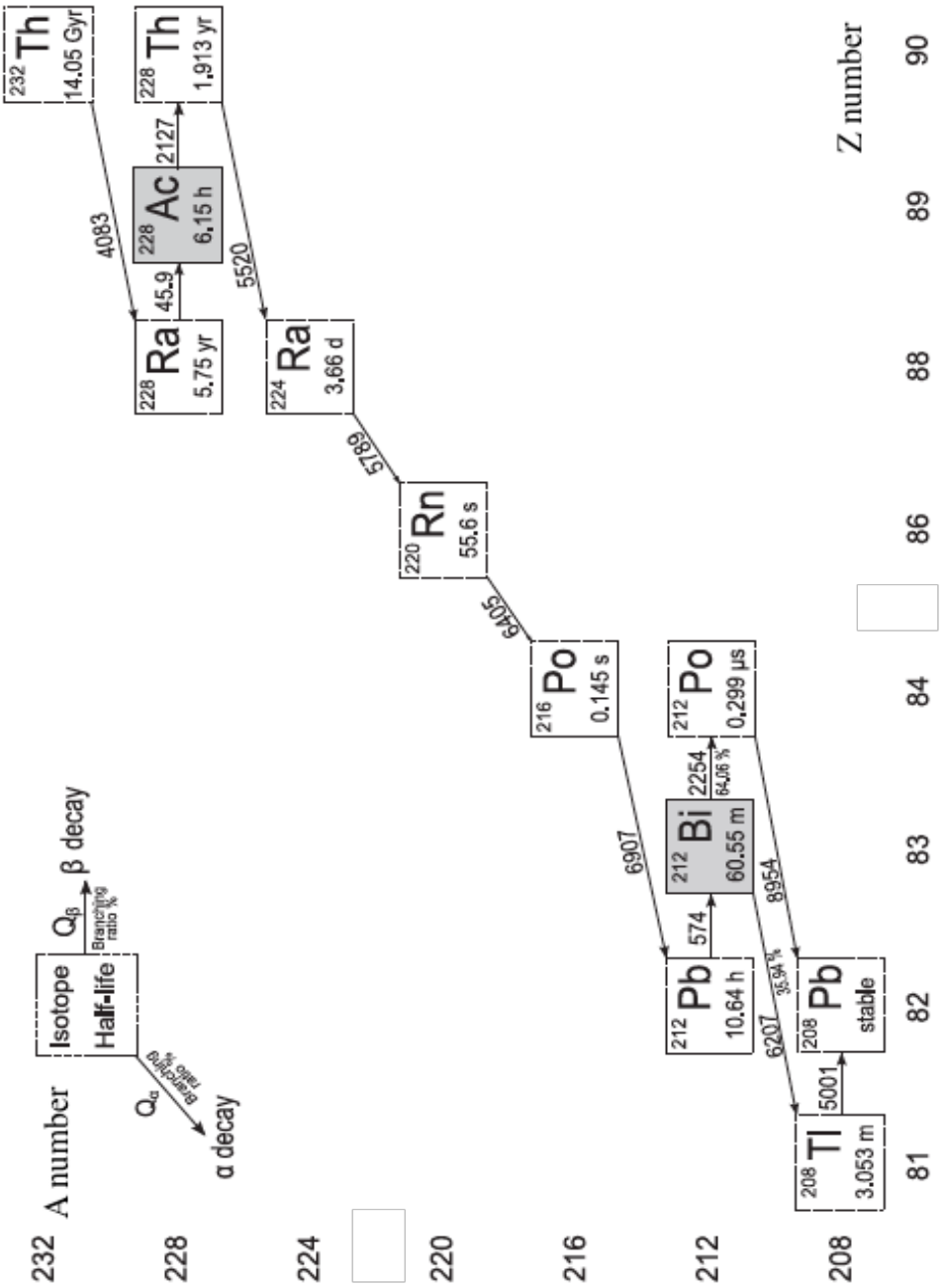


Fig. 2.4 $^{232}$*Th decay chain. The figure is taken from [15].*

## 2.2 Active Interrogation

As discussed in section 2.1, while signatures for passive detection may be detectable under the right conditions, they are also easily hidden from detection through the use of shielding. When detecting special nuclear material (SNM) for security applications it is reasonable to assume that anyone attempting to smuggle SNM, will have shielded it in order to overcome passive detection.

Active interrogation involves the use of highly penetrating particles (photons, neutrons and other particles) that have sufficient energy to pass through any surrounding shielding and/or cargo, before interacting with any SNM present. The interaction between incident radiation and target nuclei, at the appropriate energy, can result in the capture of the radiating particle by the SNM nucleus, which in-turn acts to induce nuclear fission. Fission is the process in which incident radiation is absorbed by a nucleus causing it to fragment into two or more daughter nuclei of unequal mass. In addition to this, subsequent energy is released along with other secondary products, such as neutrons and $\gamma$-rays. A simple schematic of this process is shown in Fig. 2.5 with these additional neutrons and $\gamma$-rays known as fission specific signatures.

These signatures represent the characteristic signals to be detected when determining the presence of SNM. There are four types of fission specific signature that are detectable when attempting to observe SNM. These are:

- Prompt neutrons.
- Delayed neutrons.
- Prompt $\gamma$-rays.
- Delayed $\gamma$-rays.

The multiplicity of these signatures is dependent on the energy of the interrogating particle along with the nucleus that is undergoing fission ($^{235}$U, $^{238}$U, $^{239}$Pu) [16]. Prompt signatures represent those that are emitted almost simultaneously, within $10^{-15}$ seconds of the fission event. On average upon undergoing fission by either neutrons or $\gamma$-rays, approximately 6-7 prompt $\gamma$-rays along with 2-3 prompt neutrons are emitted. The advantage of detecting these signals is that they represent some of the most numerous signatures available when attempting to observe SNM. Unlike prompt signatures,

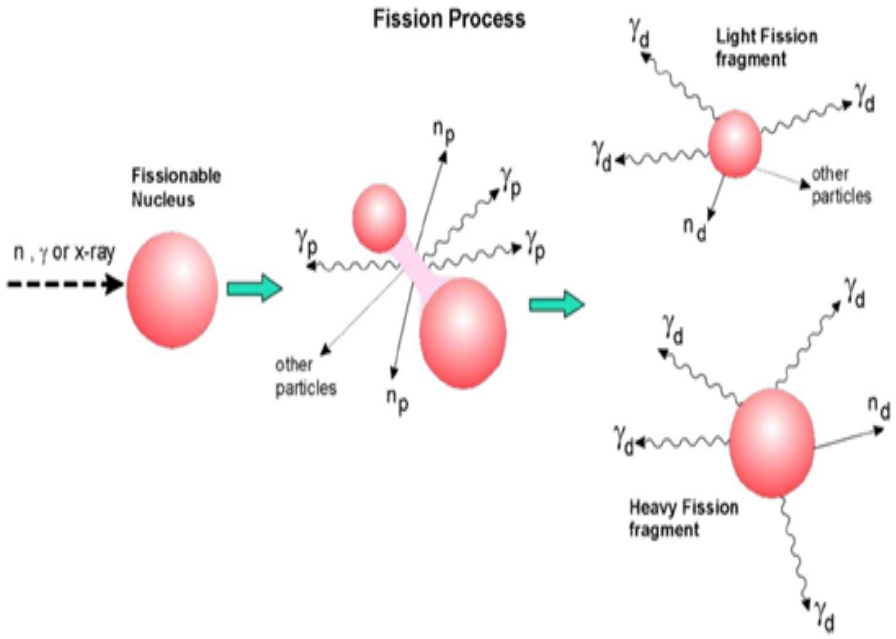


Fig. 2.5 *Simple schematic of the fission process [16].*

delayed signatures are not produced as a direct result of the fission event, but are instead emitted at a time much after interrogation. They are produced when the fission products undergo subsequent decay (usually $\beta$ decay, which is sometimes followed by neutron emission) to get to a more stable state. Since there is a wide range of fission products that can be produced all with a unique decay time, subsequent time scales for these signatures can range from seconds to minutes. Table 2.1 gives a summary of these fission signatures. Gamma-rays, whose energies exceed 3 MeV are of particular interest since there very few naturally occurring background photons having energies greater than 2.614 MeV. A description of how prompt and delayed neutrons and $\gamma$-rays are produced after the fission event is given in section 2.3.

### 2.2.1 Interrogation Sources

As mentioned previously, both neutrons and photons can be used as interrogation sources. The production of interrogating neutrons or photons can occur in a variety of ways. For neutron production, the easiest method involves using radioactive nuclei which upon decaying, emits the desired particle. Sources for this process include nuclei that un-

Table 2.1 Summary of prompt and delayed fission signatures (approximate yields per fission) for a number of radioisotopes.

| Fission Signature | Interrogation Source | $^{235}$U | $^{238}$U | $^{239}$Pu |
|---|---|---|---|---|
| Prompt neutrons | Thermal neutrons | 2.41 [17] | - | 2.88 [17] |
| Prompt neutrons | Neutrons with $E$>2.5 MeV or photofission | 2.8 [16] | 2.9 [16] | 3.16 [17] |
| Prompt $\gamma$-rays | Neutron and photofission | 6.6[18] | 6.7 [16] | 7.06 [18] |
| Prompt $\gamma$-rays ($E$>3 MeV) | Neutron and photofission | 0.2 [19] | 0.3 [16] | 0.3 [19] |
| Delayed neutrons | Neutron Fission | 0.015 [20] | 0.044 [20] | 0.0061 [20] |
| Delayed neutrons | Photofission (10.2 MeV endpoint) | 0.0113 [21] | 0.0306 [21] | 0.0037 [21] |
| Delayed $\gamma$-rays ($E$>3 MeV) | Neutron and photofission | 0.127 [20] | 0.11 [20] | 0.065 [20] |
| Delayed $\gamma$-rays ($E$>4 MeV) | Neutron and photofission | 0.046 [20] | 0.03 [20] | 0.017 [20] |

dergo spontaneous fission, such as $^{252}$Cf which produce neutrons with a most probable energy of $\sim$1.2 MeV, or ($\alpha$, n) sources such $^{241}$Am($\alpha$,n)$^{7}$Li, which produce low energy neutrons (average $E$ = 0.5 MeV). However, neutrons used for active interrogation are normally produced using pulsed neutron generators (PNG's) or electronic neutron generators (ENG's). These generators work through accelerating charged particles (deuterium or protons) into a target material (deuterium, tritium, lithium, beryllium). The target material will absorb the accelerated particle resulting in the formation of a compound nucleus. This nucleus is unstable and will result in the emission of a neutron [22]. The energy of emitted neutrons will depend on both the target material used and the energy of the incident neutron. Neutron energies emitted by several accelerator-based neutron reactions have been taken from [23], and can be viewed in Fig. 2.6 [23]. The energies of the interrogation neutrons can be altered through placing extra materials between the source neutrons and volume to be interrogated.

For photons the radioactive sources $^{137}$Cs and $^{60}$Co are used to produce $\gamma$-rays of 0.66 MeV and 1.17 or 1.33 MeV respectively [24]. Photons of this energy are typically used for imaging techniques, as they have sufficient energy to penetrate large amounts of cargo, but their energy is lower than that required for fission to occur [25]. In order to generate photons of sufficient energy to induce fission, electron accelerators are used. In a typical set-up electrons are generated by an accelerator with energies of 9-10 MeV. These electrons are fired into high-$Z$ materials such as tungsten or tantalum. The

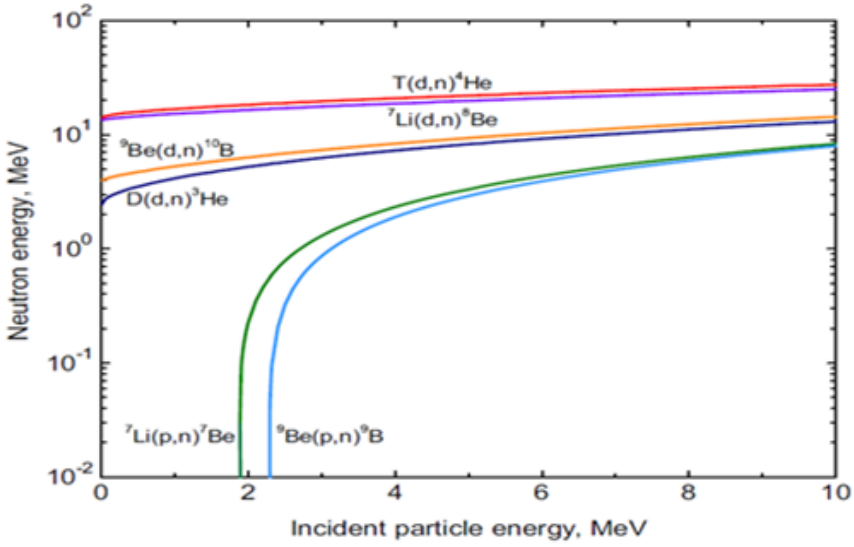


Fig. 2.6 *Neutron energies emitted as a function of incident particle kinetic energy (at the 0° emission angle) for multiple accelerator based neutron reactions [23].*

interaction between these electrons and the atomic electrons of the material, result in the formation of multiple photons. The photons produce a continuous spectrum due to bremsstrahlung, with the maximum energy possible equal to the maximum energy of the electron beam. This maximum energy is important, as in order for a high percentage of photons to induce fission this energy must be much greater than the minimum required for fission to occur. The accelerator is often operated in a pulsed mode with the pulse widths usually being a few $\mu$s in duration. A pulsed configuration reduces the interrogating source from contributing too heavily to the background, which any signals are to be detected against. This type of source is used due to its ability to generate fission in shielded SNM through two different avenues. The first being fission induced directly through the interaction between interrogation photons and SNM. The second as a result of the interrogation photons interacting with any surrounding material, producing neutrons, with these neutrons then going on too induce fission in any SNM.

### 2.2.2 Background Interferences

The main drawback to methods that utilise interrogating sources is that the source can induce certain nuclear reactions in surrounding materials. This generates additional

secondary neutrons and photons, which can act to mask both prompt and delayed signatures. For prompt signatures both photon and neutron interrogation sources produce large levels of background radiation, which act to 'drown out' the unique signatures that are looked for. Either interrogation source (neutron or photon beam) will act to mask the signature of same particle type, as well as producing excess neutrons and $\gamma$-rays through interactions with the surrounding medium. Neutron interrogation typically results in the production of a multitude of high energy photons. In photon interrogation, significant prompt neutron emissions occur through the interaction of interrogation photons with surrounding low-$Z$ materials. Both neutrons and photons produced in these processes have energies that overlap those produced through the fission of SNM. This requires any detection techniques that act to utilise prompt signatures to either account for or suppress these background signatures. A summary of some notable photon-induced interferences are shown in Table 2.2 [23].

When detecting delayed signatures, the activation of certain isotopes within the cargo can lead to their subsequent decay via emission of either neutrons or $\gamma$-rays. Following photon interrogation, the detection of delayed neutrons from nuclear materials can be hindered through the creation of delayed neutrons via the interaction of interrogation photons with surrounding cargo. Most notable here is the delayed neutron produced from the activation of $^{18}$O, which is present in both the atmosphere and water. Upon activation by a $\gamma$-ray, $^{18}$O will decay to form $^{17}$N. Since $^{17}$N is unstable, it will undergo $\beta$ decay to form $^{17}$O, with a half-life for this process of 4.173 s. $^{17}$O is left over in an excited state and will itself undergo neutron emission to form $^{16}$O. This decay chain is shown in Eq. (2.2), Eq. (2.3) and Eq. (2.4).

$$^{18}O + \gamma \rightarrow ^{17}N + p \tag{2.2}$$

$$^{17}N \rightarrow ^{17}O^{*} + e- + \overline{\nu}_e \tag{2.3}$$

$$^{17}O^{*} \rightarrow ^{16}O + n \tag{2.4}$$

For neutron interrogation, multiple neutron capture $\gamma$-rays are produced via the interaction of these interrogation neutrons with isotopes present in the surrounding medium. Activations include, $^{48}$Ca(n,p)$^{48}$K, $^{34}$S(n,p)$^{34}$P and $^{37}$Cl(n,$\alpha$)$^{34}$P however, the activa-

tion of oxygen $^{16}$O(n,p)$^{16}$N, and fluorine $^{19}$F(n,$\alpha$)$^{16}$N are of particular concern since both activations produce a 6 MeV $\gamma$-ray. The reaction threshold for $^{16}$O(n,p)$^{16}$N is $\approx$10.4 MeV therefore interrogation neutrons with an energy less than 10 MeV are used to counteract this signature. Since the reaction threshold for $^{19}$F(n,$\alpha$)$^{16}$N is much lower ($\approx$1.6 MeV) it represents a signature that is much harder to remove. Table 2.2 lists some of these neutron induced interferences [23].

Table 2.2 Some photon and neutron induced interferences.

| Reaction | Interrogation Source | Prompt or Delayed Interference | Reaction Threshold (MeV) | Significant Emissions |
|---|---|---|---|---|
| $^{2}$H($\gamma$,n)$^{1}$H | $\gamma$ | Prompt | 2.226 | n |
| $^{6}$Li($\gamma$,n)$^{5}$Li | $\gamma$ | Prompt | 5.666 | n |
| $^{6}$Li($\gamma$,p)$^{5}$He | $\gamma$ | Prompt | 4.590 | n |
| $^{6}$Li($\gamma$,np)$^{4}$He | $\gamma$ | Prompt | 3.700 | n |
| $^{7}$Li($\gamma$,n)$^{6}$Li | $\gamma$ | Prompt | 7.254 | n |
| $^{9}$Be($\gamma$,n)$^{8}$Be | $\gamma$ | Prompt | 1.666 | n |
| $^{17}$O($\gamma$,p)$^{16}$N | $\gamma$ | Delayed (7.13 s) | 13.79 | $\gamma$ ($E_\gamma$ = 6.129 MeV) |
| $^{18}$O($\gamma$,p)$^{17}$N | $\gamma$ | Delayed (4.17 s) | 15.95 | n |
| $^{19}$F(n,$\alpha$)$^{16}$N | n | Delayed (7.13 s) | 1.6 | $\gamma$ ($E_\gamma$ = 6.129 MeV) |
| $^{34}$S(n,p)$^{34}$P | n | Delayed (12.4 s) | 4.7 | $\gamma$ ($E_\gamma$ = 2.127 MeV) |
| $^{37}$Cl(n,$\alpha$)$^{34}$P | n | Delayed (12.4 s) | 1.6 | $\gamma$ ($E_\gamma$ = 2.127 MeV) |
| $^{16}$O(n,p)$^{16}$N | n | Delayed (7.13 s) | 10.4 | $\gamma$ ($E_\gamma$ = 6.129 MeV) |

There are multiple advantages of active interrogation systems over their passive counterparts. Firstly, the conditions in which detection is most favourable can be optimised through altering the interrogation radiation intensity and energy. A second advantage is the increased amount of fissions, and therefore signals available to detect. However, these techniques are hampered with higher background levels and increased dose rates, with these problems needing to be addressed. Some of the current techniques which have attempted to overcome the inherent problems with detecting prompt and/or delayed signatures will be discussed in the next section.

### 2.2.3 Techniques that Detect Prompt Signatures

The advantage of utilising techniques that detect prompt signatures are the increased multiplicity, lower dose rates and decreased scan time. These signatures are produced

within $10^{-15}$ seconds of the initial reaction. Techniques that act to detect these signatures, must overcome the issue of high background radiation. Primary in this field is differential die away analysis (DDAA), which uses a pulsed neutron beam at energies of $\sim$ 14 MeV [26, 27]. As the neutron pulses impinge on the cargo, some neutrons will rapidly lose energy, become thermalised and can be absorbed. The number of epithermal and fast neutrons present within the cargo will fall away within a few microseconds. Those neutrons that have lost energy to become thermal neutrons will decrease in number much more slowly, with times of the order of a few hundred $\mu$s to several ms. This characteristic time is dependent on the material and density of the medium being examined and is known as the die-away time of the medium. If SNM is present these thermal neutrons will cause fission to occur, resulting in the production of a new source of prompt neutrons. Therefore if fissile material is present, the population of epithermal and fast neutrons will decrease much more slowly than if no SNM is present. If no fissile material is present, only the cargos characteristic neutron 'die-away' time plus the natural background is detected. However, if fissile material is present an additional signal is detected above the mediums own characteristic signal [28]. This additional signal is a unique signature of SNM. An example of this feature is shown for $^{235}$U in Fig. 2.7 [28]. Detection is made using moderated $^{3}$He detectors.

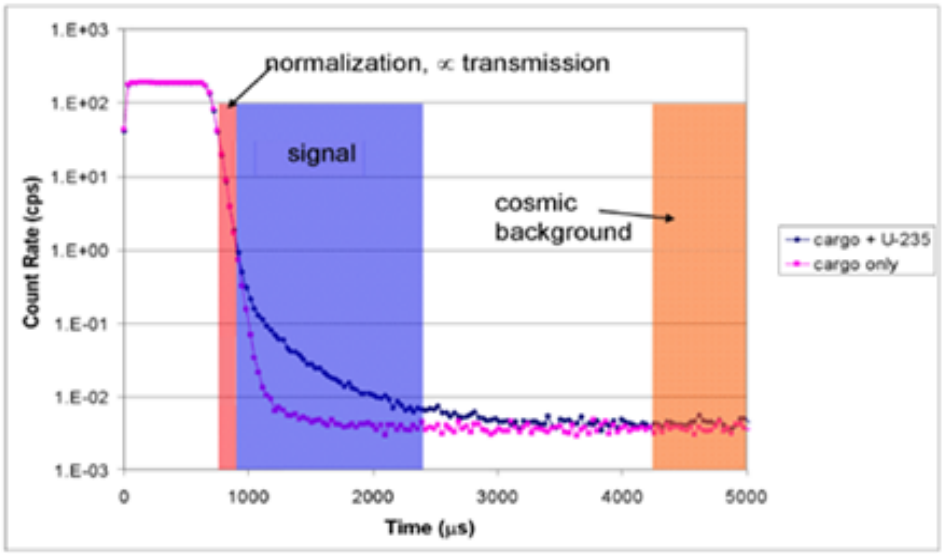


Fig. 2.7 *Representative time dependence of DDAA signals in cargo, with and without* $^{235}U$ *[28]. The target used was 350 g of 20 % enriched uranium. Neutrons were generated using a pulsed neutron beam at energies of* $\sim$ *14 MeV.*

The capability of this technique to detect $^{235}$U when surrounded by hydrogenous material has been demonstrated [28]. In particular [26, 27] has shown the proficiency this technique has when detecting $\sim$ 350 g of $^{235}$U that has been surrounded by wood or paper, with detection fully established within 100 seconds [26, 27].

As discussed, when the neutron generators are 'on', detection methods for prompt neutrons are problematic due to the high background. With this in mind, systems have been developed that use low energy (average energy $\sim$ 0.06 MeV) neutrons as their interrogation source [29, 30]. Neutrons are generated via the $^{7}$Li(p,n) reaction and due to their low energies, almost all are absorbed by the cargo. This means the background caused by the interrogation source is almost negligible; meaning even a small level of counted prompt neutrons is enough to infer the presence of SNM. The low background also enables measurements to be taken at the same time as when the cargo is being inspected. The main background comes from large levels of $\gamma$-rays produced by captured neutrons. However, although 60 keV neutrons have been shown to penetrate medium and high-$Z$ materials almost as efficiently as higher energy neutrons [30], if hydrogenous cargo is present the neutrons are much more efficiently absorbed than their higher energy counterparts. Therefore if significant levels of hydrogenous cargo are present, the neutrons will not penetrate far enough to reach any SNM.

In addition to the techniques discussed, further techniques that use prompt neutrons for SNM detection have been demonstrated. When considering photons as the interrogation source, prompt neutrons can be emitted from any surrounding materials, if the energy of the incident photon is large enough. In order to circumvent this issue, photons are used with energies low enough to prevent significant numbers of neutrons being generated from common benign materials. As incident energy decreases so does the photofission cross-section of any fissionable nuclei. Therefore a fine balancing act is required between having a high enough energy to induce fission, but low enough so neutron production will not be induced in the surrounding material. Fig. 2.8 displays the photofission and photoneutron cross sections for a number of isotopes for incident $\gamma$-ray energies of 5 - 30 MeV [16].

In such a system gross counting of neutron emissions will be enough to determine the presence of SNM, since prompt neutron production from the surrounding material should have been eliminated. The current systems that incorporate this technique use

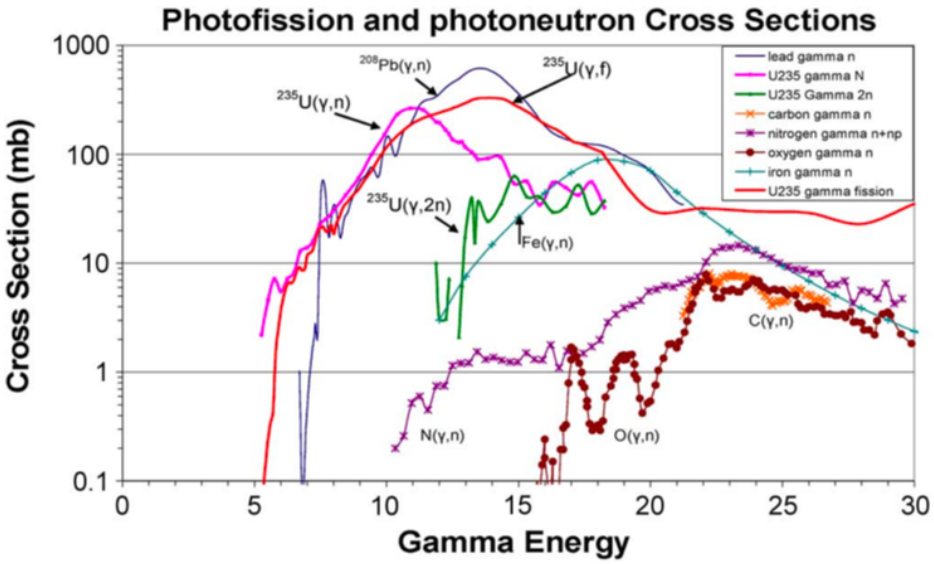


Fig. 2.8 *Photofission and photoneutron cross sections for a number of isotopes in the 5 to 30 MeV endpoint X-ray energy range [16].*

incident photons with an energy of 6-9 MeV [31]. Material detection is made through counting the level of prompt neutrons during interrogation [32, 33]. However, despite the low energy of source photons, certain isotopes (such as $^{9}$Be and deuterium) still have a ($\gamma$, n) reaction threshold that is low enough to produce significant amounts of neutrons. Therefore false alarms become a concern if a significant amount of these materials is present [31]. While $^{9}$Be is a fairly rare isotope and therefore unlikely to be present in high enough quantities to produce a false alarm, hydrogenous cargo (deuterium containing cargo) is very common and hence could result in significant background neutrons.

Currently much fewer studies have been conducted into the detection of prompt $\gamma$-rays for nuclear materials assay. Applications involving neutron sources and prompt $\gamma$-ray detection (Prompt Gamma Neutron Activation Analysis - PGNAA) have traditionally been used in assaying unwanted metal contaminants (such as mercury, cadmium or lead) in mixed nuclear waste containers [34] as opposed to illicit nuclear material detection.

### 2.2.4 Techniques that Detect Delayed Signatures

Unlike prompt signatures, delayed signatures do not have to contend with detection being made against the interrogation source. Due to their unique signature, much work has been done into detecting delayed neutrons following photon induced fission. Primary in this category is the pulsed photonuclear assessment (PPA) inspection system, which has been developed by Idaho National Laboratory (INL) in conjunction with Los Alamos National Laboratory (LANL) and Idaho State University's Idaho Accelerator Center (IAC) [35, 36]. This system uses a variable electron accelerator (2-12 MeV) to generate photons in 3 $\mu$s pulses, to inspect the cargo. These photons then produce neutrons via fission with any SNM present. Delayed neutrons are emitted by fission products. A description of the fission process and how delayed fission products are produced is given in section 2.3. If no nuclear material is present then the delayed region ($\sim$ 2 ms after the end of the pulse) will be free of neutrons. Therefore the detection of neutrons after the initial photon flash has died away ($\sim$ 2 ms), is a good indication of fissionable material being present [37]. Standard polyethylene moderated $^{3}$He gas neutron detectors are used and the system has been shown successful in detecting a 4.8 kg depleted uranium sample, amongst a variety of shielding materials including, polyethylene, wood and iron [35, 36]. However, similar to all techniques that rely on delayed neutrons, they represent a fairly low energy, low abundance signal. High levels of shielding will therefore cause significant attenuation of these signals, posing significant challenges for definitive detection.

In addition to delayed neutrons, delayed $\gamma$-rays can also be used for SNM detection. These delayed $\gamma$-rays are produced through the $\beta$ decay of fission products. For systems that use neutrons as the interrogating source, delayed $\gamma$-rays are the signal of choice. The majority of neutron interrogation set-ups use a pulsed beam configuration. Once switched off any neutrons present falloff within a few tens of milliseconds, leaving only the natural backgrounds and delayed $\gamma$-rays to detect. One of the most efficient techniques which exploits this signature is the a system developed at LLNL known as 'The Nuclear Car Wash' [20, 38]. In order to combat interferences caused by activation of background materials, the interrogation neutrons were generated with energies ranging from 3.5-7 MeV. This prevents the activation of $^{16}$O(n,p) (since the energy required for this reaction is $\sim$ 10.4 MeV), greatly reducing background interferences. The neutron generator is placed below ground, with the inspected cargo passed over the generator at a constant rate. As the cargo passes over the generator the entire sample is irradiated.

Delayed $\gamma$-rays are detected by plastic scintillators, located at either side of the cargo. A schematic of this set-up is shown in Fig. 2.9 [20]. The technique has been shown to be capable of detecting 5 kg of HEU within 30 s in a variety of different scenarios both experimentally and via computational modelling [20, 38]. Scenarios include surrounding the target with low-$Z$ material (plywood), and hydrogenous material (polyethylene) [20, 38]. However for high-$Z$ materials (lead), once the thickness of shielding increases above 40-80 g/cm$^2$, the detection of delayed $\gamma$-rays becomes more problematic, as they become readily attenuated down to background levels [20].

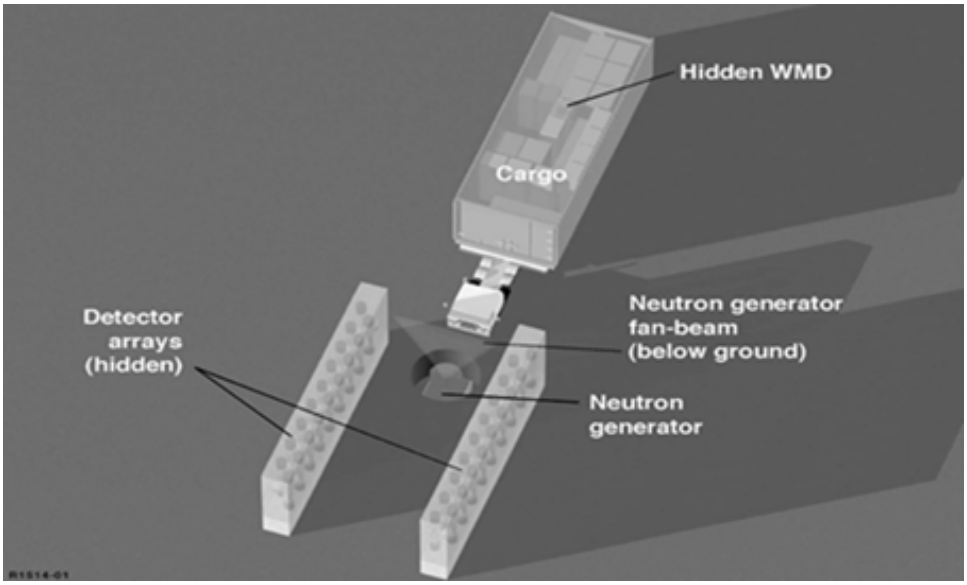


Fig. 2.9 *Schematic of nuclear car wash developed at LLNL [20].*

### 2.2.5 Summary of Active Interrogation Methods

Solutions to the problem of shielding for passive interrogation have been considered in the area of active interrogation. Active interrogation introduces beams of photons or neutrons at the cargo to be inspected. The interrogation source is used in an attempt to induce fission in any SNM and thus provides a means of increasing the intensity of the signatures emitted. However, the implementation of active interrogation techniques comes at a cost, not only financially but also in terms of dose delivered to the target, induced backgrounds and system complexity. These issues cause the benefits of active

techniques to not be as clear-cut as it first appears and are the main reasons why they are yet to be implemented. Therefore, while there must certainly be optimism in this area of inspection, this optimism must be tempered given the issues which arise from implementing active techniques.

## 2.3 Radioactive Signatures for Passive and Active Interrogation Methods

The following section will give a brief description of the physics processes that occur when radioactive nuclei undergo decay and fission.

### 2.3.1 Radioactive Decay

As discussed in section 2.1, passive detection techniques look to observe neutrons and $\gamma$-rays emitted when nuclear materials undergoes radioactive decay. Fig. 2.10 displays the chart of isotopes, along with the type of decay they will undergo in order to get back to a stable state [39].

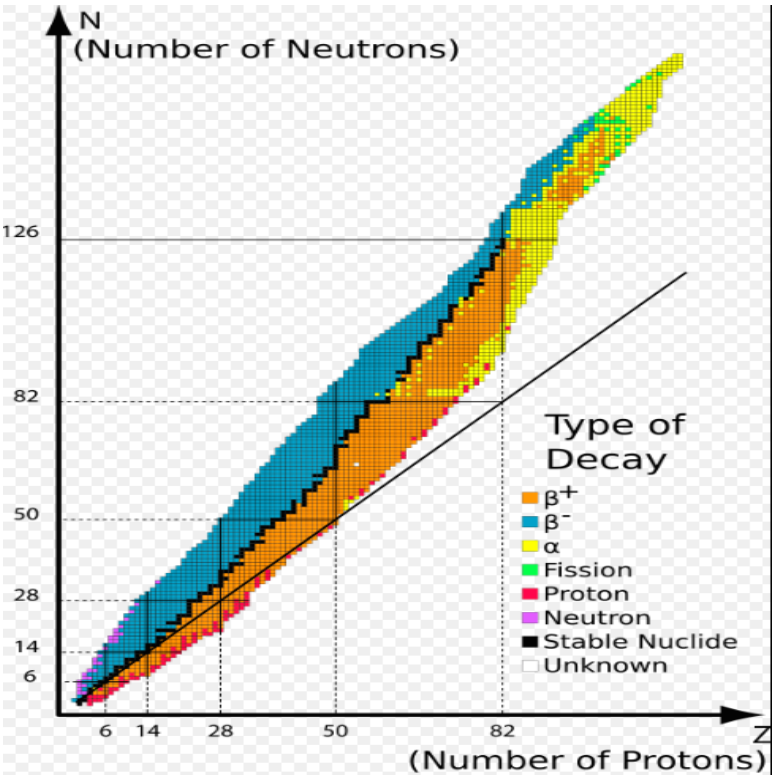


Fig. 2.10 *Chart of isotopes along with the type of decay they undergo. Black squares represent isotopes that are stable. Orange blocks display isotopes that undergo $\beta^+$ decay, blue squares are isotopes that undergo $\beta^-$ decay, yellow squares undergo $\alpha$ decay, green squares undergo fission, red squares undergo proton emission and purple squares undergo neutron emission [39].*

The primary types of decay suffered by radionuclides are $\alpha$ and $\beta$ decay. Upon under-

going $\alpha$ or $\beta$ decay, the produced nucleus can be left in an excited state. Relaxation to the ground state occurs through the emission of a $\gamma$-ray. Alpha decay mainly occurs in heavy nuclei, through emission of a helium nucleus. Beta decay can occur in one of three ways depending on the ratio of neutrons to protons within the nucleus. If this ratio is too high then $\beta^-$ decay, which involves the transformation of a neutron into a proton and emission of an electron, will occur. If this ratio is too low than the nucleus can be brought to a more stable state through either the conversion of a proton to a neutron and the emission of a positron, known as $\beta^+$ decay, or through the capture of an electron by the nucleus which turns a proton into a neutron, known as electron capture. The process of $\alpha$ decay is given by Eq. (2.5), $\beta^-$ decay by Eq. (2.6), $\beta^+$ decay by Eq. (2.7) and electron capture by Eq. (2.8).

$$ {}^{A}_{Z}N \rightarrow {}^{A-4}_{Z-2}N + {}^{4}_{2}He \tag{2.5} $$

$$ {}^{A}_{Z}N \rightarrow {}^{A}_{Z+1}N' + e^- + \overline{\nu}_e \tag{2.6} $$

$$ {}^{A}_{Z}N \rightarrow {}^{A}_{Z-1}N' + e^+ + \nu_e \tag{2.7} $$

$$ {}^{A}_{Z}N + e^- \rightarrow {}^{A}_{Z-1}N' + \nu_e \tag{2.8} $$

In addition to these decay modes, some radionuclides can also undergo spontaneous fission. This process is similar to induced fission, except the capture of a neutron is not required for the fission process to occur. The process of induced fission is discussed in the next section. Table 2.3 displays a comparison of the rate at which different isotopes produce neutrons via spontaneous fission for a number of different isotopes.

### 2.3.2 Induced Fission

As discussed in section 2.2, active interrogation techniques aim to induce fission in nuclear materials through irradiating a volume with neutrons or photons. Fig. 2.11 displays the cross-sections for neutron induced fission of $^{235}$U and $^{238}$U. It is clear from Fig. 2.11 that nuclear fission can be induced by thermal neutrons for $^{235}$U, whereas

Table 2.3 A comparison of the rate at which different isotopes produce neutrons via spontaneous fission. Given are the half-life, the probability for fission to occur, number of neutrons per fission and the number of neutrons emitted by the isotope per second per gram [40].

| Isotope | Half-life | Fission probability per decay (%) | Neutrons per fission | Neutrons/gram/sec |
|---|---|---|---|---|
| $^{233}$U | $1.59 \times 10^5$ y | $1.3 \times 10^{-10}$ | 1.76 | $8.6 \times 10^{-4}$ |
| $^{235}$U | $7.04 \times 10^8$ y | $2.0 \times 10^{-7}$ | 1.86 | $3.0 \times 10^{-4}$ |
| $^{238}$U | $4.47 \times 10^9$ y | $5.4 \times 10^{-5}$ | 2.07 | 0.0136 |
| $^{238}$Pu | 87.7 y | $1.8 \times 10^{-7}$ | 2.28 | $2.7 \times 10^3$ |
| $^{239}$Pu | $2.41 \times 10^4$ y | $4.4 \times 10^{-10}$ | 2.16 | $2.2 \times 10^{-2}$ |
| $^{240}$Pu | 6569 y | $5.0 \times 10^{-6}$ | 2.21 | 920 |
| $^{241}$Pu | 14.35 y | $5.7 \times 10^{-13}$ | 2.25 | 0.05 |
| $^{252}$Cf | 2.638 y | 3.09 | 3.73 | $2.3 \times 10^{12}$ |

only fast neutrons can cause fission to occur in $^{238}$U.

There is also the presence of multiple nuclear resonance peaks for $^{235}$U. These resonant peaks occur when the incoming neutron has an energy that is very close to the energy required to move the nucleus into an excited state. At these levels the probability of capture is increased. The extreme differences between $^{235}$U and $^{238}$U fission cross sections can be explained from the relationship between the excitation energy of the compound system formed when a neutron captures on uranium and the activation energy needed to overcome the fission barrier. The activation energy required to overcome the fission barrier for $^{236}$U is 6.2 MeV and for $^{239}$U is 6.6 MeV. For neutrons at thermal energies, we can consider them to have zero kinetic energy. The excitation energy when a neutron captures onto $^{235}$U to form the compound nucleus $^{236}$U$^*$ is given by Eq. (2.9).

$$E_{ex} = [m(^{236}U^*) - m(^{236}U)]c^2 \tag{2.9}$$

The mass of $^{236}$U$^*$ equals the mass of $^{235}$U + $m_n$ (mass of a neutron) and is 236.052589 u, where u is the atomic mass unit (1 u = 931.494061 MeV/c$^2$). The mass of $^{236}$U is 236.045563 u, therefore $E_{ex}$ = 6.5 MeV. This is greater than the 6.2 MeV required to overcome the activation barrier for fission to occur. A similar calculation for $^{239}$U yields $E_{ex}$ = 4.8 MeV, which is far smaller than the required activation energy needed for fission to occur in $^{239}$U. In order to reach this value (6.6 MeV) fast neutrons are

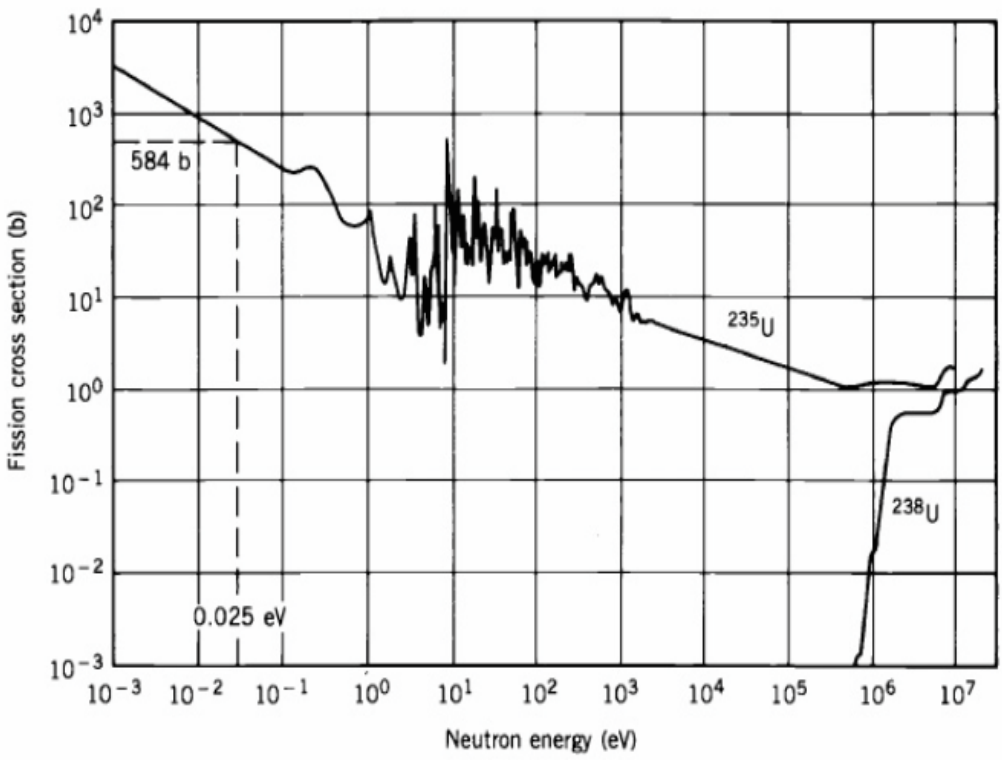


Fig. 2.11 *Cross section for neutron-induced fission of* $^{235}U$ *and* $^{238}U$ *[41].*

required.

Upon undergoing fission the nucleus of an atom splits into lighter nuclei, emits multiple neutrons and $\gamma$-rays, and emits a large amount of energy. These are known as the prompt signatures, with the multiplicity of these signatures for different nuclei given in Table 2.1. The neutron to proton ratio for uranium isotopes is $\approx 1.57$. The fission fragments (in addition to any emitted neutrons) must also have this initial ratio. However, stable nuclei around the mass of typical fission fragments, have neutron to proton ratios of $\approx$ 1.2 - 1.4, hence these fission fragments will undergo $\beta^-$ decay until a stable nuclei is reached. Both neutrons and $\gamma$-rays can be emitted from the $\beta^-$ decay products if they are left over in an excited state. An example schematic of how neutrons can be emitted from a fission decay product is displayed in Fig. 2.12 [41]. The time taken for neutrons to be emitted is dependent on the half-life of the isotope which emits them. Since few processes other than fission result in the production of delayed neutrons after the fission event they represent a strong signature for nuclear material.

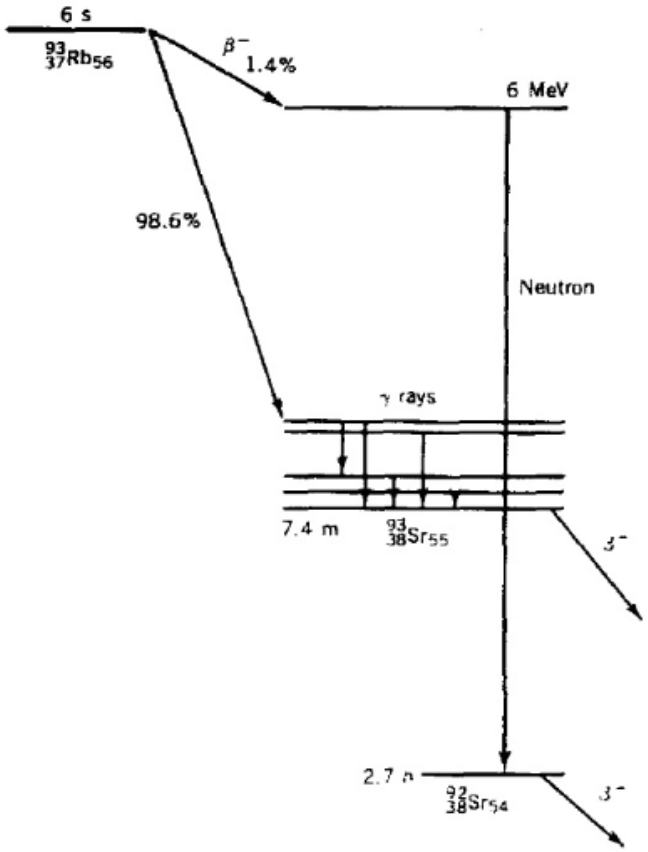


Fig. 2.12 *Delayed neutron emission from $^{93}$Rb. After the original $\beta$ decay, the excited state of $^{93}$Sr has enough energy to decay by neutron emission to $^{92}$Sr. The neutrons are delayed relative to the prompt fission neutrons by a time characteristic of the mean lifetime of $^{93}$Rb [41].*

## 2.4 Cosmic Rays

### 2.4.1 Cosmic Rays in the Atmosphere

Cosmic rays represent particles that have been accelerated to very high speeds by astrophysical sources. Although a fraction of them are generated by the sun, the majority are produced outside the solar system by multiple sources, including supernova [42, 43]. These particles are referred to as 'primary' cosmic rays and are primarily made up of nuclei ($\sim$98%, mostly high energy protons), with a fraction of electrons and positrons ($\sim$2%) [44]. They have a range of energies from 1 GeV up to $10^8$ TeV. The flux of primary cosmic-rays interacting with the Earth's atmosphere is dependent on a number of factors. For cosmic-rays that have originated outside of the solar system, the expanding magnetised plasma generated by the sun (solar wind), acts to decelerate and partially exclude the lower energy galactic cosmic-rays from the inner solar system. For the fraction of primaries generated by the sun there is a significant anti-correlation observed between solar activity (which has an alternating eleven-year cycle) and the intensity of cosmic-rays with energies below about 10 GeV. Finally, lower-energy cosmic rays are affected by the Earth's geomagnetic field, which must be penetrated to reach the top of the atmosphere [45]. Primaries have greater difficulty penetrating the Earth's magnetic field near the equator than they do near the magnetic poles, hence the intensity of any component of the cosmic radiation in the GeV range depends both on the location and time [45].

Upon entry into the Earth's atmosphere, due to the sudden increase in density, primary cosmic rays will collide with air nuclei, resulting in the production of additional 'secondary' particles. These particles are typically short lived and either decay or interact to produce more particles, before reaching the Earth's surface. This process is demonstrated in Fig. 2.13.

Muons are the result of the decay of charged mesons, such as pions. Pions can be neutral, positively charged or negatively charged. The decay of a charged pion will produce a muon with the same charge, in addition to a neutrino. Neutral pions will decay to produce $\gamma$-rays, which convert into $e$-/$e$+ pairs in what is known as the 'electromagnetic' part of the shower. Pion decays are shown in Eq. (2.10), Eq. (2.11) and Eq. (2.12).

$$\pi^+ \rightarrow \mu^+ + \nu_\mu \tag{2.10}$$

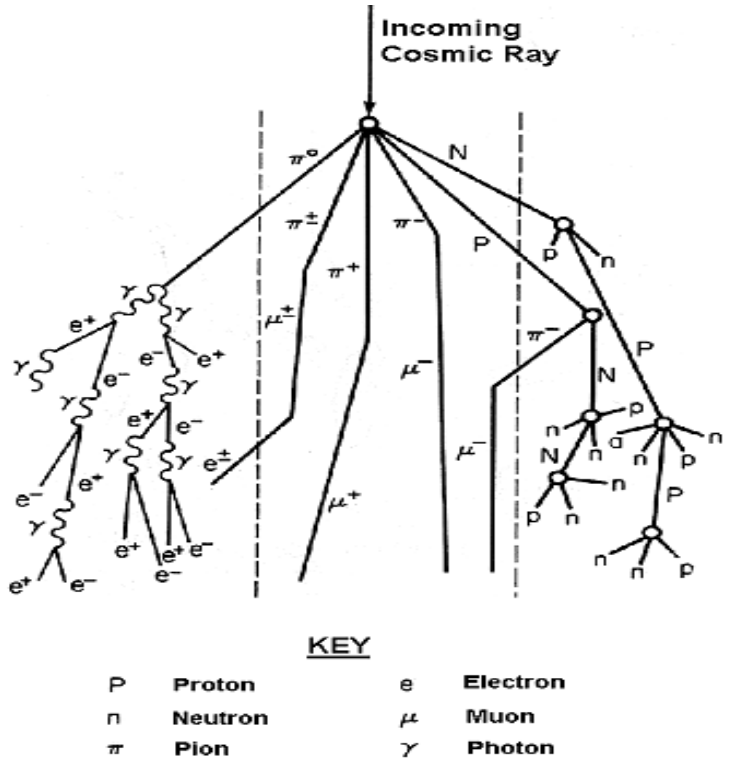


Fig. 2.13 *Illustration of the particle cascade produced in the atmosphere from a primary cosmic proton [46].*

$$\pi^- \rightarrow \mu^- + \overline{\nu}_\mu \tag{2.11}$$

$$\pi^0 \rightarrow \gamma + \gamma \tag{2.12}$$

Having a mass of 105.7 MeV/c$^2$ muons are often referred to as 'heavy electrons'. They have an average lifetime of 2.2 $\mu$s. Due to muons travelling near to the speed of light, the effects of special relativity acts to increase the lifetime of muons as we perceive it, thus enabling them to reach the surface.

Secondary cosmic-ray neutrons are also produced when primary cosmic rays collide with nitrogen and oxygen nuclei in the atmosphere. As they propagate through the atmosphere to the surface, they will also undergo interactions with atmospheric nuclei, resulting in a loss of energy and production of further additional particles.

### 2.4.2 Cosmic-Ray Muon Spectrum at the Earth's Surface

Typically produced at an altitude of 15 km [45] muons reach the Earth's surface with an average energy of $\approx 4$ GeV, having on average lost $\approx 2$ GeV of energy via ionisation in the atmosphere. The overall spectrum has a wide range of energies and angles, with the spectrum dependent on the location on the Earth it is measured, the altitude at which measurements are made and the degree of solar activity. These dependancies are a reflection of the factors affecting the primary cosmic-ray flux, energy loss in the atmosphere and decay. For example, 2.4 GeV muons have a decay length of 15 km, which is reduced to 8.7 km by energy loss [45]. Over time the muon spectrum has been well documented at various angles through experimental measurements [47, 48] and modelling [49]. In general when considering the muon spectrum the following parameters listed in the Review of Particle Physics by the Particle Data Group can be used to describe it [45]:

- They impact the Earth's surface at a rate of 0.0167 $\text{cm}^{-2}$ $\text{s}^{-1}$for horizontal detectors with an average energy of 3-4 GeV for vertical muons and $\approx 6$ GeV for all muons.

- For energies below 1 GeV the energy ($E$) distribution is almost flat. With increasing energy the spectrum becomes steeper, until it falls as $E^{-2.7}$ for energies in the range 10-100 GeV.

- For average energies the flux is greatest at the zenith before falling with an angular distribution that is $\propto \cos^2\theta$, where $\theta$ is the angle between the muon path and the vertical.

Fig. 2.14 displays the muon energy spectrum at sea level for both $\theta = 0$ degrees and $\theta = 75$ degrees. This figure has been taken from the Review of Particle Physics by the Particle Data Group [45]. For large angles the average muon energy at the surface is greater than for smaller angles. This is due to the increased distance that muons have to cover before reaching the surface, therefore low energy muons will decay before reaching the surface. The parameterisation used in this thesis for muon production is a modified Gaisser parameterisation [50] and is discussed in further detail in Chapter 3.

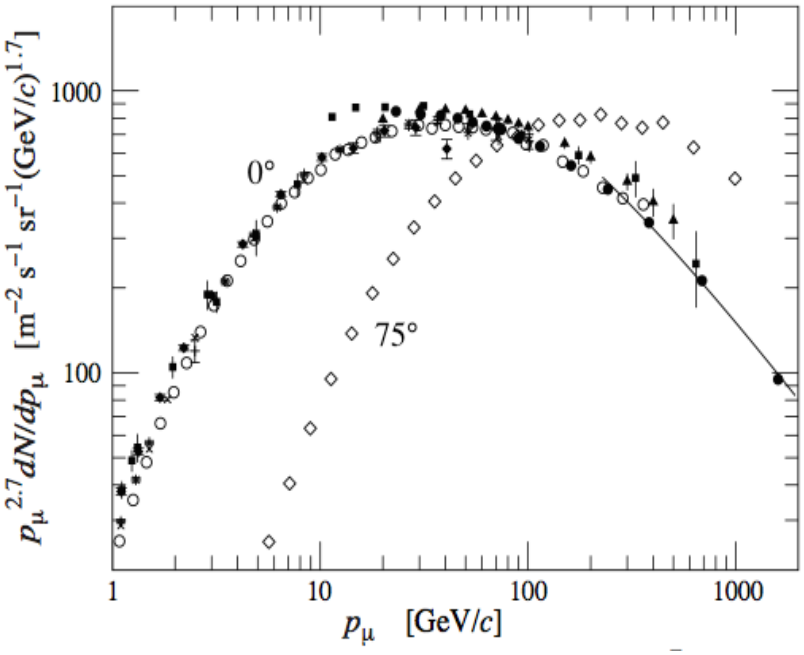


Fig. 2.14 *Spectrum of muons at $\theta$ = 0 deg (black diamonds [51], black squares [48], black triangles [52], black inverted triangles [47], cross' [53], hollow circles [54], black circles [55]) and $\theta$ = 75 deg (hollow diamonds [56]) taken from the Review of Particle Physics by the Particle Data Group [45]. $dN/d\rho_\mu$ is the differential flux and $\rho_\mu$ is the muon momentum.*

### 2.4.3 Cosmic-Ray Neutron Spectrum at the Earth's Surface

After muons, neutrons represent the most abundant particle produced by cosmic-ray interactions to reach the surface. They are produced when primary cosmic-rays collide with nuclei in the atmosphere. As they propagate through the atmosphere to the surface, they will also undergo interactions with atmospheric nuclei, resulting in a loss of energy and production of further additional particles. As with muons the overall spectrum has a wide distribution of angles and energies, which are a reflection of the factors affecting the primary cosmic-ray flux. Hence their distribution is dependent on the altitude, solar activity and physical location in which it is measured. A number of measurements and parameterisations have been made over time [49, 57–59]. A schematic of the cosmic-ray neutron energy spectrum [59] is displayed in Fig 2.15. Fig 2.15 also shows a plot of the neutron energy times the differential flux, measured on the roof of the IBM (International Business Machines Corporation) T. J. Watson Research Center in Yorktown Heights, NY [57]. The differential flux is given by the number of radiant-energy particles incident on a surface during a given period of time divided by the product of the

area of that surface, the characteristic energy of the incident particles, and the given period of time. This $2^{nd}$ plot is shown to allow finer details of the spectrum to be easier to view. There are three distinct areas in Fig. 2.15 that are to be considered:

- A thermal peak, which is a result of neutrons with thermal energies, that are in thermal equilibrium with the surrounding medium. These neutrons have lost energy until they have reached thermal energies, but are yet to have been captured by the surrounding medium.
- After the thermal peak the spectra exhibits roughly a $1/E$ dependence up until 1 MeV. This dependence is simply a result of neutrons slowing down by interacting with the surrounding nuclei. Centred at 1 - 2 MeV there is a secondary peak, which is a result of nuclear evaporation processes. Particles have collided with nuclei in the atmosphere resulting in neutron production via excitation. Upon closer inspection there is finer structure from nuclear resonances with oxygen and nitrogen in the atmosphere.
- Neutrons above 1 - 2 MeV which encompasses the high energy peak. This peak is a result of giant dipole resonances (GDR).

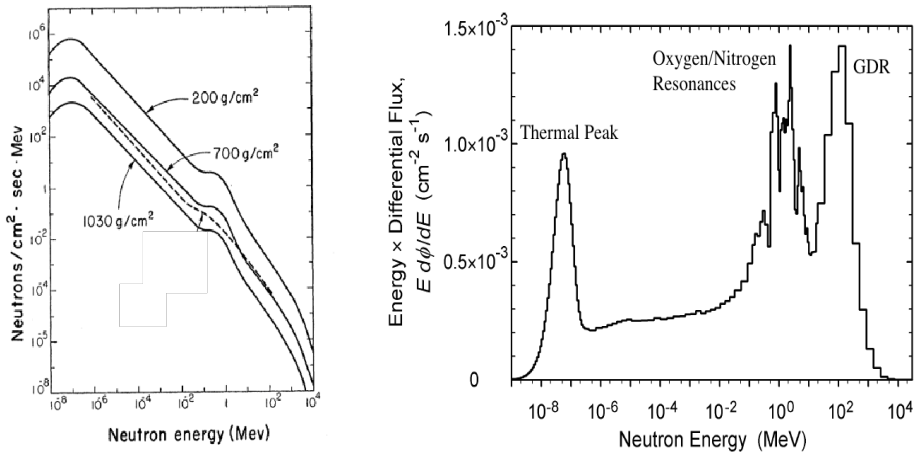


Fig. 2.15 *Illustration of the cosmic-ray neutron energy spectrum [59] (left figure) and the differential neutron energy spectrum multiplied by the energy, measured on the roof of the IBM [57] (right figure). A $2^{nd}$ plot is given to allow finer details of the spectrum to be easier to view. The numbers 200 g/cm$^2$, 700 g/cm$^2$ and 1030 g/cm$^2$ refer to the different atmospheric depths where measurements were made.*

## 2.5 Muon Interactions with Matter

Muon interactions with matter are the primary reason they represent an effective alternative for probing materials. For the purpose of interrogation there are three main areas to be considered. Firstly, energy losses of muons can occur through four main processes: ionisation, bremsstrahlung, electron-positron pair production and muon-nucleus inelastic scattering. If this energy loss is sufficient enough then muons can stop within a target. Since muons are charged, when they interact with atomic nuclei they will undergo deflections via multiple Coulomb scatterings. Muon deviation can also occur through the other interactions taking place, such as inelastic scattering, bremsstrahlung and pair production, however the process of multiple Coulomb scattering dominates. Finally, upon stopping there is the possibility that muons can be captured by the material being traversed, resulting in fission or spallation events depending on whether the material is nuclear or not. The following subsections will discuss each of these interactions.

### 2.5.1 Energy Loss

As muons traverse materials they lose energy via electronic (ionisation and excitation), radiative (bremsstrahlung and electron-positron pair production) and muon-nucleus inelastic scattering processes. The total energy loss in a material is a combination of all these processes and is referred to as the 'mean stopping power of the material' [60]. It is given by Eq. (2.13), where *a(E)* is termed the electronic stopping power, *b(E)* describes losses due to radiative processes and inelastic scattering, and $E$ is the total energy,

$$-\frac{dE}{dx} = a(E) + b(E)E. \tag{2.13}$$

The relative contribution of each of these processes is primarily dependent on whether the incident muon energy is above or below the critical energy associated with the material. The critical energy is when energy losses for both radiative and electronic processes are equal. For most materials the critical energy is of the order of several hundred GeV and hence much greater than a typical cosmic-ray muon whose average energy at sea level is 6 GeV. Since radiative losses occur at much higher energies than electronic, this indicates that the dominant process of energy loss for muons through materials is via electronic interactions such as ionisation rather than any radiative process. This effect is shown in Fig. 2.16, which displays the stopping power of positive

muons in copper as a function of kinetic energy. In practical cases the mean energy loss rate is close to the minimum and therefore cosmic-ray muons are know as 'minimum-ionising particles'.

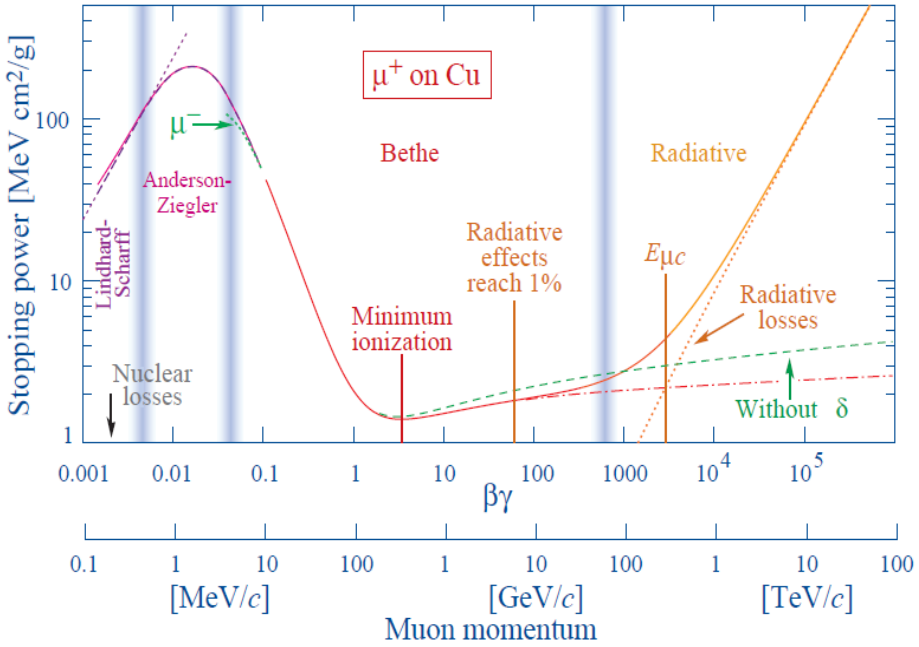


Fig. 2.16 *Stopping power of positive muons in copper [45]. The appropriate energy range for cosmic-ray muons is represented by the Bethe region (0.1 - 1000 GeV).*

As muons pass through materials they strike electrons resulting in a transfer of energy from the muon to the electron. The total energy lost by the muon is dependent on the energy of the muon and the thickness of the material. The majority of slowing down for muons at the Earth's surface occurs within the Bethe region, where muons are travelling with high speeds ($\beta = v / c$). The mean rate of energy loss in the region that occurs is well described by the Bethe formula (Eq. (2.14)) [61], while Fig. 2.17 shows the energy loss suffered by muons as they traverse different materials, which is given by,

$$\left\langle -\frac{dE}{dx} \right\rangle = Kz^2 \frac{Z}{A} \frac{1}{\beta^2} \left[ \frac{1}{2} ln \frac{2m_e c^2 \beta^2 \gamma^2 T_{MAX}}{I^2} \right] - \beta^2 - \frac{\delta(\beta\gamma)}{2}, \tag{2.14}$$

where $K$ is a constant (K = $4\pi N_A r^2 m_e c^2$), $z$ is the unit charge of the incident particle, $Z$ is the atomic number of the absorber, $A$ is the atomic mass of the absorber, $\gamma$ is the Lorentz factor, $T_{MAX}$ is the maximum energy transfer in a single collision and is given

in Eq. (2.15), $m_e$ is the electron mass, $I$ is the mean excitation energy, $\delta(\beta\gamma)$ is the density effect correction to ionisation energy loss, $N_A$ is Avogadros constant and $r$ is the classical electron radius. The units are given in MeV $g^{-1}$ $cm^2$.

$$T_{MAX} = \frac{2m_e c^2 \beta^2 \gamma^2}{1 + 2\gamma m_e/M + (m_e/M)^2} \tag{2.15}$$

where M is the mass of the incident particle.

There is always the possibility that muons will lose all their energy and be absorbed by the material they pass through. As demonstrated by Eq. (2.14) and Fig. 2.17 the energy loss for a muon as it passes through a material varies with the energy of the incoming muon and the material being traversed. In the energy range of the cosmic-ray muon spectrum (100 MeV - 1000 GeV), the approximate energy loss of a muon is 2 MeV per $g/cm^2$. For a precise calculation of the range of muons in materials, integration of the energy loss relationship outside the energy range where the 2 MeV loss per $g/cm^2$ is appropriate is required. Table 2.4 demonstrates the range of muons for multiple different materials, when calculated using an approximate energy loss of 2 MeV per $g/cm^2$. Since muons with energies of a few GeV are capable of penetrating over a metre of very dense materials, and higher energy muons up to tens of metres, this process is mainly applicable to low energy muons.

Table 2.4 Average range of muons passing through various materials.

| Material | Volume Density ($g\ cm^{-3}$) | Average range (cm) for muons with energy : | | |
|---|---|---|---|---|
| | | 0.4 GeV | 4 GeV | 40 GeV |
| Water | 1.00 | 200.00 | 2000.00 | 20,000.00 |
| Concrete | 2.20 | 90.91 | 909.09 | 9090.91 |
| Iron | 7.87 | 25.41 | 254.13 | 2541.30 |
| Lead | 11.35 | 17.62 | 176.61 | 1766.61 |
| $^{238}U$ | 18.95 | 10.55 | 105.54 | 1055.41 |

## 2.5.2 Multiple Coulomb Scattering (MCS)

As muons pass through a medium, they interact with atomic nuclei of the medium, resulting in a slight deflection from the muons original path. Since muons will pass

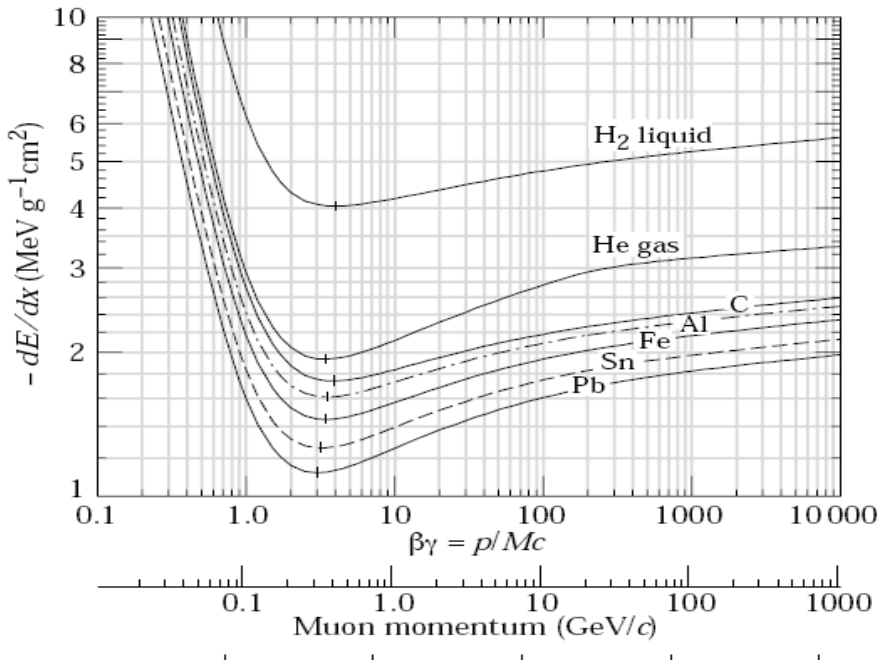


Fig. 2.17 *Mean energy losses for muons traversing different materials [45].*

close to multiple atomic nuclei, multiple deflections will take place, resulting in a total scattering angle that is non-negligible once the muon exits the medium. For small angle deflections the distribution is well represented by a zero mean Gaussian approximation, while less frequent 'hard' scatters produce non-Gaussian tails. If we define

$$\theta_0 = \theta_{plane}^{rms} = \frac{1}{\sqrt{2}}\theta_{space}^{rms} \tag{2.16}$$

for small angle deflections the distribution is well represented by a zero mean Gaussian approximation, for the central 98% of the scattering distribution [62], with a rms width given by [63],

$$\theta_0 = \frac{13.6MeV}{\beta c\rho} z\sqrt{x/X_0}[1+0.038\ln(x/X_0)]. \tag{2.17}$$

Here $\beta c$ is the muon velocity, $\rho$ is the momentum, $z$ is the charge of the incoming muon and $x/X_0$ is the thickness of the scattering medium, measured in radiation lengths ($X_0$). The value for $\theta_0$ is a fit to Molières distribution for scattering angles [62] for singly charged particles with $\beta = 1$ for all $Z$, and is accurate to 11% or better for $10^{-3} < x/X_0$

< 100 [45].

The projected (plane) and non-projected (space) angular distributions can be approximated by,

$$\frac{1}{2\pi\theta_0^2} exp\left(-\frac{\theta_{space}^2}{2\theta_0^2}\right) d\Omega, \tag{2.18}$$

$$\frac{1}{\sqrt{2\pi}\theta_0} exp\left(-\frac{\theta_{plane}^2}{2\theta_0^2}\right) d\theta_{plane}, \tag{2.19}$$

where $\theta$ is the deflection angle. For the approximation, $\theta_{space}^2 \approx (\theta_{plane,x}^2 + \theta_{plane,y}^2)$, where the $x$ and $y$ axes are orthogonal to the direction of motion, and $d\Omega \approx \theta_{plane,x}\theta_{plane,y}$. Deflections into the $\theta_{plane,x}$ and $\theta_{plane,y}$ are independent and identically distributed [45].

The radiation length represents the amount of matter there is for electromagnetic interactions. It is both the mean material depth over which a high-energy electron loses all but 1/e of its energy, and 7/9 of the mean free path for pair production by a high-energy photon. The radiation length in units of g/cm$^2$ is given by,

$$\frac{1}{X_0} = 4\alpha r_e^2 \frac{N_A}{A}\{Z^2[L_{rad} - f(Z)] + ZL_{rad}^{'}\} \tag{2.20}$$

where $\alpha$ is the fine structure constant, $r_e^2$ is the classical electron radius, $N_A$ is Avogadro's number, $A$ is the mass number, $Z$ is the atomic number of the nucleus, $L_{rad}$ = ln(184.15 $Z^{-1/3}$), $L_{rad}^{'}$ = ln(1194 $Z^{-2/3}$) and

$$f(Z) = a^2[(1+a^2)^{-1} + 0.20206 - 0.0369a^2 + 0.0083a^4 - 0.002a^6], \tag{2.21}$$

where $a = \alpha Z$ [45].

For mixtures or compounds the radiation length can be approximated by,

$$\frac{1}{X_0} = \sum w_j/X_j \tag{2.22}$$

where $w_j$ and $X_j$ are the fraction by weight and the radiation length for the j$^{th}$ element [45]. Fig. 2.18 displays the radiation length, calculated using Eq. (2.20), as a function of $Z$.

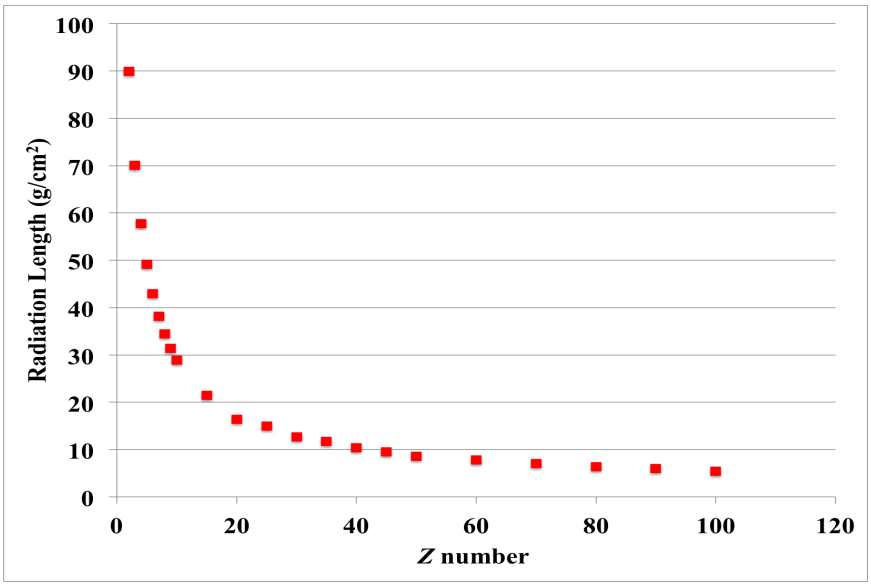


Fig. 2.18 *Radiation length in g/cm$^2$ as a function of Z calculated using Eq. (2.20).*

For materials of the same depth the radiation length is shorter for higher density materials, as there are more nuclei and electrons available for electromagnetic interactions. As the scattering width is dependent on the radiation length, higher density materials (such as SNM and its possible shielding) will on average, cause muons to scatter more than lower density materials assuming the same thickness; hence SNM can be identified through measuring the scattering width of muons. Since measuring the energy of a muon normally requires the use of a magnetic field, for nuclear security purposes the ability to measure the scattering angle is easier than the energy loss and hence is the primary source of information that is utilised for muon tomography. Simulations were run using GEANT4.9.6-p02, where mono-energetic muons were vertically propagated through 10 cm of various materials. Given in Table 2.5 is the atomic number, radiation length and average scatter for a number of materials, that demonstrate how the average scattering angle observed for muons varies.

### 2.5.3 Muon Capture

As muons pass through materials they lose energy and can slow down to the point where they stop within the material (range out). Upon stopping $\mu^-$ will be captured into an atomic orbit, resulting in the formation of a muonic atom. This capture can result in the

Table 2.5 Average scattering angle suffered for muons passing through 10 cm of various materials.

| Material | $X_0$ (g cm$^{-2}$) | $Z$ | Average scattering angle (mrad) for muons of energy : | | |
|---|---|---|---|---|---|
| | | | 0.4 GeV | 4 GeV | 40 GeV |
| Water | 36.1 | 1 and 8 | $18.52 \pm 0.17$ | $2.11 \pm 0.09$ | $0.17 \pm 0.07$ |
| Concrete | 26.6 | Z/A=0.5 | $31.10 \pm 0.23$ | $3.60 \pm 0.12$ | $0.28 \pm 0.10$ |
| Iron | 13.8 | 26 | $100.04 \pm 0.40$ | $10.79 \pm 0.23$ | $0.84 \pm 0.17$ |
| Lead | 6.4 | 82 | $192.79 \pm 0.80$ | $20.05 \pm 0.35$ | $1.92 \pm 0.31$ |
| $^{238}$U | 6 | 92 | $295.99 \pm 1.55$ | $27.26 \pm 0.44$ | $2.65 \pm 0.38$ |

production of multiple neutrons via muon induced fission. Pathways for both delayed and prompt processes exist for this procedure [64].

Upon capture onto an orbit, $\mu^-$'s will rapidly cascade down the orbital levels through Auger and radiative emissions to the lowest quantum state (1S) available. This cascade is coupled to the release of multiple muonic $X$-rays. As the muon approaches the ground state, due to its bigger mass over its electron counterpart, the muons orbital is 'pushed' closer to the nucleus. This increases the probability of interaction between the muon and a nucleus. Since the nuclear radius increases with $Z$ number, so does the probability of a $\mu^-$ finding itself within the nucleus when reaching this state. For delayed muon induced fission, upon reaching the ground level, muon absorption by the nucleus competes against muon decay, with the probability of absorption increasing as the elements become heavier. Muon absorption is mediated by the weak interaction and centres on the capture of the muon by a nuclear proton, resulting in the emission of a neutron and neutrino with the reaction shown in Eq. (2.23) [65].

$$\mu^- + p \rightarrow \nu_\mu + n \tag{2.23}$$

Typically the neutrino takes most of the mass energy of the muon ($\sim$ 100 MeV) with very little being delivered to the recoil neutron. However, the capture of the muon also acts to excite the nucleus and therefore further neutron emissions in addition to $\gamma$-ray emission can occur as the excited nucleus de-excites. The characteristic mean lifetime of this process for the actinides is 70-80 ns.

In prompt muon-induced fission, it is possible for the 2P-1S transition energy ($\sim$ 6 MeV) to exceed that of the fission or neutron emission thresholds, meaning excess neutron production can occur without the absorption of the muon. The process is described

by

$$(Z,A)(\mu^-)^* \rightarrow (Z,A)^*(\mu^-). \tag{2.24}$$

Upon fission the muon will tend to attach itself to the heavy fragment, resulting in its capture and further neutron production [66]. These excess neutrons may be measured when attempting to detect high-$Z$ and nuclear materials.

Table 2.6 displays the average neutron multiplicity from $\mu^-$ capture for a number of different elements, taken from literature [67–69]. Beams of muons were generated using the Berkeley 184-in cyclotron and fired into a $CH_2$ absorber. The thickness of this absorber was enough so that $\mu^-$ would lose enough energy to be captured by the target material. Neutrons emitted after $\mu^-$ capture have energies of the order MeV, therefore detection was made in a large (30 in. high, 30 in. diam) cadmium loaded liquid scintillator tank.

Table 2.6 Average neutron multiplicity from $\mu^-$ capture for a number of different elements.

| Material | Mass ($A$) Number | Atomic ($Z$) Number | Average Neutron Multiplicity |
|---|---|---|---|
| Aluminium | 27 | 13 | $1.26 \pm 0.06$ [68] |
| Silicon | 28 | 14 | $0.86 \pm 0.07$ [68] |
| Calcium | 40 | 20 | $0.75 \pm 0.03$ [68] |
| Iron | 56 | 26 | $1.12 \pm 0.04$ [68] |
| Silver | 108 | 47 | $1.61 \pm 0.06$ [68] |
| Gold | 197 | 79 | $1.66 \pm 0.04$ [68] |
| Lead | 207 | 82 | $1.71 \pm 0.07$ [68] |
| $^{235}$U | 235 | 92 | 2.4 [69] |
| $^{238}$U | 238 | 92 | 2.2 [69] |

From Table 2.6 it appears that the average number of neutrons emitted per muon capture increases as Z number increases, however deviations from this generalisation do occur [67]. A more accurate description can be determined if the kinematics of the system are taken into account. If the process of $\mu^-$ absorption is assumed to occur with a proton at rest, then the neutron recoils with an energy of $\approx$ 5.2 MeV. This energy transfer is assumed to be distributed amongst all other nucleons to produce a 'thermally' excited nucleus. In reality the proton will have some finite momentum. Therefore the overall energy of the recoil neutron, and hence the energy distribution ($I(Q)$) within the nucleus, will be different from this value ($Q$ is the excitation energy). The excited

nucleus will primarily undergo neutron emission until sufficient energy for this process is not available. At this point the nucleus will relax back down to its ground state via photon emission. Through measuring the number of neutrons that are emitted, a lower limit on the energy transfer to the nucleus can be determined. This limit is given by the difference in mass between the initial nucleus *(Z, A)*, and the residual nucleus *(Z - 1, A)*, plus the binding energies of the neutrons that are emitted from the residual nucleus. The average energy transferred to the nucleus has been calculated to be between 10 and 20 MeV [67], which is not high enough for proton emission to become a factor due to the effects of the coulomb barrier. The probability $N$ of the emission of $\nu$ neutrons has been demonstrated to be [67], [70]:

$$N_\nu = 1 - exp[-(Q - B_\nu/\theta_n)] \times \sum_{n=0}^{2\nu-3} [Q - B_\nu/\theta_n]^n (n!)^{-1} \tag{2.25}$$

where $Q$ is the excitation energy, $B_\nu$ is the binding energy of $\nu$ neutrons in the initial nucleus and $\theta_n$ is the temperature of the residual nucleus and assumed to be constant.

As shown by Eq. (2.25), neutron multiplicity is heavily dependent on the difference between the excitation energy and the binding energy of the neutrons. This explains the variation from the general trend of increasing neutron multiplicity with increasing $Z$ number. In order for any prediction of neutron multiplicity to be made the process behind nuclear excitation and nuclear excitation distribution, *I(Q)*, must be understood. There are a number of models of the nucleus that have been evaluated with regards to this process, including the Fermi-gas model, Gaussian model and shell model [67].

## 2.6 Neutron Interactions with Matter

As discussed in section 2.2 neutrons can be used as an effective source when attempting to detect hidden nuclear material. Since they have no charge neutrons do not lose energy via electromagnetic processes and are able to penetrate large volumes of high-$Z$ material. However, neutron interactions are mediated by the strong force and they undergo interactions with the nuclei of these materials. These interactions are of interest when using neutrons to detect nuclear material. The probability of any interaction occurring is expressed by the cross-section, which is measured in units of barns (1 b = $10^{-24}$ cm$^2$), with the probability of a particular event occurring being dependent on the energy of the incoming neutron. There are two main categories of interaction between neutrons and nuclei that are considered; these are elastic or inelastic scattering and absorption.

Elastic scattering is the process in which a neutron imparts some of its kinetic energy to the nucleus, resulting in the loss of energy and scatter of the neutron. The overall energy within the system (neutron + nucleus) remains the same. On average, the amount of energy lost by the neutron is given by the formula $2EA/(A+1)^2$ where $E$ is the kinetic energy of the neutron and $A$ is the atomic number of the material. This formula indicates that materials with low-$A$ numbers (such as hydrogen) are more efficient at lowering neutron energy than high-$A$ materials. Unlike elastic scattering, inelastic scattering does not conserve the overall energy of the system (neutron + nucleus). Instead when inelastic scattering occurs some of the energy from the neutron is used in elevating the nucleus to an excited state or producing new particles. Upon relaxation back to the ground state energy is released in the form of radiation.

Due to the wide energy range which cosmic-ray neutrons span (see Fig. 2.15) there is always the possibility that some of these neutrons will be absorbed by the target they are passing through. If this target is shielded HEU then this may result in the production of excess neutrons via fission (for nuclear material) and spallation (for shielding material). The probability of this process initiating is given by the neutron capture cross section. Fig. 2.19 shows the fission cross section for $^{235}$U, $^{238}$U and $^{239}$Pu. As can be seen the probability of capture occurring is much higher at thermal energies before falling away. There are also specific peaks located at higher energies. These represent the resonant peaks and occur when the incoming neutron has an energy that is very close to the en-

ergy required to move the nucleus into an excited state. At these levels the probability of capture is increased.

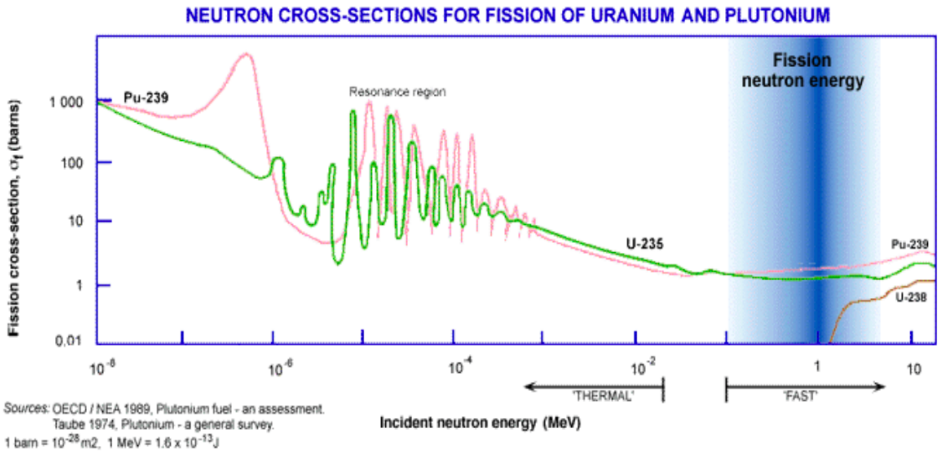


Fig. 2.19 *Fission cross section for* $^{235}U$, $^{238}U$ *and* $^{239}Pu$ *[71].*

If cosmic-ray neutrons were to be used as a substitute for active interrogation neutrons, the same signatures as active interrogation are detected. However, unlike active interrogation there would be no interrogation source. This in turn means there is no danger of harming potential stowaways, or activation of the cargo. However, since the source of neutrons cannot be controlled by the user, optimised properties of the neutron energy and direction of beam cannot be defined.

The average energy of the cosmic-ray neutrons is $\approx$ 140 MeV. At this energy the fission cross section for $^{235}$U is $\approx$ 1.45 b and for $^{238}$U is $\approx$ 1.30 b [72]. Fission with incident neutrons of this energy will produce on average 11 neutrons per fission for $^{235}$U and 10.5 neutrons per fission for $^{238}$U [73]. Fission neutrons will have an average energy of $\approx$ 2.56 MeV for $^{235}$U, and 2.45 MeV for $^{238}$U [73]. Neutrons produced via the initial fission may then escape the material for detection or cause additional neutron production to occur through additional fission events, neutron capture or neutron scattering. The probability of each of these events occurring is dependent on the size of target which is being inspected. The amount of neutrons which reach the detector is dependant on a number of factors including the detectors distance from the source, the detectors total area coverage and the detectors efficiency. Neutrons with MeV energies can be detected with $CH_4$ fast-neutron detectors. $CH_4$ fast-neutron detectors rely on the recoil of light nuclei to ionise the gas in the tube. $CH_4$ fast-neutron detectors have a

detection efficiency for 1 MeV neutrons of 78% [41]. This efficiency is the interaction probability for neutrons of energy 1 MeV striking the detector face at right angles for a detector thickness of 5 cm. The disadvantage of this type of detector is its sensitivity to $\gamma$-rays. Other types of detector available include $^3$He proportional counters, which have a detection efficiency of 77% for thermal neutrons [41]. These detectors are very insensitive to $\gamma$-rays. If this type of detector is used then a moderating material is required to surround the detector in order to reduce the neutron energy to thermal energies.

## 2.7 Cosmic-Ray Muon Radiography

### 2.7.1 History

Over the last several decades many applications have used cosmic-ray muons as a source for radiography. The initial approach into muon radiography was done by E.P. George in 1955 [74] who, through measuring the attenuation of muons as they passed through the rock above the Guthega-Munyang tunnel, was able to deduce the thickness of this overburden that the muons had passed through.

This pioneering approach of measuring the cosmic-ray muon flux to determine the depth of material was built upon in the late 1960s when Luis Alvarez and his team attempted to image the interior of the pyramid of Chepren located at Giza, in an attempt to discover any hidden chambers that may have been present [75]. Two spark chambers were placed in the Belzoni chamber of the pyramid. Through knowledge of the geometry of the pyramid, an estimation was made whereby those muons that pass through one of the faces of the pyramid, would traverse $\sim$ 2.3 m less limestone than those that pass through the corners of the pyramid. That difference corresponds to a difference in the signal intensity of $\sim$ 5% for muons passing through the faces, over those that pass through the corners. This difference is due to the increased volume of limestone in the corners. In addition to this, multiple simulations were run, which measured the attenuation of muons as they passed through the pyramid. These simulations, coupled with estimations of how much the muon flux would have been altered given a certain size of chamber, allowed Alverez and his team to deduce that in fact there were no hidden chambers within the examined region at the pyramid of Chepren.

More recently, several efforts have been made to map other large objects. This includes the Higashi-Honganji temple gate [76] and the interior of mountains and volcanoes [77–80]. Research has developed in this area over time from basic mountain measurements, to inner volcano measurements with resolutions of $\pm$50.0 m [78] and the development of a three-dimensional computed tomography system [80], all with the aim of attempting to predict when a volcano may erupt. Currently the most active area of research in this field involves the MU-RAY project [81]. This is an international collaboration whose aim is to map the inside of Mount Vesuvius, through the development of new analysis tools and the construction of muon telescopes equipped to survive the harsh environments of an active volcano.

## 2.8 Cosmic-Ray Muon Tomography

### 2.8.1 Previous Work

The work in section 2.7.1 relies on measuring muon attenuation, to build up tomographic images of the volume these muons traverse. When considering cosmic-ray muons for nuclear material detection, techniques developed rely upon the multiple scatters muons undertake as they pass through an object. These multiple small interactions add up to yield a total angular deviation, which is well represented by Eq. (2.17). The technique was originally established and validated by the team at Los Alamos National Laboratory [1–5]. Both experimental and simulation tests were conducted for a variety of different scenarios.

Initial reconstruction algorithms developed by the team at LANL used a basic point of closest approach (PoCA) method [4]. PoCA approximates the trajectory that muons travel as two straight lines joined by a single point, hence it assumes the muon only scatters once within the inspected volume. The total geometry is split into voxels. Through using the PoCA algorithm, the most probable voxel in which scattering occurs is calculated. The scattering strength in this voxel is then determined. This process is done for all muons that pass through the inspected volume. Using this algorithm discrimination between low-$Z$ (water, plastic, concrete), medium-$Z$ (iron, copper) and high-$Z$ (lead, uranium) materials was apparent in 1 minute exposure times [4]. The PoCA algorithm was validated experimentally through attempts to detect a cylinder of tungsten (radius 5 cm and height 5.7 cm) placed on a plastic sheet, with two steel support beams. Two drift chambers, spaced 27 cm apart with an active detection area of 60 cm $\times$ 60 cm were placed above and below the inspected volume. Detectors had a spatial resolution of 400 $\mu$m at full width half maximum (FWHM). Both experimental and simulation studies were conducted, with clear detection of the tungsten target made [2].

The PoCA algorithm was proven to work for detecting small isolated objects in simple geometries [4]. However, since the PoCA algorithm assumes scattering to occur at a single point, it fails to take into account the actual physics of multiple scatterings that are taking place. As a muon passes through many objects, particularly those which are stacked vertically, it will scatter at various locations. This can cause the single scattering point reconstructed using PoCA, to be located between targets and in the volumes that surround where a target is located. This effect is more apparent for high-$Z$ materi-

als and occurs more predominately in the vertical direction. The 'blurring' is caused by the inherent nature of the PoCA algorithm, with the position of a PoCA point weighted towards the element that caused the greatest scatter to occur. This causes a propensity for the misclassification of low density, medium density or even high-density materials [3]. The combination of these two issues limits the accuracy of nuclear materials detection in realistic scenarios, when solely using the PoCA algorithm.

A secondary the of algorithm, based on the actual physics taking place, has also been developed. This algorithm is known as the expectation-maximisation (EM) algorithm and was originally developed at LANL [3]. The EM algorithm is used to find maximum likelihood estimates of a statistical model, where the model is dependent on parameters that cannot be measured directly. Thus follows a two step process. First is the expectation (E) step, which creates a function for the expectation of the log-likelihood evaluated using the current estimate for the unknown parameters. This is followed by the maximisation (M) step, that computes the parameters which will maximise the expected log likelihood found on the previous step [82]. These parameters are then passed back to the E step to determine the new distribution of the hidden parameters. These two steps are done until the parameters converge, or for a predetermined number of iterations. Unlike the PoCA algorithm, the EM algorithm is based on the actual physics of multiple scattering that is taking place. Therefore EM is expected to perform better than PoCA in systems where multiple scatters are taking place. The main issue with the EM algorithm is the long running times required. A full derivation of how this type of algorithm is developed and implemented for muon tomography applications is beyond the scope of this thesis but can be found at [5].

This thesis will discuss the development of two algorithms that look to enhance nuclear materials detection. One is based on PoCA and uses a density-based clustering approach [83] to ascertain regions of high-$Z$ materials. The other makes use of muons that disappear within the inspected volume [84]. Previous work done by the group in Sheffield include the development of an empirical relation for the angle of deviation with the incident muon energy and the thickness, atomic mass, radiation length and density of the material [85].

Since the initial study conducted by the team at LANL various other people and groups have developed detectors, more complex analysis algorithms and simulated more com-

plex systems in which high-density materials could be placed. This most noticeably started with C.L. Morris [86], who simulated the capability of muon tomography to detect 1000 $cm^3$ blocks of tungsten, when placed within a cargo van [86]. Other muon tomography systems that have been built and tested, use Gas Electron Multipliers (GEMs) with the PoCA algorithm. These type of detector have extremely good spatial resolution (as low as 130 $\mu$m [87]) and have shown to be efficient in detecting metallic objects within an inspected volume both via simulations [88, 89] and experimentally [87]. Within the UK, the University of Bristol, in conjunction with the Atomic Weapons Establishment (AWE) have developed a muon tomography inspection system based on high resolution resistive plate chambers [90]. More on what Bristol and AWE have done can be viewed at the following references [91–93].

The multiple scattering muons experience as they pass through a material have been used to image objects with a variety of size, density, and atomic mass. It has been demonstrated that this technique is capable of detecting and discriminating materials from one another. In addition to detecting nuclear material at international borders the use of cosmic-ray muons is spreading to the broader scientific community. The applications they are now being used for include volcano imaging, reactor imaging and spent nuclear material imaging [77–81, 94, 95].

# Chapter 3

# Material Segregation using Muon Scattering

In this chapter an overview of the cosmic-ray muon scattering tomography concept will be discussed in section 3.1. Section 3.2 gives a discussion of the different code packages that have been used to generate the results presented in this thesis. Also presented are the initial parameters that are inherent to all simulations discussed in this Chapter. Following a discussion of these parameters, section 3.3 displays the capability of muon scattering and the PoCA algorithm for material segregation, using full energy spectrum muons in 5 minute exposure times. Section 3.4 summarises the work presented.

## 3.1 Concept

As mentioned in section 2.4.2, muons cascade down upon the surface of the Earth at a rate of 0.0167 $cm^{-2}$ $s^{-1}$ for horizontal detectors. Due to this low rate, individual muons can be tracked one at a time as they pass through sets of detectors that have been placed around a volume to be inspected. The focus of this thesis is to make use of the various interactions of muons with different materials, to detect shielded nuclear materials, in particular HEU located within shipped cargo containers. The first interaction to be discussed is the multiple scatters a muon undergoes as it passes through a material. The system envisaged for this purpose involves placing a volume to be inspected between a minimum of four sets of detectors. Individual muons are tracked as they pass through each set of detectors. The initial position and direction cosines for each of the incoming and outgoing muon tracks are recorded. Upon determination of the direction of both the incoming and outgoing tracks, these muon tracks are passed through a reconstruction

algorithm, which is used to deduce the most likely position where scattering has occurred. The amount of scattering is determined through calculating the angle between the two tracks. As discussed in section 2.5.2 higher density materials such as shielded HEU will cause muons to scatter more than lower density materials, such as any surrounding clutter. Through measuring muons as they pass through the inspected volume, analysis of the volume can be conducted based on the amount of scattering each muon undertakes. Further analysis is then conducted to determine if there are any areas within the cargo that may contain high density material. A schematic of the muon scattering tomography concept is shown in Fig. 3.1. The average scattering angle suffered for muons passing through 10 cm of various materials is given in Table 2.5.

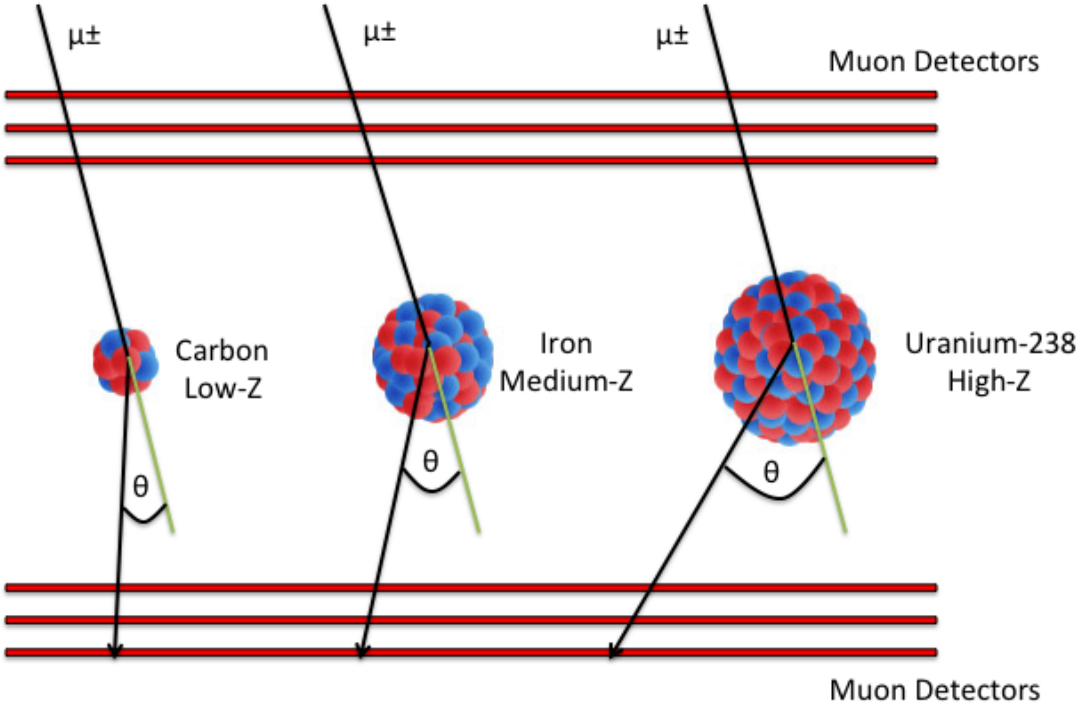


Fig. 3.1 *Schematic of the cosmic-ray muon scattering tomography concept. The scattering angles described are not drawn to scale.*

## 3.2 Initial Parameters

### 3.2.1 GEANT4

For this study, simulations have been conducted using GEANT4.9.6-p02 with the 'Shielding 2.0' physics list [96]. GEANT4 (GEometry ANd Tracking), is a simulation toolkit written in C++ that uses Monte-Carlo methods for simulating the passage of particles through matter [97]. Due to the wide variety of applications it can be used for, users are able to tune the simulations they run to their individual needs. All aspects of the simulation process are covered, with the most important three being the system geometry along with their materials, production and tracking of the particles of interest, and detection and storage of the particles produced [98]. This set-up allows the user to have control over the geometry of the system, the ability to generate primary particles, the choice of which particles to track and store and most importantly, the physics processes at the heart of the particle interactions. Several physics lists have been created in GEANT4, which have their advantages and disadvantages depending on the purpose of the simulation. For the applications discussed in this thesis the Shielding physics list is used. This list has been specifically designed for simulations involving shielding purposes. The Shielding physics list was originally developed for neutron penetration studies and ion-ion collisions, but is also used for high energy calorimetry and for underground or low background experiments. Its high energy part is taken from the FTFP_BERT_HP physics list (recommended by GEANT4 for HEP) and radioactive decay has been added to deal with background radiation. It is the recommended list for shielding, space and HEP applications. Scheduled validation tests can be viewed at [96]. The physics processes on which GEANT4 is built have been extensively tested and validated, the details of which can be viewed in 'GEANT4 Developments and Applications' by [98].

The set-up used for all simulations discussed in Chapter 3 involve placing detectors above, below and at two of the sides of the volume to be inspected (much like a tunnel). An example schematic can be viewed in Fig. 3.2. In order to run simulations of interest, an appropriate cosmic-ray muon spectrum at sea level is required. For this other software packages are used.

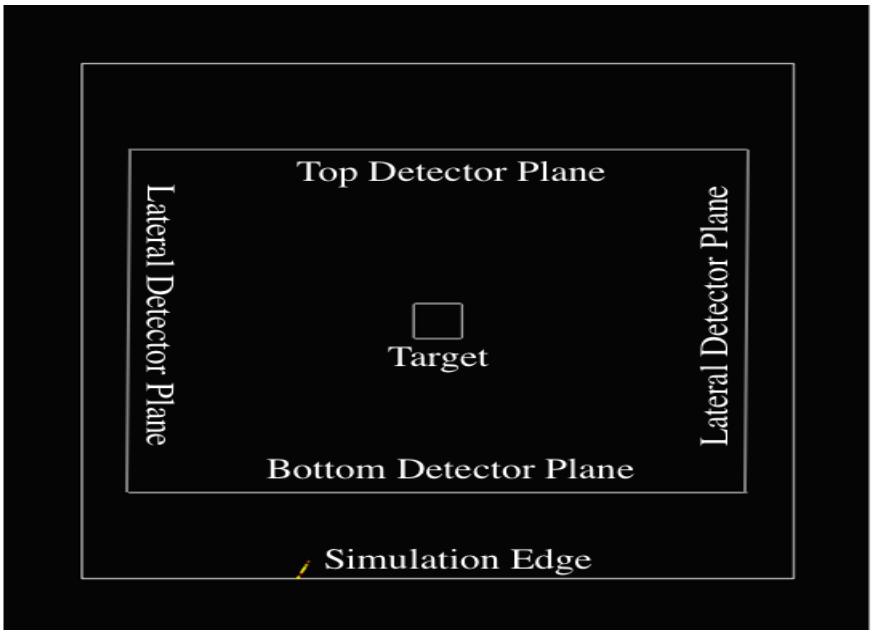


Fig. 3.2 *Simple GEANT4 schematic of four detectors placed above, below and at the sides of the volume to be inspected.*

### 3.2.2 Muon Spectrum

The muon energy spectrum at sea level is calculated using the parameterisation proposed by Gaisser [99], but modified so that large zenith angles, muon decay in the atmosphere and fraction of prompt muons are included [50]:

$$\frac{dN}{dE_\mu d\Omega}(E_\mu,\theta^*) = 0.14(E_\mu+\Delta E_\mu)^{-2.7}\left(\frac{1}{1+\frac{1.1(E_\mu+\Delta E_\mu)\cos\theta_1}{115GeV}}+\frac{0.054}{1+\frac{1.1(E_\mu+\Delta E_\mu)\cos\theta_1}{850GeV}}+R_c\right)\times p_d \tag{3.1}$$

- $\frac{dN}{dE_\mu d\Omega}(E_\mu,\theta^*)$ is the differential muon intensity at sea level in units $\mathrm{cm}^{-2}\mathrm{s}^{-1}\mathrm{sr}^{-1}\mathrm{GeV}^{-1}$
- $E_\mu$ is the muon energy at the surface in GeV.
- $\theta^*$ is the muon zenith angle at the surface.
- $\theta_1$ is the muon zenith angle at the height of muon production.
- $\cos\theta_1 = \sqrt{1-0.99(1-\cos^2\theta^*)}$.
- $\Delta E_\mu = 2.06\times 10^{-3}(1030/\cos\theta_1 - 120)$ is the muon energy loss in the atmosphere.

- $R_c = 10^{-4}$ is the ratio of prompt muons to pions.
- $p_d$ is the probability for a muon to not decay in the atmosphere, which can be expressed as $p_d = a^b$, where $a = \frac{120}{1030/\cos\theta_1}$ and $b = \frac{1.04}{\cos\theta_1 (E_\mu + \Delta E_\mu/2)}$ [50].

For the work presented in this thesis the modified Gaisser parameterisation (MGP) is used to generate a muon spectrum, which is then incorporated into the simulations so that the true distribution of cosmic-ray muons at sea level are represented. Fig. 3.3 shows a comparison of the MGP muon spectra at two different angles with computational data (CRY) [49], experimental data [47, 56] and a different modified Gaisser parameterisation [100]. Tests of vertical muons (0°), show good agreement (within a few %) with theoretical and experimental results for muon momentum greater than 1 GeV/c. Below this momentum is where deviations start to occur. Experimental measurements are only given down to 0.4 GeV/c. From these results it appears the flux from CRY [49] gives a systematic underestimation of the muon flux at low energies, the flux from Mengyum's MGP [100] gives a systematic overestimation of the flux at low energies, and the flux from Kudryavtsev's MGP [50] yields the most reasonable agreement. For muons which arrive at much larger angles (75°), both MGPs demonstrate good agreement with experimental data for all energies. The muon flux from CRY gives a systematic underestimation of the muon flux for momentum greater than $\approx$ 30 GeV.

### 3.2.3 PoCA Algorithm

PoCA is a heuristic algorithm originally designed as a proof of principle concept to show that muon scattering could be used to distinguish between low density, medium density and high density material [3]. Instead of treating each individual scatter a muon undertakes as it passes through a volume, it assumes the muon scatters just once, at a single point. It is assumed that the initial and final tracks of the muon are known, and therefore their entry and exit paths can be extrapolated back to their point of closest approach. Since scattering has been assumed to occur in a single location, the tracks can be thought of as points moving along two fixed lines in space. PoCA represents the position where these two tracks reach their closest possible distance, with the scattering point being the midpoint between these two lines.

(a) Generate an $N \times N \times N$ grid over the inspected volume and split into $L \times L \times L$ voxels. Establish a cartesian co-ordinate system in three dimensions with $z$

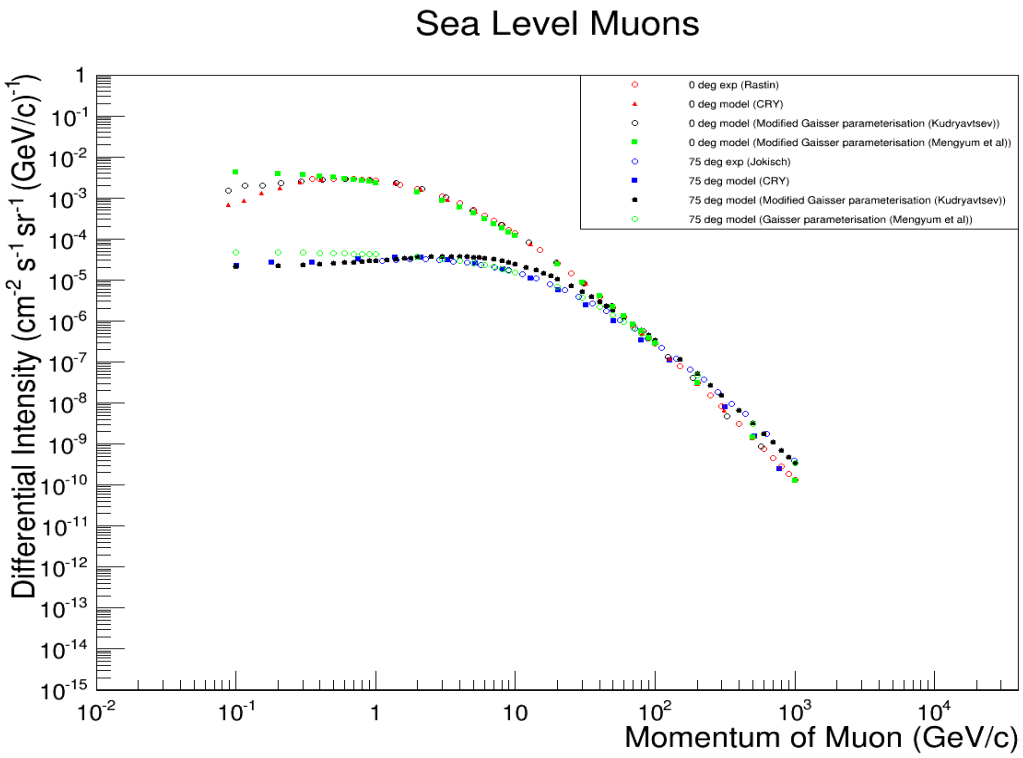


Fig. 3.3 *Comparison of the CRY generated, two modified Gaisser parameterisation and experimental data muon spectra at sea level for two different zenith angles. Red open circle - 0 deg experimental [47]; red triangle - 0 deg CRY [49]; black open circle - 0 deg modified Gaisser parameterisation used in this thesis [50]; green filled square - 0 deg a different modified Gaisser parameterisation [100]; black filled circle - 75 deg modified Gaisser parameterisation used in this thesis [50]; blue square - 75 deg CRY [49]; blue open circle - 75 deg experimental [56]; green hollow circle - 75 deg a different modified Gaisser parameterisation [100].*

as the vertical. Measured data is position ($x_{pos}$, $y_{pos}$, $z_{pos}$) and direction cosines ($mx$, $my$, $mz$) of each of the incoming $(x_{pos}, y_{pos}, z_{pos}, mx, my, mz)_{in}$ and outgoing $(x_{pos}, y_{pos}, z_{pos}, mx, my, mz)_{out}$ muon tracks ($M$).

(b) For $i$:=1 to $M$ tracks get incoming $((x_{pos}, y_{pos}, z_{pos}, mx, my, mz)_{in})_i$ and outgoing $((x_{pos}, y_{pos}, z_{pos}, mx, my, mz)_{out})_i$ muon track data.

(c) For each muon track calculate the PoCA point using Eq. (3.2), Eq. (3.3), Eq. (3.4) and Eq. (3.5).

(d) For each muon track calculate the scattering angle using Eq. (3.6).

(e) Add the calculated scatter angle to the PoCA voxel it resides within.

(f) Calculate the average scatter angle for all scatter points that reside in the calculated voxel.

(g) Repeat steps c - f for all $M$ tracks.

### PoCA Mathematics

Consider two infinite lines $\mathbf{L}_1$: $P(s) = P_0 + s\,(P_1\text{-}P_0) = P_0 + s\mathbf{u}$ and $\mathbf{L}_2$: $Q(t) = Q_0 + t\,(Q_1\text{-}Q_0) = Q_0 + t\mathbf{v}$, where a vector between points on the two lines can be created: $\mathbf{w}(s,t) = P(s)\text{-}Q(t)$. In any n-dimensional space, $\mathbf{L}_1$ and $\mathbf{L}_2$ are closest at the unique points $P(s_c)$ and $Q(t_c)$, for which $\mathbf{w}(s_c,t_c)$ achieves its minimum length. Also, for the situation when $\mathbf{L}_1$ and $\mathbf{L}_2$ are not parallel, then the line segment from $P(s_c)$ to $Q(t_c)$ joining the closest points becomes uniquely perpendicular to both lines at the same time, while also being the only line segment to have this property. In other terms, the vector $\mathbf{w}_c = \mathbf{w}(s_c,t_c)$ is uniquely perpendicular to the line direction vectors of $\mathbf{L}_1$ and $\mathbf{L}_2$, $\mathbf{u}$ and $\mathbf{v}$, and obtaining this vector is equivalent to satisfying the two equations: $\mathbf{u} \cdot \mathbf{w}_c = 0$ and $\mathbf{v} \cdot \mathbf{w}_c = 0$. This concept is shown graphically by Fig 3.4 [101].

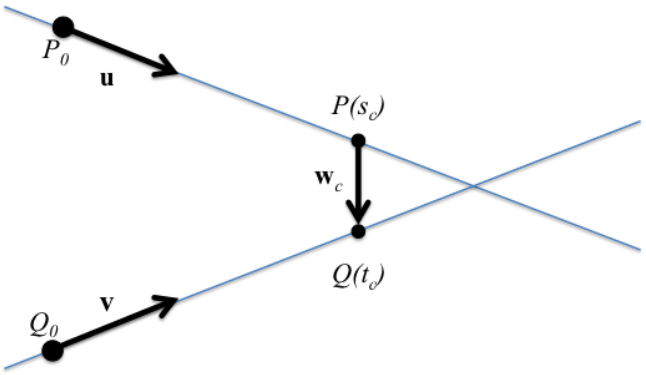


Fig. 3.4 *Points of closest approach ($P(s_c)$, $Q(t_c)$) are the end points of the line segment where the length of $w_c$ is at a minimum [101].*

By substituting $\mathbf{w}_c = P(s_c)\text{-}Q(t_c) = \mathbf{w}_0 + \mathbf{s}_c\mathbf{u} - \mathbf{t}_c\mathbf{v}$, where $\mathbf{w}_0 = P_0\text{-}Q_0$, into each of these two equations we get two simultaneous linear equations:

$$(\mathbf{u}\cdot\mathbf{u})s_c - (\mathbf{u}\cdot\mathbf{v})t_c = -\mathbf{u}\cdot\mathbf{w_0} \tag{3.2}$$

$$(\mathbf{v}\cdot\mathbf{u})s_c - (\mathbf{v}\cdot\mathbf{v})t_c = -\mathbf{v}\cdot\mathbf{w_0} \tag{3.3}$$

Then, letting $a = \mathbf{u} \cdot \mathbf{u}$, $b = \mathbf{u} \cdot \mathbf{v}$, $c = \mathbf{v} \cdot \mathbf{v}$, $d = \mathbf{u} \cdot \mathbf{w}_0$, and $e = \mathbf{v} \cdot \mathbf{w}_0$, we solve for $s_c$ and $t_c$ as:

$$s_c = \frac{be - cd}{ac - b^2} \tag{3.4}$$

$$t_c = \frac{ae - bd}{ac - b^2} \tag{3.5}$$

whenever the denominator $ac - b^2$ is nonzero. When $ac - b^2 = 0$, the two equations are dependent, the two lines are parallel, and the distance between the lines is constant. Having solved for $s_c$ and $t_c$, through substituting each of these values into the equation of each line ($\mathbf{L}_1$ and $\mathbf{L}_2$), we can determine the points *P($s_c$)* and *Q($t_c$)* where the two lines $\mathbf{L}_1$ and $\mathbf{L}_2$ are closest. The PoCA point is the mid-point between these two points.

The angle between the two vectors can be calculated using the following equation:

$$\theta = \cos^{-1}\left(\frac{a \cdot b}{|a|\,|b|}\right) \tag{3.6}$$

where $a$ and $b$ are the vectors of the incoming and outgoing muon rays.

### 3.2.4 Simulation Parameters

Five million muons are generated over a 10 m $\times$ 10 m surface area. This corresponds to a 5 minute exposure time. These muons are implemented into the simulations so that the true distribution of cosmic-ray muons with respect to their energies and zenith angles at sea level are represented. Muons are generated using the MGP (Eq. (3.1)) and interfaced with GEANT4, which is used to simulate and track the passage of particles through the inspected volume and detectors. A standard setup for the muon tomography system implemented in GEANT4 is displayed in Fig. 3.2.

When using GEANT4 each volume created needs to be designated as a specific material. For this study the total volume in which target materials are placed is designated as being made of air, with each of the virtual detectors being comprised of a vacuum. Detectors are comprised of a vacuum so that any muons passing through them will not undergo any scattering. The detectors are placed above, below and at the sides of the

volume to be inspected. They are assumed to have 100% detection efficiency, so an idealised scenario could be simulated. For the simulations discussed in this chapter the top and bottom detector planes are of size 7 m $\times$ 4 m and are 0.1 mm thick. This size of detector is chosen so that all muons generated will pass through the top detector plane, with a thickness chosen to limit the amount of time a muon will spend in each detector. There is a distance of 4 m separating the top detector from the bottom detector. This gap size was chosen as it is large enough to fit three 100 cm $\times$ 100 cm $\times$ 100 cm sized blocks stacked vertically with a 50 cm gap between each block. Upon passing through a detector the muons are tagged, with their energy, position and direction recorded.

The targets to be inspected are blocks of different sizes. These are 10 cm $\times$ 10 cm $\times$ 10 cm, 50 cm $\times$ 50 cm $\times$ 50 cm or 100 cm $\times$ 100 cm $\times$ 100 cm and are made up of low density (water, polyethylene, concrete), medium density (iron) or high density (lead, $^{238}$U) material. Muon scattering between the two sets of detectors is assumed to occur at a single point. This point of muon scattering is then reconstructed using the PoCA algorithm [101]. Since the volume is not totally enclosed by detectors some muons will be missed that pass through the sides that are not covered. Secondly, as discussed in section 2.5, muons will lose energy as they pass through materials and can stop within the material. Finally, muons will also sometimes undergo decay within the total volume. Therefore in addition to missing some muons, others may stop in a target or undergo decay within the total volume and hence be unavailable for analysis.

Only muons that pass through the top detector then either side detector, or the top detector then bottom detector, are available for analysis. Since only those muons that initially pass through the top detector are used in the analysis, a muon plane surface area of 10 m $\times$ 10 m is chosen. The muons are generated with a $z$-position directly above the top detector plane. As the muon plane is implemented directly above the top detector, a surface area of 10 m $\times$ 10 m is large enough for muons of all angles and energies to meet the initial criteria to be considered for analysis (passing through the top detector). In this system it is extremely unlikely that muons with large zenith angles, which pass through the top detector, will also interact with targets in the inspected volume. This reduces the acceptance of the system for large zenith angle muons. Muons with large zenith angles typically have higher energies than overhead muons. Since the amount of scatter a muon undergoes is based on the muon energy, these large angle muons will scatter less in a given material then muons which arrive from overhead. Therefore the

rejection of these muons will have little impact on the ability to differentiate between materials based on muon scattering. To incorporate these muons, an analysis system that also uses muons which pass through a side detector then bottom detector, or side detector to side detector, can be used. In such a system the muon plane surface area would need to be made larger so that large zenith angle muons are not restricted.

## 3.3 Material Segregation using Muon Scattering

### 3.3.1 Material Segregation using Realistic Muon Momentum Spread

Table 2.5 shows the ability to distinguish between different materials using mono-energetic muons. This section presents a similar study but using muons generated via the MGP. Table 3.1 displays the average 3D scattering angle a muon undergoes when it passes through a material and the reconstructed ratio for each material that has been tested. Values are given for both the 3D scattering angle observed when propagating 5 million muons through the volume displayed in Fig. 3.2 using GEANT4 (Average Scatter (mrad) - GEANT4), and when using Eq. (2.17) (Calculated Scatter (mrad) - Eq. (2.17)). The reconstructed ratio is defined as the total number of muons that have interacted with the target and been correctly reconstructed where the target is located (correct reconstructions), divided by the total amount of muons that have interacted with the target and are available for reconstruction (muons detected in detectors). As discussed previously some muons that interact with the target may stop, miss a secondary detector, or decay. Therefore when calculating the average scattering angle by muons in each target, only those muons that have both interacted with the target and been detected in the surrounding detectors are included. As it can be seen for targets of the same depth, higher density materials such as $^{238}$U and its possible shielding components, such as lead or iron, are clearly distinguishable from lower density materials, such as polyethylene, concrete or water. This clearly displays the ability of the PoCA algorithm to categorise different densities of materials under simple systems, assuming it is known that a muon passed through a target.

However, a feature that may cause concern is the similar average scattering angle observed for low density materials with high thicknesses, against high density materials with low thicknesses. As shown in Eq. (2.17), the amount of scattering by a muon depends on the radiation length of the material being traversed. Through increasing the thickness of low density materials their thickness, as measured in radiation lengths, can become the same as high density materials. Since the amount of scattering undertaken by a muon as it passes through a material is dependent on this quantity, materials with the same lengths as measured in radiation lengths may result in similar scattering angles being observed. This therefore causes concern over whether different density materials can be clearly identified based on this measurement alone. It is generally counteracted

through estimating the projected scattering angle distribution width per unit length.

As material density increases so does the reconstructed ratio for blocks of the same size. Since the PoCA algorithm assumes scattering to take place at a single point, this point will be most heavily weighted towards the object that causes the greatest degree of scattering. In the simulations, only the block and air can contribute to the overall path of a muon. Low density materials cause muons to undergo less scattering on average than high density materials. It is therefore more likely that when muons interact with air, this interaction will have greater significance on a muons overall path for systems involving low density materials, than those involving high density materials. Hence the reconstruction ratio increases from low density to high density materials. A secondary feature is that the reconstruction ratio increases for larger volumes of the same material. This is for the same reasons as discussed above. As the average scattering angle by a muon increases with increasing thickness, the reconstructed scattering point will become more heavily weighted towards the target as opposed to the surrounding air.

Table 3.1 Average scattering angle suffered by a muon (Average Scatter (mrad) - GEANT4), and reconstructed ratio when propagating 5 million muons through an inspected volume containing various sized blocks of different density materials. The average scattering angle calculated using Eq. (2.17) is also given (Calculated Scatter (mrad) - Eq. (2.17)). This value has been calculated using muon energy of 4 GeV.

| Material | Dimensions | Muon Interactions with Target | Muons Passing through Detectors | Correct Reconstructions | Average Scatter (mrad) - GEANT4 | Calculated Scatter (mrad) - Eq. (2.17) | Reconstructed Ratio |
|---|---|---|---|---|---|---|---|
| Water | $10 \times 10 \times 10$ cm$^3$ | 1009 | 941 | 90 | $8.55 \pm 0.52$ | 1.70 | 0.09 |
| Polyethylene | $10 \times 10 \times 10$ cm$^3$ | 998 | 948 | 65 | $0.46 \pm 0.35$ | 1.45 | 0.07 |
| Concrete | $10 \times 10 \times 10$ cm$^3$ | 986 | 944 | 135 | $12.92 \pm 0.52$ | 2.92 | 0.14 |
| Iron | $10 \times 10 \times 10$ cm$^3$ | 1056 | 985 | 286 | $30.54 \pm 1.40$ | 8.66 | 0.30 |
| Lead | $10 \times 10 \times 10$ cm$^3$ | 1053 | 967 | 408 | $55.68 \pm 2.62$ | 15.88 | 0.44 |
| $^{238}$U | $10 \times 10 \times 10$ cm$^3$ | 968 | 922 | 448 | $68.94 \pm 2.97$ | 21.61 | 0.49 |
| Water | $50 \times 50 \times 50$ cm$^3$ | 23917 | 22845 | 10667 | $14.31 \pm 0.17$ | 4.05 | 0.47 |
| Polyethylene | $50 \times 50 \times 50$ cm$^3$ | 23911 | 22855 | 10146 | $12.57 \pm 0.17$ | 3.45 | 0.44 |
| Concrete | $50 \times 50 \times 50$ cm$^3$ | 23912 | 22581 | 12524 | $21.99 \pm 0.17$ | 6.92 | 0.55 |
| Iron | $50 \times 50 \times 50$ cm$^3$ | 23913 | 21300 | 14506 | $49.92 \pm 0.52$ | 20.47 | 0.68 |
| Lead | $50 \times 50 \times 50$ cm$^3$ | 23918 | 20987 | 15369 | $87.62 \pm 0.87$ | 37.47 | 0.73 |
| $^{238}$U | $50 \times 50 \times 50$ cm$^3$ | 23920 | 19628 | 14592 | $104.02 \pm 1.05$ | 50.94 | 0.74 |
| Water | $100 \times 100 \times 100$ cm$^3$ | 94906 | 89037 | 56149 | $17.28 \pm 0.17$ | 5.88 | 0.63 |
| Polyethylene | $100 \times 100 \times 100$ cm$^3$ | 94914 | 89343 | 54983 | $15.71 \pm 0.17$ | 5.01 | 0.62 |
| Concrete | $100 \times 100 \times 100$ cm$^3$ | 94907 | 87237 | 60060 | $26.00 \pm 0.17$ | 10.04 | 0.69 |
| Iron | $100 \times 100 \times 100$ cm$^3$ | 94902 | 76826 | 58190 | $57.77 \pm 0.35$ | 29.62 | 0.76 |
| Lead | $100 \times 100 \times 100$ cm$^3$ | 94903 | 74423 | 58359 | $102.28 \pm 0.52$ | 54.19 | 0.78 |
| $^{238}$U | $100 \times 100 \times 100$ cm$^3$ | 94901 | 64889 | 51138 | $115.37 \pm 0.70$ | 73.64 | 0.79 |

### 3.3.2 Comparison of Three Block Scenarios

The three block scenario consists of either three 10 cm $\times$ 10 cm $\times$ 10 cm, 50 cm $\times$ 50 cm $\times$ 50 cm or 100 cm $\times$ 100 cm $\times$ 100 cm blocks of low density, medium density and high density materials placed in air. Both horizontal and vertically placed blocks, separated along with the $x$-plane or $z$-plane are tested. As in section 3.3.1, both the average scattering angle of a muon and the reconstruction ratio for each of the blocks within a simulation have been calculated. These tests has been conducted to demonstrate the capability of the PoCA algorithm to accurately differentiate blocks of materials with different densities, in simple geometries. Visual analysis is conducted through first splitting the total geometry into 5 cm $\times$ 5 cm $\times$ 5 cm voxels. For all muons reconstructed with PoCA in a particular voxel, the average scattering angle for this voxel is calculated. Only those voxels that have three or more muon scattering points reconstructed within it are included in the analysis. This is done for two reasons. Firstly through using at least three muon scattering points per voxel, it helps account for any large scattering angles that may have been calculated through incorporating it into an average. Secondly, muon scattering points are more likely to be reconstructed where targets are located. Therefore through using three or more it helps remove reconstructed scatter points from the volumes surrounding the targets, where no targets are located. 3D images are plotted with a colour gradient based on the scattering angle observed in each voxel. All voxels with an average scattering angle of less than 1° are made transparent. The transparency of the voxels then decreases uniformly until all those voxels with an angle greater than 8° are completely solid. Full results for all three block scenarios are given in Table 3.2. Fig. 3.5 displays the ability to distinguish different density materials in a horizontal system along with a schematic of the system. The schematic is not drawn to scale. Water (right) is centred at $x$ = 150 cm, $y$ = 0 cm, $z$ = 0 cm, $^{238}$U (middle) at $x$ = 0 cm, $y$ = 0 cm, $z$ = 0 cm and iron (left) at $x$ = -150 cm, $y$ = 0 cm, $z$ = 0 cm. As shown by Table 3.2, under this configuration approximately the same amount of muons will interact with each block.

The PoCA reconstruction of the three block scenario shows similar results to that of the one block under the same conditions. All blocks of size 50 cm $\times$ 50 cm $\times$ 50 cm and 100 cm $\times$ 100 cm $\times$ 100 cm have been clearly reconstructed, with each of the different density materials being clearly distinguishable from one another. For blocks of size 10 cm $\times$ 10 cm $\times$ 10 cm, iron and $^{238}$U have been clearly reconstructed, whereas water cannot be detected above the background. This is due to the low number of muon tracks

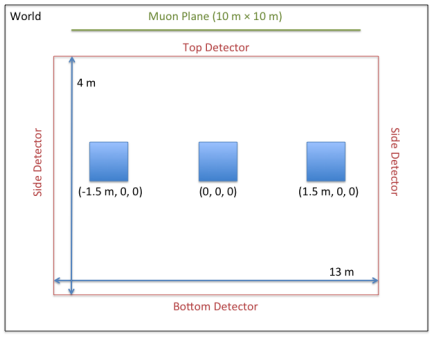


(a) *Schematic for the three block set-up with iron (left),* $^{238}U$ *(middle) and water (right).*

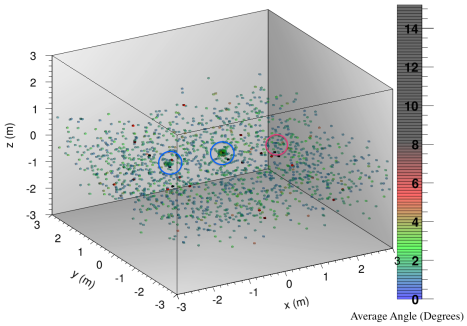


(b) *PoCA reconstruction for 10 cm* $\times$ *10 cm* $\times$ *10 cm blocks.*

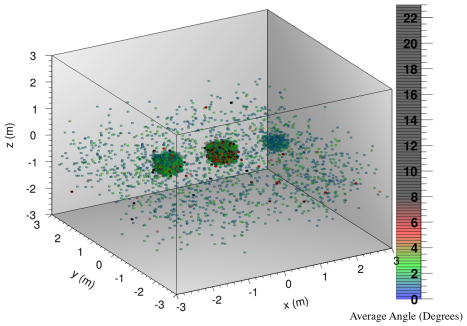


(c) *PoCA reconstruction for 50 cm* $\times$ *50 cm* $\times$ *50 cm blocks.*

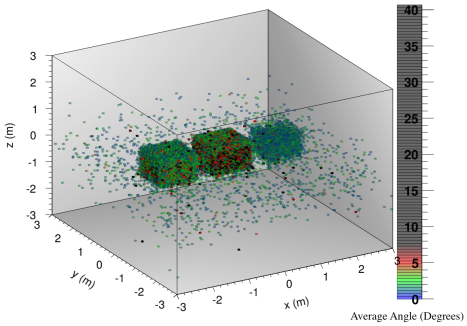


(d) *PoCA reconstruction for 100 cm* $\times$ *100 cm* $\times$ *100 cm blocks.*

Fig. 3.5 *Reconstructed image of the three block scenario where blocks are separated along the x-axis. Blue circles represent targets that have been reconstructed. Red circles represent targets that have not been reconstructed.*

reconstructed where the target is located, which is caused by additional scatters in air. From Table 3.1 (and Eq. (2.17)) the average scatter of a 4 GeV muon passing through water of depth 10 cm is 1.7 mrad. In the setup used for these simulations, muons that pass through a block of 10 cm $\times$ 10 cm $\times$ 10 cm water will also traverse a minimum of 390 cm of air. The average scatter of a 4 GeV muon passing through air ($X_0$ = 37.1 g/cm$^2$) of depth 390 cm, when using Eq. (2.17), is 0.322 mrad. As muons scatter less in water then higher density materials (assuming the same depth) the additional scatters from air have a larger weight to the total scatter of a muon through the system. This is reflected in the reconstruction ratio of a block of water of size 10 cm $\times$ 10 cm $\times$ 10 cm. From Table 3.2 it is only 0.09. The combination of fewer muon tracks correctly

reconstructed where the target is located, along with the condition for reconstruction of a voxel requiring 3 or more muon tracks to be reconstructed within it, demonstrates an inability to reconstruct small, low density materials. This shows a limitation of the PoCA algorithm. However, since most shielding that will be used consists of higher density materials such as iron or lead, the inability to correctly reconstruct small blocks of low density materials does not offer too much concern.

Table 3.2 Average scattering angle of a muon, and the reconstructed ratio for three block scenarios.

| Material | Dimensions | Muon Interactions with Target | Position | Muons Passing through Detectors | Correct Reconstructions | Average Scattering Angle (mrad) | Reconstructed Ratio |
|---|---|---|---|---|---|---|---|
| Horizontal | | | | | | | |
| Water | $10 \times 10 \times 10$ cm$^3$ | 908 | (1.5 m, 0, 0) | 899 | 83 | $9.60 \pm 0.70$ | 0.09 |
| Iron | $10 \times 10 \times 10$ cm$^3$ | 945 | (-1.5 m, 0, 0) | 912 | 307 | $30.89 \pm 1.40$ | 0.34 |
| $^{238}$U | $10 \times 10 \times 10$ cm$^3$ | 925 | (0, 0, 0) | 892 | 431 | $65.62 \pm 3.49$ | 0.48 |
| Water | $50 \times 50 \times 50$ cm$^3$ | 23328 | (1.5 m, 0, 0) | 22755 | 11027 | $13.79 \pm 0.17$ | 0.49 |
| Iron | $50 \times 50 \times 50$ cm$^3$ | 23428 | (-1.5 m, 0, 0) | 21035 | 14512 | $48.69 \pm 0.52$ | 0.69 |
| $^{238}$U | $50 \times 50 \times 50$ cm$^3$ | 23699 | (0, 0, 0) | 20051 | 14988 | $98.79 \pm 1.05$ | 0.75 |
| Water | $100 \times 100 \times 100$ cm$^3$ | 93286 | (1.5 m, 0, 0) | 89087 | 55879 | $17.28 \pm 0.17$ | 0.63 |
| Iron | $100 \times 100 \times 100$ cm$^3$ | 93284 | (-1.5, 0, 0) | 75387 | 55225 | $57.60 \pm 3.49$ | 0.73 |
| $^{238}$U | $100 \times 100 \times 100$ cm$^3$ | 94725 | (0, 0, 0) | 66432 | 50262 | $112.92 \pm 6.98$ | 0.76 |
| Vertical | | | | | | | |
| Water | $10 \times 10 \times 10$ cm$^3$ | 801 | (0, 0, -1.8 m) | 799 | 50 | $11.86 \pm 0.52$ | 0.06 |
| Iron | $10 \times 10 \times 10$ cm$^3$ | 1006 | (0, 0, 0.8 m) | 948 | 238 | $33.16 \pm 1.40$ | 0.25 |
| $^{238}$U | $10 \times 10 \times 10$ cm$^3$ | 940 | (0, 0, -0.5 m) | 909 | 463 | $62.83 \pm 2.49$ | 0.51 |
| Water | $50 \times 50 \times 50$ cm$^3$ | 19841 | (0, 0, -1.8 m) | 19462 | 8202 | $15.36 \pm 1.57$ | 0.42 |
| Iron | $50 \times 50 \times 50$ cm$^3$ | 24656 | (0, 0, 0.8 m) | 21606 | 13167 | $45.90 \pm 1.57$ | 0.61 |
| $^{238}$U | $50 \times 50 \times 50$ cm$^3$ | 22827 | (0, 0, -0.5 m) | 19359 | 13736 | $100.88 \pm 1.57$ | 0.71 |
| Water | $100 \times 100 \times 100$ cm$^3$ | 64389 | (0, 0, -1.8 m) | 62472 | 27388 | $19.72 \pm 2.97$ | 0.44 |
| Iron | $100 \times 100 \times 100$ cm$^3$ | 98425 | (0, 0, 0.8 m) | 69543 | 39044 | $53.58 \pm 3.49$ | 0.56 |
| $^{238}$U | $100 \times 100 \times 100$ cm$^3$ | 84227 | (0, 0, -0.5 m) | 59174 | 38629 | $116.41 \pm 6.98$ | 0.65 |

A secondary concern is the build up of multiple scattering points in volumes where targets are not located, which have scattering angles similar to that of high density materials. This effect is mainly due to the interactions of muons with air. Through requiring multiple voxels with high average scattering angles to be located close together, it can be determined whether these voxels are attributed to high density materials or whether they are a product of occasional high scatters in air.

There is also a build-up of multiple voxels in volumes that surround where a target is located, with this effect more apparent for high density materials. This 'blurring' is caused by the inherent nature of the PoCA algorithm in which scattering is assumed to have occurred at a single point, with this point weighted towards the element that caused the greatest scatter to occur. As a muon path consists of multiple small deviations, the reconstructed scattering point can end up occurring close to but outside the voxels occupied by the target. As most muons arrive from angles close to directly overhead, and the PoCA point must lie somewhere along the incoming muon tracks trajectory, this effect is more noticeable along the vertical axis as opposed to the horizontal. Overall this system again displays the success of PoCA at reconstructing simple scenarios, with the capabilities and issues discussed consistent with previous results [3].

A three block scenario was also run in which the blocks were stacked vertically. This type of scenario is significantly different from previous simulations and looks to explore the difficulties PoCA has been shown to have in reconstructing vertical objects, compared to how it performs with non-vertical systems [3]. The reconstruction uses the same materials as before where 10 cm $\times$ 10 cm $\times$ 10 cm, 50 cm $\times$ 50 cm $\times$ 50 cm and 100 cm $\times$ 100 cm $\times$ 100 cm blocks of iron (top) centred at $x$ = 0 cm, $y$ = 0 cm, $z$ = 80 cm, $^{238}$U (middle) centred at $x$ = 0 cm, $y$ = 0 cm, $z$ = -50 cm and water (bottom) centred at $x$ = 0 cm, $y$ = 0 cm, $z$ = -180 cm were placed between four sets of detectors. A schematic and results for the reconstruction of this geometry is shown in Fig. 3.6. The schematic is not drawn to scale.

The PoCA reconstruction shows both the capabilities and issues of the PoCA algorithm. Once again all 50 cm $\times$ 50 cm $\times$ 50 cm and 100 cm $\times$ 100 cm $\times$ 100 cm blocks are clearly distinguishable from both the background and each other, while the 10 cm $\times$ 10 cm $\times$ 10 cm block of water is again not visible against the background. As it can be seen in Fig. 3.6, many scattering points have been reconstructed in the volumes

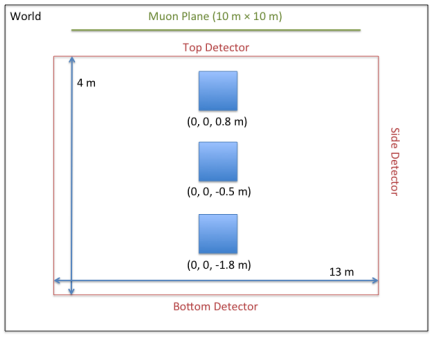


(a) *Schematic for the three block set-up with iron (top),* $^{238}U$ *(middle) and water (bottom).*

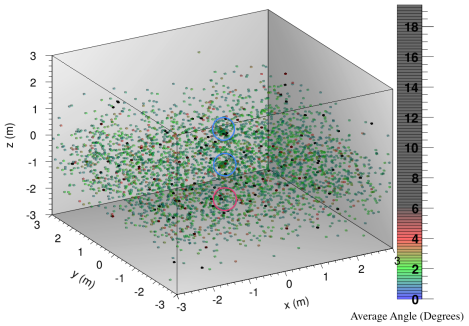


(b) *PoCA reconstruction for 10 cm* $\times$ *10 cm* $\times$ *10 cm blocks.*

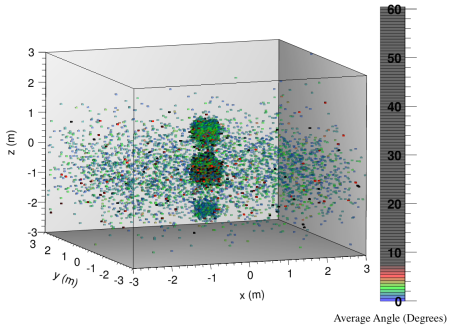


(c) *PoCA reconstruction for 50 cm* $\times$ *50 cm* $\times$ *50 cm blocks.*

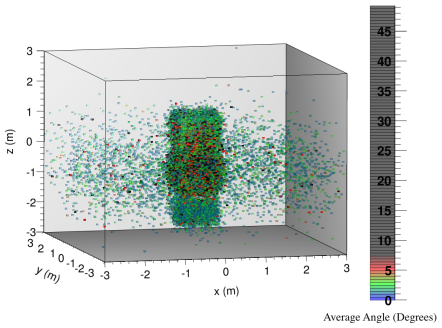


(d) *PoCA reconstruction for 100 cm* $\times$ *100 cm* $\times$ *100 cm blocks.*

Fig. 3.6 *Reconstructed image of the three block scenario where blocks are stacked vertically. Blue circles represent targets that have been reconstructed. Red circles represent targets that have not been reconstructed.*

between where targets are located, with the effect becoming more apparent as material size increases. Despite the correct reconstruction of all of the targets (except 10 cm $\times$ 10 cm $\times$ 10 cm of water) this effect creates the propensity for the misclassification of low density, medium density or even high density materials in volumes where no targets are located. As mentioned previously due to the nature of the PoCA algorithm the reconstructed scattering point will be most heavily weighted towards the element that causes the greatest amount of scattering to occur. As muons arrive from overhead, for vertically stacked targets a muon is likely to interact with and scatter in more than one target. This can cause the scattering point to be reconstructed in the volumes between where these targets are located. This effect is demonstrated in Fig. 3.7 where three

separate test cases are considered. Test case *a* considers two volumes of same density and equal size. Test case *b* considers two volumes of equal size but with a high density volume placed above a low density volume. Test case *c* considers the opposite of test case *b*. For muons that pass through same size, same density materials (test case *a*) the

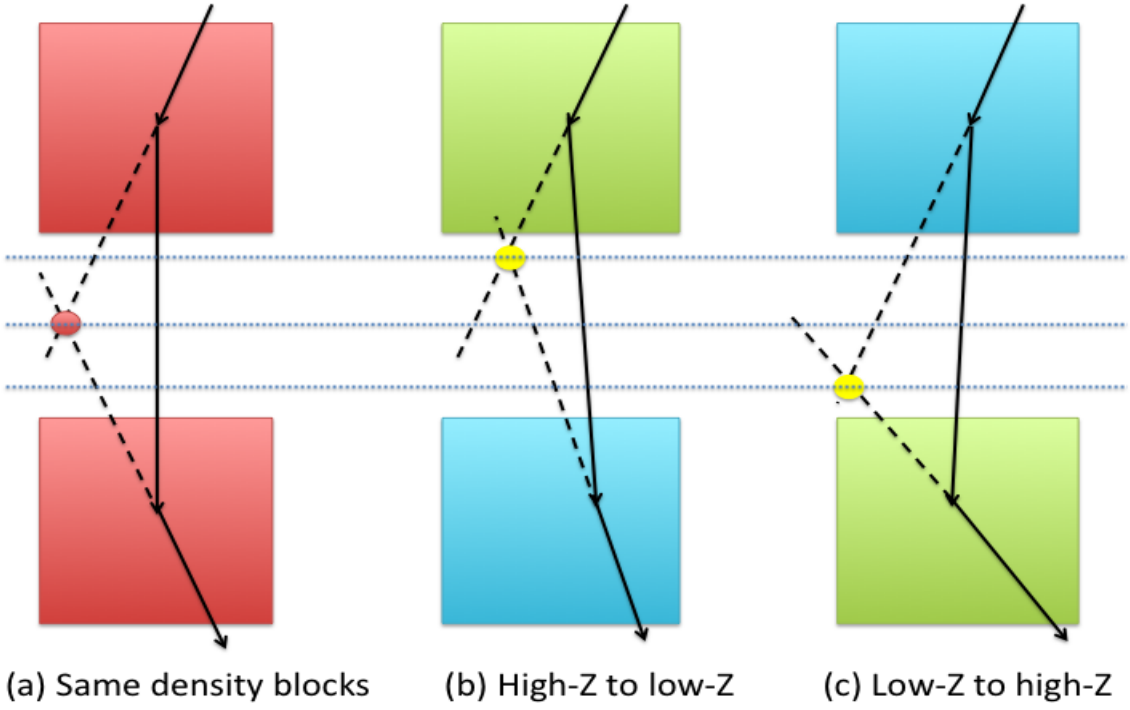


Fig. 3.7 *Illustration of why the reconstruction of multiple muon scattering points can occur outside a target material when passing through multiple targets. For simplicity muon tracks are shown to only scatter once within the target it is passing through.*

amount of scattering that occurs within each target will tend to be the same. This will in turn result in the muon scattering point being incorrectly reconstructed between the two targets. As the density of one target increases relative to the second (test case *b* and *c*) the amount of scattering caused by the higher density target will increase, causing the reconstructed scattering point to tend to lie towards this target. This effect of scattering points being incorrectly reconstructed is confirmed by the reconstruction ratios measured in all targets in the vertical scenario as compared to the horizontal scenario. From Table 3.2 the reconstruction ratio, and therefore the amount of correctly reconstructed muon scattering points within a target, is slightly higher for all materials in the horizontal system over the vertical. The majority of those muons that have been 'lost' represent ones that have been reconstructed in the volumes between where the targets

are located, as is shown in Fig. 3.7.

In realistic systems, multiple detector planes are placed around the inspected volume and a line fitting algorithm is used reconstruct the muons incoming and outgoing trajectory. In these systems the inherent position resolution of the detector will determine how accurately a muon track can be reconstructed. As resolution decreases the uncertainties in the line fit lead to vertical uncertainties in the calculated PoCA point. The uncertainties in the line fit become the dominant source of error in where a PoCA point is reconstructed (as opposed to the multiple deviations adding up). To counteract the line fit uncertainties, detectors can either be placed further apart or additional detectors can be used. Both these solutions have their positives and negatives. More detectors provide additional muon data points, but also increase the cost and complexity of the detector system. Increasing the distance between detectors will decrease the uncertainty in the line fit, but will also increase the overall inspection volume. This in turn will increase the complexity of the system and reduce the total number of muons passing through the inspected volume and therefore being available for analysis.

## 3.4 Summary

This chapter has discussed the initial concept of muon scattering tomography and the performance of the PoCA reconstruction technique in detecting different materials. Muon scattering tomography represents a feasible technique in detecting high density materials, such as shielded HEU, with the ability to locate and distinguish different density materials in simple geometries being demonstrated. However, since the PoCA algorithm only assumes scattering to occur at a single point it fails to take into account the actual physics of multiple scatterings that will be taking place. Upon the introduction of clutter this may result in multiple muon tracks being incorrectly reconstructed and therefore hinder the ability to detect shielded nuclear materials. In addition to this, due to the nature of the cosmic-ray muon spectrum, materials surrounded with vertical clutter may result in erroneous scatters being reconstructed in volumes where no materials are located, thus increasing the probability for false positives to occur.

# Chapter 4

# Material Segregation using Stopping Muons

In this chapter an overview of the concept of muon capture coupled to the production of secondaries is given in section 4.1. Section 4.2 displays the validity of GEANT4 when applied to muon capture and the processes that occur. Using GEANT4 the multiple physical processes that arise when $\mu^-$ and $\mu^+$ stop in different density materials has been investigated. This study is presented in section 4.3. A discussion of the secondaries produced when muons stop within a material and how they can be used to distinguish different materials then concludes this section. Following this, section 4.4 will present and discuss a new reconstruction algorithm that uses 3D line extrapolation of muons, which disappear in the inspected volume. Material differentiation using this new reconstruction algorithm in single and three block systems are tested. These tests are done for full energy spectrum muons in 5 minute exposure times. Scenarios are tested assuming 100% detector coverage and efficiencies and realistic detector coverage and efficiencies. Section 4.5 summarises the work presented.

## 4.1 Concept

As muons pass through a material they undergo energy losses via ionisation and $\mu^-$ can be captured on the orbital of a nucleus. This capture is followed by the release of muonic $X$-rays as the $\mu^-$ cascades down the energy levels towards to nucleus. Upon reaching the nucleus $\mu^-$ can be absorbed resulting in the production of excess neutrons and $\gamma$-rays via spallation or fission events. The process of absorption on the nucleus competes against decay whilst in the orbital. High-$Z$ materials such as HEU and its

shielding components are more likely to absorb a $\mu^-$ than low-$Z$ materials. Therefore the disappearance of a $\mu^-$ coupled to the detection of either prompt neutrons or $\gamma$-rays represents a strong signature for high density and nuclear materials, which can distinguish them from lower density clutter. Unlike $\mu^-$, $\mu^+$ cannot be captured on an orbital. Upon stopping in a material $\mu^+$ will always undergo decay. Muons used for analysis are those that are recorded in the top set of detectors but not in any subsequent set. For techniques that require the detection of a secondary, the disappearance of a muon must be coupled to the subsequent detection of either a prompt neutron or prompt $\gamma$-ray. If multiple muons meet this criteria, the identification of high density materials is made through ascertaining regions within the inspected volume where multiple muon disappearances have occurred. It should be noted that all simulations in this Chapter use GEANT4.9.6-p02 (unless otherwise specified) with the 'Shielding 2.0' physics list. All realistic muons used have been generated using the MGP. A full description of these two packages has been given in sections 3.2.1 and 3.2.2.

## 4.2 Testing the Validity of GEANT4

The accuracy of GEANT4 for $\mu^-$ capture and subsequent secondary production has been tested through measuring the neutron multiplicity and lifetime of muons when stopping in different elements. Simulation runs generated 10,000 muons at the centre of 1 cm $\times$ 1 cm $\times$ 1 cm blocks of different elements. These muons were given an initial energy of 1 eV so that all stopped within the target material. Both positive and negative muons were tested with all subsequent particle production that occurred recorded.

### 4.2.1 Neutron Multiplicity from Muon Capture

In general the process of $\mu^-$ absorption on a nucleus results in the production of a neutrino, a secondary residual nucleus and a transfer of energy to the residual nucleus:

$$\mu^- + (Z,A) \rightarrow (Z-1,A)^* + \nu_\mu \tag{4.1}$$

Bobodyanov [102] has demonstrated that the general trend of $\upsilon$ (= average number of neutrons per capture) is approximately described by the empirical function given in Eq. (4.2):

$$\upsilon = \alpha A^{1/3} \tag{4.2}$$

where Bobodyanov gives $\alpha = 0.30 \pm 0.02$ [102].

However, this increase in the average multiplicity of neutrons is only a rough description. As discussed in section 2.5.3, due to particular nuclear structure effects, the deviations from the smooth line that this formula predicts, can be quite large.

Table 4.1 displays the average neutron multiplicity observed per $\mu^-$ capture. Simulations were run using GEANT4-9.6p02, where 10,000 $\mu^-$ were generated at the centre of 1 cm $\times$ 1 cm $\times$ 1 cm targets of different density materials. The average multiplicity calculated using GEANT4 is given along with comparisons to experimental [68] and theoretical [69, 102] values. Muons were given a starting energy of 1 eV so that all stopped within the inspected target. The target in which muons were generated was made into a sensitive volume (GEANT4 detector) so that the production processes of all secondary neutrons were recorded. Table 4.2 displays the total number of $\mu^-$ captures, $\mu^-$ decays, the total amount of secondary neutrons produced and the total amount of secondary neutrons produced by $\mu^-$ capture. Only those neutrons produced directly via $\mu^-$ capture were used when calculating the average neutron multiplicity given in Table 4.1. It should be noted that not all muons will be captured by a nucleus upon stopping within a material. Some will undergo decay. Therefore, of the 10,000 muons that stop within a material only a portion of these will capture and produce secondary neutrons. Other neutron production processes that occur include neutron inelastic scattering, photon inelastic scattering and fission (for nuclear materials).

The average multiplicity of neutrons for $^{235}$U and $^{238}$U show reasonable agreement between simulations run in GEANT4.9.6-p02 with the 'Shielding 2.0' physics list and those from literature. For neutron multiplicities of non-nuclear materials, some discrepancy is observed between simulations when compared to literature. Although the general trend is consistent with values from literature (when taking into account the nuclear structure of different elements), there is a systematic underestimation of the number of neutrons emitted per $\mu^-$ capture for non-nuclear materials. However, since low density materials will not undergo neutron production via $\mu^-$ absorption as frequently as nuclear materials and due to the accuracy observed for the multiplicities of nuclear materials, it was concluded that GEANT4.9.6-p02 with the 'Shielding 2.0' physics list would be used. A secondary reason for this is demonstrated in Table 4.3. Table 4.3 dis-

Table 4.1 A comparison between experimental and GEANT4.9.6-p02 results of the $\mu^-$ capture neutron multiplicity when generating 10,000 muons of 1 eV at the centre of 1 cm $\times$ 1 cm $\times$ 1 cm blocks of various materials. Given are the multiplicities measured using GEANT4, Eq. (4.2) and found in literature.

| Material | Mass ($A$) Number | Atomic ($Z$) Number | GEANT4 | Eq. (4.2) | Literature |
|---|---|---|---|---|---|
| Aluminium | 27 | 13 | $0.71 \pm 0.01$ | $0.90 \pm 0.06$ | $1.26 \pm 0.06$ [68] |
| Silicon | 28 | 14 | $0.34 \pm 0.01$ | $0.91 \pm 0.06$ | $0.86 \pm 0.07$ [68] |
| Calcium | 40 | 20 | $0.24 \pm 0.01$ | $1.03 \pm 0.07$ | $0.75 \pm 0.03$ [68] |
| Iron | 56 | 26 | $0.96 \pm 0.01$ | $1.15 \pm 0.08$ | $1.12 \pm 0.04$ [68] |
| Silver | 108 | 47 | $1.33 \pm 0.01$ | $1.43 \pm 0.10$ | $1.61 \pm 0.06$ [68] |
| Gold | 197 | 79 | $1.19 \pm 0.01$ | $1.75 \pm 0.12$ | $1.66 \pm 0.04$ [68] |
| Lead | 207 | 82 | $1.31 \pm 0.01$ | $1.77 \pm 0.12$ | $1.71 \pm 0.07$ [68] |
| $^{235}$U | 235 | 92 | $2.51 \pm 0.01$ | $1.85 \pm 0.12$ | 2.4 [69] |
| $^{238}$U | 238 | 92 | $2.33 \pm 0.01$ | $1.86 \pm 0.12$ | 2.2 [69] |

Table 4.2 Total number of $\mu^-$ captures, $\mu^-$ decays, secondary neutrons and secondary capture neutrons when generating 10,000 muons of 1 eV at the centre of 1 cm $\times$ 1 cm $\times$ 1 cm blocks of various materials.

| Material | Stopping Muons | Capture Muons | Decay Muons | Total Neutron Production | muMinusCaptureAtRest Neutrons |
|---|---|---|---|---|---|
| Aluminium | 10,000 | 6058 | 3942 | 5039 | 4273 |
| Silicon | 10,000 | 6466 | 3534 | 2500 | 2177 |
| Calcium | 10,000 | 8485 | 1515 | 2226 | 2125 |
| Iron | 10,000 | 9116 | 884 | 12687 | 8704 |
| Silver | 10,000 | 9631 | 369 | 20901 | 12820 |
| Gold | 10,000 | 9726 | 274 | 19911 | 11559 |
| Lead | 10,000 | 9722 | 278 | 14289 | 12736 |
| $^{235}$U | 10,000 | 9718 | 282 | 205290 | 24351 |
| $^{238}$U | 10,000 | 9739 | 261 | 51517 | 22670 |

plays the $\mu^-$ capture neutron multiplicity of iron, lead, $^{235}$U and $^{238}$U for the different versions of GEANT4 available. All other versions of GEANT4 have a discrepancy in the multiplicities observed for non-nuclear materials and for nuclear materials. Therefore no other versions of GEANT4 that are available, offer more accurate results than the version that is used here.

### 4.2.2 Muon Lifetime Measurements

The average lifetime of an unbound muon is well known to be $\approx$ 2200 ns. At this time a muon will undergo decay via Eq. (2.23). For $\mu^-$ captured onto an atomic orbital the

Table 4.3 A comparison between the different versions of GEANT4 and experimental results of the $\mu^-$ capture neutron multiplicity when generating 10,000 muons of 1 eV at the centre 1 cm $\times$ 1 cm $\times$ 1 cm blocks of various materials.

| GEANT4 Version | Physics List | Iron | Lead | $^{235}$U | $^{238}$U |
|---|---|---|---|---|---|
| 9.5 | 0.1 | $1.48 \pm 0.01$ | $1.32 \pm 0.01$ | $1.64 \pm 0.01$ | $1.52 \pm 0.01$ |
| 9.5 | 1 | $1.47 \pm 0.01$ | $1.33 \pm 0.01$ | $1.65 \pm 0.01$ | $1.53 \pm 0.01$ |
| 9.6-p02 | 0.1 | $1.43 \pm 0.01$ | $1.39 \pm 0.01$ | $1.63 \pm 0.01$ | $1.51 \pm 0.01$ |
| 9.6-p02 | 2 | $0.96 \pm 0.01$ | $1.31 \pm 0.01$ | $2.51 \pm 0.01$ | $2.33 \pm 0.01$ |
| Literature Results | [68], [69] | $1.12 \pm 0.04$ | $1.71 \pm 0.07$ | 2.4 | 2.2 |

process of decay competes against $\mu^-$ absorption by the nucleus. Eq. (4.3) gives the Bohr radius. The Bohr radius ($a_0$) is equal to the most probable distance between the proton and electron in a hydrogen atom in its ground state.

$$a_0 = \frac{4\pi\varepsilon_0\hbar^2}{m_e e^2} \tag{4.3}$$

where $\varepsilon_0$ is the permittivity of free space, $\hbar$ is the reduced Planck's constant, $m_e$ is the electron rest mass and $e$ is the electric charge carried by an electron.

It can be seen that the Bohr radius is dependent on the mass of an electron. Due to the increased mass of a muon over its electron counterpart, when a $\mu^-$ becomes captured on the orbital of a nucleus, this increased mass acts to push its orbit closer to the nucleus. For electrons $a_0$ = 5.3 $\times$ $10^{-11}$ m, whereas for muons $a_0$ = 2.56 $\times$ $10^{-13}$ m. As $Z$ number increases so does the radius of the nucleus. Due to the 'pushing' of the $\mu^-$ on its orbital, for some high density materials such as uranium, the ground state (1s) orbital resides within the nucleus itself. When captured in an outer orbital a $\mu^-$ will cascade down the energy levels to the 1s state in $\approx 10^{-13}$ s. Since the nuclear radius increases with $Z$ number, so does the probability of a $\mu^-$ finding itself within the nucleus when reaching this state. This in turn increases the probability for $\mu^-$ absorption by the nucleus and therefore reduces the characteristic lifetime of a $\mu^-$. At some critical value of $Z$, the muon Bohr radius will lie inside the nuclear radius. The mean nuclear radius can be approximated by,

$$R = R_0 A^{1/3} \tag{4.4}$$

where $R$ is the mean nuclear radius, $R_0 \approx 1.2 \times 10^{-15}$ m and $A$ is the atomic mass number. The approximate point at which the muon Bohr radius will overlap the mean nuclear radius is calculated using Eq. (4.3) and Eq. (4.4). This line is demonstrated on

Fig. 4.1 and occurs at $Z \approx 45$. Fig. 4.1 demonstrates the average lifetime of negative muons when captured on nuclei. The results show a comparison between experimental measurements [103] and those calculated using GEANT4.9.6-p02. Good agreement is observed and it is clearly evident that as $Z$ number increases the lifetime of a muon decreases. Since $\mu^+$ will not be captured on the orbit of a material, upon stopping within a material a $\mu^+$ will always decay with a lifetime of $\approx 2200$ ns.

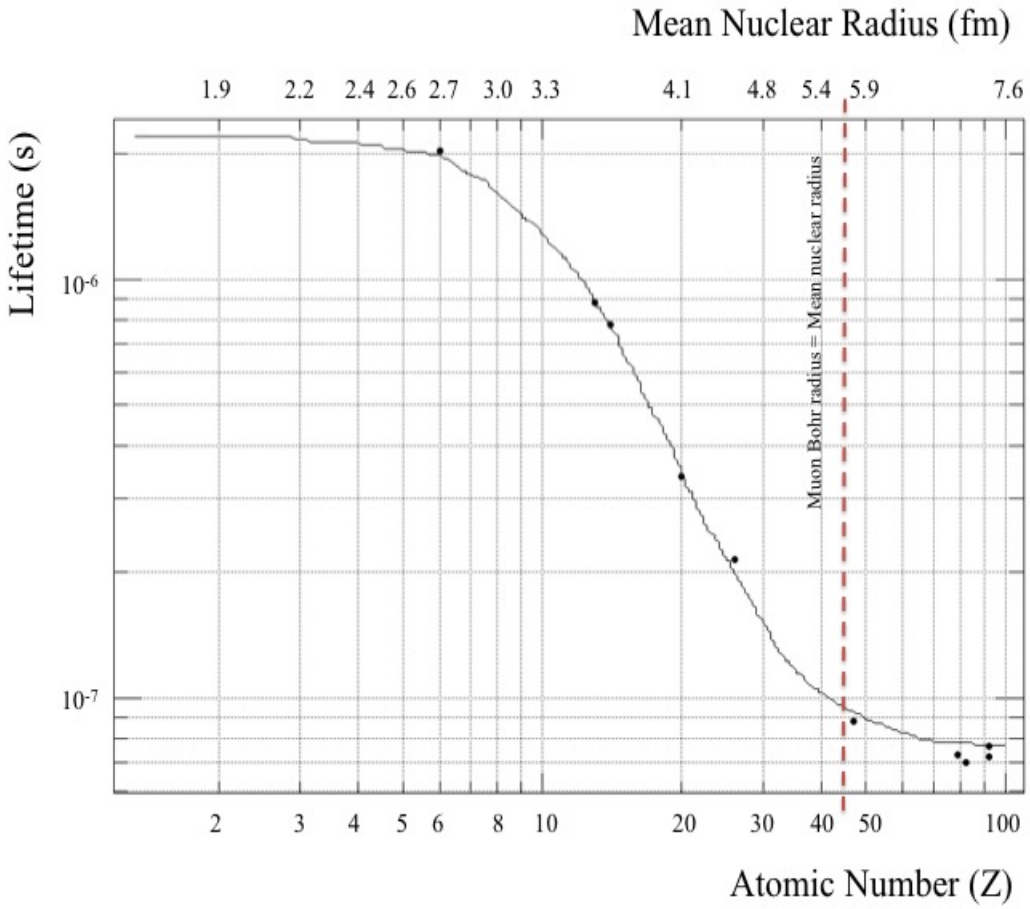


Fig. 4.1 *Average lifetime of $\mu^-$ when captured on various nuclei. The results show a comparison between experiment measurements [103] (trend line) and those calculated using GEANT4.9.6-p02 (black circles). Also given is the point at which the muon Bohr radius equals to mean nuclear radius (dashed red line).*

## 4.3 GEANT4 Simulations on Distinguishing Between Different Density Materials

### 4.3.1 Simulation Parameters

The following simulations in GEANT4.9.6-p02 involved vertically propagating either 500,000 $\mu^+$ or 500,000 $\mu^-$ through several 10 cm $\times$ 10 cm $\times$ 10 cm blocks of different materials. This was done to study the energy distribution of secondary particles with adequate statistics, both before and after a timing cut of 1 $\mu$s was made. The materials tested were water, iron, lead, $^{235}$U and $^{238}$U. Both $^{235}$U and $^{238}$U were tested as they emit differing levels of neutrons and $\gamma$-ray energies that may act as a marker for the detection of HEU. Detectors have been placed completely around the target so that it is fully encompassed. These detectors are assumed to be 100% efficient, and detect any neutrons or $\gamma$-rays that are produced within the simulation. The particles have been tagged as they pass through the detectors with their name, energy, parent, position, timing, momentum direction and process of production recorded. The target being inspected was made into a sensitive volume (GEANT4 detector) so that the production processes of all secondary neutrons and $\gamma$-rays were recorded.

Muons were positioned 1 mm above the target to be inspected and propagated vertically into the target. Two types of simulation (for both $\mu^+$ or $\mu^-$) have been conducted. The first used muon source energies of 0.1 eV, to ensure all 500,000 $\mu^+$ or $\mu^-$ stopped within the inspected target. The second used muon source energies of the full energy spectrum. For full energy spectrum generated muons, five million muons were generated using the MGP discussed in section 3.2.2. This was done so that the full spectrum with respect to their energies and angles were represented, hence muon source energies ranged from 100 MeV to 1000 GeV. Of these five million muons with realistic energies and angular distribution, 500,000 were randomly selected. Their realistic directions were then ignored and instead they were vertically propagated into the target to be inspected.

### 4.3.2 Gamma-ray and Neutron Spectra

Secondary neutrons and $\gamma$-rays have been analysed for muons with a fixed energy of 0.1 eV and full energy spectrum muons, of both charges. Energy spectra for each of these four studies, both before and after a timing cut is made have been plotted. A timing cut

of 1 $\mu$s is taken. 1 $\mu$s is used as it represents a realistic cut for which prompt neutrons and $\gamma$-rays can be detected when coupled to the disappearance of a muon, whilst also minimising the probability of an erroneous neutron or $\gamma$-ray from the environment, causing a false reading.

**Stopped Muons**

The dominant process of neutron production occurs when stopped $\mu^-$ are absorbed, resulting in $\mu^-$ induced fission or spallation. As discussed, negative muons will cascade down the orbital levels to the nucleus on times scales of the order $10^{-13}$ s. This cascade is coupled to the release of Auger electrons and muonic $X$-rays, which are unique for different elements. These muonic $X$-rays are a result of the movement down the energy levels on an atomic orbital. Fig. 4.2 shows the theoretical and experimental values expected for muonic $X$-rays with respect to $Z$ [65] for the $2p^{1/2} \rightarrow 1s^{1/2}$ and $3d^{5/2} \rightarrow 2p^{3/2}$ transitions. The high energies are due to the increased mass of the $\mu^-$ over its electron counterpart. Due to their intrinsically high energies, muonic $X$-rays produced will have no issues in overcoming any self-absorption or shielding present and therefore their detection represents a clear signal of the material that produces it. The process of $\mu^-$ capture is regulated by the 'muMinusCaptureAtRest' process in GEANT4.

For $\mu^-$, after capture on the orbital the process of absorption on the nucleus competes against decay in the orbital. As mentioned in section 4.2.2, the probability of a $\mu^-$ being absorbed by the nucleus increases as $Z$ number increases. The process of decay can cause the nucleus to become unstable, with neutrons and $\gamma$-rays released through de-excitation to subsequent spallation products. These 'de-excitation' $\gamma$-rays are of interest since they are unique to the elements that produce them. While lower energy $\gamma$-rays can be attenuated by self-shielding or intentional shielding, those with energies greater than 3 MeV have significant energy to penetrate any shielding present. These $\gamma$-rays are of particular interest, since there are no naturally occurring $\gamma$-rays of this energy or higher. Secondary processes that produce neutrons include photo-nuclear and neutron-nuclear interactions. For example, electrons that are produced from the decay of a $\mu^-$ in the orbital, can undergo bremsstrahlung, producing $\gamma$-rays. These $\gamma$-rays can then interact with a nucleus resulting in further production of neutrons and $\gamma$-rays.

For nuclear materials fission can occur when neutrons interact with the target nuclei,

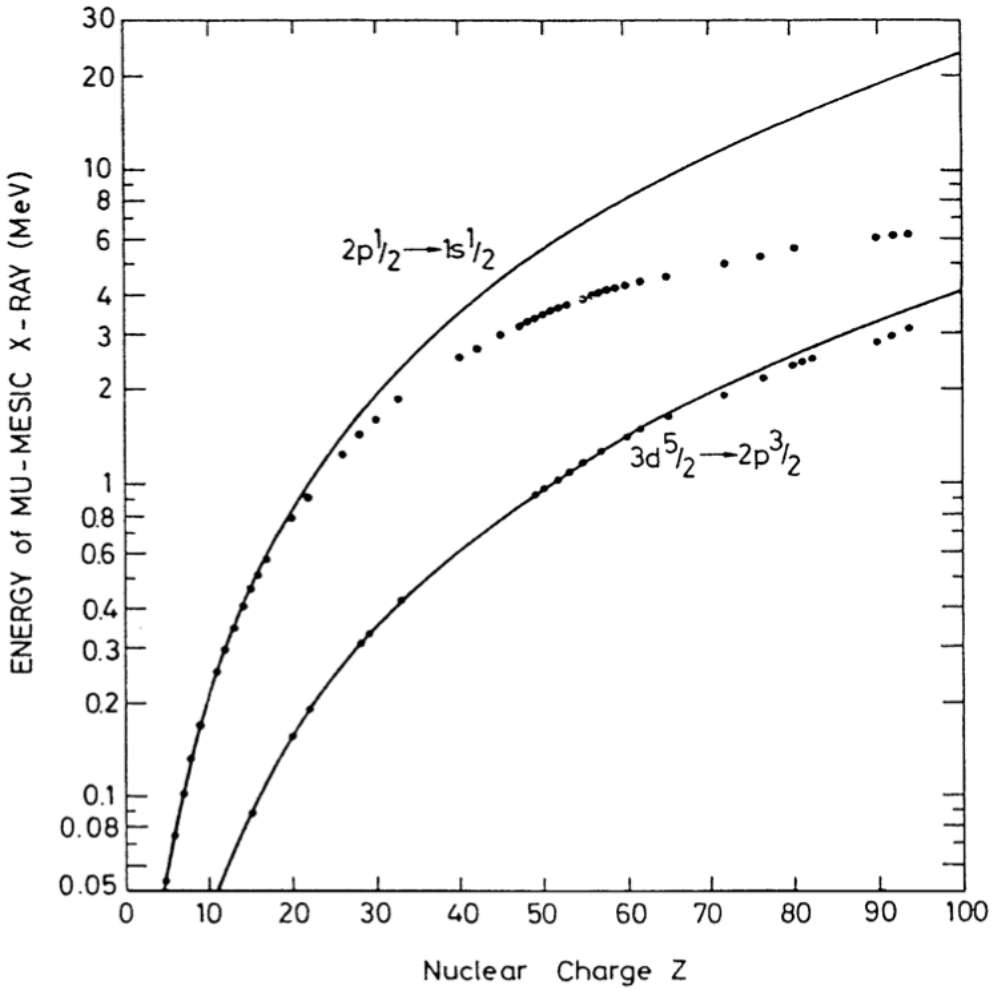


Fig. 4.2 *Muonic X-rays as a function of Z for theoretical (curved lines) and data (circles) values [65].*

thus creating an additional source of neutrons and $\gamma$-rays. After undergoing fission, any daughter products can also undergo radioactive decay, which adds an additional source of secondary particles. A final process that can occur is the capture of a neutron onto a nucleus, which doesn't result in fission. This process is mitigated by the 'nCapture' process in GEANT4 and results with the nucleus being left over in an excited state. Relaxation to the ground state will occur through the emission of a $\gamma$-ray. An example of this process is the capture of a neutron onto a $^{235}$U nucleus resulting in the production of $^{236}$U in an excited state. $^{236}$U will release a $\gamma$-ray of energy 6.545 MeV to get back to the ground state, before undergoing radioactive decay through to $^{208}$Pb, where it remains stable. Since radioactive decay can occur over timescales of seconds to years,

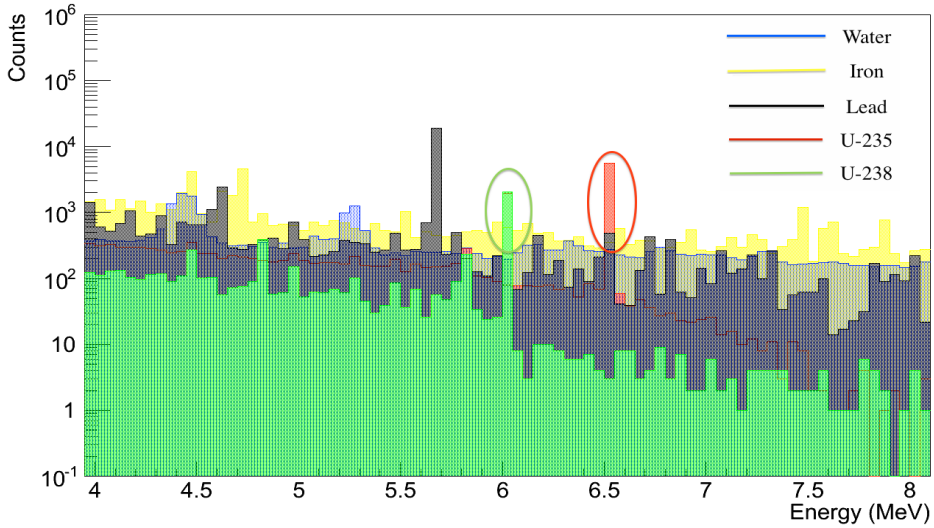


Fig. 4.3 *Secondary $\gamma$-ray spectrum from 4 MeV - 8 MeV, for stopping $\mu^-$ in cubes of water (blue), iron (yellow), lead (black), $^{235}U$ (red) and $^{238}U$ (green) after the timing cut is made.*

through taking a timing cut of 1 $\mu$s most of the signals observed from radioactive decay are removed.

The 6.545 MeV $\gamma$-ray described is demonstrated in Fig. 4.3. Fig. 4.3 displays the $\gamma$-ray spectrum from 4 MeV - 8 MeV, for stopping $\mu^-$ in cubes of water (blue), iron (yellow), lead (black), $^{235}$U (red) and $^{238}$U (green) after the timing cut is made. The 6.545 MeV line produced in $^{235}$U represents an attractive signature for HEU detection. In addition to this line there is also a $\gamma$-ray peak located at 6.035 MeV for both $^{235}$U and $^{238}$U. This peak is due to the instantaneous release of muonic $X$-rays as a $\mu^-$ cascades down the energy levels to reach the 1s state. The full $\gamma$-ray spectrum for stopping muons is displayed in Fig. 4.5. Due to their high penetrating power muonic X-rays represent an attractive signature for HEU detection.

Upon stopping within a material $\mu^+$ will not become captured on the orbital of the material. Instead $\mu^+$ will always undergo decay within the material, which leads to the production of positrons in the MeV range. These positrons will release $\gamma$-rays through bremsstrahlung and can also interact with nuclei, leading to the production of neutrons and secondary spallation products. Finally, positrons and electrons can annihilate resulting in the production of two 0.511 keV $\gamma$-rays.

### Muons with Full Energy Spectrum

Full energy spectrum muons undergo neutron and $\gamma$-ray production through the same processes as their stationary counterparts. As discussed their initial energies range from 100 MeV to 1000 GeV. Due to their high initial energies fewer stop within each material than low energy muons, hence a lower production rate is observed. Both the 6.545 MeV and the 6.035 MeV $\gamma$-ray peaks displayed in Fig. 4.3 are observed in the $\gamma$-ray spectrum produced when propagating full energy spectrum $\mu^-$ through the same materials. These peaks are produced by via the same processes described for stopping muons. They have a much lower intensity as fewer $\mu^-$ will stop in each material. This is shown in Fig. 4.4.

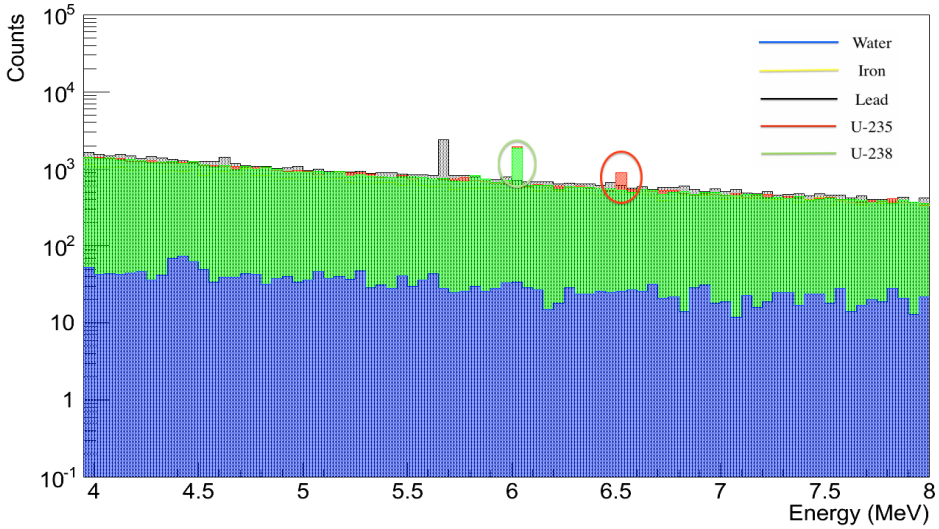


Fig. 4.4 *Secondary $\gamma$-ray spectrum from 4 MeV - 8 MeV, for full energy spectrum $\mu^-$ (range 100 MeV to 1000 GeV) in cubes of water (blue), iron (yellow), lead (black), $^{235}U$ (red) and $^{238}U$ (green) after the timing cut is made.*

As discussed in section 2.5.1, upon interacting with a target, muons in the energy range 100 MeV to 1000 GeV will primarily undergo energy loss via ionisation with the subsequent release of electrons. The rate of energy loss by muons has been discussed in section 2.5.1, with this rate described for a number of materials by Fig. 2.17. The energy loss for muons can be approximated as 2 MeV per g/cm$^2$. For blocks of uranium, which have a density of 18.95 g/cm$^3$, muons of energy 100 MeV will range out within

0.0264 cm, whereas muons of energy 1000 GeV require a depth of 264 m.

Electrons released as muons undergo ionisation will have higher energies on average than those that are produced via the decay of a muon. Gamma-rays produced when these electrons undergo bremsstrahlung, will have a higher endpoint energy than $\gamma$-rays produced via electron bremsstrahlung from decay muons. This causes a higher endpoint energy for $\gamma$-rays to be observed for cosmic muons over their stopped counterparts.

Gamma-rays can also be produced through muon bremsstrahlung, with this process more likely to occur in high density materials. Due to the much lower capture rate, there are fewer neutrons and $\gamma$-rays produced when full spectrum muons interact with target materials, than there are for stopping muons. A secondary process for production also occurs, which is defined in GEANT4 as 'muonNuclear'. This is where energetic muons collide directly with a nucleus resulting in a transfer of energy and subsequent excitation of the nucleus, from which excess neutrons, $\gamma$-rays and spallation products are produced.

Table 4.4 demonstrates the total number of neutrons produced via each GEANT4 production process for both stopping $\mu^-$ and $\mu^+$ and spectrum $\mu^-$ and $\mu^+$. The conclusions of the study presented in section 4.3 are that the dominant source of initial neutron production come from $\mu^-$ capture at rest, with this process more apparent for nuclear materials than those of a lower density. Further neutron production occurs when neutrons produced via $\mu^-$ capture interact with atomic nuclei. For non-nuclear material the dominant process of secondary neutron production occurs via neutron inelastic scattering, whereas for nuclear materials secondary neutrons are primarily produced through fission. For $\mu^+$, capture will not occur. Therefore the dominant source of primary neutron production comes from photon inelastic scattering with a nucleus (PhotonInelastic). The increased production rate of neutrons observed for $^{235}$U over other materials is of particular interest as it represents a signal that can be used to distinguish $^{235}$U from other materials. The average neutron energies for muon-induced fission of $^{235}$U and $^{238}$U have been found to be 2.24 MeV and 2.05 MeV respectively.

Additional signals that can be used to differentiate materials are the characteristic $\gamma$-rays emitted upon $\mu^-$ capture. Table 4.5 displays a number of these $\gamma$-ray peaks along with their GEANT4 production process. While low energy $\gamma$-rays are unfavourable due

to attenuation via self or intentional shielding, there are multiple high energy muonic $X$-rays produced from $\mu^-$ captured on the orbital of a nucleus. These $X$-rays are produced as the captured $\mu^-$ cascades down the energy levels to the 1s state and represent high energy, unique signatures for different elements. There has been much experimental work conducted into deducing the muonic $X$-ray intensities for different elements. The energies of muonic $X$-rays displayed in Fig. 4.5, Fig. 4.6, Fig. 4.7 and Fig. 4.8 are consistent with values obtained experimentally [104–106]. In each of these figures the $\gamma$-ray and neutron spectra for the materials tested has been superimposed on top of one another.

As displayed in Fig. 4.5, Fig. 4.6, Fig. 4.7 and Fig. 4.8, given a high resolution detector, with a large detection area and adequate statistics, the detection of nuclear materials through measuring these muonic $X$-rays is apparent. Unfortunately for the realistic applications discussed in this thesis, the detection of shielded HEU is required to occur under shorter time scales (5 minutes), with low resolution plastic scintillator detectors that are currently in use at ports. The inherent resolution of plastic scintillator detectors prevents the ability to accurately resolve different $\gamma$-ray peaks. Instead we must rely on techniques that measure the disappearance of a muon in coincidence with the detection of a secondary product. For this there are a number of techniques that can be considered, given the range of secondaries that are produced. These are:

1. Muon disappearance.
2. Muon disappearance coupled with prompt neutron detection.
3. Muon disappearance coupled with prompt $\gamma$-ray detection.
4. Muon disappearance coupled with the detection of a prompt $\gamma$-ray of energy $> 3$ MeV.
5. Muon disappearance coupled with prompt neutron or prompt $\gamma$-ray detection.
6. Muon disappearance coupled with the detection of a prompt neutron or prompt $\gamma$-ray of energy $> 3$ MeV.

Section 4.4.3 will discuss the capability of differentiating between materials using each of the different techniques available.

In reality the cosmic ray muon spectrum will be around half positive and half negative

muons. Fig. 4.9 displays the $\gamma$-ray and neutron spectra when combining the results of both full energy spectrum $\mu^-$ and full energy spectrum $\mu^+$ before and after a timing cut is made. From Fig. 4.9 it is clear that the characteristic $\gamma$-ray lines, which represent $^{235}$U and $^{238}$U, are still observable. There is also still a higher production rate for neutrons observed for $^{235}$U and $^{238}$U over non-nuclear materials.

Table 4.4 A comparison of the different GEANT4 neutron production processes when vertically propagating both 500,000 stopping $\mu^-$ and $\mu^+$ and spectrum $\mu^-$ and $\mu^+$ through 10 cm $\times$ 10 cm $\times$ 10 cm blocks of water, iron, lead, $^{235}$U and $^{238}$U.

| Material | Muon Energy | Muon Charge | Total | muMinusCaptureAtRest | NeutronInelastic | PhotonInelastic | muonNuclear | Other | Fission |
|---|---|---|---|---|---|---|---|---|---|
| Water | Stopping | Negative | 18,174 | 17,562 | 599 | 9 | 0 | 4 | 0 |
| Iron | Stopping | Negative | 679,807 | 483,835 | 195,811 | 125 | 0 | 36 | 0 |
| Lead | Stopping | Negative | 734,811 | 658,490 | 75,828 | 482 | 0 | 11 | 0 |
| $^{238}$U | Stopping | Negative | 2,615,956 | 1,160,398 | 1,221,426 | 3794 | 0 | 0 | 230,338 |
| $^{235}$U | Stopping | Negative | 10,336,222 | 1,255,261 | 3,231,665 | 3225 | 0 | 0 | 5,846,170 |
| Water | Stopping | Positive | 12 | 0 | 0 | 11 | 0 | 1 | 0 |
| Iron | Stopping | Positive | 2382 | 0 | 443 | 1926 | 0 | 13 | 0 |
| Lead | Stopping | Positive | 3847 | 0 | 192 | 3646 | 0 | 9 | 0 |
| $^{238}$U | Stopping | Positive | 28,958 | 0 | 13,078 | 12,648 | 0 | 7 | 3225 |
| $^{235}$U | Stopping | Positive | 133,017 | 0 | 41,305 | 15,382 | 0 | 53 | 76,278 |
| Water | Spectrum | Negative | 149 | 125 | 9 | 0 | 14 | 1 | 0 |
| Iron | Spectrum | Negative | 18,628 | 12,101 | 5399 | 551 | 408 | 169 | 0 |
| Lead | Spectrum | Negative | 27,537 | 19905 | 3396 | 2046 | 1708 | 482 | 0 |
| $^{238}$U | Spectrum | Negative | 169,520 | 53,914 | 77,575 | 13,902 | 5264 | 2071 | 16,794 |
| $^{235}$U | Spectrum | Negative | 597,789 | 59,520 | 186,158 | 16,607 | 4789 | 1859 | 328,856 |
| Water | Spectrum | Positive | 35 | 0 | 0 | 1 | 30 | 4 | 0 |
| Iron | Spectrum | Positive | 1568 | 0 | 446 | 639 | 382 | 101 | 0 |
| Lead | Spectrum | Positive | 5327 | 0 | 1204 | 2233 | 1578 | 312 | 0 |
| $^{238}$U | Spectrum | Positive | 53,323 | 0 | 26,111 | 14,892 | 4330 | 1436 | 6554 |
| $^{235}$U | Spectrum | Positive | 180,373 | 0 | 58,045 | 16,318 | 4308 | 1542 | 100,160 |

Table 4.5 A selection of $\gamma$-ray peaks observed when muons interact with water, iron, lead, $^{235}$U and $^{238}$U.

| Material | Energy (MeV) | Description | GEANT4 Process |
|---|---|---|---|
| Water | 4.43 | $\mu^-$ absorbed on $^{16}$O nucleus, which undergoes $\alpha$-decay to $^{12}$C. $^{12}$C releases 4.43 MeV $\gamma$-ray to get to ground state. | muMinusCaptureAtRest |
| Water | 5.27 | $\mu^-$ absorbed on $^{16}$O nucleus, which undergoes proton emission to $^{15}$N. $^{15}$N releases 5.27 MeV $\gamma$-ray to get to ground state. | muMinusCaptureAtRest |
| Water | > 15 | Result of high energy electrons undergoing bremsstrahlung. | Electron Bremsstrahlung |
| Iron | 4.71 | $\mu^-$ absorbed on $^{56}$Fe nucleus, which becomes excited and relaxes back to ground state through emission of 4.71 MeV $\gamma$-ray. | muMinusCaptureAtRest |
| Iron | 10.48 | $\mu^-$ absorbed on $^{56}$Fe nucleus, which undergoes proton emission to $^{55}$Mn. $^{55}$Mn releases 10.48 MeV $\gamma$-ray to get back to ground state. | muMinusCaptureAtRest |
| Iron | > 15 | Result of high energy electrons undergoing bremsstrahlung. | Electron Bremsstrahlung |
| Lead | 2.6247 | Instantaneous release of muonic *X*-rays as $\mu^-$ cascades down the energy levels to reach the 1s state. | muMinusCaptureAtRest |
| Lead | 5.6739 | Instantaneous release of muonic *X*-rays as $\mu^-$ cascades down the energy levels to reach the 1s state. | muMinusCaptureAtRest |
| Lead | 10.302 | Instantaneous release of muonic *X*-rays as $\mu^-$ cascades down the energy levels to reach the 1s state. | muMinusCaptureAtRest |
| Lead | > 15 | Result of high energy electrons undergoing bremsstrahlung. | Electron Bremsstrahlung |
| $^{235}$U | 6.545 | Explained within the text in Chapter 4.3.2 at the second paragraph in the section on stopped $\mu^-$. | nCapture |
| $^{235}$U and $^{238}$U | 2.614 | Produced as a result of the $^{236}$U decay chain. Once the chain reaches $^{208}$Pb it releases a $\gamma$-ray of 2.614 MeV to get to the ground state. | RadioactiveDecay |
| $^{235}$U and $^{238}$U | 3.304 | Instantaneous release of muonic *X*-rays as $\mu^-$ cascades down the energy levels to reach the 1s state. | muMinusCaptureAtRest |
| $^{235}$U and $^{238}$U | 6.035 | Instantaneous release of muonic *X*-rays as $\mu^-$ cascades down the energy levels to reach the 1s state. | muMinusCaptureAtRest |
| $^{235}$U and $^{238}$U | 9.341 | Instantaneous release of muonic *X*-rays as $\mu^-$ cascades down the energy levels to reach the 1s state. | muMinusCaptureAtRest |
| $^{235}$U and $^{238}$U | 10.497 | Instantaneous release of muonic *X*-rays as $\mu^-$ cascades down the energy levels to reach the 1s state. | muMinusCaptureAtRest |
| $^{235}$U and $^{238}$U | 11.0324 | Instantaneous release of muonic *X*-rays as $\mu^-$ cascades down the energy levels to reach the 1s state. | muMinusCaptureAtRest |
| $^{235}$U and $^{238}$U | 11.818 | Instantaneous release of muonic *X*-rays as $\mu^-$ cascades down the energy levels to reach the 1s state. | muMinusCaptureAtRest |
| All | 0.511 | Produced when *e*- and *e*+ annihilate resulting in the production of two 0.511 keV $\gamma$-rays. | Annihilation |

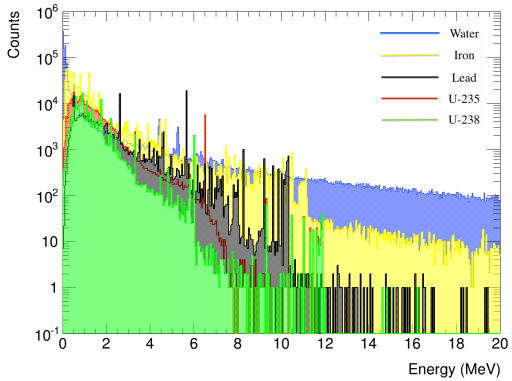


(a) *Secondary γ-ray spectrum before timing cut.*

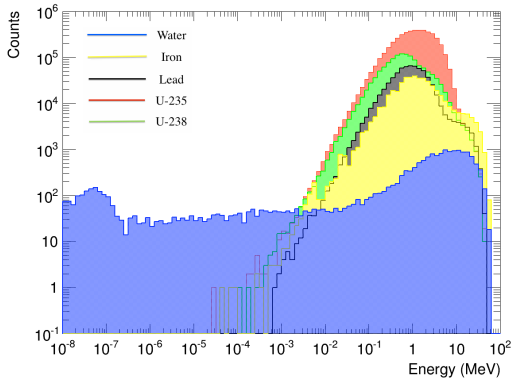


(b) *Secondary neutron spectrum before timing cut.*

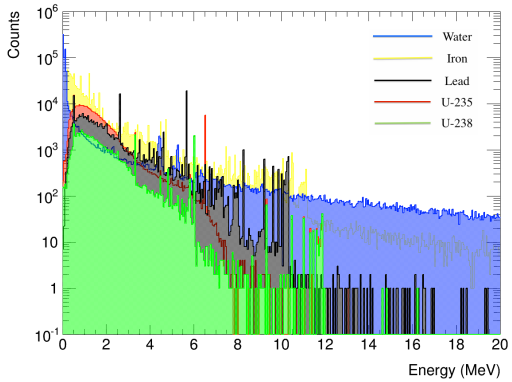


(c) *Secondary γ-ray spectrum after timing cut.*

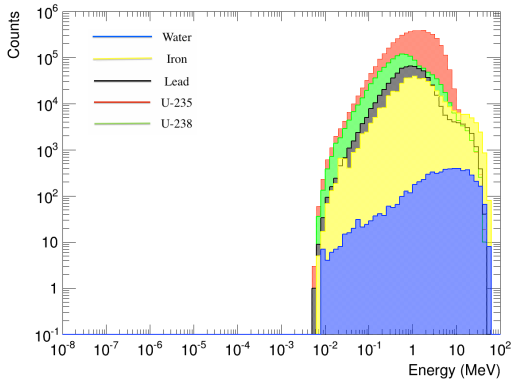


(d) *Secondary neutron spectrum after timing cut.*

Fig. 4.5 *Secondary γ-ray (left) and neutron (right) energy spectra both before (top) and after (bottom) a timing cut of 1 μs. The results are for 500,000 stopping $\mu^-$ (initial energy 0.1 eV) in cubes of water (blue), iron (yellow), lead (black), $^{235}U$ (red) and $^{238}U$ (green).*

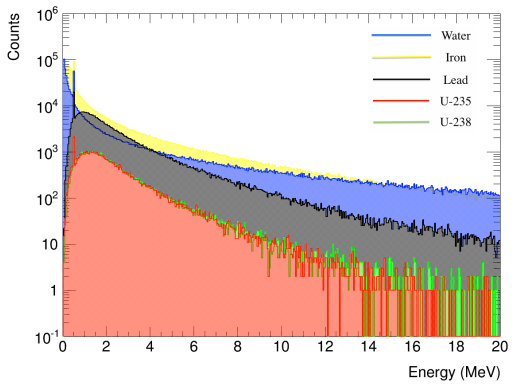


(a) *Secondary γ-ray spectrum before timing cut.*

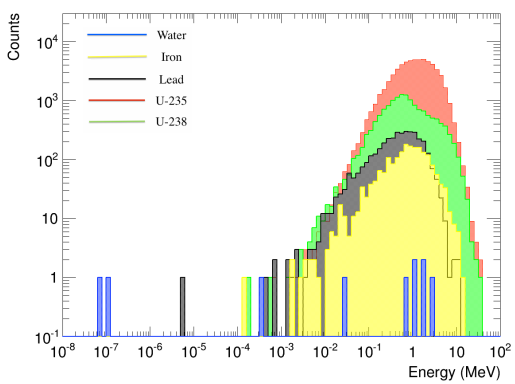


(b) *Secondary neutron spectrum before timing cut.*

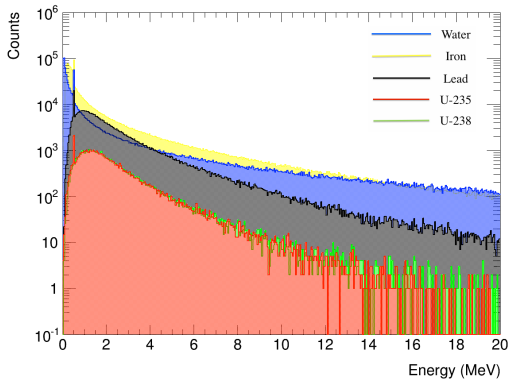


(c) *Secondary γ-ray spectrum after timing cut.*

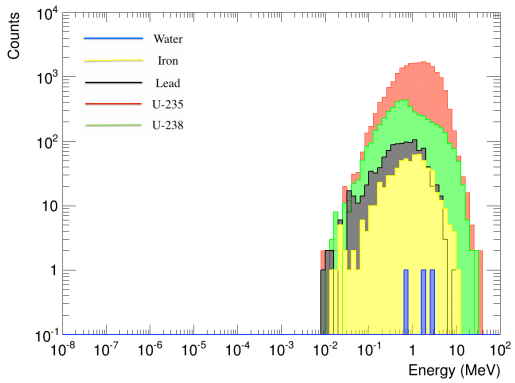


(d) *Secondary neutron spectrum after timing cut.*

Fig. 4.6 *Secondary γ-ray (left) and neutron (right) energy spectra both before (top) and after (bottom) a timing cut of 1 μs. The results are for 500,000 stopping $\mu^+$ (initial energy 0.1 eV) in cubes of water (blue), iron (yellow), lead (black), $^{235}U$ (red) and $^{238}U$ (green).*

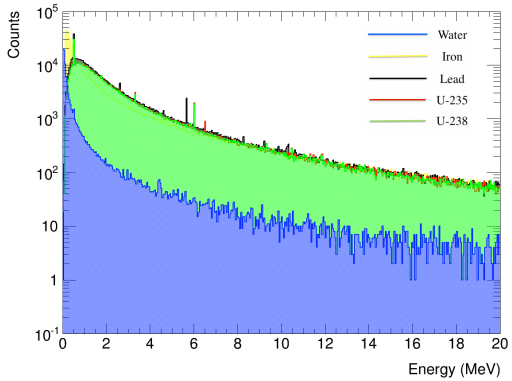


(a) *Secondary γ-ray spectrum before timing cut.*

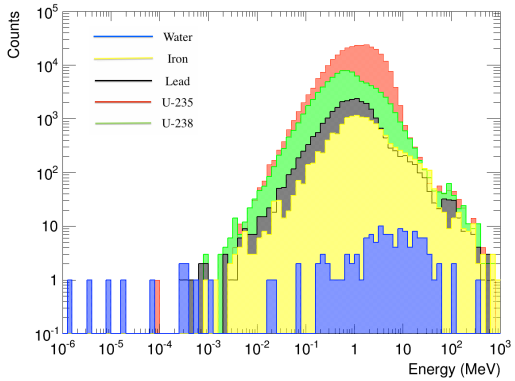


(b) *Secondary neutron spectrum before timing cut.*

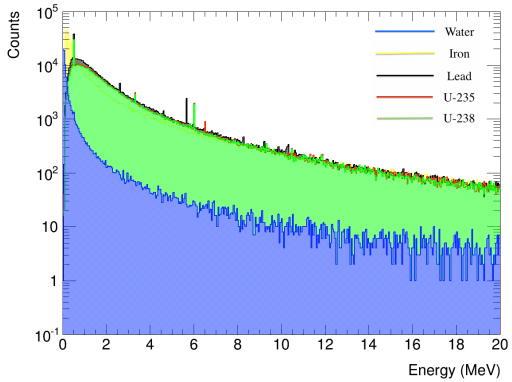


(c) *Secondary γ-ray spectrum after timing cut.*

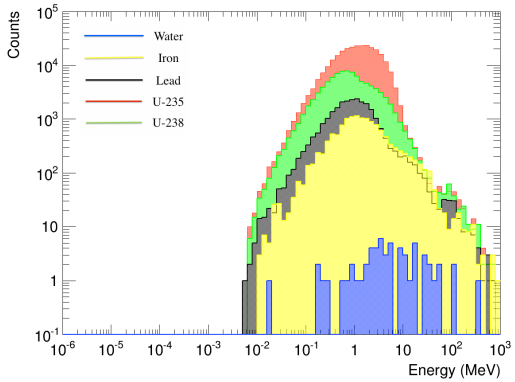


(d) *Secondary neutron spectrum after timing cut.*

Fig. 4.7 *Secondary γ-ray (left) and neutron (right) energy spectra both before (top) and after (bottom) a timing cut of 1 μs. The results are for 500,000 full $\mu^-$ energy spectrum (range from 100 MeV - 1000 GeV) in cubes of water (blue), iron (yellow), lead (black), $^{235}U$ (red) and $^{238}U$ (green).*

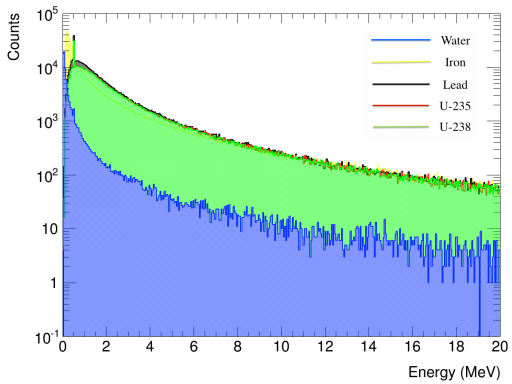


(a) *Secondary γ-ray spectrum before timing cut.*

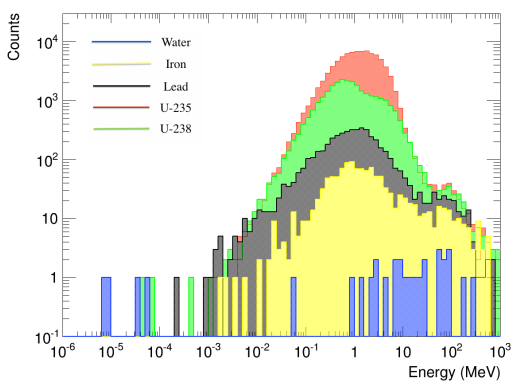


(b) *Secondary neutron spectrum before timing cut.*

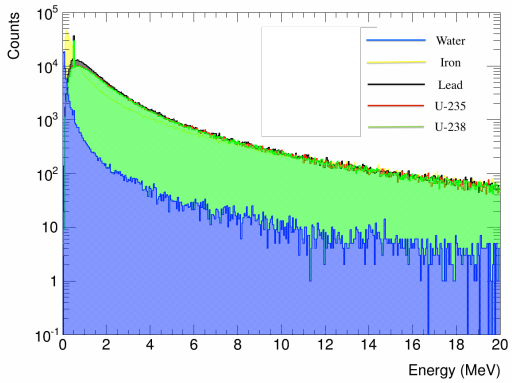


(c) *Secondary γ-ray spectrum after timing cut.*

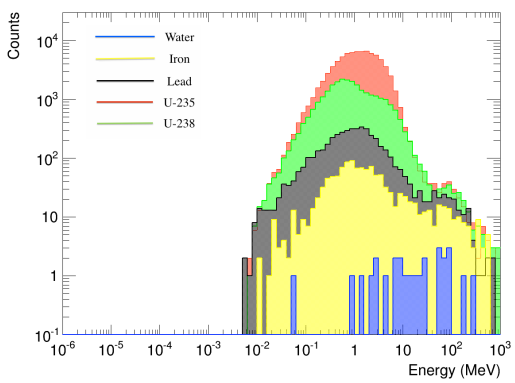


(d) *Secondary neutron spectrum after timing cut.*

Fig. 4.8 *Secondary γ-ray (left) and neutron (right) energy spectra both before (top) and after (bottom) a timing cut of 1 μs. The results are for 500,000 full $\mu^+$ energy spectrum (range from 100 MeV - 1000 GeV) in cubes of water (blue), iron (yellow), lead (black), $^{235}U$ (red) and $^{238}U$ (green).*

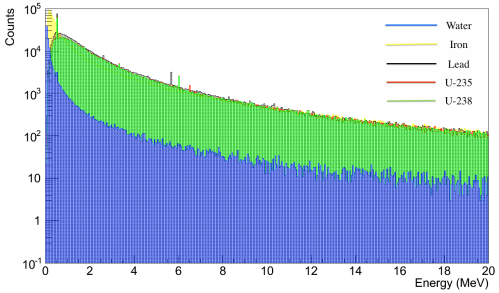


(a) *Secondary γ-ray spectrum before timing cut.*

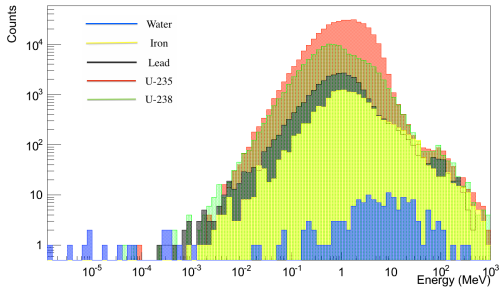


(b) *Secondary neutron spectrum before timing cut.*

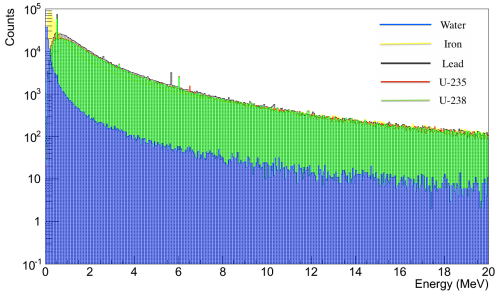


(c) *Secondary γ-ray spectrum after timing cut.*

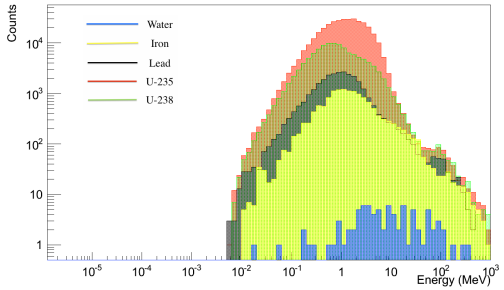


(d) *Secondary neutron spectrum after timing cut.*

Fig. 4.9 *Secondary γ-ray (left) and neutron (right) energy spectra both before (top) and after (bottom) a timing cut of 1 μs. The results are for the combined 500,000 full $\mu^+$ energy spectrum and 500,000 full $\mu^-$ energy spectrum (range from 100 MeV - 1000 GeV) in cubes of water (blue), iron (yellow), lead (black), $^{235}U$ (red) and $^{238}U$ (green).*

## 4.4 Material Segregation using Realistic Momentum Spread

### 4.4.1 Simulation Parameters

Muons generated over a 10 m $\times$ 10 m area were propagated through a box made of air that housed a single 10 cm $\times$ 10 cm $\times$ 10 cm or 50 cm $\times$ 50 cm $\times$ 50 cm block of different density materials. Muons were generated using the MGP and implemented so that the full muon energy spectrum and momentum distribution were used. Muon detectors comprised of gaseous material (65% Argon, 30% $CO_2$ and 5% $CF_4$) were placed above, below and at two of the sides of the volume to be inspected. Detectors are 2 cm thick with a distance of 4 m separating the lower most top detector and the upper most bottom detector. Simulations have been run using five detectors per set with detectors in each set spaced 25 cm apart. The detectors operate with perfect resolution. A schematic of the set-up used is shown in Fig. 4.10. Results are given for 5 million muons, which represents approximately a 5 minute exposure time.

For muon disappearance tomography only those muons that pass through the top set of detectors, and no subsequent set, are used for analysis. The muons are generated with a $z$-position directly above the top detector plane. As the muon plane is implemented directly above the top detector, a surface area of 10 m $\times$ 10 m is large enough for muons of all angles and energies to meet the initial criteria to be considered for analysis (passing through the top detector). In this system it is extremely unlikely that muons with large zenith angles, which pass through the top detector, will also interact with targets in the inspected volume. This reduces the acceptance of the system for large zenith angle muons. Muons with large zenith angles typically have energies greater then overhead muons. Since muon disappearance tomography requires a muon to lose all its energy and stop within the inspected volume, this process is less likely to occur for higher energy muons. Therefore the rejection of these muons will have little impact on the ability to differentiate between materials based on muon disappearance. To incorporate these muons, an analysis system that also uses muons which pass through a side detector then disappear, could be used. In such a system the muon plane surface area would need to be made larger so that large zenith angle muons are not restricted.

All secondary particles produced were recorded in detectors that are placed around the geometry to be inspected. These detectors are 0.1 mm thick, made out of vacuum and assumed to be 100% efficient. Upon passing through these detectors the ID, name,

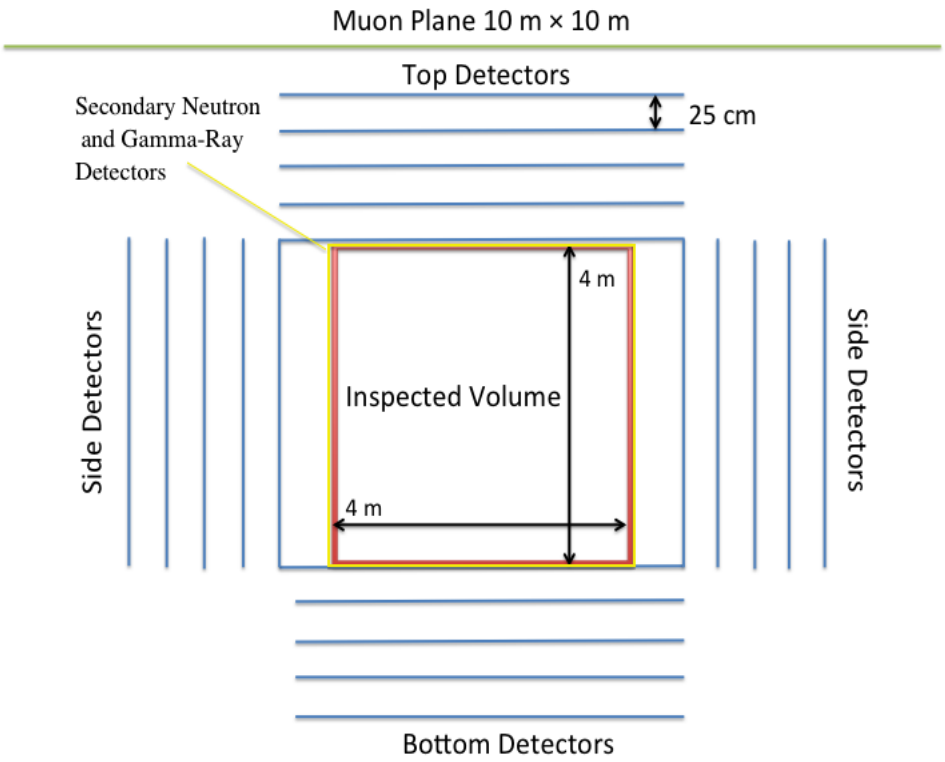


Fig. 4.10 *Standard set-up for the muon tomography system (not to scale). The spacing between detectors is 25 cm with 5 detectors per set.*

process of production, energy, position, parent, time and momentum direction of any secondary particles are recorded.

### 4.4.2 Tomographic Reconstruction for Muon Disappearance Tomography

Reconstruction for the technique described in this section (section 4.4) is done using a technique similar to a branch of tomography known as algebraic based computed tomography [107]. This type of reconstruction technique is used when a large number of incoming tracks are not available, or when these tracks are not uniformly distributed over 180° or 360°. For cases involving nuclear detection using stopped cosmic-ray muons in a defined time limit, both of these criteria are not met, hence reconstruction is considered using this technique. For simplicity it is demonstrated from a 2D viewpoint, before extending the case to 3D. Fig. 4.11 illustrates some target volume *f(x, y)* contained within an object area, in which a uniform square grid is superimposed over

the top of it. To begin with, it is assumed that the target volume *f(x, y)* is constant in each cell since in reality we are unaware of where the target may be. We define $N$ as the total number of pixels, with the $j^{th}$ pixel defined by a constant of value $f_j$.

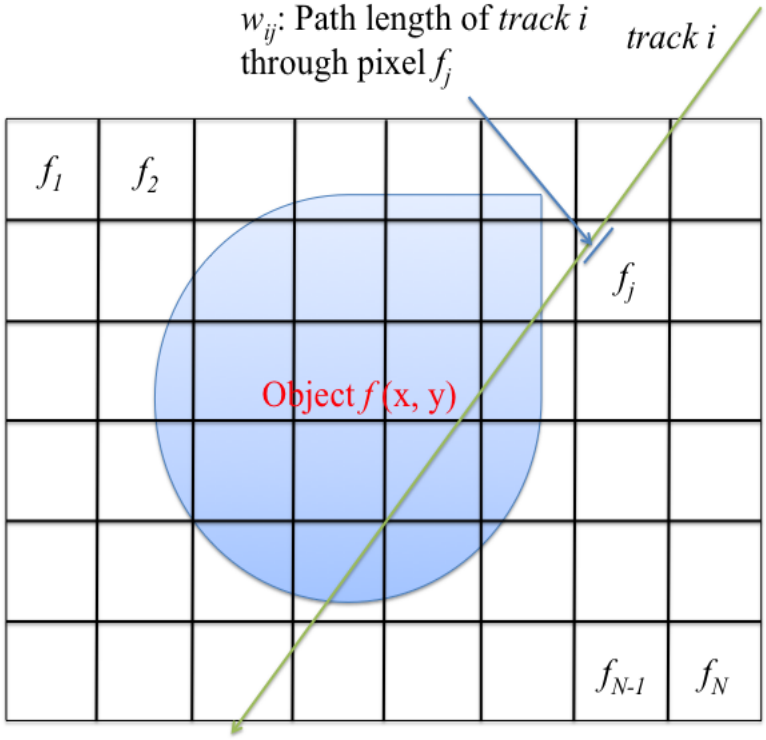


Fig. 4.11 *Illustration of how an object area is sampled when passing muon tracks through it.*

For a muon to be considered for analysis it must have been detected in all detectors in the top set and not detected exiting in any subsequent set. Detectors are located at four sides of the inspected volume. Any muons that are not detected exiting the volume can be assumed to have disappeared somewhere within the inspected volume (via decay or absorption), or exited where no side detectors are located. The rate of absorption or decay in air surrounding the target will remain fairly constant, independent of target material. However, since the probability of a $\mu^-$ being absorbed increases with atomic number ($Z$), as target $Z$ increases from low to high, more $\mu^-$s that interact with the target will be absorbed and therefore disappear. Due to the low rate at which muons cascade upon the Earth, individual muons can be tracked one at a time. For muons that have disappeared, the top detectors will have recorded an initial position and direction of the muon track. Incoming muon tracks are reconstructed using a 3D least-square

regression fit. If it is assumed the muon travels in a straight line we can extrapolate its path from the top detector, to where it would have exited the volume had it not disappeared. In order to reject side-exiting muons at the two sides where no detectors are located, if the extrapolated track passes out of these sides, then it will be removed from the analysis in order to remove any biasing towards these areas occurring.

As $M$ muon tracks meet the disappearance criteria and pass through the total volume, each track will pass through a number of individual voxels. For example, as the $i^{th}$ track passes through the inspected volume, its fractional path length through each voxel it passes through is recorded. Each extrapolated muon track can be expressed as a set of weights ($w_{ij}$), which represent the fractional path length of the $i^{th}$ track through voxel $j$. The fractional path length is defined as the ratio between the distance covered by an extrapolated muon track in a particular voxel, divided by the maximum distance a track can cover in each voxel. It is therefore a dimensionless quantity. As each extrapolated muon track passes through the inspected volume, the fractional path length of the track in each voxel is recorded. For voxels that have multiple muon tracks passing through them, all individual fractional path lengths recorded in each voxel are added together. The final signal represents the total fractional path length recorded for a set of $M$ tracks passing through an inspected volume of set $N$ voxels. The total fractional path length is defined as the summation of all fractional path lengths for a set of $M$ muon tracks in a particular voxel. Cosmic ray muons will lose more energy within voxels of higher density materials than lower density materials. This in turn will cause more muons to stop within these volumes of high density materials. Therefore those voxels that have higher total fractional path lengths will represent volumes where the most muon disappearances have occurred and in turn high density materials.

For techniques that involve the disappearance of a muon plus the detection of a secondary, only those muon tracks that meet the criteria for each technique are used when calculating the total fractional path length per voxel. It should be noted that since a muon path is assumed to travel in a straight line, the reconstruction algorithm fails to take into account any scatters that may occur along its trajectory. Voxel sizes used for this study are 5 cm $\times$ 5 cm $\times$ 5 cm. Voxels of this size have a maximum length in which a muon track can traverse of 8.66 cm.

(a) Generate an $N \times N \times N$ grid over the inspected volume and split into $L \times L \times L$ voxels. Establish a cartesian co-ordinate system in three dimensions with $z$ as

the vertical. Measured data is position ($x_{pos}$, $y_{pos}$, $z_{pos}$) and direction cosines ($mx$, $my$, $mz$) of each of the incoming ($x_{pos}$, $y_{pos}$, $z_{pos}$, $mx$, $my$, $mz)_{in}$ muon tracks ($M$).

(b) For $i$:=1 to M tracks that pass through the top detector but are not recorded in any subsequent detector (lateral or bottom), get incoming (($x_{pos}$, $y_{pos}$, $z_{pos}$, $mx$, $my$, $mz)_{in})_i$ muon track data.

(c) For each muon track extrapolate its trajectory through the inspected volume had it not disappeared, using a 3D least-squares regression fit.

(d) Calculate the voxels the extrapolated muon track would have passed through using Eq. (4.5), Eq. (4.6) and Eq. (4.7).

(e) Calculate the distance travelled by the extrapolated muon track through each voxel it would have passed through using Eq. (4.8).

(f) Divide the distance calculated by the maximum distance an extrapolated track could pass through in a single voxel. This quantity if known as the fractional path length.

(g) Add the calculated fractional path length of each individual voxel to that voxel. This quantity is known as the total fractional path length.

(h) Repeat steps c - g for all $M$ tracks.

**Mathematics of Reconstruction Code**

As the total inspected volume is split into a series of voxels, this volume (in which a muon track passes through) can be thought of as a series of planes that a line may pass through. To determine the fractional path length in each voxel, we need to find the position on a plane where a line, with given initial position and direction, intersects. The amount of distance traversed per voxel is then determined through finding the distance between two points - the initial point and the point at which the line intersects the plane.

A line is described by all points that are a given direction from an initial point. Thus the parametric form of a line can be described by any of the two positions ($x_0$ and $x_1$) along the line:

$$\bar{r}(t) = (x_0, y_0, z_0) + t[(x_1 - x_0), (y_1 - y_0), (z_1 - z_0)] = (x_0, y_0, z_0) + t\mathbf{u} \tag{4.5}$$

where $t$ is a real number and $\mathbf{u} = (x_1 - x_0, y_1 - y_0, z_1 - z_0)$, represents the direction of the line. The equation of a plane can be given as:

$$ax + by + cz + d = 0 \tag{4.6}$$

The line will intersect the plane only once at some unique point ($P_x$, $P_y$, $P_z$) provided the line and plane are not parallel. This position is determined through substituting the equation of a line (Eq. (4.5)) into Eq. (4.6), in order to determine $t$:

$$a(x_0 + tu_x) + b(y_0 + tu_y) + c(z_0 + tu_z) + d = 0 \tag{4.7}$$

Since values for ($x_0$, $y_0$, $z_0$) (initial position) and $\mathbf{u}$ (direction vectors) are known it is simply a case of rearranging to determine $t$. Once $t$ is determined this value is substituted back into Eq. (4.5), to determine the point of intersection. The distance between the initial point of the line and where it intersects the plane is then calculated using Eq. (4.8):

$$Distance = [(P_x - x_0)^2 + (P_y - y_0)^2 + (P_z - z_0)^2]^{1/2} \tag{4.8}$$

### 4.4.3 Material Segregation using Muon Capture

As described in section 4.3.2, material segregation using muon disappearance can be split into 6 different techniques. Each technique involves the disappearance of a muon coupled to the detection of various prompt secondaries. The main premise behind each of these techniques is that as material density increases, more muons will stop within a target material and more secondaries will be produced. Therefore the disappearance of multiple muons in coincidence with the detection of a prompt secondary, represents a clear signature of high density material. Fig. 4.12 displays the fractional number of decays and absorptions plus various prompt secondaries per muon interaction, when propagating 5 million muons through a volume that contained 10 cm $\times$ 10 cm $\times$ 10 cm or 50 cm $\times$ 50 cm $\times$ 50 cm blocks of different density materials.

The ability to differentiate between materials using solely muon disappearance, or any techniques that involve muon disappearance plus prompt neutron detection is apparent for either sized blocks. Nuclear materials, its shielding components and low density materials are all clearly identifiable from one another. However, for techniques involving detection of prompt $\gamma$-rays of any energy or of energies > 3 MeV, only low density ma-

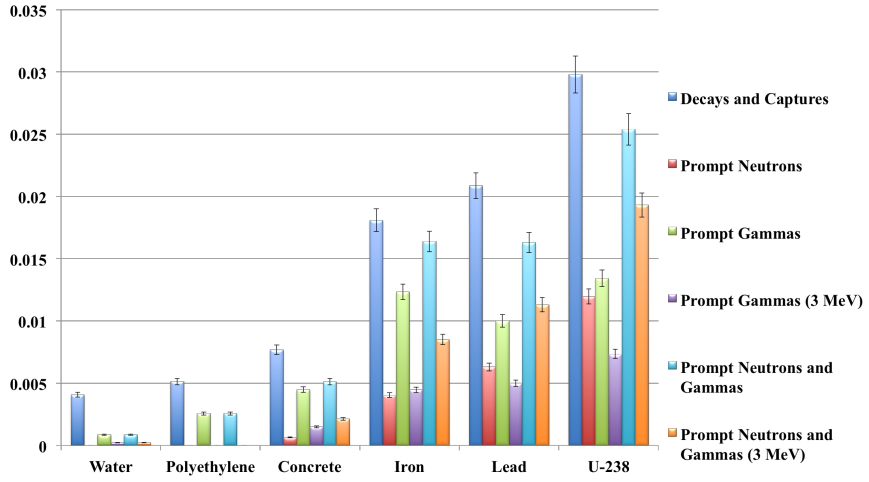


(a) *10 cm × 10 cm × 10 cm blocks.*

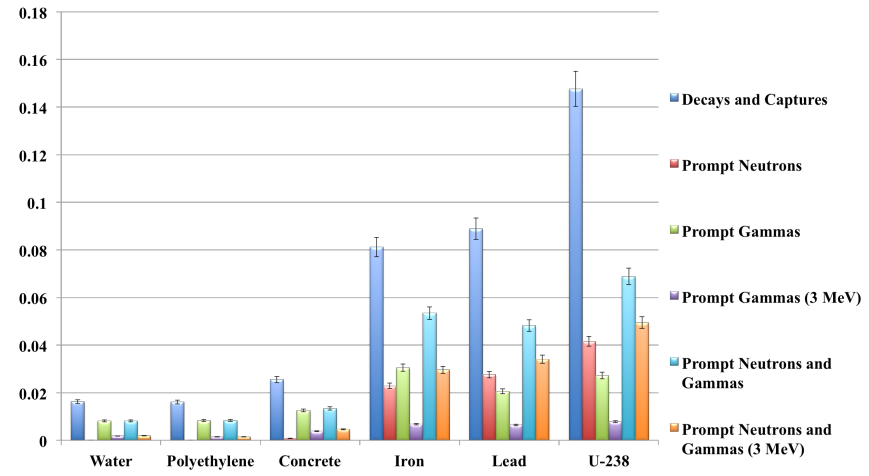


(b) *50 cm × 50 cm × 50 cm blocks.*

Fig. 4.12 *Fractional number of decays and absorptions plus various prompt secondaries per muon interaction in 10 cm × 10 cm × 10 cm (top) and 50 cm × 50 cm × 50 cm (bottom) blocks of different density materials.*

terials can be identified from nuclear or shielding type components (typically medium or high density). This is due to the high level of $\gamma$-rays observed from iron upon $\mu^-$ capture, making iron indistinguishable from high density and nuclear materials. The observed high levels are caused by the effects of self-shielding. Despite more $\gamma$-rays being produced as $Z$ increases, in higher density and higher-$Z$ materials, low energy $\gamma$-rays are more likely to undergo significant energy losses and be reabsorbed by the target material. If we consider a 3 MeV $\gamma$-ray generated at the centre of a block of size 10 cm $\times$ 10 cm $\times$ 10 cm, this $\gamma$-ray is required to travel at least 5 cm to exit the material. The intensity of $\gamma$-rays exiting a material is given by:

$$I = I_0 e^{-\mu x} \tag{4.9}$$

where $I$ is the intensity of $\gamma$-rays exiting, $I_0$ is the initial intensity, $\mu$ is the mass attenuation coefficient in units cm$^2$/g and $x$ is the depth of material in units g/cm$^2$. For $\gamma$-rays of energy 3 MeV passing out of 5 cm of iron or $^{238}$U, Eq. (4.9) gives the fraction escaping as 24.12% for iron and 1.48% for $^{238}$U. Therefore even though more $\gamma$-rays are produced when neutrons interact with $^{238}$U, much fewer escape the target to be available for detection. This effect creates a propensity for the misclassification of nuclear material when using techniques that involve the detection of $\gamma$-rays. Despite this, the ability to differentiate between materials is apparent for all techniques that involve muon disappearance plus secondary detection.

### 4.4.4 Comparison of Three Block Scenarios

Verification of the muon disappearance algorithm to locate and differentiate between materials has been tested. Systems involved placing three 10 cm $\times$ 10 cm $\times$ 10 cm or three 50 cm $\times$ 50 cm $\times$ 50 cm blocks of water (low density), iron (medium density) and $^{238}$U (high density) within the inspected volume shown in Fig. 4.10. For the tests it is assumed that the location of each target material is known a priori. Fifty million muons were propagated through the inspected volume, with the results presented scaled to 5 million. This represents approximately a 5 minute exposure time. The rest of the inspected volume was made of air. Both horizontal and vertical systems have been tested with blocks separated along with the $x$-plane or $z$-plane. For the horizontal system water (right) is centred at $x$ = 150 cm, $y$ = 0 cm, $z$ = 0 cm, $^{238}$U (middle) at $x$ = 0 cm, $y$ = 0 cm, $z$ = 0 cm and iron (left) at $x$ = -150 cm, $y$ = 0 cm, $z$ = 0 cm. For vertical systems iron (top) was centred at $x$ = 0 cm, $y$ = 0 cm, $z$ = 80 cm, $^{238}$U (middle) centred at $x$ = 0 cm, $y$ = 0 cm, $z$ = -50 cm and water (bottom) centred at $x$ = 0 cm, $y$ = 0 cm, $z$ = -180 cm.

Analysis is conducted through splitting the total geometry up into 5 cm $\times$ 5 cm $\times$ 5 cm voxels. The total fractional path length in each of the voxels occupied by the targets is calculated and a 3D image plotted. The colour gradient of this image is based on the total fractional path length.

In addition to techniques that solely rely on muon disappearances, as discussed previously, upon stopping within a material muons can produce secondary neutrons and $\gamma$-rays. This effect is more likely to occur for higher-$Z$(A) materials than lower-$Z$(A) materials for the same column density and thus represents a strong signature for possible nuclear materials and its shielding. For the detection of secondary signatures, 100% detector coverage and efficiency is assumed. In each of these systems the probability of detecting a background neutron or $\gamma$-ray in coincidence with a muon disappearance is considered to be negligible. Estimations of this background are given at the end of this section. In total six different techniques that involve muon disappearance coupled to the detection of a secondary are tested.

For each of the three block scenarios, Table 4.6 gives a description of each of the techniques that were tested. Table 4.7 displays the total number of muons within each target that met the criteria required to be considered for 3D line extrapolation.

Table 4.6 Description of each of the techniques tested for muon disappearance tomography.

| Technique Number | Description |
|---|---|
| #1 | Muon disappearance. |
| #2 | Muon disappearance coupled with prompt neutron detection. |
| #3 | Muon disappearance coupled with prompt $\gamma$-ray detection. |
| #4 | Muon disappearance coupled with the detection of a prompt $\gamma$-ray of energy > 3 MeV. |
| #5 | Muon disappearance coupled with prompt neutron or prompt $\gamma$-ray detection. |
| #6 | Muon disappearance coupled with the detection of a prompt neutron or prompt $\gamma$-ray of energy > 3 MeV. |

Gamma-rays of this energy > 3 MeV were chosen, as there are no naturally occurring $\gamma$-rays whose energies exceed this value. Therefore the subsequent detection of $\gamma$-rays of this energy represents a clear indication that something within the inspected volume has produced it. The total amount of muon disappearances, coupled to the detection of a prompt secondary, within the air surrounding the targets is also given. This represents

a total volume of 10 m × 10 m × 10 m (minus the volume the target occupies) and is defined in Table 4.7 as 'Air'. With an approximate muon energy loss of 2 MeV per g/cm$^2$, muons in air will lose ≈ 0.0025 MeV per cm. This in turn leads to an energy loss of ≈ 2.5 MeV when traversing 10 m of air (density = 0.001225 g/cm$^3$). Therefore muons that disappear within the air surrounding the target are unlikely to have lost sufficient energy to stop but instead will have undergone decay. The error given is the error on the mean for 50 million muons, scaled down to represent 5 million muons.

Table 4.7 Total number of muon disappearances plus secondary detection in each of the targets and rest of the inspected volume (air) for 100% detector coverage and efficiency. See Table 4.6 for a description of each of the techniques tested.

| Target | Technique 1 | Technique 2 | Technique 3 | Technique 4 | Technique 5 | Technique 6 |
|---|---|---|---|---|---|---|
| 10 cm × 10 cm × 10 cm horizontal setup | | | | | | |
| Water | 3.8 ± 0.6 | 0 | 1.2 ± 0.3 | 0.2 ± 0.15 | 1.2 ± 0.3 | 0.2 ± 0.15 |
| Iron | 16.2 ± 1.3 | 3.8 ± 0.6 | 11.1 ± 1.1 | 4.2 ± 0.6 | 14.9 ± 1.7 | 8.0 ± 1.2 |
| $^{238}$U | 28.4 ± 1.7 | 11.4 ± 1.1 | 12.4 ± 1.1 | 7.0 ± 0.8 | 23.8 ± 1.9 | 18.4 ± 1.9 |
| Air | 1860 ± 15 | 0 | 195 ± 4 | 65 ± 3 | 195 ± 4 | 65 ± 3 |
| 10 cm × 10 cm × 10 cm vertical setup | | | | | | |
| Water | 2.6 ± 0.5 | 0 | 0.8 ± 0.3 | 0.2 ± 0.15 | 0.8 ± 0.3 | 0.2 ± 0.15 |
| Iron | 17.0 ± 1.3 | 2.7 ± 0.5 | 11.6 ± 1.1 | 3.6 ± 0.6 | 14.3 ± 1.6 | 6.3 ± 1.1 |
| $^{238}$U | 30.4 ± 1.7 | 10.8 ± 1.0 | 12.8 ± 1.1 | 6.7 ± 0.8 | 23.6 ± 2.7 | 17.5 ± 1.8 |
| Air | 1860 ± 15 | 0 | 200 ± 5 | 70 ± 3 | 200 ± 5 | 70 ± 3 |
| 50 cm × 50 cm × 50 cm horizontal setup | | | | | | |
| Water | 390 ± 6 | 1.4 ± 0.4 | 190 ± 4 | 40 ± 2 | 191.4 ± 4.4 | 41.4 ± 2.4 |
| Iron | 1925 ± 15 | 540 ± 7 | 695 ± 8 | 155 ± 4 | 1235 ± 15 | 695 ± 11 |
| $^{238}$U | 3510 ± 20 | 990 ± 10 | 685 ± 8 | 180 ± 4 | 1675 ± 18 | 1170 ± 14 |
| Air | 1860 ± 15 | 0 | 195 ± 5 | 65 ± 3 | 195 ± 5 | 65 ± 3 |
| 50 cm × 50 cm × 50 cm vertical setup | | | | | | |
| Water | 380 ± 6 | 0.8 ± 0.3 | 190 ± 4 | 45 ± 2 | 190.8 ± 4.3 | 45.8 ± 2.3 |
| Iron | 1920 ± 15 | 490 ± 7 | 700 ± 9 | 160 ± 4 | 1190 ± 16 | 650 ± 11 |
| $^{238}$U | 3420 ± 20 | 970 ± 10 | 695 ± 8 | 185 ± 4 | 1665 ± 18 | 1155 ± 14 |
| Air | 1855 ± 15 | 0 | 205 ± 5 | 70 ± 3 | 205 ± 5 | 70 ± 3 |

### 50 cm × 50 cm × 50 cm blocks in the horizontal set-up

Fig. 4.13 displays visual analysis for the 50 cm × 50 cm × 50 cm horizontal scenario for each of the six techniques discussed. Voxels of 5 cm × 5 cm × 5 cm are used with the total fractional path length calculated for each of the voxels occupied by the targets. Only those voxels occupied by the targets are plotted. Fig. 4.14 displays the

total fractional path lengths measured in the voxels occupied by each of the targets, for each of the six techniques discussed.

### Technique 1: Muon disappearance

Reconstruction of the three 50 cm $\times$ 50 cm $\times$ 50 cm block horizontal scenario using muon disappearance is given in Fig. 4.13. This demonstrates the success of the muon disappearance algorithm to correctly detect volumes where targets are positioned, if the initial position of the targets is known. The results are supported with Fig. 4.14, which shows the total fractional path length recorded for each voxel where the 50 cm $\times$ 50 cm $\times$ 50 cm blocks are located. Different density materials can be differentiated from one another using the total fractional path length observed per voxel. This demonstrates the potential of the muon disappearance algorithm to differentiate materials from one another, if target position is known. In reality the location of any targets within an inspected volume will not be known. For such a system, a threshold cut on the total fractional path length will have to be made, where voxels below this cut are not plotted. As displayed in Fig. 4.14 there is some overlap in the total fractional path length observed in voxels for iron and $^{238}$U. In a system where target location is not known, this may result in occasional misclassification of medium-$Z$ (iron) targets as high-$Z$ ($^{238}$U).

### Technique 2: Muon disappearance coupled with prompt neutron detection

As shown in Table 4.7, for both iron and $^{238}$U, multiple muon tracks meet the criteria of stopping within the material and producing neutrons. These materials are correctly reconstructed and as shown in Fig. 4.13, can be clearly differentiated from one another. Water is not reconstructed. This is due to the low number of muons that stop within water and produce neutrons. From Table 4.7, only 1.4 $\pm$ 0.4 muon tracks meets this criterion. Due to the low probability of neutrons being produced from $\mu^-$ capture in water, this target is not identified using this technique. This indicates a potential ability of this technique to accurately locate nuclear materials, but not those low-density materials that can make up clutter. From Fig. 4.14 there is once again a large overlap between the total fractional path length distributions of iron and $^{238}$U. In realistic systems where target location is not known, dependant on the threshold cut taken, this may lead to the misclassification of medium-$Z$ targets as high-$Z$.

**Techniques 3 and 4: Muon disappearance coupled with prompt $\gamma$-ray detection (technique 3) of energy > 3 MeV (technique 4)**

As shown in Fig. 4.13, there is clear identification of all three targets. However, an issue with these techniques is the inability to differentiate medium density targets (iron) from high-density targets ($^{238}$U). This is indicated in both Table 4.7 and Fig. 4.14. From Table 4.7, the number of muons that have disappeared coupled to the detection of a prompt $\gamma$-ray is similar for iron and $^{238}$U. This results in the average total fractional path length of the voxels occupied by iron, to be similar to those voxels occupied by the $^{238}$U target. This effect is due to the self-shielding effects of $^{238}$U (described in more detail in section 4.4.3) and is confirmed when analysing the total fractional path length observed per voxel in Fig. 4.14. More muons are stopped within $^{238}$U than iron and therefore more $\gamma$-rays are produced in total. However, due to the higher density of $^{238}$U, more $\gamma$-rays reabsorbed by the target and therefore fewer are available for detection.

The capability to detect the three blocks was also considered when using muon disappearance coupled to the detection of prompt $\gamma$-rays with energies > 3 MeV (technique 4). Unlike other techniques the position of water is not clearly defined. This is due to the smaller number of muon tracks that met the analysis criteria for this technique. Similar to technique 3, another issue is the inability to differentiate between iron and $^{238}$U. This is again due to the self-shielding effects of $^{238}$U. A $\gamma$-ray will undergo greater energy losses as it exits $^{238}$U than if the same $\gamma$-ray exited iron. Therefore many of the $\gamma$-rays generated with energies > 3 MeV in $^{238}$U will have lost sufficient energy before detection to no longer be above the 3 MeV threshold.

**Techniques 5 and 6: Muon disappearance coupled with prompt neutron or prompt $\gamma$-ray detection (technique 5) of energy > 3 MeV (technique 6)**

Finally, the capability to detect the three targets when both prompt neutrons and prompt $\gamma$-rays can be used as secondaries to detect is tested. Similar to previous techniques that utilise the detection of either of these secondaries, the positions of iron and $^{238}$U are clearly identified. Unlike techniques that only involve the detection of prompt $\gamma$-rays, due to the inclusion of muon disappearance coupled to prompt neutron detection, this system is able to differentiate between iron and $^{238}$U.

The capability to detect the three targets when both prompt neutrons and $\gamma$-rays > 3

MeV can be used is also considered. As with techniques that use either of these secondaries, the ability to locate medium and high-density materials is apparent. However, due to the inclusion of neutrons both medium and high-density materials can be differentiated from one another.

Once again with these two techniques there is significant overlap between he total fractional path length distributions of iron and $^{238}$U, which may cause target misclassification in systems where target location is not known a priori.

**Other systems**

For both horizontal and vertical 10 cm $\times$ 10 cm $\times$ 10 cm set-ups, the number of muon tracks required to pass through the muon disappearance algorithm for each of the techniques for reconstruction to be made, needs to be $\approx$ 11 or above. From Table 4.7, due to this criterion water is not reconstructed for any of the techniques. For 10 cm $\times$ 10 cm $\times$ 10 cm blocks of iron, technique 1 (muon disappearances), technique 3 (muon disappearance coupled to prompt $\gamma$-ray detection) and technique 5 (muon disappearance coupled to prompt neutron or prompt $\gamma$-ray detection) have enough muon tracks for reconstruction to be made. The inability of technique 2 (muon disappearance coupled to prompt neutron detection), technique 4 (muon disappearance coupled to prompt $\gamma$-ray > 3 MeV detection) and technique 6 (muon disappearance coupled to prompt neutron or $\gamma$-ray > 3 MeV detection) to reconstruct 10 cm $\times$ 10 cm $\times$ 10 cm blocks of iron, is due to the low number of muon tracks available (less than 11). Finally, it can be seen from Table 4.7 that for $^{238}$U all techniques except technique 4 (muon disappearance coupled to prompt $\gamma$-ray detection > 3 MeV) have enough muon tracks available for detection to be made in this scenario.

Fig. 4.15 and Fig. 4.16 display the results for each of the techniques discussed when considering 50 cm $\times$ 50 cm $\times$ 50 cm blocks stacked vertically. Similar results to the horizontal set-up were observed, however water was reconstructed for technique 2. This is due to the nature of the muon disappearance algorithm, whereby some extrapolated muon tracks from iron or $^{238}$U also pass through where the water target is located, thus skewing the results. This is discussed in greater detail in the next section. All materials can be distinguished from one another when using techniques 1, 2, 5 and 6. For techniques 3 and 4 there is again a difficulty in differentiating between iron and $^{238}$U. A difference of note is the reconstruction of 50 cm $\times$ 50 cm $\times$ 50 cm blocks of water for

technique 2 with the vertical scenario, which does not occur for the horizontal scenario. Since muons arrive from directly overhead, for vertically stacked targets each extrapolated muon track is likely to pass close to or even through more than one target. As additional muon tracks pass through materials, the total fractional path length of each voxel occupied by a target will increase. This in turn may cause the misclassification of low or medium density materials as high density. Overall if 100% detector coverage and efficiencies are assumed (with no background), the ability to detect and distinguish different materials for a number of techniques using the muon disappearance algorithm has been demonstrated.

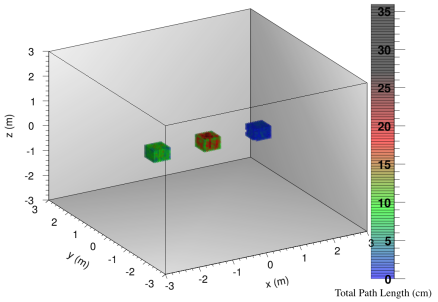


(a) Muon disappearance.

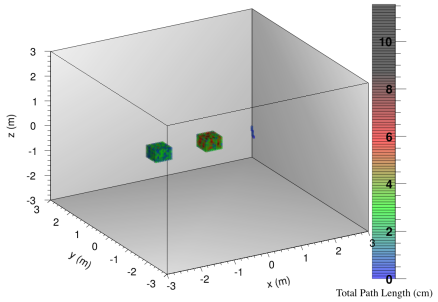


(b) Muon disappearance with prompt neutron detection.

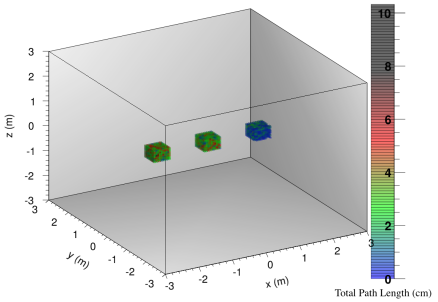


(c) Muon disappearance with prompt $\gamma$-ray detection.

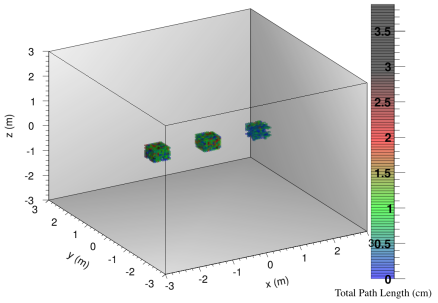


(d) Muon disappearance with prompt $\gamma$-ray of energy > 3 MeV detection.

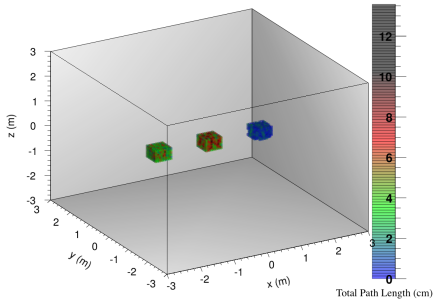


(e) Muon disappearance with prompt neutron or $\gamma$-ray detection.

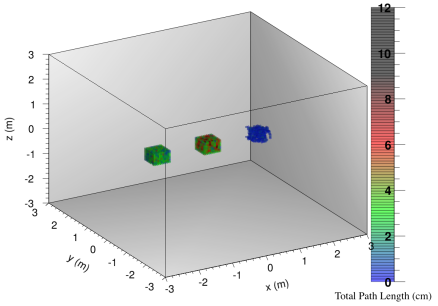


(f) Muon disappearance with prompt neutron or $\gamma$-ray of energy > 3 MeV detection.

Fig. 4.13 *Reconstruction of the 50 cm × 50 cm × 50 cm horizontal scenario. Plotted are only the voxels occupied by the target. Displayed are the results where decays and absorptions are measured (top left), decays and absorptions with prompt neutrons (top middle), decays and absorptions with prompt $\gamma$-rays (top right), decays and absorptions with prompt $\gamma$-rays > 3 MeV (bottom left), decays and absorptions with prompt neutrons or $\gamma$-rays (bottom middle) and decays and absorptions with prompt neutrons or $\gamma$-rays > 3 MeV (bottom right).*

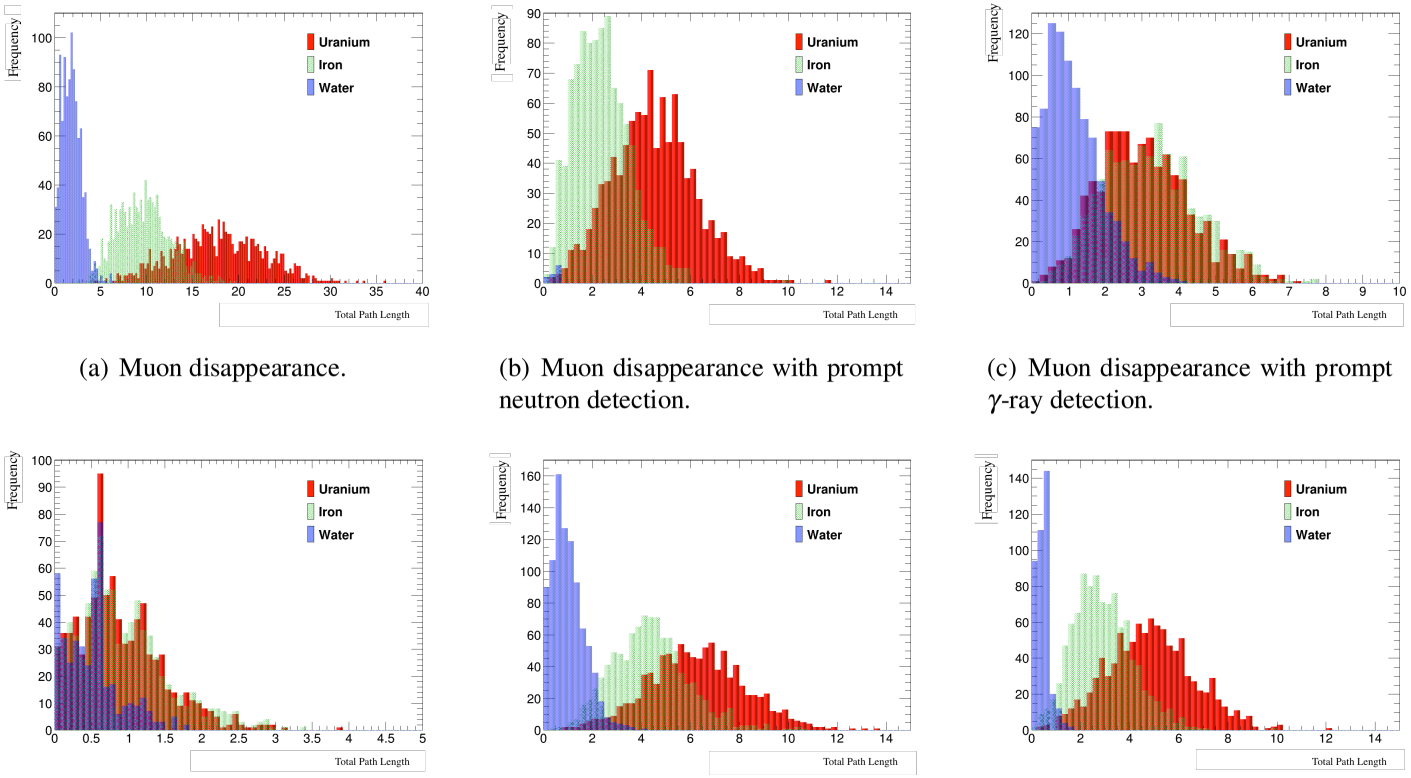


(a) Muon disappearance.

(b) Muon disappearance with prompt neutron detection.

(c) Muon disappearance with prompt $\gamma$-ray detection.

(d) Muon disappearance with prompt $\gamma$-ray of energy > 3 MeV detection.

(e) Muon disappearance with prompt neutron or $\gamma$-ray detection.

(f) Muon disappearance with prompt neutron or $\gamma$-ray of energy > 3 MeV detection.

Fig. 4.14 *Discrimination of materials using energy spectrum muons over a 5 minute exposure time. Displayed are the total fractional path lengths measured in each voxel occupied by the target for decays and absorptions (top left), decays and absorptions with prompt neutrons (top middle), decays and absorptions with prompt $\gamma$-rays (top right), decays and absorptions with prompt $\gamma$-rays > 3 MeV (bottom left), decays and absorptions with prompt neutrons or $\gamma$-rays (bottom middle) and decays and absorptions with prompt neutrons or $\gamma$-rays > 3 MeV (bottom right).*

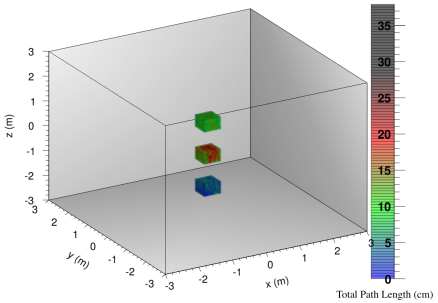


(a) Muon disappearance.

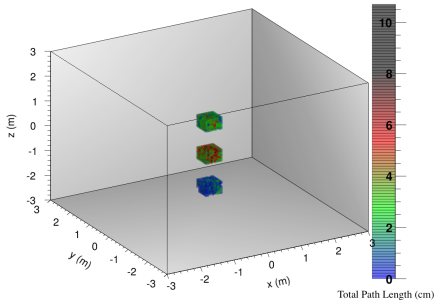


(b) Muon disappearance with prompt neutron detection.

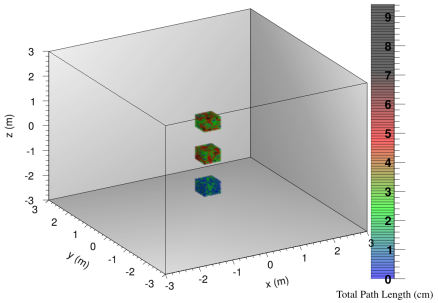


(c) Muon disappearance with prompt $\gamma$-ray detection.

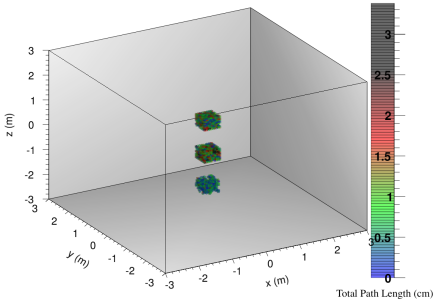


(d) Muon disappearance with prompt $\gamma$-ray of energy > 3 MeV detection.

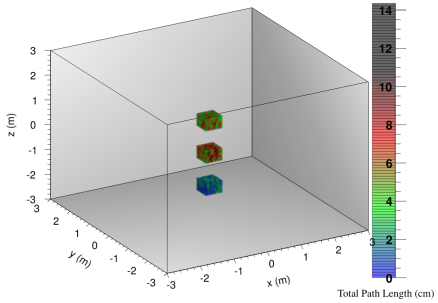


(e) Muon disappearance with prompt neutron or $\gamma$-ray detection.

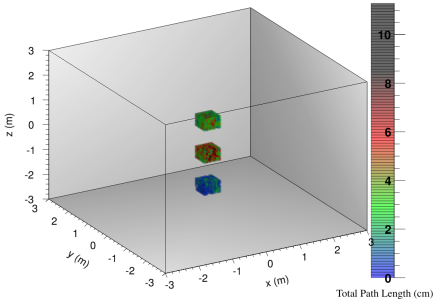


(f) Muon disappearance with prompt neutron or $\gamma$-ray of energy > 3 MeV detection.

Fig. 4.15 *Reconstruction of the 50 cm $\times$ 50 cm $\times$ 50 cm vertical scenario. Plotted are only the voxels occupied by the target. Displayed are the results where decays and captures are measured (top left), decays and absorptions with prompt neutrons (top middle), decays and absorptions with prompt $\gamma$-rays (top right), decays and absorptions with prompt $\gamma$-rays > 3 MeV (bottom left), decays and absorptions with prompt neutrons or $\gamma$-rays (bottom middle) and decays and absorptions with prompt neutrons or $\gamma$-rays > 3 MeV (bottom right).*

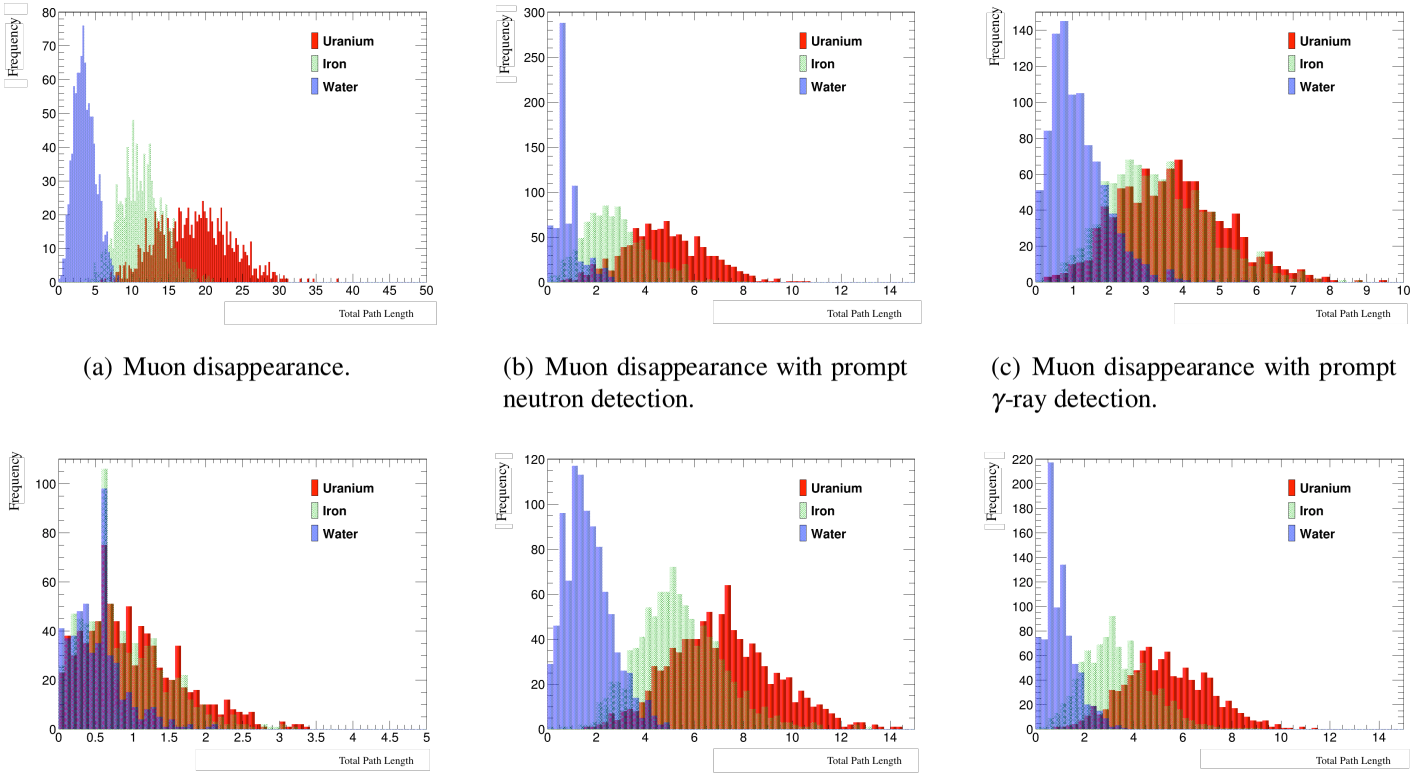


(a) Muon disappearance.

(b) Muon disappearance with prompt neutron detection.

(c) Muon disappearance with prompt $\gamma$-ray detection.

(d) Muon disappearance with prompt $\gamma$-ray of energy > 3 MeV detection.

(e) Muon disappearance with prompt neutron or $\gamma$-ray detection.

(f) Muon disappearance with prompt neutron or $\gamma$-ray of energy > 3 MeV detection.

Fig. 4.16 *Discrimination of materials using energy spectrum muons over a 5 minute exposure time. Displayed are the total fractional path lengths measured in each voxel occupied by the target for decays and absorptions (top left), decays and absorptions with prompt neutrons (top middle), decays and absorptions with prompt $\gamma$-rays (top right), decays and absorptions with prompt $\gamma$-rays > 3 MeV (bottom left), decays and absorptions with prompt neutrons or $\gamma$-rays (bottom middle) and decays and absorptions with prompt neutrons or $\gamma$-rays > 3 MeV (bottom right).*

**Potential Issues of the muon disappearance algorithm**

For an extrapolated muon track, it is known that the muon will have disappeared somewhere along this track. However since it is unknown where, disappearance is just as likely to have occurred at the start of the track than at the end. Volumes where multiple muon tracks meet will indicate more probable regions where a muon has disappeared. However, this feature will cause a significant amount of blurring to occur around the regions where targets are located. Since muons arrive from directly overhead this blurring will most predominately occur above and below the volumes where targets are located and be more apparent for vertical clutter scenarios.

Fig 4.17 illustrates the potential issues connected with the muon disappearance algorithm. Reconstruction of the 50 cm horizontal (top) and 50 cm vertical (bottom) scenarios, when voxels with total fractional path lengths < 4 (left), total fractional path lengths < 8 (middle) and total fractional path lengths < 12 (right) are made transparent, are presented. These transparency cuts are chosen to remove voxels in volumes surrounding where targets are located, and to demonstrate what sort of cuts need to be made in order to discriminate different density materials. For the horizontal scenarios it is clear that, dependent on the transparency cut made, there is the build-up of erroneous voxels around volumes where targets are located. This causes the propensity for the misclassification of volumes where no targets are located, as medium or even high density materials.

The issue is even more prevalent in vertical clutter scenarios. Since muons arrive from directly overhead, for vertically stacked targets, each extrapolated muon track is likely to pass close to, or even through more than one target. As additional muon tracks pass through materials, the total fractional path length of each voxel occupied by a target will increase. This in turn may cause the misclassification of low or medium density materials as high density. This feature is demonstrated if we consider the detection of 50 cm $\times$ 50 cm $\times$ 50 cm blocks of water. It can be seen for horizontal scenarios that blocks of water are not reconstructed when voxels with total fractional path lengths less than 4 are made transparent. However, when considering the vertical scenario, water is reconstructed when voxels with total fractional path lengths less than 4 and 8 are made transparent. This demonstrates how different density materials can be built up and misclassified based on this feature and represents a possible limitation of the 3D disappearance algorithm, when considering vertical clutter scenarios. In addition to

this, multiple voxels will be built up in the regions between targets. This can cause the misclassification of these regions as medium or high density materials. This feature is demonstrated in Fig. 4.17.

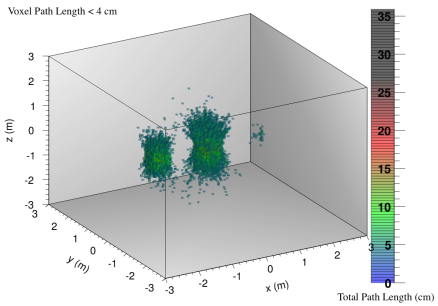


(a) Voxel total fractional path length < 4 transparent.

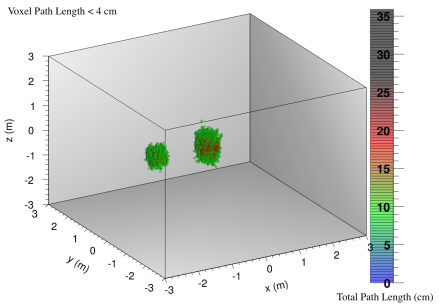


(b) Voxel total fractional path length < 8 transparent.

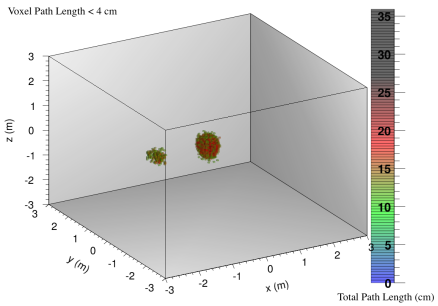


(c) Voxel total fractional path length < 12 transparent.

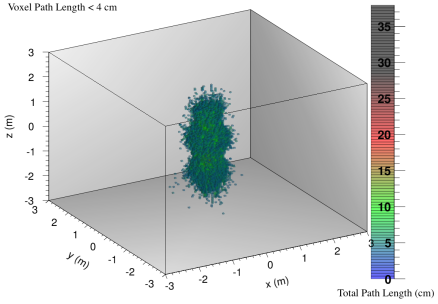


(d) Voxel total fractional path length < 4 transparent.

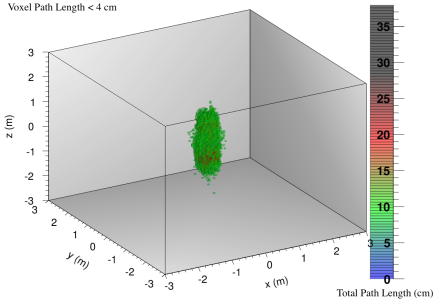


(e) Voxel total fractional path length < 8 transparent.

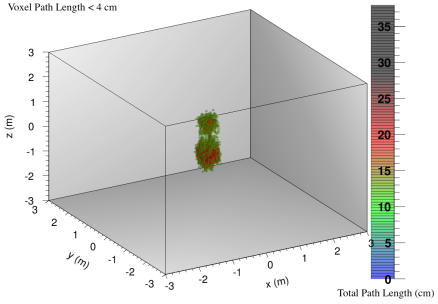


(f) Voxel total fractional path length < 12 transparent.

Fig. 4.17 *Illustration of the potential issues connected with the muon disappearance algorithm. Reconstruction of the 50 cm horizontal (top) and 50 cm vertical (bottom) scenarios when voxel total fractional path length < 4 (left), voxel total fractional path length < 8 (middle) and voxel total fractional path length < 12 (right) are made transparent.*

### 4.4.5 Three Block Scenarios with Reduced Detector Coverage

In reality, the detection of secondaries will not be done using 100% detector coverage with 100% efficiencies. For realistic detector coverage, four PVT scintillator detectors of dimensions 180 cm $\times$ 35 cm $\times$ 6 cm and eight pressurised $^3$He tubes of dimensions 2 cm radius and 55 cm length are placed around the inspected volume. Realistic detector coverage and efficiencies were used and simulations were run to test the capability of each of the techniques presented, to detect each target in the three block scenarios. Muons were generated over a 10 m $\times$ 10 m surface area and propagated through the inspected volume. 2.52 m$^2$ detector area was taken for $\gamma$-ray detection and 0.287 m$^2$ for neutron detection. Despite more efficient neutron detectors being commercially available for the detection of MeV neutrons (e.g. liquid scintillators), $^3$He detectors were used as they represent the primary neutron detectors currently in use at ports. A GEANT4 schematic of the setup used is demonstrated in Fig. 4.18. Detectors were located in the $x$-plane at ($\pm$ 1.75 m, 0, 0). The same starting random seed was used for the simulations with realistic detector coverage and efficiencies, as for those run with 100% detector coverage with 100% efficiencies. Neutrons were considered 'detected' if the interaction with $^3$He yielded the production of tritium plus a proton. Gamma-rays were considered detected if the interaction with the scintillator produced an electron of any energy.

Table 4.8 displays the total number of muons within each target that met the criteria for 3D line extrapolation, when using realistic detector coverage and efficiencies. For neutron detection of all energies this efficiency is equal to $\approx$ 1.3%. For $\gamma$-rays of all energies detector efficiency is equal to $\approx$ 67%. For both horizontal and vertical 10 cm $\times$ 10 cm $\times$ 10 cm set-ups, the number of muon tracks required to pass through the muon disappearance algorithm for each of the techniques for reconstruction to be made, needs to be $\approx$ 11 or above. It is apparent for 10 cm $\times$ 10 cm $\times$ 10 cm block systems, no technique that requires the detection of a secondary is capable of detecting any of the targets present when using the detector coverage and efficiencies described earlier in this section. From Table 4.8, when the detection of a secondary is not required (technique 1), both iron and $^{238}$U are able to be reconstructed for both horizontal and vertical scenarios. These results suggest that given simple scenarios, 10 cm $\times$ 10 cm $\times$ 10 cm blocks of $^{238}$U are able to be identified and distinguished from other density materials by using muons that disappear within the target volume. No techniques that

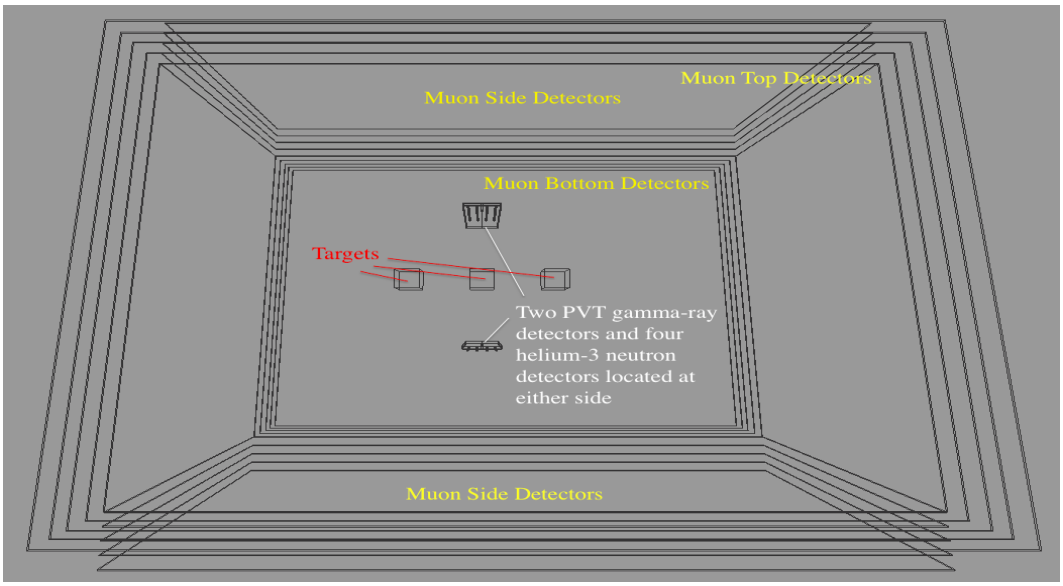


Fig. 4.18 *GEANT4 schematic of the inspected volume. Two PVT $\gamma$-ray detectors and four $^{3}$He neutron detectors are located at the sides of the targets to be inspected. Muon detectors are located above, below and at two of the sides of the volume to be inspected.*

require the detection of a secondary are able to detect any density material.

For both horizontal and vertical 50 cm $\times$ 50 cm $\times$ 50 cm set-ups, the number of muon tracks required to pass through the muon disappearance algorithm for each of the techniques for reconstruction to be made, also needs to be $\approx$ 11 or above. From Table 4.8 it is apparent that when the detection of a secondary is not required (technique 1) all targets are able to be identified and distinguished from one another. For 50 cm $\times$ 50 cm $\times$ 50 cm horizontal scenarios, when techniques require the detection of a prompt secondary, no techniques are able to detect blocks of water or iron. For blocks of $^{238}$U only muon disappearance coupled to the detection of a prompt $\gamma$-ray (technique 3 and technique 5) has enough associated muon tracks for detection to be made. Similar to the horizontal scenario, for 50 cm $\times$ 50 cm $\times$ 50 cm vertical scenarios, when techniques require the detection of a prompt secondary, no techniques are able to detect blocks of water. For blocks of iron or $^{238}$U only muon disappearance coupled to the detection of a prompt $\gamma$-ray (technique 3 and technique 5) has enough associated muon tracks for detection to be made.

Table 4.9 shows the amount of detector coverage needed for each technique that re-

Table 4.8 Total number of muon disappearances plus secondary detection in each of the targets and rest of the inspected volume (Air) for realistic detector coverage and efficiency. See Table 4.6 for a description of each of the techniques tested.

| Target | Technique 1 | Technique 2 | Technique 3 | Technique 4 | Technique 5 | Technique 6 |
|---|---|---|---|---|---|---|
| 10 cm × 10 cm × 10 cm horizontal setup | | | | | | |
| Water | $3.8 \pm 0.6$ | 0 | 0 | 0 | 0 | 0 |
| Iron | $16.2 \pm 1.3$ | 0 | 0 | 0 | 0 | 0 |
| $^{238}$U | $28.4 \pm 1.7$ | 0 | 0 | 0 | 0 | 0 |
| Air | $1860 \pm 15$ | 0 | $1.1 \pm 0.3$ | $0.7 \pm 0.3$ | $1.1 \pm 0.3$ | $0.7 \pm 0.3$ |
| 10 cm × 10 cm × 10 cm vertical setup | | | | | | |
| Water | $1.6 \pm 0.5$ | 0 | 0 | 0 | 0 | 0 |
| Iron | $17.0 \pm 1.3$ | 0 | 0 | 0 | 0 | 0 |
| $^{238}$U | $30.4 \pm 1.7$ | 0 | 0 | 0 | 0 | 0 |
| Air | $1860 \pm 15$ | 0 | $1.6 \pm 0.4$ | $0.4 \pm 0.2$ | $1.6 \pm 0.4$ | $0.4 \pm 0.2$ |
| 50 cm × 50 cm × 50 cm horizontal setup | | | | | | |
| Water | $390 \pm 6$ | 0 | $1.2 \pm 0.3$ | $0.2 \pm 0.15$ | $1.2 \pm 0.3$ | $0.2 \pm 0.15$ |
| Iron | $1925 \pm 15$ | 0 | $10.1 \pm 1.0$ | $1.9 \pm 0.4$ | $10.1 \pm 1.0$ | $1.9 \pm 0.4$ |
| $^{238}$U | $3510 \pm 20$ | 0 | $15.2 \pm 1.2$ | $2.1 \pm 0.5$ | $15.2 \pm 1.2$ | $2.1 \pm 0.5$ |
| Air | $1860 \pm 15$ | 0 | $1.2 \pm 0.3$ | $0.4 \pm 0.2$ | $1.2 \pm 0.3$ | $0.4 \pm 0.2$ |
| 50 cm × 50 cm × 50 cm vertical setup | | | | | | |
| Water | $380 \pm 6$ | 0 | $1.3 \pm 0.4$ | $0.3 \pm 0.2$ | $1.3 \pm 0.4$ | $0.3 \pm 0.2$ |
| Iron | $1920 \pm 15$ | 0 | $21.2 \pm 1.5$ | $3.2 \pm 0.6$ | $21.2 \pm 1.5$ | $3.2 \pm 0.6$ |
| $^{238}$U | $3420 \pm 20$ | 0 | $28.4 \pm 1.4$ | $4.1 \pm 0.6$ | $28.4 \pm 1.7$ | $4.1 \pm 0.6$ |
| Air | $1855 \pm 15$ | 0 | $1.1 \pm 0.3$ | $0.3 \pm 0.2$ | $1.1 \pm 0.3$ | $0.3 \pm 0.2$ |

quires the detection of a secondary (either neutron or $\gamma$-ray), to accurately locate each 50 cm × 50 cm × 50 cm target, when using realistic detector efficiencies. The coverage is given in m$^2$. From Table 4.8, for both 50 cm × 50 cm × 50 cm horizontal and vertical systems, techniques that involve solely the detection of neutrons, or $\gamma$-rays with energies > 3 MeV, or combinations of the two, are not capable of detecting any of the targets when using realistic detectors. This indicates that these techniques will not work under realistic detector coverage and efficiencies. Furthermore, no amount of detector coverage will allow the detection of water using these techniques. When considering the detection of a secondary neutron, in order to detect iron a detector coverage of 3.3 m$^2$ is required. To detect $^{238}$U, a detector coverage of 2.2 m$^2$ is required. For techniques that require the detection of $\gamma$-rays with energies > 3 MeV, the detection of iron requires a coverage of 69.8 m$^2$ for horizontal scenarios and 47.1 m$^2$ for vertical scenarios. For the detection of $^{238}$U, a detector coverage of 47.1 m$^2$ is required for the

horizontal setup, whereas 40.5 $m^2$ is required for the vertical.

For those techniques that involve the detection of prompt $\gamma$-rays there are a number of muon tracks associated with this. However, due to the low number of muons available to pass to the muon disappearance algorithm, only blocks of 50 cm $\times$ 50 cm $\times$ 50 cm $^{238}$U can be identified for the horizontal scenario. Both iron and $^{238}$U can be identified for the vertical scenario. While this appears to be a promising result for this technique, for realistic scenarios that involve the detection of shielded nuclear materials in cargo containers, nuclear targets of this size will not be available. Secondly there will be many more additional muon disappearances coupled to the detection of prompt $\gamma$-rays that will act to mask this signal. These additional signatures are due to muons that stop within the cargo container walls and components of the lorry. Finally, it has already been demonstrated in section 4.4.3 that techniques which involve the detection of prompt $\gamma$-rays, struggle to differentiate between medium and high-density materials. For these reasons this technique will not be considered under realistic conditions. To detect iron in the horizontal scenario a detector coverage of 3.0 $m^2$ is needed, whereas water cannot be reconstructed even with 100% detector coverage.

Table 4.9 Detector coverage area (in $m^2$) required for the detection of each target, when using a technique that requires the detection of a secondary. See Table 4.6 for a description of each of the techniques tested.

| Target | Technique 2 | Technique 3 | Technique 4 | Technique 5 | Technique 6 |
|---|---|---|---|---|---|
| 50 cm $\times$ 50 cm $\times$ 50 cm Horizontal Setup | | | | | |
| Iron | 3.3 | 3.0 | 69.8 | 3.0 ($\gamma$-ray) | 69.8 ($\gamma$-ray) |
| $^{238}$U | 2.2 | 2.5 | 47.1 | 2.5 ($\gamma$-ray) | 47.1 ($\gamma$-ray) |
| 50 cm $\times$ 50 cm $\times$ 50 cm Vertical Setup | | | | | |
| Iron | 3.3 | 2.2 | 47.1 | 2.2 ($\gamma$-ray) | 47.1 ($\gamma$-ray) |
| $^{238}$U | 2.2 | 1.8 | 40.5 | 1.8 ($\gamma$-ray) | 40.5 ($\gamma$-ray) |

### Background Calculation

The background rate of neutrons and $\gamma$-rays at sea level has been calculated using GEANT4.9.6-p02. The primary source of background neutrons comes from cosmic-rays. 50 million cosmic-ray neutrons, generated over a 10 m $\times$ 10 m surface area were propagated through the inspected volume. This inspected volume contained four PVT $\gamma$-ray scintillators and eight $^3$He neutron detectors, configured like radiation portal monitors. The total neutron count was measured in the neutron detectors for 50 million

cosmic-ray neutrons. This was then converted to a count rate, which represents a 5 minute exposure time. From CRY [49], a 5 minute exposure time is equal to 850,000 cosmic-ray neutrons, generated over a 10 m $\times$ 10 m surface area. Table 4.10 displays the total amount of neutrons detected in all detectors and the amount of neutrons detected in each individual detector, for both 50 million cosmic-ray neutrons and 850,000 cosmic-ray neutrons. The error given is that of the mean for 50 million, scaled to 850,000. Since $\approx$ 2000 muon disappearances occur within the inspected volume every 5 minutes, there are 2000, 1 $\mu$s windows after a muon has disappeared for an erroneous neutron to be detected. From Table 4.10 the number of background neutrons detected within a 5 minute exposure time is 41.1 $\pm$ 0.8. For realistic detector coverage and efficiency this count rate results in the total amount of background neutrons detected in a 1 $\mu$s window after a muon disappearance as $\approx$ 0.0003.

Table 4.10 Number of neutrons detected in each $^{3}$He detector, when propagating 50 million cosmic-ray neutrons through the inspected volume.

| Detector | Number in 50 million | Number for 5 min exposure |
|---|---|---|
| 1 | 260.0 $\pm$ 16.1 | 4.4 $\pm$ 0.3 |
| 2 | 324.0 $\pm$ 18.0 | 5.5 $\pm$ 0.3 |
| 3 | 278.0 $\pm$ 16.7 | 4.7 $\pm$ 0.3 |
| 4 | 354.0 $\pm$ 18.8 | 6.0 $\pm$ 0.3 |
| 5 | 290.0 $\pm$ 17.0 | 4.9 $\pm$ 0.3 |
| 6 | 310.0 $\pm$ 17.6 | 5.3 $\pm$ 0.3 |
| 7 | 298.0 $\pm$ 17.3 | 5.1 $\pm$ 0.3 |
| 8 | 306.0 $\pm$ 17.5 | 5.2 $\pm$ 0.3 |
| **Total** | **2420.0 $\pm$ 50.0** | **41.1 $\pm$ 0.8** |

For $\gamma$-rays the primary source of background radiation comes from $^{238}$U and $^{232}$Th nuclei decay, in the Earth's surface. The amount of each radioisotope present within the Earth's surface varies with location. When calculating the background $\gamma$-ray rate, it is assumed there are 1 ppm of $^{238}$U and 6 ppm of $^{232}$Th present in the surface [108]. Simulations placed four PVT $\gamma$-ray scintillators and eight $^{3}$He neutron detectors, configured like radiation portal monitors, above 1000 cm $\times$ 1000 cm $\times$ 20 cm of rock. In the rock, $^{238}$U and $^{232}$Th nuclei were randomly positioned. These nuclei then underwent radioactive decay, with $\gamma$-rays that penetrate to the surface detected by the PVT scintillators. One billion disintegrations of $^{238}$U and $^{232}$Th nuclei were simulated, with the results then scaled to the equivalent of a 5 minute exposure time. The error given is that of the mean for 1 billion disintegrations, scaled to the number of disintegrations that represent

5 minutes.The amount of disintegrations that represents a 5 minute exposure time is given by Eq. (4.10), where $N$ is the number of disintegrations required, $m$ is the mass of rock in kg, $t$ is the time of exposure in seconds and $\frac{dN}{dt}$ represents the activity of each isotope in the soil.

$$N = m \times t \times \frac{dN}{dt} \tag{4.10}$$

The density of rock is 2.7 g/cm$^3$. Therefore the mass of rock is equal to: (2.7 g/cm$^3$ $\times$ 1000 cm $\times$ 1000 cm $\times$ 20 cm) = 54,000 kg. The time of exposure is 5 minutes. For $^{238}$U, 1 Bq/kg of $^{238}$U = 81 ppb $^{238}$U. Therefore, 1 ppm of $^{238}$U is equal to 12.35 Bq/kg. From Eq. (4.10) the number of $^{238}$U disintegrations, which represents a 5 minute exposure time is $2.0007 \cdot 10^8$. For $^{232}$Th, 1 Bq $^{232}$Th/kg = 246 ppb $^{232}$Th. Therefore 6 ppm of $^{232}$Th is equal to 24.4 Bq/kg. From Eq. (4.10) the number of $^{232}$Th disintegrations, which represents a 5 minute exposure time is $3.9528 \cdot 10^8$. Table 4.11 displays the number of $\gamma$-rays detected in each of the PVT scintillators for this amount of disintegrations, for each isotope. From Table 4.11 the total amount of background $\gamma$-rays, for a 5 minute exposure time is equal to 300,170 $\pm$ 430. For realistic detector coverage and efficiency this count rate results in the total number of background $\gamma$-rays detected in a 1 $\mu$s window after a muon disappearance as $\approx 2$. These results would indicate the background is not in fact negligible, therefore any techniques that would look to use muon disappearance coupled to the detection of a prompt secondary would have to be shielded from background neutrons and $\gamma$-rays.

Table 4.11 Number of $\gamma$-rays detected in each PVT scintillator when propagating $2.0007 \cdot 10^8$ disintegrations of $^{238}$U and $3.9528 \cdot 10^8$ disintegrations of $^{232}$Th through the inspected volume.

| Detector | Number of $\gamma$-rays for $2.0007 \cdot 10^8$ disintegrations of $^{238}$U | Number of $\gamma$-rays for $3.9528 \cdot 10^8$ disintegrations of $^{232}$Th |
|---|---|---|
| 1 | 26,320 $\pm$ 70 | 45,550 $\pm$ 135 |
| 2 | 27,690 $\pm$ 70 | 48,340 $\pm$ 140 |
| 3 | 26,210 $\pm$ 70 | 46,530 $\pm$ 135 |
| 4 | 27,130 $\pm$ 75 | 51,950 $\pm$ 140 |
| **Total** | **107,800 $\pm$ 150** | **192,370 $\pm$ 280** |

## 4.5 Summary

This chapter has discussed the initial concept of muon induced fission and how it can be applied to nuclear threat detection. The main premise of the technique is that as material density increases, muons are more likely to lose sufficient energy to stop. Upon stopping in a material, $\mu^-$'s can be captured onto the orbit of a nucleus. This capture will result in the production of multiple neutrons and $\gamma$-rays, with the effect more apparent for high-$Z$ materials. Therefore the disappearance of a muon, coupled to the detection of either prompt neutrons or $\gamma$-rays represents a clear signature of possible high density material. Simulations have been conducted that demonstrate the validity of GEANT4.9.6-p02 with the 'Shielding 2.0' physics list for this process. Neutron and $\gamma$-ray spectra have been measured when propagating 500,000 $\mu^-$ and $\mu^+$ through different density materials. These spectra illustrate the characteristic $\gamma$-rays unique to $^{235}$U and $^{238}$U that can be detected when attempting to ascertain the presence of HEU. Of primary interest for this are muonic $X$-rays, which occur when $\mu^-$ are captured on the orbital of a nucleus. Muonic $X$-rays are emitted as the captured $\mu^-$ cascades down the orbital levels to the nucleus. For the applications discussed in this thesis, detector coverage is required to be representative of the realistic coverage currently in use at ports. This involves placing four plastic scintillators and eight pressurised $^3$He tubes around the inspected target. The inherent resolution of plastic scintillator detectors is not good enough to resolve different $\gamma$-ray peaks accurately. Instead we must rely on techniques that measure the disappearance of a muon in coincidence with the detection of a secondary product. For this approach six different techniques were tested.

The creation and performance of a new type of 3D muon disappearance algorithm in differentiating materials has been discussed. Muon disappearance tomography represents a new technique in detecting high density materials, such as shielded HEU. Six techniques are available for this approach. Each technique involves the disappearance of a muon, coupled to the detection of either prompt neutrons or prompt $\gamma$-rays. For each of the six techniques, muons that meet the required criteria have their initial track extrapolated through the volume, to where the track would have exited had disappearance not occurred. The identification of high density materials is made through ascertaining regions within the inspected volume where multiple muon disappearances have occurred. For 100% detector coverage and efficiency, the ability of all six techniques to detect different sized, different density targets in simple geometries is apparent, as long

as background neutrons and $\gamma$-rays are accounted for. Upon the introduction of realistic detectors, only muon disappearance is capable of detecting different density targets in simple geometries.

Due to the nature of the 3D muon disappearance algorithm, there is the propensity for volumes surrounding targets to be misclassified as high density materials. Since it is unknown where a muon has disappeared within the inspected volume, disappearance is just as likely to have occurred at the start of the track than at the end. Regions where multiple tracks meet, represent volumes where targets are located. This results in the build-up of multiple voxels in the volumes that surround targets. Due to the nature of the cosmic-ray muon spectrum, this effect is more apparent in the vertical direction. For vertical clutter scenarios multiple voxels are built up in the regions between targets. This can cause the misclassification of these regions as medium or high density materials. Since muons arrive from above, for vertically stacked targets each extrapolated muon track is likely to pass close too, or even through more than one target. This effect may result in the misclassification of low density materials as medium or high density.

# Chapter 5

# Material Segregation using Cosmic-Ray Muons for Empty Cargo Container

This chapter discusses the capability of using cosmic-ray muons to detect shielded HEU in otherwise empty cargo containers. Section 5.1 presents simulation parameters inherent to all simulations in this chapter. Section 5.2 discusses the capability of muon scattering tomography to detect five shielded HEU targets in realistic empty cargo containers. The dependence of the detector capability to detect high-$Z$ targets in empty cargo containers, on spatial resolution has been studied. A number of different resolutions representative of gaseous and scintillator detectors are tested. The development of a new secondary analysis algorithm that is applied to the reconstructed PoCA points is discussed. This algorithm efficiently ascertains clusters of voxels with high average scattering angles to identify 'areas of interest' within the inspected volume. Using this approach the effect of other parameters, such as the distance between detectors and the number of detectors per set, on material detection is discussed. This results in an optimum set-up being established. Using this optimum setup, section 5.3 displays the capability of the muon disappearance algorithm to correctly detect five shielded HEU targets in empty cargo containers. Section 5.4 shows the capability of detecting five shielded HEU threats in an empty cargo container when using both muon scattering tomography and muon disappearance tomography in conjunction with one another. Section 5.5 will summarise the work discussed.

## 5.1 Simulation Parameters

Each simulation attempted to detect five 10 kg spheres (5 cm radius) of 20% enriched uranium (20% $^{235}$U and 80% $^{238}$U) placed randomly in a cargo container of dimensions 6.058 m $\times$ 2.438 m $\times$ 2.591 m. HEU was surrounded by either lead or steel shielding. Five million muons generated over a 10 m $\times$ 10 m area are passed through the inspected geometry, which is equivalent to a 5-minute exposure time. The validity of this size muon surface area is described in section 3.2.4. The thickness of the shielding was enough to attenuate the characteristic 1.001 MeV $\gamma$-ray line emitted by $^{234m}$Pa (in the $^{238}$U decay chain). A calculation for the amount of shielding required in given in section 5.1.1.

### 5.1.1 Shielding Calculation

When looking to detect shielded HEU the most prominent signal detected is the 1.001 MeV $\gamma$-ray emitted via radioactive decay of $^{238}$U. Therefore the concentration of $^{238}$U within the threat material will have an effect on the amount of shielding required. $^{238}$U emits 81 $\gamma$-rays per second per gram at 1.001 MeV [109]. The amount of shielding required to mask this signal is dependent on a number of factors including detector area ($A$), detector efficiency ($\varepsilon$), and background noise. The distance between detector and target will also influence the amount of shielding, as after certain distances the solid angle subtended ($P$) by the detector is likely to reduce the signal as much as any reasonable amount of shielding would. The total signal received at the detector is a convolution of these factors and is given by,

$$S = NGFP. \tag{5.1}$$

$N$ is the total number of 1.001 MeV $\gamma$-rays emitted by the target, $G$ is a factor that represents the fraction of $\gamma$-rays that have not scattered from self-shielding, $F$ is a factor that represents the fraction of $\gamma$-rays that have not scattered from intentional shielding and $P$ is the path loss.

Signals emitted by HEU below the background can be detected when the total counts due to the signal exceeds the fluctuations in the background. If a source is present, the size of fluctuations in the background grows with the square root of time, while the signal grows linearly with time. If $S$ is the signal received at the detector and $t$ is the time

over which counts are integrated, then $S\varepsilon t$ will be the counts due to the signal, while the standard deviation of fluctuations in the background will be proportional to $(Ab\varepsilon t)^{1/2}$. Therefore the signal can be detected when the average signal exceeds a multiple, $m$, of standard deviations of the background,

$$S\varepsilon t > m(Ab\varepsilon t)^{1/2}. \tag{5.2}$$

Where $b$ is the background level for 1.001 MeV photons received by the detector. The background level for 1.001 MeV photons, for a typical (0.3 $m^2$) sodium iodide detector, has been measured to be 860 $m^{-2}$ $s^{-1}$ [109]. This value takes into account the energy resolution (10%) and detector efficiency (0.57) of the detector. From Eq. (5.2) for a 5 minute exposure time ($t$ = 300 s), identification of a threat will be made once the total signal detected is greater than 630.

Monte Carlo simulations have been conducted to determine the amount of shielding required to attenuate the characteristic 1.001 MeV $\gamma$-ray line emitted from HEU down to background levels. Five minute exposure times were considered for both lead and steel shielding. Simulations were run using GEANT4, where a 5 cm radius, 10 kg sphere of 20% enriched uranium, was shielded by different thickness of either lead or steel and placed 50 cm from a 0.3 $m^2$ sodium iodide detector. Fig. 5.1 shows a schematic of the simulation. For a 5 minute exposure time, 10 kg of 20% enriched uranium will emit $1.944 \cdot 10^8$ $\gamma$-rays of energy 1.001 MeV. This many $\gamma$-rays were randomly generated within the HEU sphere. Each $\gamma$-ray had a random direction and was propagated through the target volume. The thickness of external shielding required was enough so that detection could not be made within 5 minutes at 3 standard deviation level. As demonstrated by Eq. (5.2), this requires the total signal received by the detector to be less than 630. For lead shielding this requires a thickness of 7 cm whereas for steel shielding, a thickness of 11 cm is needed. Since the background measurement was made with 10% energy resolution, all $\gamma$-rays with energies from 0.95 - 1.05 MeV were considered as 1.001 MeV $\gamma$-rays.

### 5.1.2 Simulation Package and Muon Generator

The muon energy spectrum at sea level is calculated using the parameterisation proposed by Gaisser [99] modified for large zenith angles and muon decay in the atmosphere (Modified Gaisser Parameterisation - MGP). Muons have been generated over a

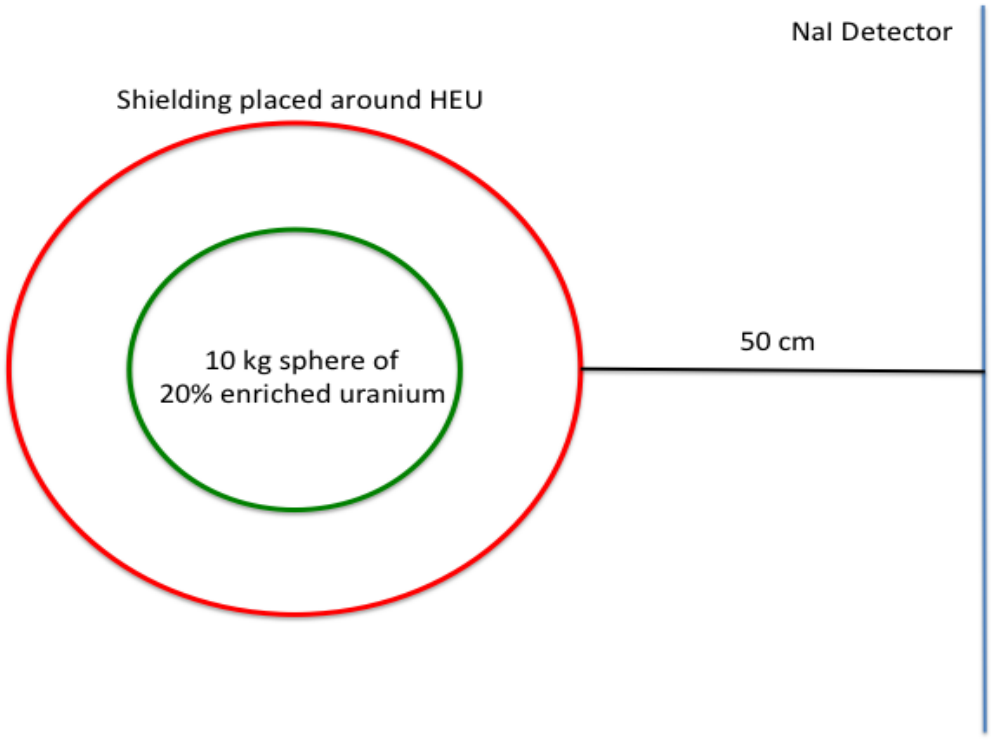


Fig. 5.1 *Schematic of GEANT4 simulation to determine the amount of shielding required to attenuate the characteristic 1.001 MeV line emitted by* $^{238}U$ *down to background levels.*

10 m $\times$ 10 m surface area, which is implemented into the simulations so that the true distribution of cosmic-ray muons with respect to their energies and zenith angles at sea level are represented. Muon energies generated using the MGP range from 100 MeV - 1000 GeV. Muons generated from the MGP are interfaced with GEANT4, which has been used to simulate and track the passage of particles through the inspected volume and detectors. For these simulations GEANT4.9.6-p02 is used with the 'Shielding 2.0' physics list.

### 5.1.3 Target Geometry

A standard setup for the muon tomography system implemented in GEANT4 is displayed in Fig. 5.2. Detectors comprised of either scintillator or gaseous material, are placed above, below and at the sides of the volume to be inspected. These detectors are 2 cm thick with a distance of 4 m separating the lower most top detector and the upper most bottom detector. Scintillators have an average density of 1.032 g/cm$^3$ and a chem-

ical makeup of $C_9H_{10}$. Gaseous detectors have an average density of 0.00203 g/cm$^3$ and consist of 65% Argon, 30% $CO_2$ and 5% $CF_4$. Simulations have been run using either three or five detectors per set with detectors in each set spaced 10 cm, 25 cm or 50 cm apart. The volume to be inspected is a lorry containing five shielded nuclear materials in an empty cargo container.

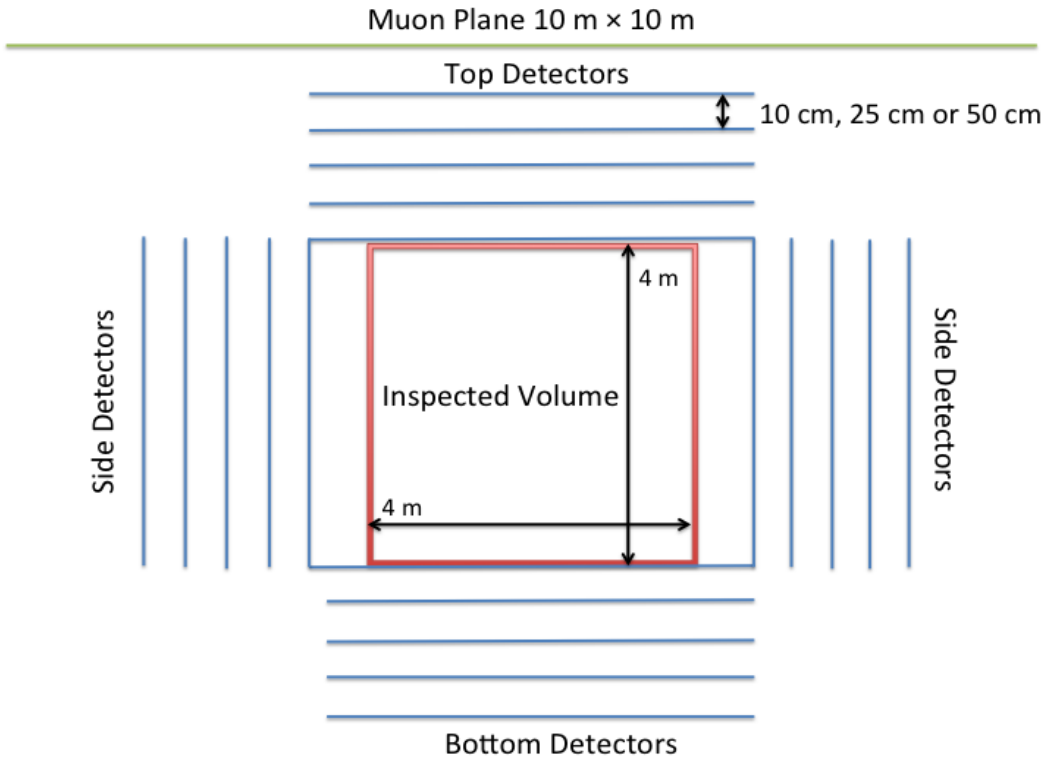


Fig. 5.2 *Standard set-up for the muon tomography system (not to scale) in which the inspected volumes will be placed. The lorry is expected to drive into the inspected volume. The spacing between detectors is 10 cm, 25 cm or 50 cm and there can be 3 or 5 detectors per set. The inspected volume is a lorry pulling a shipped cargo container housing shielded HEU.*

## 5.2 Techniques for Muon Scattering

### 5.2.1 Muon Tracking

Only muons that are tracked through two sets of detectors (top-bottom, top-lateral), and recorded within all detectors in a set, are considered for track reconstruction. Since vehicles are required to enter and exit the inspection volume, it cannot be completely encompassed by detectors. As such not all muons passing through the volume will be eligible for reconstruction. Incoming and outgoing muon tracks are reconstructed using a 3D least-square regression fit (LSR). Spatial resolution is simulated via simultaneously smearing the $x$ and $y$ co-ordinates for muons detected in the top and bottom sets, and the $x$ and $z$ co-ordinates for those in the lateral detector sets. Simulations run to mimic gaseous detector resolutions use Gaussian widths ($\sigma$) of 0.2 mm, 1 mm and 2 mm. Those run for scintillator resolutions use Gaussian widths of 1 cm, 2 cm and 3 cm. The detectors are assumed to be 100% efficient with each detector plane having a coverage of 7 m $\times$ 4 m. Muon scattering between the two sets of detectors has been assumed to occur at a single point. This point of muon scattering has been reconstructed using the PoCA algorithm described in section 3.2.3.

### 5.2.2 Analysis Algorithm

A new analysis approach has been developed that attempts to locate 'areas of interest', which represent regions of high-$Z$ or nuclear materials. Upon reconstruction of the incoming and outgoing muon tracks using LSR, the PoCA algorithm presented in Chapter 3 is used to determine the muon scatter point. As discussed previously, PoCA points tend to form dense clouds around high-$Z$ materials. Therefore high-$Z$ materials are characterised by multiple muon tracks with high scattering angles, reconstructed within a particular volume. Our analysis takes advantage of this through using a secondary algorithm that builds upon the traditional PoCA algorithm. The geometry is split into voxels, with the average scattering angle of all PoCA points within each voxel calculated. Identification of clusters of voxels with high average scattering angles is then made. By identifying dense clusters of voxels, only those volumes that have had several muons undergo scatters with materials within the inspected volume, are used for analysis. This approach removes voxels that are not attributed to any targets within the inspected volume. The approach discussed, as well as all parameters presented are calculated assuming a target size of 10 kg sphere HEU, surrounded by either 7 cm of

lead or 11 cm of iron.

The total geometry is split into 5 cm $\times$ 5 cm $\times$ 5 cm voxels, with voxels retained for further analysis if they have 3 or more PoCA's reconstructed within it. Fig. 5.3 shows an example of this, where the total lorry is clearly identified. All muons reconstructed

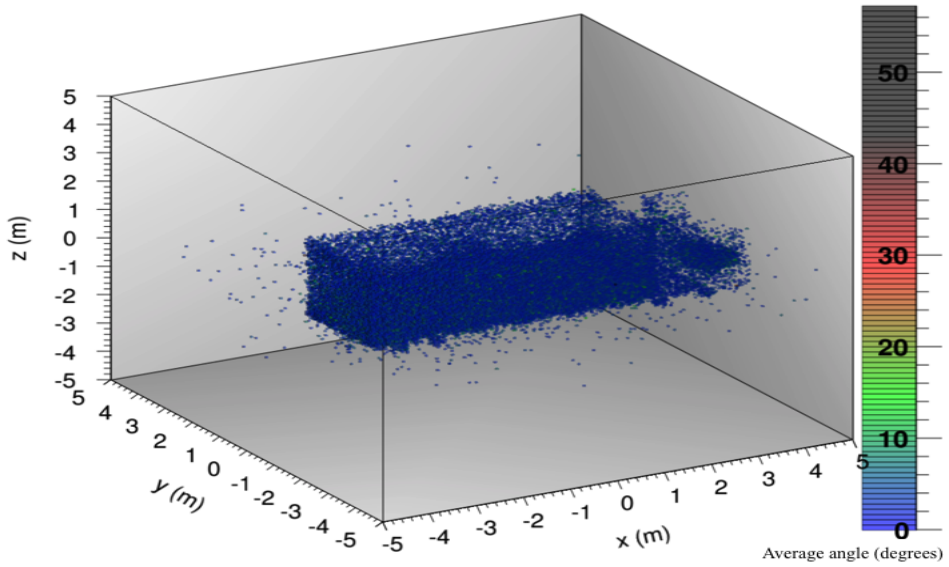


Fig. 5.3 *Image reconstruction of the total geometry where voxels have 3 or more PoCA's reconstructed within it.*

in voxels that are outside the cargo container are removed from the analysis. This is demonstrated in Fig. 5.4, where it can be seen that only the voxels attributed to the cargo container remain. The remaining volume is split into four equal sections along the $z$-axis. Each section is then split up into 20 cm slices. Every 20 cm slice is analysed so that no threats are potentially missed. For example, if the first 20 cm slice runs from voxels 1 to 5 along the $z$-axis, the next slice runs from voxels 2 to 6. Fig. 5.5 displays an example of one of these 20 cm slices, in which 5 shielded nuclear materials have been placed where the red circles are. All voxels that have been reconstructed using solely a PoCA algorithm are plotted. Fig. 5.5 demonstrates the limitations of techniques that solely rely on the PoCA algorithm, as multiple voxels with high average scattering angles are reconstructed in volumes where no targets are located. This is evident in Fig. 5.5 by the number of voxels plotted with high average scattering angles (red voxels in Fig. 5.5). For targets much smaller than 20 cm $\times$ 20 cm $\times$ 20 cm, the same approach can be used but with an alteration to the calculated optimum parameters. For example,

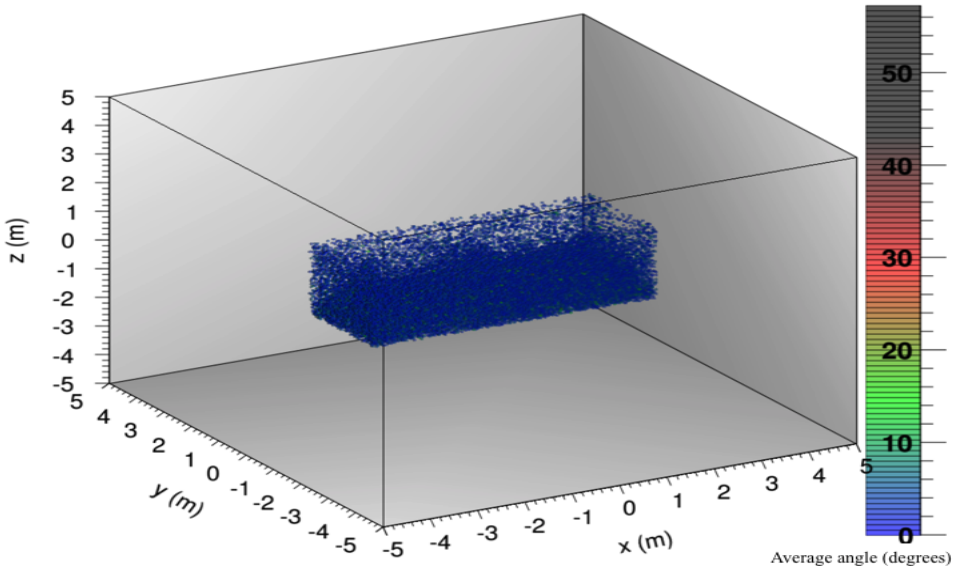


Fig. 5.4 *Image reconstruction of total geometry after the removal of all muons reconstructed outside the cargo container.*

instead of using 5 cm × 5 cm × 5 cm and 20 cm slices, 2 cm × 2 cm × 2 cm voxels and 10 cm slices could be used. Such an approach would require a recalculation of the optimum reconstruction parameters and longer CPU time, but the general sequence described would be the same.

Every group of sixty-four voxels within each 20 cm slice is analysed using a set of reconstruction parameters. Optimum parameters have been calculated for each of the four sections. The total volume of hidden threat plus shielding drives the choice of 64 voxels in each group: 20 cm in each dimension. The volumes highlighted by red circles in Fig. 5.5 represent regions where shielded nuclear materials were positioned. Due to additional voxel build-up, these volumes are difficult to identify with certainty using solely the PoCA algorithm. To clearly ascertain 'areas of interest' a second analysis algorithm is used to locate volumes of closely related voxels with high average scattering angles. The algorithm analyses every group of sixty-four voxels within each 20 cm slice. Groups of sixty-four voxels have a total size of 4 voxels × 4 voxels × 4 voxels which is 20 cm × 20 cm × 20 cm. The first group of 64 voxels analysed are always in the top left corner of the slice. This group represents voxel numbers 1 - 5 in all dimensions. So that no groups of voxels are missed, if the first group of sixty-four runs from voxels 1 - 5 (in all dimensions), the next group of sixty-four voxels analysed will run

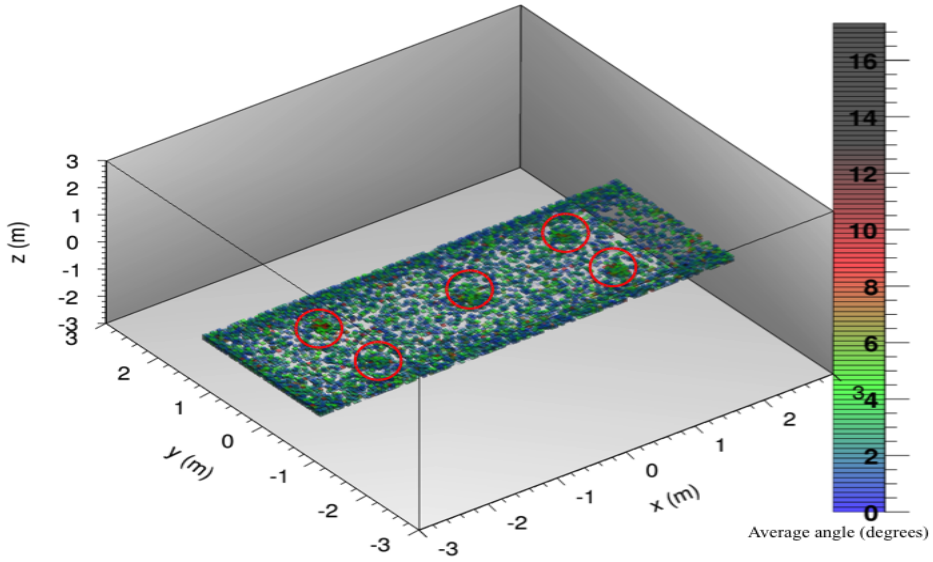


Fig. 5.5 *Image reconstruction of one of the slices to be analysed, when propagating 5 million muons through an empty cargo container housing 5 shielded threat materials. The red circles represent volumes where shielded HEU were located.*

from voxels 1 - 5 in two dimensions and voxels 2 - 6 in the other dimension. Fig. 5.6 shows an example of the analysis algorithm identifying the 'areas of interest' present in Fig. 5.5.

Upon reconstruction for each group of sixty-four voxels within each 20 cm slice, there are three parameters in the analysis algorithm that can be optimised. These are the minimum number of muons, $R$, reconstructed within a particular voxel to become eligible for analysis, the number of voxels, $V$ (out of the sixty-four), with an average scattering angle bigger than the plane average and the plane average multiplied by some factor, $M$. The parameters listed in Table 5.1 have been calculated as the optimum for detecting all nuclear materials present in each of the sixteen simulations run for cargo containers housing low-$Z$ clutter (discussed in Chapter 6). These parameters give the lowest false positive and false negative rates assuming a perfect resolution. A description of how these parameters are calculated is given in section 5.2.3

The optimum reconstruction parameters generally increase with depth in the cargo. Since the PoCA algorithm assumes scattering to take place at a single point, if a muon undergoes multiple scatters this reconstructed point will be weighted towards the ele-

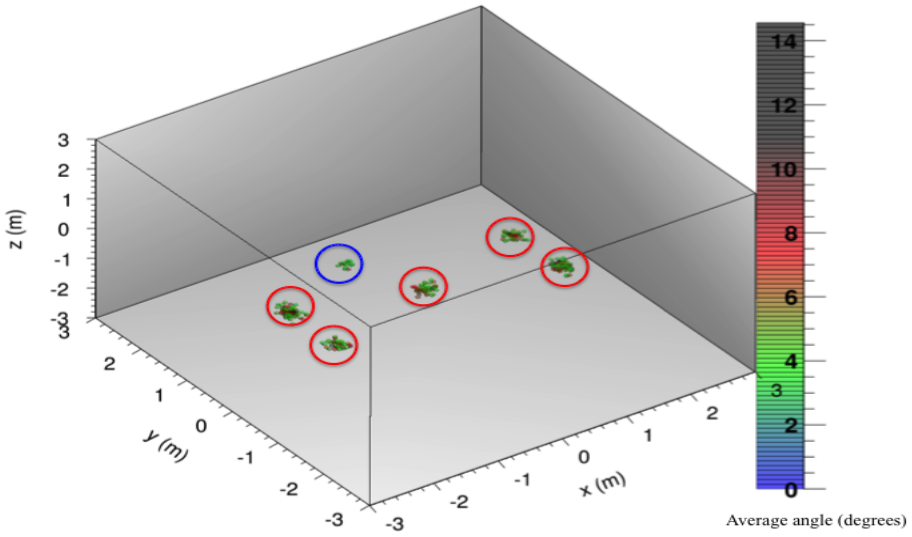


Fig. 5.6 *Image reconstruction of all volumes that have been extracted using the analysis algorithm when propagating 5 million muons through an empty cargo container housing 5 shielded threat materials. Those circled in red are threat materials whereas those circled in blue can be attributed to the cargo walls.*

Table 5.1 Optimum parameters determined for the detection of shielded HEU in each section.

| Section | $R$ | $V$ | $M$ |
|---|---|---|---|
| 1 | 3 | 16 / 64 | 1.5 |
| 2 | 3 | 17 / 64 | 1.3 |
| 3 | 3 | 22 / 64 | 1.3 |
| 4 | 4 | 16 / 64 | 1.5 |

ment that caused the greatest degree of scattering to occur. The degree of scattering depends on the target and the momentum of the muon. Upon reaching targets lower in the cargo, muons will have already undergone multiple interactions resulting in a loss of energy. Due to this energy loss, upon interacting with a material lower in the cargo, a muon will undergo a greater degree of scattering than if the same muon had interacted with the same material higher up. Furthermore, if a muon interacts with a material lower in the cargo, it has less additional material to then pass through before exiting the lorry. If there is less material left for the muon to pass through, the probability of interaction with any other material is reduced. This in turn reduces the probability of the muon undergoing a large deflection that influences the position where scattering is

assumed to have occurred.

The combination of these two reasons cause more muons in total to be reconstructed lower in the cargo. This is why the minimum number of muons required to be reconstructed within a voxel, $R$, increases with depth. It also results in more accurate reconstructions occurring at lower depths in the cargo and therefore why the number of voxels with large scattering angles, $V$, increases with depth.

The two anomalies in this rule are: when $V$ equals 16 / 64 for section 4 and when $M$ equals 1.5 for section 1. The first abnormal result ($V$ in section 4) is due to the increase in the minimum number of muons, $R$. As this quantity ($R$) increases, the total number of voxels, $V$, required for a positive identification will decrease, as an extra muon track per voxel is required as compared to the previous sections. The second abnormal result ($M$ in section 1) is most likely due to low statistics available for that section. When calculating optimum parameters, 80 shielded HEU targets were placed randomly within the cargo container. Due to the weight of shielded HEU, it is unlikely to be placed towards the roof of the cargo, as it would need to be stacked upon something heavy. Cargo containers for transport require an even weight distribution of the cargo. This is unlikely to occur if two particularly heavy items are stacked together. Therefore of the 80 shielded threat materials, only 2 were placed in section 1.

(a) Generate an $N \times N \times N$ grid over the inspected volume and split into $L \times L \times L$ voxels. Establish a cartesian co-ordinate system in three dimensions with $z$ as the vertical. Measured data is position ($x_{pos}$, $y_{pos}$, $z_{pos}$) and direction cosines ($mx$, $my$, $mz$) of each of the incoming ($x_{pos}$, $y_{pos}$, $z_{pos}$, $mx$, $my$, $mz$)$_{in}$ and outgoing ($x_{pos}$, $y_{pos}$, $z_{pos}$, $mx$, $my$, $mz$)$_{out}$ muon tracks ($M$).

(b) For $i$:=1 to M muons get incoming (($x_{pos}$, $y_{pos}$, $z_{pos}$, $mx$, $my$, $mz$)$_{in}$)$_i$ and outgoing (($x_{pos}$, $y_{pos}$, $z_{pos}$, $mx$, $my$, $mz$)$_{out}$)$_i$ muon track data for each detector.

(c) For $i$:=1 to M muon reconstruct their muon track using a 3D least-squares regression fit.

(d) For each muon track calculate the PoCA point using Eq. (3.2), Eq. (3.3), Eq. (3.4) and Eq. (3.5).

(e) Add the calculated scatter angle to the PoCA voxel it resides within.

(f) Calculate the average scatter angle for all scatter points that reside in the calculated voxel.

(g) Repeat steps c - f for all $M$ tracks.

(h) Remove all voxels that have less than 3 muon PoCA points reconstructed within it.

(i) Remove all voxels located outside where the cargo container is positioned.

(j) Split the remaining voxels into 4 equal sections along the $z$-axis.

(k) For each of the 4 sections, split into every possible 20 cm slice along the $z$-axis. For example, if the first 20 cm slice runs from voxels 1 to 5 along the $z$-axis, the next slice runs from voxels 2 to 6.

(l) Analyse every possible group of sixty-four voxels within each 20 cm slice of each section, with a set of optimum parameters that have been calculated for that section. This will include groups of 64 voxels that partially overlap other groups of 64 voxels.

(m) Repeat step h - k for all sections.

### 5.2.3 Description of how the Optimum Parameters were Calculated

Any optimum parameters that are given in this thesis have been calculated using the following approach:

(a) Sixteen simulations have been run where shielded HEU was placed randomly in cargo containers filled with various clutter. A full description of these scenarios is discussed in Chapter 6 and Appendix A.

(b) For each configuration the reconstruction parameters ($R$, $V$ and $M$) were varied to determine which combination was most efficient in identifying all shielded HEU, with the minimum number of erroneous voxel build-up. Since the position of the threats were known a priori, an erroneous voxel is defined as a reconstructed voxel not located where a threat is positioned.

(c) Each of the four sections was analysed with $R$ varied from 2 - 12, $V$ varied from 20 - 64 and $M$ varied from 0.8 - 2.2 (in steps of 0.1). All combinations of these ranges were tested.

(d) Since the location of threats in each of the sixteen configurations are known, any voxels not reconstructed (for a particular set of parameters) where the threats are located are considered erroneous.

(e) The total amount of erroneous reconstructed voxels, for all sixteen configurations, for each set of parameters is then calculated. This is done separately for each section.

(f) The total amount of erroneous voxels is compared to the total amount of false negatives observed, for all sixteen configurations, for each set of parameters.

(g) The set of parameters that gives the lowest false negative rate coupled to the lowest erroneous voxel build-up, for each section, is then established as the optimum set of parameters for that section.

(h) Steps d - f are done separately for each section.

### 5.2.4 Results for Cargo Container Housing 5 Shielded Threats

The ability to detect shielded HEU in empty cargo containers as a function of detector resolution, detector spacing and number of detectors per set using the analysis algorithm presented in section 5.2.2 has been studied. All results presented here use the cargo configuration shown in Fig. 5.7. This consists of placing five 5 cm radius spheres of 20% enriched uranium surrounded by 11 cm of steel (targets 1, 2, 3) or 7 cm of lead (targets 4, 5) at random locations in the cargo container. Due to this each threat is not necessarily aligned with the centre of a voxel. All shielded threat materials are located on the floor of the container. This places the threat materials in section 4 of the inspected volume. The total geometry is split into 5 cm $\times$ 5 cm $\times$ 5 cm voxels. The average scattering angle is taken from all muon tracks that are reconstructed within a particular voxel. As shown in Table 5.1, for detection of materials located in section 4, the analysis algorithm requires 16 voxels per each set of 64 analysed to have 4 or more muons reconstructed within it. These voxels must have an average scattering angle greater than 1.5$\times$ that of the slice as a whole (see Table 5.1 for optimum parameters). Upon undergoing analysis via the process described in section 5.2.2, 3D images are

plotted with a colour gradient based on the scattering angle observed. All voxels with an average scattering angle of less than 1° are made transparent. The transparency of voxels then increases uniformly until all voxels with an average scattering angle greater than 5° are completely solid.

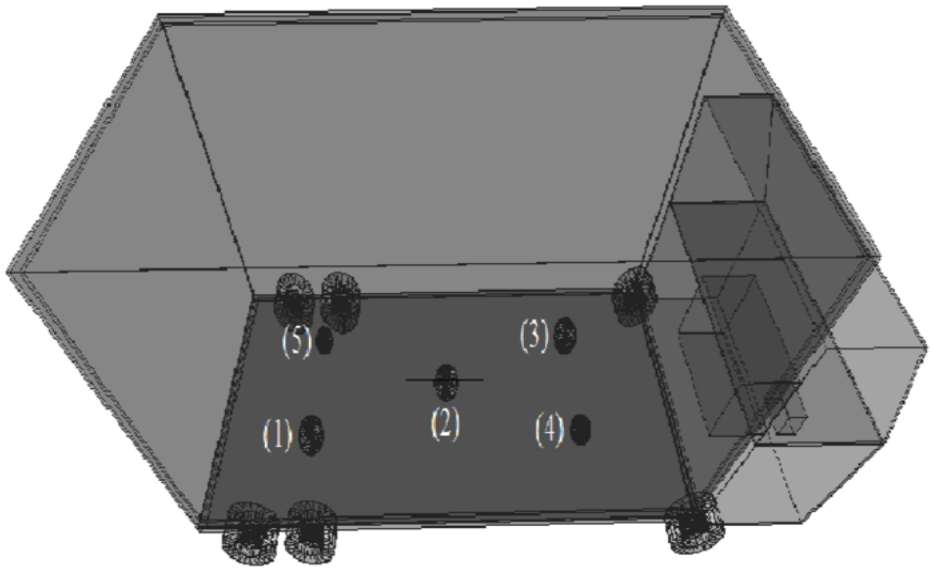


Fig. 5.7 *Schematic of the empty cargo configuration. The five materials are 5 cm radius spheres of 20% enriched uranium surrounded by 11 cm of steel (targets 1, 2, 3) or 7 cm of lead (targets 4, 5).*

### 5.2.5 Effect of Detector Spacing

To monitor the effects of detector spacing, simulations were run with three detectors per set. The inspected volume is displayed in Fig. 5.7. The ability to detect five shielded threat materials for all spatial resolutions (0.2, 1, 2, 10, 20 and 30 mm) for detectors spaced at 10 cm, 25 cm and 50 cm has been analysed. Fig. 5.8 shows the effect of increasing the distance between detectors on the average scattering angle for each threat material and the plane as a whole. Using the analysis algorithm with the reconstruction parameters defined in Table 5.1, Table 5.2 shows the number of voxels that meet the selection criteria defined, in the volumes where each threat was located. This represents the number of voxels used to calculate the average scattering angle displayed in Fig. 5.8. The smallest threats (HEU shielded by lead) have diameters of 24 cm. Since every 20 cm slice in the $z$-axis is analysed, each threat will reside very close to the centre of one of these slices. Every group of 64 voxels is then analysed for each 20 cm slice.

Since each group of 64 voxels represents an analysis size of 20 cm $\times$ 20 cm $\times$ 20 cm, there will be a set of 64 voxels in which the threat is very close to the centre. It is this set of 64 voxels that are selected and analysed for the results in Table 5.2. Threats where very few voxels are used in calculating the average scattering angle (Fig. 5.8 - Threat 5 - 1 cm and 2 cm resolution and threat 1 - 2 cm resolution) can result in unexpectedly high average scattering angles, as erroneously large scatters are not as well incorporated into the average.

From Table 5.2 and Fig. 5.8, for all detector spacing scenarios, as spatial resolution becomes worse the average scattering angle for each shielded nuclear material increases and becomes comparable to that of the plane average. Secondly, the number of muon tracks reconstructed in volumes where the threats are located reduces. As shown in Table 5.2, these reasons result in a reduction of the number of voxels found where the threats are positioned, causing the threat to become more difficult to detect. Increasing spacing between each individual detector increases the accuracy of reconstructed muon tracks. This improves material detection capabilities as due to the increased accuracy, fewer tracks are reconstructed in volumes where no materials are located, with more tracks correctly reconstructed within targets. As the distance between each individual detector increases (from 10 cm to 25 cm to 50 cm) the total average scattering angle observed in the inspected slice reduces. This is shown in Fig. 5.8. However, the average scattering angle for each threat stays approximately the same. This further increases material detection capabilities as the threats become more clearly observed above the background.

The combined results in Fig. 5.8 and Table 5.2 indicate that for all detector spacing tested, the ability to detect all shielded HEU using the analysis algorithm for 0.2 mm, 1 mm and 2 mm spatial resolutions is apparent. The average scattering angle of each threat material is clearly above that of the plane average. Sufficient numbers of voxels clustered together in regions where threats are located, are observed to allow positive threat detection. Due to the low number of muon tracks reconstructed where the threats are located and the inability to observe the threat materials above the plane average, no system with 3 cm position resolution will allow the reconstruction of nuclear targets. The same can be concluded for 1 cm and 2 cm position resolution where detectors are spaced at 10 cm and 25 cm. For 50 cm detector spacing it would appear from Fig. 5.8 that threat materials can clearly be observed above the background. However, due

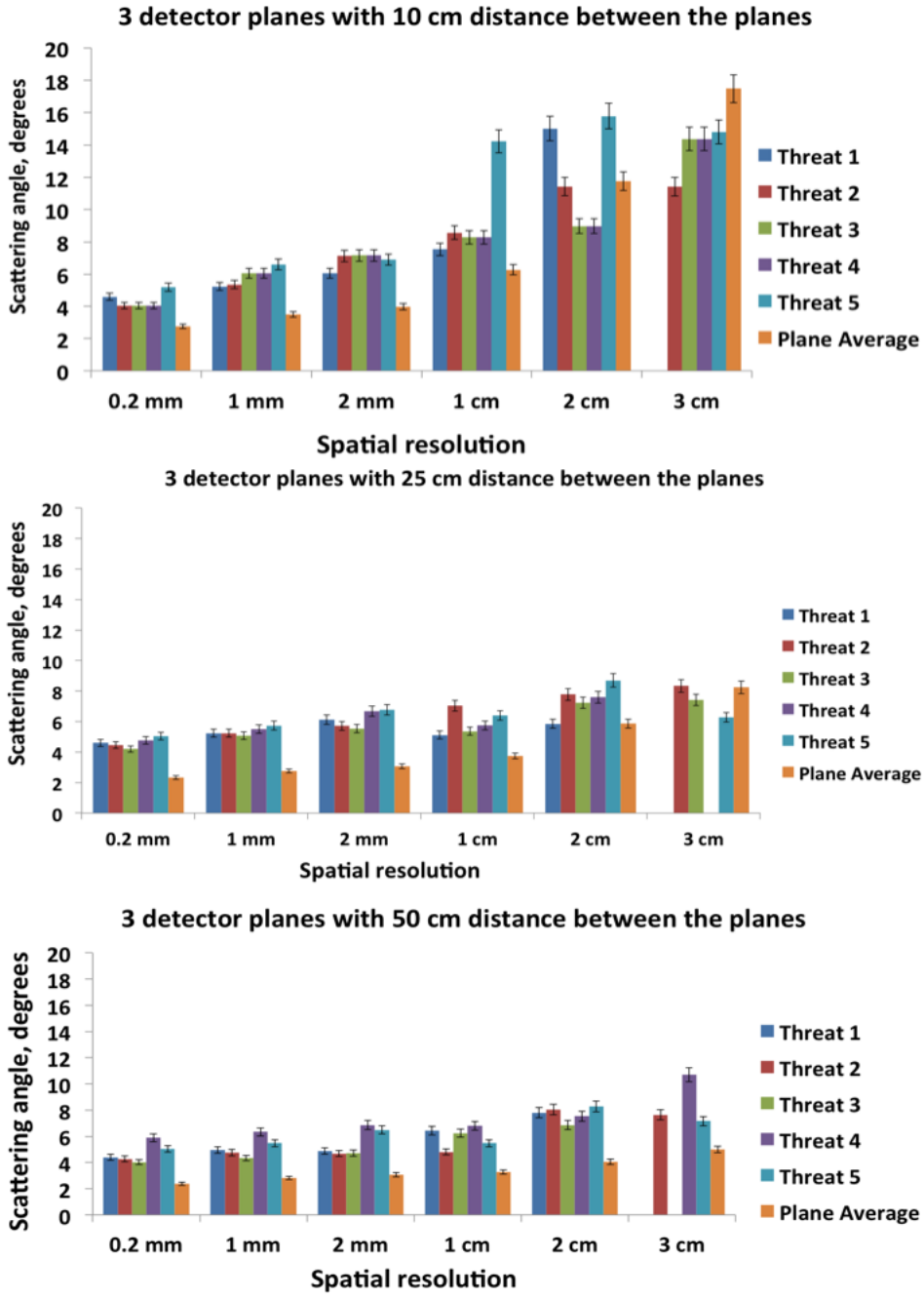


Fig. 5.8 *Mean scattering angle vs spatial resolution for a configuration with 3 detectors per plane. The five materials are 5 cm radius spheres of 20% enriched uranium surrounded by 11 cm of steel (threat 1, 2, 3) or 7 cm of lead (threat 4, 5). Detector planes are separated by 10 cm (top), 25 cm (middle) and 50 cm (bottom). Any empty peaks that are observed are caused by no voxels meeting the reconstruction criteria in the volume where the threat material is located.*

to the low number of muon tracks reconstructed in volumes where the targets are located, material detection cannot be made. For this scenario there are not enough voxels clustered together in the volumes where targets are located with an average scattering angle higher than 1.5$\times$ the planes average. Therefore any voxels measured with large scattering angles could be erroneous points, as opposed to evidence of threat materials. For 10 cm detector spacing and 3 cm position resolution the plane average appears greater than the average scatter in each threat. This is due to the low number of muon tracks reconstructed where each threat is located. Therefore an accurate estimation of the scatter in each threat cannot be made.

In general the average scatter observed decreases with increasing detector spacing. The increased distance between detectors will result in is less error being associated with the path reconstruction, as there is a smaller angle through which the track can be reconstructed. This smaller angle will in turn reduce the calculated average scatter of a muon and hence a reduction in the average scatter observed as detector spacing increases (for the same resolution) is observed. It should be noted that while further increases in spacing would continue to increase the accuracy of track reconstruction, as the distance between each individual detector increases, fewer muons are likely to pass through all detectors in a particular set. This reduces the total number of muons eligible for track reconstruction. Furthermore, increasing detector spacing will increase the overall size of the detector system, thus making it less practical. Finally any empty peaks that are observed in Fig. 5.8 are caused by no voxels meeting the reconstruction criteria in the volume where the threat material is located.

### 5.2.6 Number of Detector Planes

The effect of increasing the number of detector planes for each set of detectors (top, bottom or sides) on material detection has also been analysed. For these simulations five planes were used per set instead of three. These detector planes were separated by 25 cm and therefore covered the same total area as simulations run with three planes spaced 50 cm apart. The inspection volume displayed in Fig. 5.7 was used. Planes separated by 10 cm were not considered due to poor material detection in comparison to 25 cm and 50 cm spacing when using three planes. Five detectors with spaces of 50

Table 5.2 Number of voxels out of 64 passing the selection criteria given in Table 5.1, using the analysis algorithm in the volumes where each threat is located.

| Spacing | Resolution | Threat 1 | Threat 2 | Threat 3 | Threat 4 | Threat 5 |
|---|---|---|---|---|---|---|
| 10 cm | 0.2 mm | 36 | 50 | 44 | 53 | 57 |
| 10 cm | 1.0 mm | 23 | 29 | 27 | 37 | 39 |
| 10 cm | 2.0 mm | 22 | 15 | 19 | 25 | 23 |
| 10 cm | 1.0 cm | 1 | 5 | 4 | 5 | 2 |
| 10 cm | 2.0 cm | 1 | 1 | 3 | 2 | 2 |
| 10 cm | 3.0 cm | 0 | 1 | 5 | 3 | 2 |
| 25 cm | 0.2 mm | 37 | 48 | 49 | 57 | 56 |
| 25 cm | 1.0 mm | 28 | 38 | 39 | 45 | 48 |
| 25 cm | 2.0 mm | 22 | 32 | 31 | 36 | 43 |
| 25 cm | 1.0 cm | 5 | 3 | 7 | 11 | 12 |
| 25 cm | 2.0 cm | 2 | 5 | 6 | 3 | 1 |
| 25 cm | 3.0 cm | 0 | 4 | 5 | 0 | 2 |
| 50 cm | 0.2 mm | 34 | 45 | 54 | 53 | 56 |
| 50 cm | 1.0 mm | 29 | 36 | 48 | 46 | 52 |
| 50 cm | 2.0 mm | 31 | 36 | 43 | 46 | 44 |
| 50 cm | 1.0 cm | 7 | 11 | 10 | 13 | 9 |
| 50 cm | 2.0 cm | 2 | 7 | 6 | 3 | 2 |
| 50 cm | 3.0 cm | 0 | 3 | 0 | 4 | 2 |

cm were not considered either, as they would act to increase the inspection range by a further 2 m making it less practical. Fig. 5.9 shows the effect that increasing the number of detector planes per set has on the average scattering angle of the threat materials and the slice in which they are located. Table 5.3 shows this effect on the number of voxels passing the selection criteria defined in Table 5.1, in volumes where targets are located.

In general increasing the number of detectors per set results in an increase in the number of voxels that meet the reconstruction criteria in volumes where threats are located. For 2 cm and 3 cm position resolutions there are still not enough voxels grouped together where the nuclear materials are located, with an average scattering angle higher than 1.5$\times$ the plane average, for clear detection to be made. However, for 1 cm spatial resolution there is a rise in the number of voxels that meet these criteria, in particular for HEU shielded with lead. Hence nuclear material detection is more apparent for the system of five detectors with 25 cm distance between each detector, than the system of three detectors spaced 50 cm apart. This is due to the additional two detector planes that record the muons trajectory. Multiple Coulomb scattering will occur between de-

Table 5.3 Number of voxels identified out of 64 passing the selection criteria given in Table 5.1, using the analysis algorithm in the volumes where each threat is located.

| Spacing | Resolution | Threat 1 | Threat 2 | Threat 3 | Threat 4 | Threat 5 |
|---|---|---|---|---|---|---|
| 3 Detectors per set | | | | | | |
| 50 cm | 0.2 mm | 34 | 45 | 54 | 53 | 56 |
| 50 cm | 1.0 mm | 29 | 36 | 48 | 46 | 52 |
| 50 cm | 2.0 mm | 31 | 36 | 43 | 46 | 44 |
| 50 cm | 1.0 cm | 7 | 11 | 10 | 13 | 9 |
| 50 cm | 2.0 cm | 2 | 7 | 6 | 3 | 2 |
| 50 cm | 3.0 cm | 0 | 3 | 0 | 4 | 2 |
| 5 detectors per set | | | | | | |
| 25 cm | 0.2 mm | 31 | 52 | 51 | 49 | 52 |
| 25 cm | 1.0 mm | 33 | 47 | 44 | 50 | 50 |
| 25 cm | 2.0 mm | 33 | 47 | 42 | 40 | 47 |
| 25 cm | 1.0 cm | 10 | 13 | 15 | 16 | 17 |
| 25 cm | 2.0 cm | 6 | 5 | 7 | 4 | 6 |
| 25 cm | 3.0 cm | 3 | 4 | 3 | 1 | 3 |

tectors. The introduction of additional detectors will limit the effect this has on the track reconstruction as additional positions along the muon trajectory will be known. This in turn makes muon track reconstruction more accurate. In addition to the increase in number of voxels that meet the criteria, there is a slight decrease in the plane average. This results in reducing the noise from erroneous scatters and increases the potential for nuclear material detection.

### 5.2.7 Results for Cargo Containing 5 Shielded Nuclear Materials with no Clutter

The capability of observing five shielded nuclear materials located randomly in an empty cargo container has been studied. Following the results obtained from simulations conducted for detector spacing and numbers of detectors per set, simulations are only run for detectors spaced 25 cm apart with five detectors per set. All resolutions representative of gaseous detectors (0.2 mm, 1 mm, and 2 mm) are considered. For resolutions representative of scintillator bars only 1 cm position resolutions are considered. The inspection volume is the same as that displayed in Fig. 5.7. Fig. 5.10 shows the capability of the analysis algorithm developed to identify dense clusters of voxels,

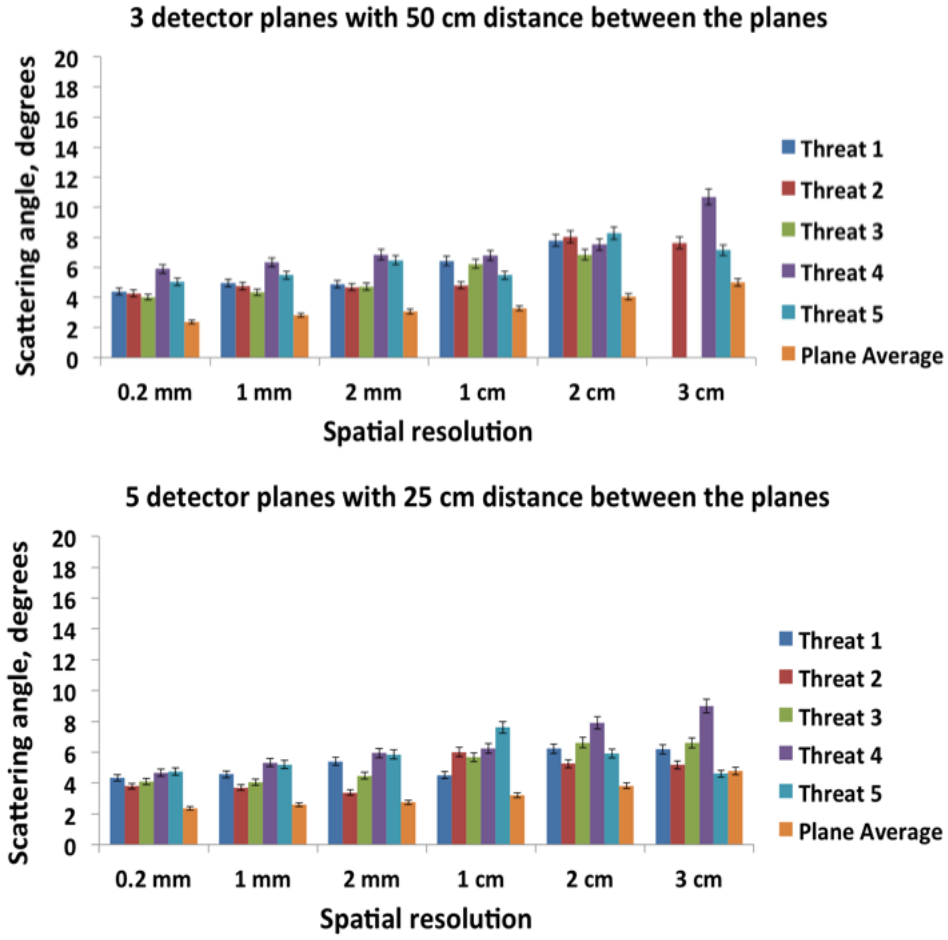


Fig. 5.9 *Mean scattering angle vs spatial resolution for a configuration with three detectors per set (top) and five detectors per set (bottom). Detector planes are separated by 50 cm when three detectors are used and 25 cm when five detectors are used. Simulations are run using the same detectors and nuclear materials as with Fig. 5.8. Any empty peaks that are observed are caused by no voxels meeting the reconstruction criteria in the volume where the threat material is located.*

using the parameters given in Table 5.1.

For perfect, 0.2 mm, 1 mm and 2 mm spatial resolutions all nuclear materials are clearly identified. This demonstrates the capability of the new analysis algorithm developed, to correctly extract dense clusters of voxels that are attributed to shielded HEU. For spatial resolutions of 0.2 mm and 1 mm there is also the build-up of two false positives, located just inside the cargo, next to the walls. A false positive is defined as a region of high-$Z$ material identified by the analysis algorithm, where no shielded HEU was placed. This

is caused by muons that have been scattered by the walls of the cargo container, but reconstructed just inside these walls. In a realistic scenario, potential threat materials can be placed close to the wall. It would therefore be unknown whether these regions represent shielded nuclear materials, or false positives due to the cargo container walls. This indicates a potential limitation of muon scattering tomography with the analysis algorithm, to clearly detect high-$Z$ materials attributed to shielded HEU, from occasional build-ups due to the cargo container itself. As detector spatial resolution becomes worse those voxels identified, which are attributed to the cargo container walls, are no longer observed. As detector spatial resolution decreases the plane average scatter increases. This results in multiple muon tracks associated with the cargo wall to no longer meet the criteria of being $1.5\times$ above the plane average. Therefore the number of voxels with an average scattering angle greater than $1.5\times$ the plane average reduces. The number of voxels becomes less than the number required by the analysis algorithm for material detection, hence the false positives are no longer identified.

For 10 mm spatial resolution only HEU shielded with lead are correctly identified. This is due to the same reasons described above, when discussing the disappearance of false positives associated with cargo container walls. As spatial resolution gets worse, there is a decrease in the number of muon tracks correctly reconstructed in volumes where the threats are located. These muon tracks are subsequently reconstructed in regions where no threats are located. This results in a decrease in threat detection, as fewer voxels with high scattering angles are located close together where nuclear materials are present. This demonstrates a limitation of the analysis algorithm when using spatial resolutions representative of scintillator detectors.

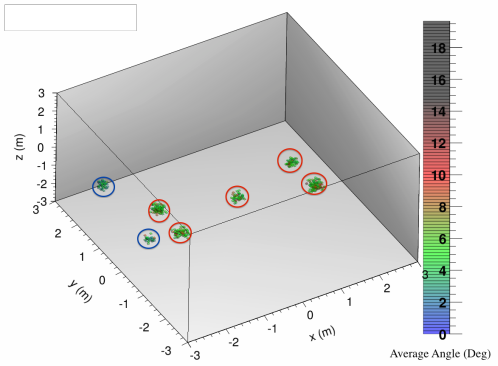


(a) *0.2 mm spatial resolution.*

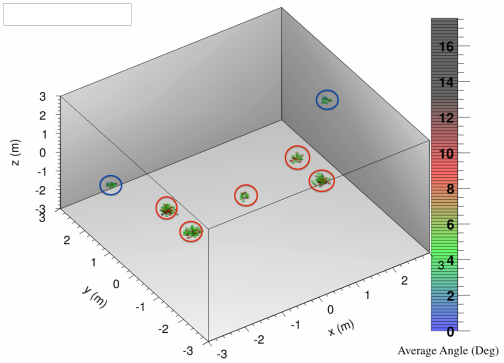


(b) *1 mm spatial resolution.*

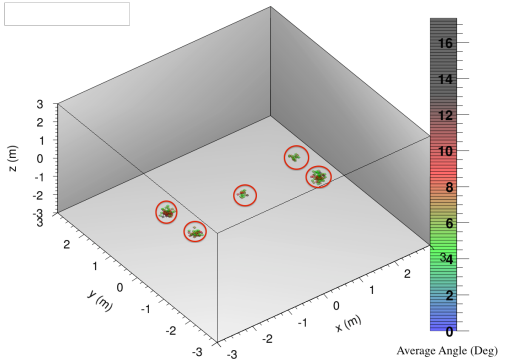


(c) *2 mm spatial resolution.*

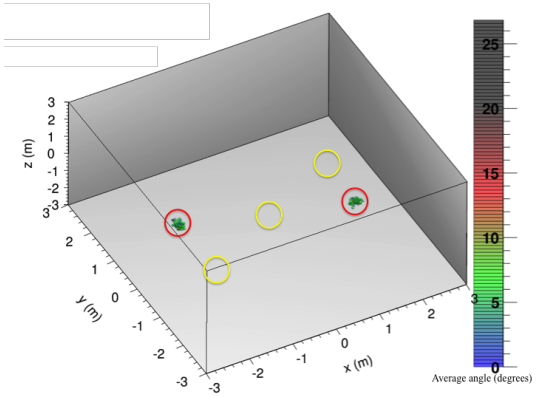


(d) *10 mm spatial resolution.*

Fig. 5.10 *Illustration of voxels that pass the selection criteria given in Table 5.1 when using the analysis algorithm for 0.2 mm (top left), 1 mm (top middle), 2 mm (top right) and 10 mm (bottom middle) spatial resolutions. Voxels with red circles represent volumes where shielded threat materials were located. Voxels with blue circles represent false positives identified with the analysis algorithm. Voxels with yellow circles represent volumes where threat materials were located, but not identified with the analysis algorithm.*

### 5.2.8 Comparison Between Four 5 cm × 5 cm × 5 cm Voxels and a Single 20 cm × 20 cm × 20 cm Voxel to Detect 5 Shielded Nuclear Materials in a Cargo Container Housing 5 Shielded Threats

For the analysis discussed in section 5.2.3, the analysis algorithm grouped together 4 × 4 × 4 voxels of size 5 cm × 5 cm × 5 cm. This represents a total volume of 20 cm × 20 cm × 20 cm. An interesting study can be made to see whether splitting the total geometry into voxels of size 20 cm × 20 cm × 20 cm will allow an efficient detection of shielded HEU. Unlike for the analysis algorithm with 5 cm × 5 cm × 5 cm voxels, a single voxel now covers each 20 cm × 20 cm × 20 cm volume analysed. Therefore the number of voxels, $V$ (out of the 64), with an average scattering angle larger than the plane average, can no longer be considered. Instead, the only parameters available to optimise are the minimum number of muons, $R$, reconstructed within a particular voxel, and the plane average multiplication factor, $M$. Due to the increase in voxel size the number of muons reconstructed per voxel increases. The capability of observing five shielded nuclear materials located randomly in an empty cargo container has again been studied. The inspection volume is displayed in Fig. 5.7. All resolutions representative of gaseous detectors (0.2 mm, 1 mm, and 2 mm) are considered, as are 1 cm spatial resolutions representative of scintillator bars. Analysis was conducted as before, except the voxels analysed for each 20 cm slice were now of size 20 cm × 20 cm × 20 cm. Fig. 5.11 shows a colour map of the inspected volume of the the volumes identified when using the analysis algorithm with 20 cm × 20 cm × 20 cm voxels for the empty cargo scenario, for perfect resolution. Optimum parameters for detecting the threat materials with the lowest false positive rate were obtained. This involved using 160 reconstructed scatter points per voxel ($R$), with a factor ($M$) of 1.3. All voxels with an average scattering angle less than 3° have been made transparent. A description of how optimum parameters are calculated is given in section 5.2.3.

All volumes where shielded HEU are located have been accurately identified. There is also the build-up of two additional volumes. As with analysis conducted for 5 cm × 5 cm × 5 cm sized voxels, one of these false positives is attributed to the cargo container walls. However, unlike the analysis for 5 cm × 5 cm × 5 cm sized voxels, there is a second false positive built up in a volume where no materials are located. Due to the size of the voxels, any voxels that are reconstructed have to be considered high-density

materials. The build-up of a false positive where no threats are located is particularly concerning. This demonstrates a drawback of this algorithm that is not present for smaller sized voxels. Consequently voxel sizes of 5 cm $\times$ 5 cm $\times$ 5 cm will be used when aiming to detect shielded HEU in all future scenarios with clutter. Results with 0.2 mm, 1 mm and 2 mm resolutions were equivalent to those in Fig. 5.11, whereby all nuclear materials were correctly identified along with two additional volumes. For 1 cm spatial resolutions only HEU shielded by lead were reconstructed.

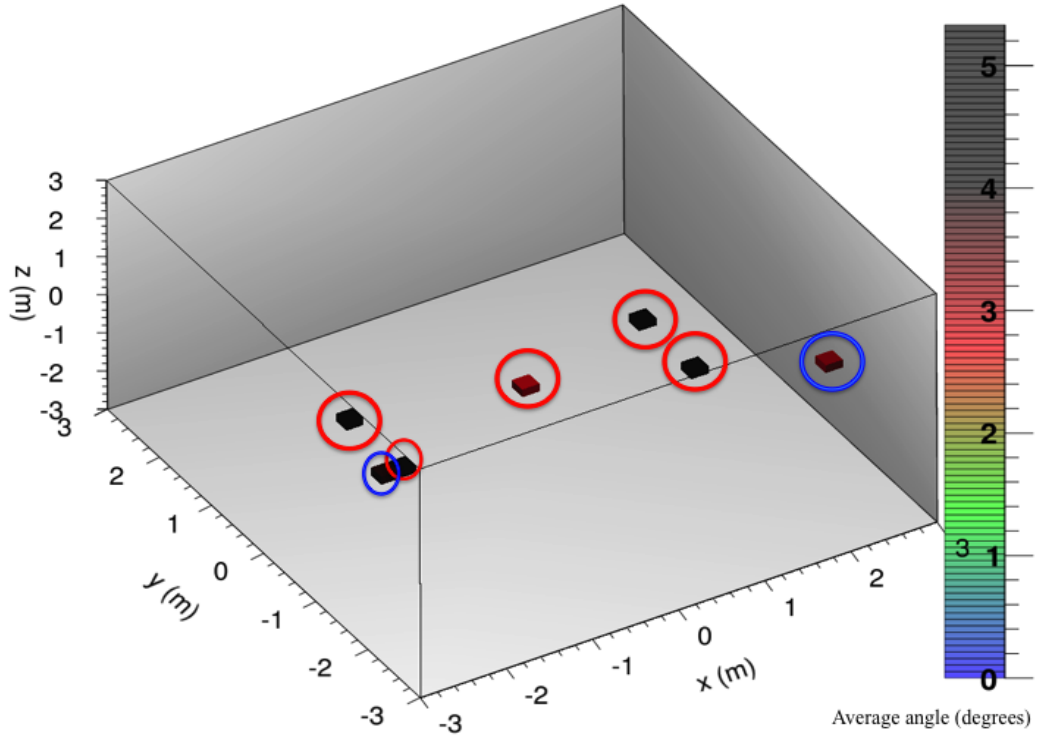


Fig. 5.11 *Illustration of those voxels identified using the analysis algorithm with 20 cm $\times$ 20 cm $\times$ 20 cm sized voxels for perfect resolution. Voxels with red circles represent volumes where shielded threat materials were located. Voxels with blue circles represent false positives identified with the analysis algorithm. The colour scale is based in the average scattering angle observed per voxel.*

## 5.3 Techniques for Stopping Muons

### 5.3.1 Muon Tracking

Muons considered for analysis must pass through all detectors in the top set, but do not pass through any subsequent set. A schematic for the simulated system is displayed in Fig. 5.2. The geometry inspected is displayed in Fig 5.7. Any muons that are not detected exiting the volume can be assumed to have disappeared somewhere within the inspected volume, or exited where no detectors are located. For 5 million muons $\approx$ 500,000 muons in total will pass through the sides where no detectors are located. For muons that have disappeared, the top detectors will have recorded an initial position and direction of the muon track. If it is assumed that the muon travels along a straight line, then its path from the top detector to where it would have exited the volume had it not disappeared can be extrapolated. Muons that meet the disappearance criteria of not being detected exiting the inspected volume, are passed to the muon disappearance algorithm outlined in section 4.4.2, with a 3D tomographic image built up based on the total fractional path length calculated per voxel. Voxels of size 5 cm $\times$ 5 cm $\times$ 5 cm are used.

### 5.3.2 Results for Cargo Container Housing 5 Shielded Threats using Muon Disappearance Tomography

Analysis is made along the same process as muon scattering tomography. The total fractional path length in each voxel is determined before splitting the total geometry into four equal sections along the $z$-axis. Every 20 cm slice within each section is analysed using the set of parameters given in Table 5.4. The general trend observed in these parameters is that the number of reconstructions required per voxel, ($R$), and the number of voxels greater than the plane average ($V$) times some factor, $M$, decreases with depth in the cargo. This is to be expected since fewer extrapolated muon tracks will pass through voxels that are lower within the cargo. Clusters of voxels that meet the criteria given in Table 5.4 for each section are then plotted. The ability of the muon disappearance algorithm presented in section 4.2.2 to detect shielded HEU in otherwise empty cargo containers (with perfect resolution), is demonstrated in Fig. 5.12.

Red circles represent volumes where threat materials are located in Fig. 5.12. As it can be seen, the volumes where threat materials are located have been clearly iden-

tified using the muon disappearance algorithm. However, similar to the three block systems tested in Chapter 4, there is also the build-up of multiple voxels surrounding the volumes where each threat material is located. This build-up makes the accurate localisation of the threat materials problematic and may result in the misclassification of volumes where no threats are located, as high-$Z$ materials. In addition to these issues, there is also the build-up of multiple additional voxels in volumes located far away from threat materials. These voxels have total fractional path lengths similar to that of the threat materials. The additional reconstructed voxels are attributed to muons that have disappeared in the components of the lorry and the lorry container that house the shielded threat materials. In particular the build-up towards the front of the cargo container is in part due to muons that have stopped within the engine and battery of the lorry. The inability to sufficiently distinguish between these different components represents a limitation of the muon disappearance algorithm to detect shielded nuclear materials in an empty cargo container. However, since threat materials are identified using this technique, it may be used as a secondary technique to enhance muon scattering tomography systems, which look to detect the same threat materials. Similar results are found for all other spatial resolutions (0.2 mm, 1 mm and 2 mm) tested, whereby there is the build-up of multiple additional voxels that act to mask the detection of shielded HEU.

Table 5.4 Optimum parameters determined for the detection of shielded HEU in each section for muon disappearance tomography. A description of how optimum parameters are calculated is given in section 5.2.3

| Section | $R$ | $V$ | $M$ |
|---|---|---|---|
| 1 | 16 | 26 / 64 | 1.4 |
| 2 | 15 | 26 / 64 | 1.4 |
| 3 | 15 | 22 / 64 | 1.3 |
| 4 | 13 | 22 / 64 | 1.3 |

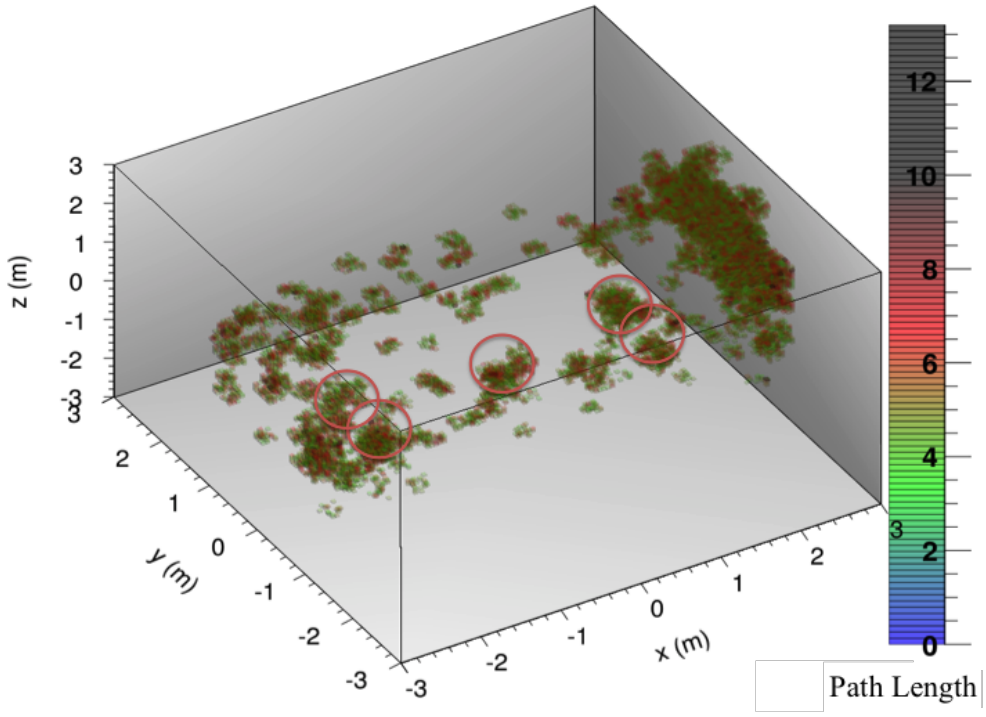


(a) Full reconstruction.

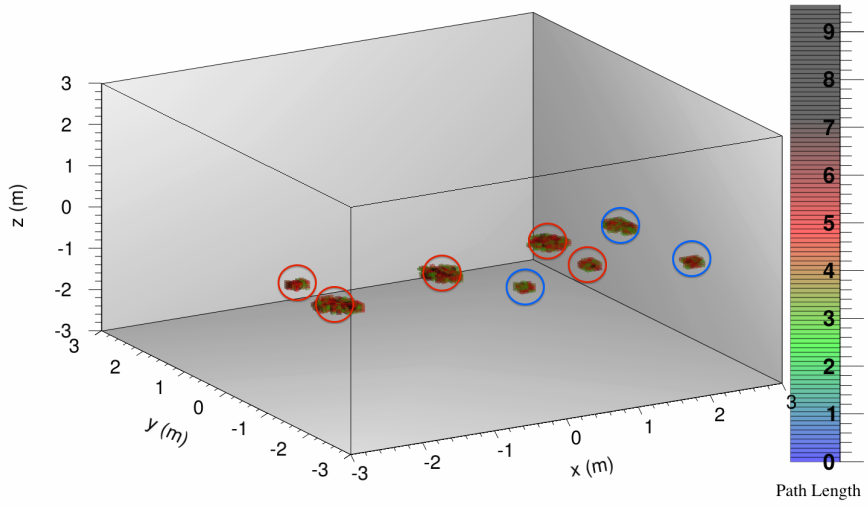


(b) Reconstruction centered in $z$-slice where threats are located.

Fig. 5.12 *Image reconstruction for 3D line disappearance algorithm of the empty cargo scenario. Reconstruction for both the full lorry and the $z$-slice where the threats are located are given. The scale gives the total fractional path length calculated for each voxel.*

## 5.4 Results for Cargo Container Housing 5 Shielded Threats using Muon Disappearance and Muon Scattering Tomography

Firstly, using muon scattering tomography with the new analysis algorithm, volumes assumed to be high-$Z$ materials are identified. These volumes are labelled as 'areas of interest'. Further analysis is then made using muon disappearance tomography, to confirm whether or not these materials are indeed high-$Z$ materials. Muons that have disappeared within the inspected volume are identified and passed through the muon disappearance algorithm. This in turn is used to build-up a 3D image of the inspected volume. An example of this is displayed in Fig. 5.12. Instead of inspecting the total volume with the muon disappearance algorithm, further analysis is made via taking 20 cm thick slices along the $z$-axis, centred on the 'areas of interest' identified using muon scattering tomography. All other areas built-up using the muon disappearance algorithm are ignored. Fig. 5.13 displays the voxels identified by the muon disappearance algorithm along the slices taken. From Fig 5.13, all five 'areas of interest' that are attributed to the shielded threat materials are reconstructed. The volumes identified from muon scattering tomography that represented the false positives have not been reconstructed. The additional voxels reconstructed, shown within the blue circles of Fig. 5.13, represent volumes that have been built up just inside the walls of the cargo container, using the muon disappearance algorithm. However, since these volumes were not identified in the muon scattering analysis, they can be ignored. For an 'area of interest' to be confirmed as possible high density material, the criterion is used that it must be identified with both muon scattering and muon disappearance techniques. In this scenario, this requirement results in the positive detection of all five-threat materials and the removal of those areas that are not due to the threat materials. Table 5.5 and Table 5.6 display the false positives that are associated with both the muon scattering and muon disappearance techniques for all resolutions. As it can be seen, when using muon disappearance, no false positives identified using muon scattering tomography are reconstructed. This displays the advantage of using muon disappearance in conjunction with muon scattering tomography in being able to correctly ascertain which volumes reconstructed using muon scattering tomography, represent high-$Z$ materials and which volumes are false positives. This therefore has the advantage over techniques that rely on solely one of these methods.

Table 5.5 Location, reconstruction parameters and average scattering angle observed for each false positive identified for muon scattering tomography of the empty cargo scenario.

| Resolution | $R$ | $V$ | $M$ | $x$ (m) | $y$ (m) | $z$ (m) | Avg Scatter (Deg) |
|---|---|---|---|---|---|---|---|
| Perfect | 3 | 18 | 1.3 | -3 | 0.95 | 0 | $3.12 \pm 0.22$ |
| Perfect | 3 | 17 | 1.3 | -3 | -1.15 | 0 | $3.19 \pm 0.19$ |
| 0.2 mm | 3 | 18 | 1.3 | -3 | 0.95 | 0 | $3.16 \pm 0.26$ |
| 0.2 mm | 3 | 17 | 1.3 | -3 | -1.15 | 0 | $3.28 \pm 0.22$ |
| 1 mm | 3 | 17 | 1.3 | -3 | 0.95 | 0 | $4.95 \pm 0.69$ |
| 1 mm | 3 | 17 | 1.3 | 2.8 | 1.05 | 0.3 | $3.62 \pm 0.32$ |

Table 5.6 Location, reconstruction parameters and average total fractional path length observed for each false positive identified for muon disappearance tomography of the empty cargo scenario for slices where 'areas of interest' are located.

| Resolution | $R$ | $V$ | $M$ | $x$ (m) | $y$ (m) | $z$ (m) | Avg Total Path Length |
|---|---|---|---|---|---|---|---|
| Perfect | 15 | 26 | 1.4 | 0.4 | -1.15 | 0 | $5.69 \pm 0.15$ |
| Perfect | 15 | 28 | 1.4 | 2.8 | -1.1 | 0 | $5.78 \pm 0.15$ |
| Perfect | 15 | 27 | 1.4 | 2.85 | 0.8 | 0 | $5.82 \pm 0.12$ |
| 0.2 mm | 15 | 28 | 1.4 | 2.8 | 0.8 | 0 | $5.76 \pm 0.16$ |
| 0.2 mm | 15 | 27 | 1.4 | 2.85 | 0.8 | 0 | $5.83 \pm 0.12$ |
| 1 mm | 15 | 27 | 1.4 | 2.8 | 0.8 | 0 | $5.77 \pm 0.15$ |
| 1 mm | 15 | 26 | 1.4 | 2.85 | 0.8 | 0 | $5.82 \pm 0.12$ |
| 2 mm | 15 | 26 | 1.4 | 2.8 | -1.1 | 0 | $5.79 \pm 0.16$ |
| 2 mm | 15 | 26 | 1.4 | 2.85 | 0.8 | 0 | $5.84 \pm 0.12$ |

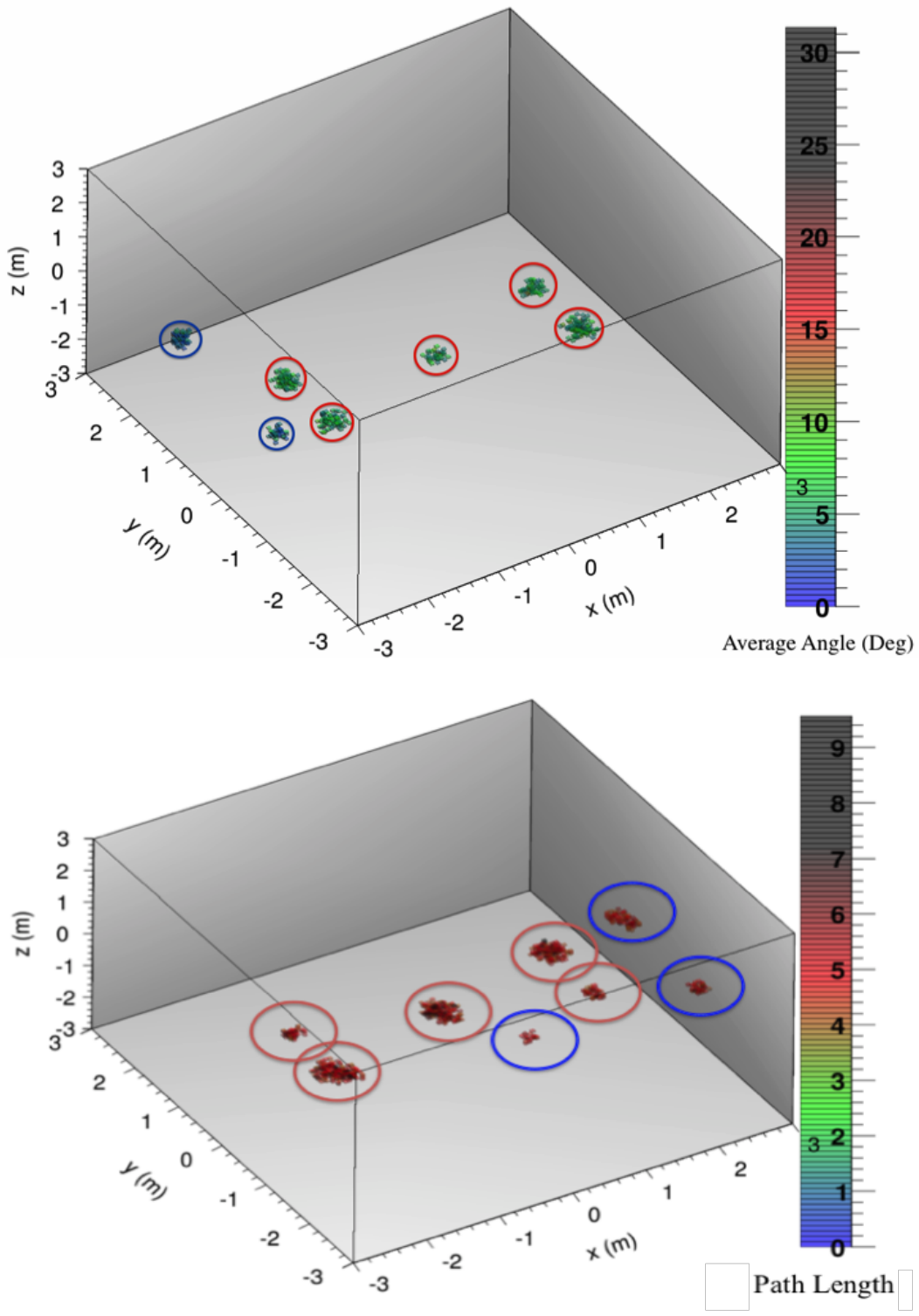


Fig. 5.13 *Top: Image reconstruction using PoCA and a density based clustering algorithm, of the empty cargo scenario to identify areas of interest. The scale gives the average scattering angle calculated per each voxel (degrees). Bottom: Image reconstruction using the 3D line disappearance algorithm for the empty cargo scenario for the areas of interest identified using the PoCA algorithm. The scale gives the total fractional path length calculated for each voxel.*

## 5.5 Summary

Results of Monte Carlo simulations for muon scattering in different types of target materials have been presented. The effectiveness of a new analysis algorithm that identifies dense clusters of voxels with high scattering angles has been demonstrated. Using this new analysis algorithm, the effect of the detector configuration and spatial resolution on detecting high-$Z$ targets in empty cargo containers has been studied. This involves different scenarios where the detector spacing and number of detector planes per set were varied. An optimum set-up of 5 detectors per set, located 25 cm apart has been established. One may have expected the optimum setup (of those tested) to be 50 cm spacings. However, only 3 detectors spaced 50 cm apart were considered. Therefore 5 detectors spaced 25 cm apart will cover the same area as 3 detectors spaced 50 cm apart. The additional two detector planes will yield a more accurate reconstruction of the muon track. The optimum setup (5 detectors spaced 25 cm apart) requires spatial resolutions of 2 mm or better to detect shielded HEU in empty cargo containers. Resolutions representative of scintillator detectors (2 cm and 3 cm), are unable to accurately detect all types of shielded HEU in empty cargo containers. Spatial resolutions of 1 cm are only capable of accurately locating HEU shielded by lead. Therefore resolutions representative of scintillator detectors (1 cm, 2 cm, 3 cm) will not be considered for realistic clutter scenarios.

The technique of muon disappearance has been applied to detecting shielded HEU in empty cargo containers. The optimum detector configuration (5 detectors planes spaced 25 cm apart) obtained with muon scattering tomography has been used. The same analysis algorithm applied to muon scattering tomography, was applied to muon disappearance tomography, in attempt to identify dense clusters of voxels with large total fractional path lengths. Although capable of detecting shielded HEU in empty cargo containers, there is also the build-up of other additional voxels due to the lorry and container itself. This makes accurate detection of shielded HEU unlikely, when solely using muon disappearance. However, since the build-up of shielded HEU does occur, it has been demonstrated that this technique can be used as a supplementary technique to muon scattering tomography to help enhance overall detection capabilities. This is done through first identifying ‘areas of interest’ using muon scattering tomography be-

fore confirming whether they are threats with the muon disappearance algorithm.

Finally, it is also possible that anyone attempting to smuggle shielded HEU may use smaller component sizes than those that have been considered here. While unable to detect smaller objects with the given parameters, these parameters can be altered given different scenarios. For detector efficiencies less than 100%, the validity of the algorithm is not compromised, but just means a larger amount of data will be required to ascertain the results given. Larger exposure times may require an increase in the amount of shielding to avoid passive detection, thus the efficiency of the muon tomography may not be compromised. While longer exposure times will work up until a point, there will eventually be a cut-off point in which the longer exposure times will no longer be able to identify smaller objects. This is due to inherent error always associated with the tracking angular resolution.

# Chapter 6

# Material Segregation using Cosmic-Ray Muons for Cargo Containers with Clutter

This chapter analyses the feasibility of using muons to correctly detect shielded HEU when placed in a cargo container, filled with different levels of clutter. Two types of clutter scenario are considered. Ones where shielded HEU is surrounded by low-$Z$ clutter and ones where shielded HEU is surrounded by medium-$Z$ clutter. The ability to detect shielded HEU in each of these scenarios is considered using muon scattering tomography, muon disappearance tomography and the two techniques in conjunction with one another. For each low-$Z$ and medium-$Z$ clutter scenario, twenty different clutter configurations have been interrogated. The ability of each muon analysis technique when applied to one of these clutter configurations is presented in detail. The analysis approach described in detail is repeated for all twenty configurations for each clutter scenario, before all the results are discussed.

Section 6.1 introduces the simulation parameters that are used in all simulations in this Chapter. A description of the clutter configuration (for both low-$Z$ and medium-$Z$ clutter) is given for the configuration that will be analysed in detail. Section 6.2 discusses the capability of muon scattering tomography with the new analysis algorithm, muon disappearance tomography with the new analysis algorithm, and using the two in conjunction with one another, to correctly detect shielded HEU in a cargo container filled with low-$Z$ clutter. Detailed analysis is given for each processing technique when applied to the configuration described in section 6.1. False positive and false negative

rates are given for all twenty configurations. Section 6.3 has the same layout as section 6.2, except shielded HEU is housed within medium-$Z$ clutter. Section 6.4 summarises the findings of the Chapter.

## 6.1 Simulation Parameters

In a realistic scenario the cargo container will be filled with some materials to be transported together with HEU or similar. Twenty different clutter configurations have been simulated for both low-$Z$ and medium-$Z$ clutter scenarios. Of these twenty configurations, sixteen contain five shielded HEU threats. The remaining four have no threat materials within them. Each of the configurations places the clutter and shielded HEU in different locations. The maximum gross mass for a 20-foot cargo container is 24,000 kilograms. Subtracting the tare mass of the container itself, the maximum amount of cargo allowed is reduced to approximately 21,600 kilograms. This mass restriction has been considered when developing the different configurations tested. The combination of clutter and hidden threat materials have been evenly distributed around the container. In general, particularly heavy items of clutter have been placed in crates at the bottom of the container and towards the centre, so that the mass remains evenly distributed throughout the whole container.

Five million muons generated over a 10 m $\times$ 10 m surface area, which correspond to a 5-minute exposure time, are transported through the inspected volume. The validity of this muon surface area size is discussed in section 3.2.4. Due to the ability to accurately detect shielded HEU in an empty cargo container for 0.2 mm, 1 mm and 2 mm spatial resolutions, simulations have been conducted for all of these resolutions as well as 0.1 mm. Simulations for 10 mm spatial resolution have not been considered since only HEU shielded with lead was identified when using this resolution in empty cargo scenarios. Gaseous detectors that cover a total size of 7 m $\times$ 4 m are used. There are five detector planes per set. Detectors are located 25 cm apart and assumed to be 100% efficient. A schematic of the set-up is displayed in Fig. 4.10. There is a distance of 4 m separating the top detector from the bottom detector. This distance is chosen as it represents the approximate height of a lorry plus cargo container. In reality muon detection efficiency may not be 100%. If this is the case then longer exposure times will be needed to observe the determined results, provided the tracking system does not have any redundancy. If longer exposure times are required, the amount of shielding

surrounding any nuclear material will need to be increased, so that detection by passive means is avoided. This will in turn make the detection of high density materials using muons more efficient, provided shielding is placed directly around the HEU.

### 6.1.1 Description of the Scenario Tested

As discussed, twenty clutter configurations have been conducted for each of different clutter type scenario. Each section will present in detail one of the configurations that has been simulated for all resolutions tested, for each of the muon analysis techniques. The analysis approach described for this one configuration, is applied to all twenty configurations conducted for each clutter scenario. For sixteen of the twenty configurations, five shielded HEU targets have been placed per configuration. The remaining four configurations (out of the twenty) have no shielded HEU placed in them. Optimum reconstruction parameters for threat identification have been calculated using the sixteen configurations that contain threat materials. As the parameters are optimised with the same configurations that will be tested, there is the propensity for the parameters to be overtrained for the clutter configurations used in this thesis. The 4 configurations where no threats are placed are extremely important as they allow the testing of these optimum parameters, as no material should be built up in these configurations. The total amount of false positives and false negatives (out of 80) for all configurations is also presented. A false positive is defined as a region of high-$Z$ material identified by the analysis algorithm where no shielded HEU was placed. A false negative is defined as the inability to reconstruct one shielded HEU target within each configuration. There can be more than one false positive or false negative per configuration. A schematic of the setup that is to be analysed in detail, is displayed in Fig. 6.1.

In order to practically train the algorithm for many more cargo configurations, the optimum parameters calculated would need to be tested on realistic containers that contain hidden threat materials, in unknown locations. This would need to be done for hundreds of cargo configurations to be able to fully refine the parameters. The focus of this Chapter is to present how the analysis algorithm that has been developed would be applied to nuclear materials detection, upon determination of suitable parameters.

Table 6.1 displays the positions and dimensions of the different items of clutter, which were placed in the cargo container in Fig. 6.1. Both low-$Z$ and medium-$Z$ clutter con-

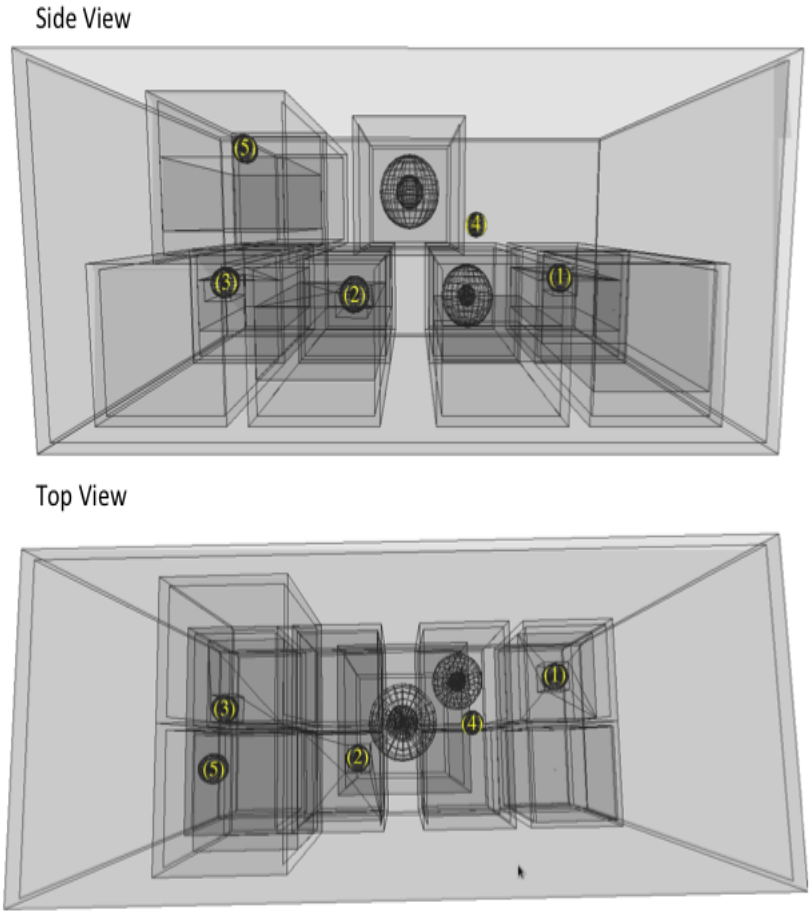


Fig. 6.1 *Schematic of side and top views of the lorry filled with clutter. Two shielded nuclear materials are located in the upper set of crates (4, 5) and three in the lower set (1, 2, 3). The crates are randomly filled with air, polystyrene, carbon, aluminium, gravel or sand for low-Z clutter scenarios. For medium-Z scenarios the crates are filled with different sized blocks of aluminium, weathering steel, stainless steel and iron.*

figurations are described. It is this clutter configuration described in Table 6.1 and Fig. 6.1 that will be analysed in detail. The clutter consists of eleven wooden crates of size 1.1 m $\times$ 1.1 m $\times$ 1.1 m placed in the cargo container. Each crate is filled with different sized blocks of either low-$Z$ or medium-$Z$ materials. For low-$Z$ clutter configurations the crates are filled with various sized blocks of aluminium, carbon, polystyrene, gravel, sand and air. For medium-$Z$ clutter configurations the crates are filled with various sized blocks of aluminium, weathering steel, stainless steel and iron. Table 6.2 displays the densities and elemental composition of all materials that have been used as clutter. The crates are at most stacked two crates high and placed in random locations. All twenty configurations simulated have this same general set-up. It is the location of shielded HEU, the location and amount of clutter and the type of clutter material that varies for each configuration. Of the twenty configurations, sixteen contain five 10 kg spheres (5 cm radius) of 20% enriched uranium (20% $^{235}$U and 80% $^{238}$U) surrounded by either lead or steel shielding placed randomly amongst the clutter. The remaining four configurations have no nuclear materials present. A description of all clutter configurations for both low-$Z$ and medium-$Z$ scenarios in given in Appendix A.

Table 6.1 Description of the different types of clutter placed within the cargo container in Fig. 6.1. Both low-$Z$ and medium-$Z$ clutter configurations are described.

| Material (low-$Z$) | Material (medium-$Z$) | Description | $x$ (m) | $y$ (m) | $z$ (m) |
|---|---|---|---|---|---|
| Aluminium | Aluminium | Solid block of dimensions 101.9 cm $\times$ 101.9 cm $\times$ 50 cm | -1.55 | -0.56 | 0.412 |
| Polyethylene | Weathering Steel | Hollow sphere of outer radius 35 cm and inner radius 16 cm | 0 | 0 | 0.512 |
| Air | Sand | Solid block of dimensions 101.9 cm $\times$ 101.9 cm $\times$ 90 cm | 2.1 | -0.56 | -0.5 |
| Sand | Aluminium | Hollow block of outer dimensions 101.9 cm $\times$ 101.9 cm $\times$ 101.9 cm and inner dimensions 33 cm $\times$ 33 cm $\times$ 33 cm | 2.1 | 0.56 | -0.608 |
| Sand | Iron | Hollow block of outer dimensions 101.9 cm $\times$ 101.9 cm $\times$ 50.5 cm and inner dimensions 33 cm $\times$ 33 cm $\times$ 33 cm | -0.8 | -0.56 | -0.608 |
| Gravel | Stainless Steel | Hollow block of outer dimensions 101.9 cm $\times$ 101.9 cm $\times$ 101.9 cm and inner dimensions 33 cm $\times$ 33 cm $\times$ 33 cm | -2.1 | 0.56 | -0.608 |
| Carbon | Aluminium | Hollow sphere of outer radius 35 cm and inner radius 12 cm | 0.8 | 0.56 | -0.608 |
| Gravel | Iron | Solid block of dimensions 101.9 cm $\times$ 101.9 cm $\times$ 25 cm | 0.8 | -0.56 | -0.608 |
| Carbon | Aluminium | Solid block of dimensions 100 cm $\times$ 100 cm $\times$ 70 cm | -0.8 | 0.56 | -0.608 |

Table 6.2 Description of densities and chemical composition of all materials that have been used as clutter in both low-$Z$ and medium-$Z$ configurations.

| Material | Density (g cm$^{-3}$) | Chemical Composition |
|---|---|---|
| Polyethylene | 0.94 | 100% $C_2H_4$ |
| Carbon | 2.26 | 100% C |
| Sand | 1.60 | 100% $SiO_2$ |
| Concrete | 2.20 | 16% $H_2O$, 6% Air, 11% Portland Cement, 41% Gravel, 26% Sand |
| Gravel | 1.52 | 46.6% O, 27.72% $Si_2$, 9.13% Al, 5.41% Fe, 3.63% Ca, 2.83% Na, 2.59% K, 2.09% Mg |
| Aluminium | 2.70 | 100% Al |
| Weathering Steel | 7.85 | 96.965% Fe, 0.875% Cr, 0.65% Ni, 0.5% Si, 0.4% Cu, 0.35% Mn, 0.12% C, 0.11% P, 0.03% S |
| Stainless Steel | 8.03 | 66.595% Fe, 20.0% Cr, 10.5% Ni, 2% Mn, 0.75% Si, 0.08% C, 0.045% P, 0.03% S |
| Iron | 7.87 | 100% Fe |

## 6.2 Shielded HEU Placed within Low-$Z$ Clutter

### 6.2.1 Results using Muon Scattering Tomography

#### Analysis for a Single Configuration

Using muon scattering tomography with the analysis algorithm presented in section 5.2.2, the capability to detect 20% enriched uranium shielded by either steel or lead in realistic low-$Z$ clutter scenarios for multiple detector resolutions has been studied. Optimum parameters for the detection of shielded HEU in these configurations have been calculated for perfect resolution. These parameters are given in Table 5.1. Fig. 6.2 shows the capability of muon scattering tomography, when applying these parameters to accurately locate shielded HEU for the configuration displayed in Fig. 6.1. The position of each of the threat materials, along with the average scattering angle per voxel is given in Table 6.3.

The ability to identify dense clusters of voxels that represent shielded HEU is apparent. Since the parameters given in Table 5.1 were defined to give optimum detection capabilities under perfect resolution, all shielded threat materials are clearly identified for perfect resolution. This demonstrates the success of muon scattering tomography, to identify dense clusters of voxels with high average scattering angles that represent shielded HEU. Table 6.4 lists the false positives and false negatives observed in Fig. 6.2. As spatial resolution decreases, there is an occurrence of a false negative for all spatial resolutions representative of gaseous detectors (0.1 mm, 0.2 mm, 1 mm, 2 mm). This false negative represents HEU shielded by steel and is located within the $3^{rd}$ section of the inspected cargo at position (2.1 m, 0.56 m, -0.408 m). The build-up of this false negative represents a concern of the analysis algorithm in being able to correctly detect shielded HEU with the given parameters that have been calculated for perfect

resolution.

The false negative is caused by the number of voxels ($V$) above the plane average (times 1.3), being less than the amount required for detection to be made. Table 6.3 displays the average scattering angle per voxel observed for each of the threat materials, the average scattering angle observed in the plane where each threat is located and the reconstructed ratio for each of the threat materials. The reconstructed ratio is defined as the total number of muons that have interacted with the target and been correctly reconstructed where the target is located, divided by the total amount of muons that have interacted with the target and are available for reconstruction. It can be seen that the average scattering angle per voxel observed in the false negative, is lower than other threat materials located within the same section. A lower average scattering angle per voxel will mean fewer voxels are greater than the minimum required by Table 5.1, to be considered as a threat material.

Furthermore, as resolution decreases the accurate reconstruction of a muon track also decreases. This causes muon scattering points, which should be located in volumes where threat materials are located, to be located in other volumes. The reconstructed ratio gives a numerical value to this feature. It can be seen that the reconstructed ratio for this threat material (F.N.1), is systematically lower than the other threat materials located within the same section. A smaller reconstructed ratio means fewer muons that have interacted with a threat material, have their muon scattering point located in the volume where the threat is located. This in turn may cause the number of voxels ($V$) that meet the criteria for detection to be made, to be lower than that required in Table 5.1. The low reconstructed ratio observed for this threat may be due to two reasons. Firstly, a block of sand has been placed around the threat. Muons that interact with the threat will also pass through this large item of clutter. This clutter causes the muon to undergo large additional scattering, which results in the muon scattering point being located outside the volume where the threat is located. Secondly this threat is located towards the front of the cargo container. Outside the front of the container is the engine and battery of the lorry, which are effectively large blocks of iron and lead. Therefore some muons that are scattered by the threat material may also be scattered by the engine or battery, thus reducing the accuracy of the muon scattering point.

Table 6.3 Position, average scattering angle per voxel and reconstructed ratio for each of the threats materials. Also given is the average scatter per voxel of the plane the threat material is located within.

| Resolution | $x$ (m) | $y$ (m) | $z$ (m) | Muons Detected | Muons Correctly Reconstructed | Average Scattering Angle of Threat (degrees) | Average Scattering Angle of Plane (degrees) | Reconstructed Ratio |
|---|---|---|---|---|---|---|---|---|
| Perfect | 2.1 | 0.56 | -0.408 | 3820 | 592 | $2.66 \pm 0.23$ | $2.12 \pm 0.01$ | 0.155 |
| Perfect | -0.6 | -0.36 | -0.408 | 4213 | 707 | $2.82 \pm 0.26$ | $2.12 \pm 0.01$ | 0.168 |
| Perfect | -2.4 | 0.26 | -0.408 | 3699 | 598 | $2.71 \pm 0.27$ | $2.12 \pm 0.01$ | 0.162 |
| Perfect | -1.75 | -0.36 | 0.85 | 2325 | 208 | $3.35 \pm 0.34$ | $1.45 \pm 0.01$ | 0.089 |
| Perfect | 0.8 | 0 | 0.2 | 2483 | 273 | $3.37 \pm 0.28$ | $1.70 \pm 0.01$ | 0.110 |
| 0.1 mm | 2.1 | 0.56 | -0.408 | 3820 | 565 | $2.67 \pm 0.24$ | $2.13 \pm 0.01$ | 0.148 |
| 0.1 mm | -0.6 | -0.36 | -0.408 | 4213 | 724 | $2.79 \pm 0.30$ | $2.13 \pm 0.01$ | 0.172 |
| 0.1 mm | -2.4 | 0.26 | -0.408 | 3699 | 598 | $2.74 \pm 0.26$ | $2.13 \pm 0.01$ | 0.162 |
| 0.1 mm | -1.75 | -0.36 | 0.85 | 2325 | 210 | $3.21 \pm 0.40$ | $1.46 \pm 0.01$ | 0.090 |
| 0.1 mm | 0.8 | 0 | 0.2 | 2483 | 283 | $3.29 \pm 0.30$ | $1.70 \pm 0.01$ | 0.112 |
| 0.2 mm | 2.1 | 0.56 | -0.408 | 3820 | 571 | $2.67 \pm 0.25$ | $2.13 \pm 0.01$ | 0.149 |
| 0.2 mm | -0.6 | -0.36 | -0.408 | 4213 | 709 | $2.82 \pm 0.27$ | $2.13 \pm 0.01$ | 0.168 |
| 0.2 mm | -2.4 | 0.26 | -0.408 | 3699 | 586 | $2.79 \pm 0.31$ | $2.13 \pm 0.01$ | 0.158 |
| 0.2 mm | -1.75 | -0.36 | 0.85 | 2325 | 219 | $3.23 \pm 0.41$ | $1.49 \pm 0.01$ | 0.094 |
| 0.2 mm | 0.8 | 0 | 0.2 | 2483 | 277 | $3.23 \pm 0.29$ | $1.71 \pm 0.01$ | 0.112 |
| 1 mm | 2.1 | 0.56 | -0.408 | 3820 | 516 | $2.82 \pm 0.31$ | $2.27 \pm 0.01$ | 0.135 |
| 1 mm | -0.6 | -0.36 | -0.408 | 4213 | 687 | $2.98 \pm 0.26$ | $2.27 \pm 0.01$ | 0.163 |
| 1 mm | -2.4 | 0.26 | -0.408 | 3699 | 542 | $2.97 \pm 0.38$ | $2.27 \pm 0.01$ | 0.147 |
| 1 mm | -1.75 | -0.36 | 0.85 | 2325 | 195 | $3.46 \pm 0.42$ | $1.63 \pm 0.01$ | 0.084 |
| 1 mm | 0.8 | 0 | 0.2 | 2483 | 251 | $3.63 \pm 0.33$ | $1.80 \pm 0.01$ | 0.101 |
| 2 mm | 2.1 | 0.56 | -0.408 | 3820 | 474 | $3.02 \pm 0.31$ | $2.43 \pm 0.01$ | 0.124 |
| 2 mm | -0.6 | -0.36 | -0.408 | 4213 | 614 | $3.24 \pm 0.24$ | $2.43 \pm 0.01$ | 0.146 |
| 2 mm | -2.4 | 0.26 | -0.408 | 3699 | 482 | $3.19 \pm 0.37$ | $2.43 \pm 0.01$ | 0.130 |
| 2 mm | -1.75 | -0.36 | 0.85 | 2325 | 192 | $3.69 \pm 0.38$ | $1.75 \pm 0.01$ | 0.082 |
| 2 mm | 0.8 | 0 | 0.2 | 2483 | 235 | $3.92 \pm 0.29$ | $1.90 \pm 0.01$ | 0.095 |

Table 6.4 False positives and false negatives observed for the different resolutions using parameters determined for perfect resolution.

| Type | Figure I.D | Resolution | Section | $R$ | $V$ | $M$ | Avg Scatter (degrees) | $x$ (m) | $y$ (m) | $z$ (m) | Cause |
|---|---|---|---|---|---|---|---|---|---|---|---|
| False Positive | F.P.1 | Perfect | 2 | 3 | 20 | 1.3 | $3.56 \pm 0.17$ | -1.55 | -0.56 | 0.412 | Block of Aluminium of dimensions 101.9 $\times$ 101.9 $\times$ 50 cm |
| False Positive | F.P.1 | 0.1 mm | 2 | 3 | 19 | 1.3 | $3.36 \pm 0.08$ | -1.55 | -0.56 | 0.412 | Block of Aluminium of dimensions 101.9 $\times$ 101.9 $\times$ 50 cm |
| False Positive | F.P.1 | 0.2 mm | 2 | 3 | 17 | 1.3 | $3.58 \pm 0.14$ | -1.55 | -0.56 | 0.412 | Block of Aluminium of dimensions 101.9 $\times$ 101.9 $\times$ 50 cm |
| False Positive | F.P.1 | 1 mm | 2 | 3 | 17 | 1.3 | $3.65 \pm 0.21$ | -1.55 | -0.56 | 0.412 | Block of Aluminium of dimensions 101.9 $\times$ 101.9 $\times$ 50 cm |
| False Positive | F.P.1 | 2 mm | 2 | 3 | 17 | 1.3 | $4.65 \pm 0.20$ | -1.55 | -0.56 | 0.412 | Block of Aluminium of dimensions 101.9 $\times$ 101.9 $\times$ 50 cm |
| All other false positives for all resolutions (F.P.2 - F.P.3) are volumes that have been built up just inside where the cargo container walls are located. | | | | | | | | | | | |
| False Negative | F.N.1 | 0.1 mm | 3 | 3 | 18 | 1.3 | $2.67 \pm 0.24$ | 2.1 | 0.56 | -0.408 | Not identified with the analysis algorithm |
| False Negative | F.N.1 | 0.2 mm | 3 | 3 | 18 | 1.3 | $2.67 \pm 0.25$ | 2.1 | 0.56 | -0.408 | Not identified with the analysis algorithm |
| False Negative | F.N.1 | 1 mm | 3 | 3 | 16 | 1.3 | $2.82 \pm 0.31$ | 2.1 | 0.56 | -0.408 | Not identified with the analysis algorithm |
| False Negative | F.N.1 | 2 mm | 3 | 3 | 15 | 1.3 | $3.02 \pm 0.31$ | 2.1 | 0.56 | -0.408 | Not identified with the analysis algorithm |

In addition to a false negative, a number of false positives are also observed for the different resolutions. These false positives are listed in Table 6.4. For perfect resolution, there is the detection of two false positives. F.P.1 represents the misclassification of a block of aluminium of size 101.9 cm $\times$ 101.9 cm $\times$ 50 cm and position -1.55 m, -0.56 m, 0.412 m as high-$Z$ material. This false positive has been observed for all resolutions and represents a limitation of muon scattering tomography to correctly differentiate shielded HEU from blocks of aluminium. As discussed previously, one way to counteract this is to consider the scattering width per unit length. In addition to the block of aluminium, for perfect and 0.1 mm spatial resolutions there is also the build up of false positives (F.P.2 and F.P.3) located just inside where cargo walls are located. These false positives are due to muons that have scattered within the cargo container walls. As resolution decreases, these false positives disappear. This is for the same reasons why a false negative is observed, whereby as resolution becomes poorer so does the accurate reconstruction of a muon track. Consequently fewer reconstructed muon scatter points will be accurately reconstructed, meaning the required criteria for a set of 64 voxels to be classified as high-$Z$ material will not be met.

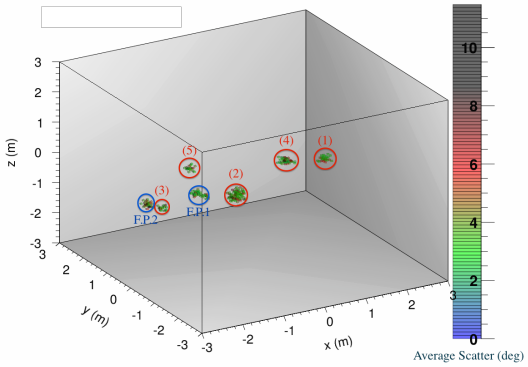


(a) *Perfect spatial resolution.*

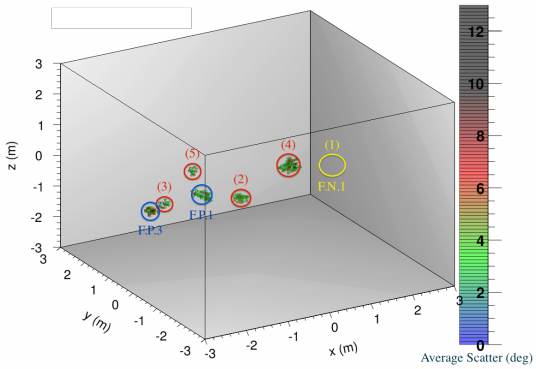


(b) *0.1 mm spatial resolution.*

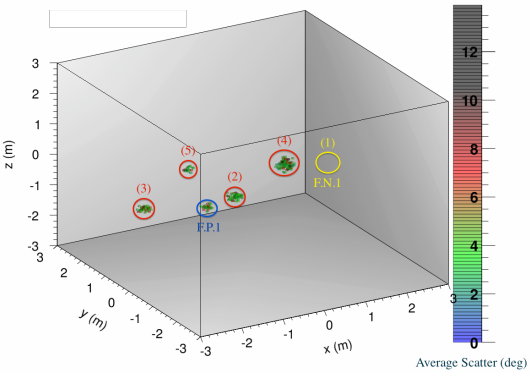


(c) *0.2 mm spatial resolution.*

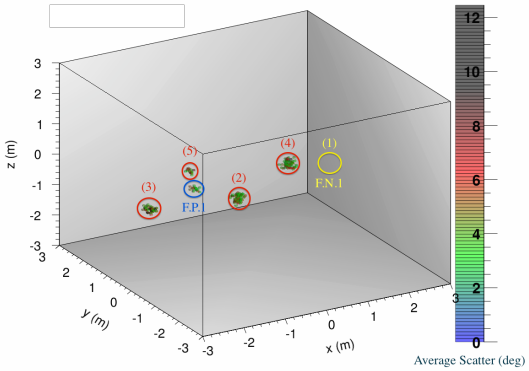


(d) *1 mm spatial resolution.*

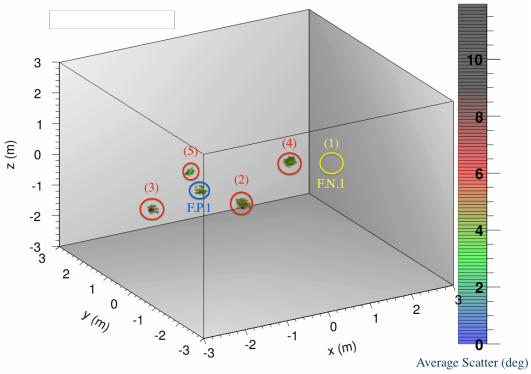


(e) *2 mm spatial resolution.*

Fig. 6.2 *Image reconstruction of Fig. 6.1 when using muon scattering tomography, for the low-Z clutter configuration. Displayed are perfect resolution (a), 0.1 mm resolution (b), 0.2 mm resolution (c), 1 mm resolution (d) and 2 mm resolution (e). Red circles represent shielded HEU that have been identified. Blue circles represent false positives attributed to the clutter or cargo. Yellow circles represent volumes where shielded HEU was located, but not identified. All volumes identified have been numbered.*

### Analysis for all Twenty Configurations

The analysis approach described for the single configuration with muon scattering tomography, has been applied to the other fifteen configurations for shielded HEU contained within low-$Z$ clutter and four configurations with just low-$Z$ clutter. Similar to Table 6.3, Appendix B gives an example table of data for one of these twenty configurations. These tables show the position, average scattering angle per voxel and reconstructed ratio for each of the threats materials. Also given is the average scatter per voxel of the plane the threat material is located within. Table 6.5 describes the total amount of false positives (f.pos) and false negatives (f.neg) observed for all configurations with different resolutions, when applying the set of parameters given in Table 5.1. At maximum there are 5 false negatives per configuration. For some configurations more than one false positive or false negative has been observed. Since four of the configurations out of each twenty had no threat materials located within them, total false positive rates are taken from all twenty configurations conducted, whereas false negatives rates are taken from sixteen configurations conducted. The percentage of configurations observed to have a false positive or false negative is also given.

As resolution worsens the number of false positives decreases. This is expected, as when resolution becomes poorer so does the accurate reconstruction of a muon track. Consequently fewer muon scattering points will be correctly reconstructed. For 0.1 mm and 0.2 mm spatial resolutions the false positive rate is particularly high (35% of configurations reconstruct a false positive). However, the majority (7 out of 9) of these false positives are caused by the presence of large blocks of aluminium. Therefore if a secondary process can be introduced that accounts for these blocks, the false positive rate will drop significantly. Despite this the analysis algorithm has shown to be efficient in removing volumes that are attributed to other low-$Z$ materials (carbon, sand, gravel, concrete etc).

### Detection Rates when Altering Parameters for only Detecting HEU Shielded with Lead

As resolution worsens the number of false negatives increases. From the results it would appear that when applying optimum parameters calculated for perfect resolution to all resolutions, the false negative rate becomes too high to be reasonable. This is

Table 6.5 False positive and false negative rates for the detection of shielded HEU in cargo containing low-$Z$ clutter, with different resolutions, using parameters given in Table 5.1. There are twenty different configurations. Sixteen of the twenty contain 5 shielded HEU threats. The remaining four have no shielded HEU placed within them.

| Resolution | Total f.pos | % of configurations with f.pos | Total f.neg | % of configurations with f.neg |
|---|---|---|---|---|
| Perfect | 8 | 35% | 1/80 | 6.25% |
| 0.1 mm | 9 | 35% | 5/80 | 31.5% |
| 0.2 mm | 9 | 35% | 5/80 | 31.5% |
| 1.0 mm | 8 | 35% | 11/80 | 50% |
| 2.0 mm | 2 | 10% | 16/80 | 75% |

expected since fewer muon tracks are accurately reconstructed and therefore materials can be missed (same reasons as the false positives). However, all false negatives are HEU shielded by steel. As discussed previously, the reconstruction parameters have been calculated as the minimum conditions needed to detect all threat materials with the lowest false positive rate for perfect resolution. The main driver of these parameters is the detection of HEU when shielded by steel. Therefore an interesting case can be made. If we alter the optimum parameters so that we only attempt to detect HEU shielded by lead, then the optimum parameters given in Table 6.6 can be determined. Table 6.7 demonstrates the false positive and false negative rates for the different resolutions when using parameters optimised to only detect HEU shielded by lead.

Table 6.6 Optimum reconstruction parameters altered to detect only shielded HEU shielded by lead.

| Section | $R$ | $V$ | $M$ |
|---|---|---|---|
| 1 | 3 | 16 / 64 | 1.5 |
| 2 | 3 | 20 / 64 | 1.3 |
| 3 | 3 | 29 / 64 | 1.3 |
| 4 | 4 | 21 / 64 | 1.5 |

The main change in the reconstruction parameters is the increase in the number of voxels, $V$, which the threat needs to occupy. Due to the higher threshold of the number of

Table 6.7 False positive and false negative rates for the different resolutions when using parameters optimised to only detect HEU shielded by lead.

| Resolution | Total f.pos | % of configurations with f.pos | Total f.neg | % of configurations with f.neg |
|---|---|---|---|---|
| Perfect | 3 | 15% | 0 | 0% |
| 0.1 mm | 0 | 0% | 0 | 0% |
| 0.2 mm | 1 | 5% | 0 | 0% |
| 1 mm | 1 | 5% | 3 | 18.75% |
| 2 mm | 0 | 0% | 3 | 18.75% |

voxels required with a greater mean scattering angle then that of the plane, the number of false positives is significantly reduced. Only resolutions of the order of 1-2 mm result in an elevated false negative rate.

### Detection Rates when Tuning the Detection Parameters for each Resolution

As stated previously the parameters used for reconstruction have been optimised assuming a perfect resolution. Due to increasing false negative rates as the resolution worsens, the analysis parameters have been tuned for each resolution. After analysing the results gathered for each different resolution when applying perfect conditions, new conditions have been calculated for each resolution that detect all nuclear materials with the lowest false positive rate. Table 6.8 show the new conditions calculated. Table 6.9 gives the false positive and false negative rates observed, when applying these new parameters.

Table 6.8 New conditions optimised for each resolution to be applied to the systems where shielded HEU is placed in a cargo container with low-$Z$ clutter.

| Resolution | Section 1 | | | Section 2 | | | Section 3 | | | Section 4 | | |
|---|---|---|---|---|---|---|---|---|---|---|---|---|
| | $R$ | $V$ | $M$ | $R$ | $V$ | $M$ | $R$ | $V$ | $M$ | $R$ | $V$ | $M$ |
| Perfect | 3 | 16 | 1.5 | 3 | 17 | 1.3 | 3 | 22 | 1.3 | 4 | 16 | 1.5 |
| 0.1 mm | 3 | 16 | 1.5 | 3 | 16 | 1.3 | 3 | 22 | 1.3 | 4 | 15 | 1.5 |
| 0.2 mm | 3 | 16 | 1.5 | 3 | 15 | 1.3 | 3 | 22 | 1.3 | 4 | 15 | 1.5 |
| 1 mm | 3 | 16 | 1.5 | 3 | 14 | 1.3 | 3 | 22 | 1.3 | 4 | 14 | 1.5 |
| 2 mm | 3 | 14 | 1.5 | 3 | 12 | 1.3 | 3 | 22 | 1.3 | 4 | 13 | 1.5 |

Table 6.9 False positive and false negative rates for the different resolutions using new parameters described in Table 6.8.

| Resolution | Total f.pos | % of configurations with f.pos | Total f.neg | % of configurations with f.neg |
|---|---|---|---|---|
| Perfect | 8 | 35% | 1/80 | 6.25% |
| 0.1 mm | 11 | 45% | 1/80 | 6.25% |
| 0.2 mm | 11 | 45% | 1/80 | 6.25% |
| 1 mm | 13 | 55% | 2/80 | 12.5% |
| 2 mm | 13 | 55% | 2/80 | 12.5% |

Upon changing the parameters the false negative rate becomes lower but the false positive rate increases. Since the parameters for threat detection have been lowered, more false positives will be observed, as more will be above the detection threshold. Table 6.10 shows the false negatives produced for each of the different configurations, along with the cause of each particular false negative.

Table 6.10 False negatives produced for each of the different configurations, along with the cause of each particular false negative. All represent HEU shielded by steel.

| Resolution | Configuration Number | Section | $R$ | $V$ | M | $x$ (m) | $y$ (m) | $z$ (m) | Cause |
|---|---|---|---|---|---|---|---|---|---|
| Perfect | 16 | 3 | 3 | 18 | 1.3 | -2.40 | 0.26 | -0.41 | 2 |
| 0.1 mm | 15 | 3 | 3 | 18 | 1.3 | 2.10 | 0.56 | -0.41 | 1 |
| 0.2 mm | 15 | 3 | 3 | 18 | 1.3 | 2.10 | 0.56 | -0.41 | 1 |
| 1mm | 15 | 3 | 3 | 18 | 1.3 | 2.10 | 0.56 | -0.41 | 1 |
| 1mm | 16 | 3 | 3 | 18 | 1.3 | -2.40 | 0.26 | -0.41 | 2 |
| 2 mm | 15 | 3 | 3 | 18 | 1.3 | 2.10 | 0.56 | -0.41 | 1 |
| 2 mm | 16 | 3 | 3 | 18 | 1.3 | -2.40 | 0.26 | -0.41 | 2 |

1. The cause of the false negative in configuration 15 is due to surrounding the threat with a block of sand 80 cm thick plus location towards front of lorry.
2. The cause of the false negative in configuration 16 is because it has a block of 101.9 cm x 101.9 cm x 80 cm concrete directly below it.

All of the false negatives are located within the $3^{rd}$ section. For each resolution, when altering the parameters to decrease the number of false negatives, the parameters used in reconstructing the $3^{rd}$ section were not altered. A reduction of the parameters to the lowest point in which these nuclear materials could be correctly reconstructed, results

in an extremely large buildup of false positives in that section.

As shown in Table 6.10 there are a total of seven false negatives for the different resolutions, all located in the $3^{rd}$ section. These false negatives occur in two different configurations. The false negative that is found in configuration number 15 (Table 6.10, rows 2, 3, 4 and 6) can be explained by the location of the clutter surrounding it. Muons that pass through the threat also pass through the block of 80 cm thick sand surrounding it. When a muon is in the lower sections of the cargo it will have a lower momentum due to previous interactions with other materials and therefore the degree of scatter caused by any subsequent materials will be greater than if the muon had encountered the same material higher up. Since the PoCA algorithm assumes scattering to have occurred at a single point, the muon track is more likely to be reconstructed below the threat material. The second reason for this threat to be less likely reconstructed is due to its position towards the front of the cargo. In addition to passing through the cargo and subsequent clutter, muons that pass through threats located towards the front of the lorry may also pass through the engine compartment of the lorry, that in addition to other things holds the engine (made from predominantly iron) and the battery (made from predominantly lead). These higher density materials can cause any muons that pass through them to undergo large deflections. The false negative found within configuration number 16 (Table 6.10, rows 1, 5 and 7) has a block of concrete 80 cm thick for any muons that pass through the target to also pass through. The threats have been not correctly reconstructed for the same first reason as discussed above.

The location of the false positives varies evenly within the different sections and positions in the cargo; therefore little conclusion can be made upon the dependence of reconstruction of these materials, upon its location within the cargo. As for results with previous parameters, it appears that the majority of false positives are a result of large blocks of aluminium. Table 6.11 shows the false positive rate if those false positives caused by large blocks of aluminium are excluded.

Table 6.11 False positive and false negative rates for the different resolutions using new parameters described in Table 6.8, if we assume blocks of aluminium have been excluded.

| Resolution | Total f.pos | % of configurations with f.pos | Total f.neg | % of configurations with f.neg |
|---|---|---|---|---|
| Perfect | 2 | 5% | 1/80 | 6.25% |
| 0.1 mm | 2 | 5% | 1/80 | 6.25% |
| 0.2 mm | 2 | 5% | 1/80 | 6.25% |
| 1.0 mm | 1 | 5% | 2/80 | 12.5% |
| 2.0 mm | 1 | 5% | 2/80 | 12.5% |

### 6.2.2 Discussion of the Muon Disappearance Algorithm

The capability of muon disappearance tomography to correctly detect shielded HEU amongst low-$Z$ clutter scenarios (given in Fig. 6.1) is discussed. Optimum parameters calculated for the detection of shielded HEU with the lowest false positive build-up have been used. These parameters are given in Table 5.4 and have been calculated as the same for each resolution tested. Fig 6.3 displays dense clusters of voxels that have been extracted when using this technique for perfect resolution. It is clear that when solely using this technique, no shielded HEU can be clearly distinguished from the background clutter. This is due to other muons that have disappeared in the clutter and the cargo container itself. As with the empty lorry scenarios, all shielded HEU have been reconstructed, but they are masked due to additional voxel build-up. Similar results are observed for all other resolutions tested, whereby shielded HEU is identified, but unable to be distinguished from the additional voxels that are built up from muons that have disappeared in the lorry and clutter. Due to the nature of the algorithm, multiple voxels above and below the threats have also been reconstructed. This further indicates the issues the muon disappearance algorithm has with vertical clutter systems. These limitations demonstrate why the muon disappearance algorithm should only be used as a secondary technique to help enhance muon scattering tomography.

The same results have been observed in all of the twenty configurations conducted, whereby all shielded HEU is indistinguishable from background clutter. For those configurations that have no shielded HEU present, there is the build-up of multiple voxels due to clutter, when using the parameters given in Table 5.4. This further confirms the inability of the muon disappearance algorithm to clearly detect shielded HEU with

a low false positive rate. Thus techniques involving solely the muon disappearance algorithm in medium-$Z$ clutter scenarios have not been considered.

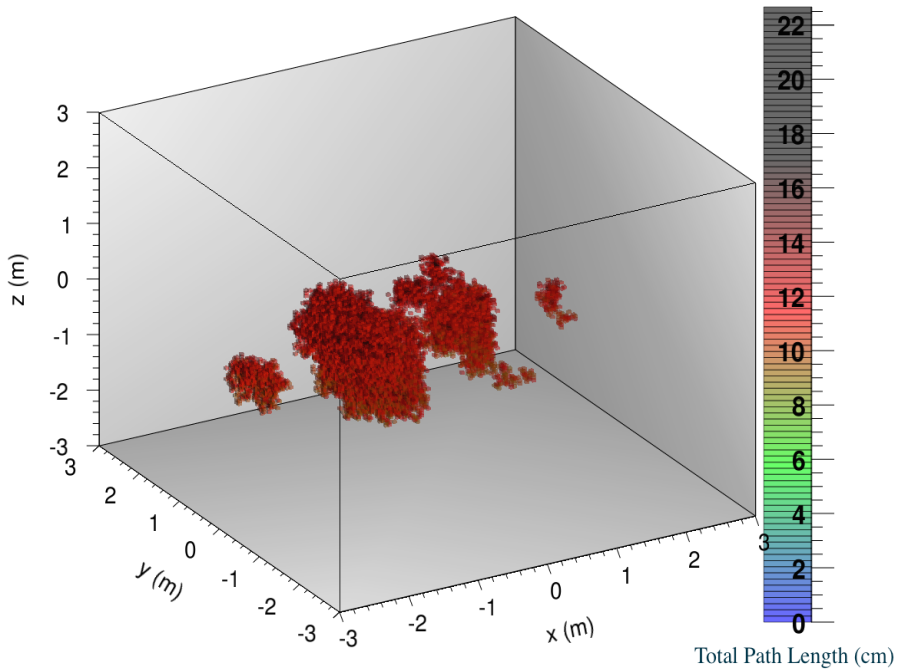


Fig. 6.3 *Image reconstruction of Fig. 6.1 using the muon disappearance tomography with the analysis algorithm (discussed in section 5.3) for low-Z clutter scenario. Displayed are all voxels identified assuming perfect detector resolution.*

### 6.2.3 Results using Muon Scattering and Muon Disappearance Tomography

#### Analysis for a Single Configuration

The capability of using the muon disappearance algorithm in conjunction with muon scattering tomography, to enhance overall detection capabilities is discussed. The premise of this technique is that muon scattering tomography is used to identify 'areas of interest', which may or may not represent shielded HEU. Upon identification of these 'areas of interest', the muon disappearance algorithm is then used to confirm whether they are indeed high-$Z$ materials. The criterion is made that for a reconstructed volume to

be confirmed as high-$Z$ material, it must be determined as such by both muon scattering tomography and muon disappearance tomography. Optimum parameters for the detection of shielded HEU, with the lowest false positive rate for muon disappearance tomography, are given in Table 5.4. Fig. 6.4 displays the volumes identified as 'areas of interest' by muon scattering tomography for the low-$Z$ clutter scenario given in Fig. 6.1, for perfect resolution. Fig. 6.4 also displays the volumes identified using just muon disappearance tomography when analysing the $z$-slices where areas of interest were located with muon scattering tomography. Table 6.12 displays the average total path length of each of the threats identified with muon scattering tomography and confirmed as such using muon disappearance tomography.

Table 6.12 Position and average total path length per voxel of each of the threats materials identified by applying muon disappearance tomography, to the 'areas of interest' obtained using the muon scattering algorithm.

| Target I.D | Resolution | $x$ (m) | $y$ (m) | $z$ (m) | Muons Disappearances (Target) | Average Total Path Length | Average Total Path Length of Plane |
|---|---|---|---|---|---|---|---|
| (1) | Perfect | 2.1 | 0.56 | -0.408 | 247 | $10.30 \pm 0.29$ | $7.09 \pm 0.02$ |
| (2) | Perfect | -0.6 | -0.36 | -0.408 | 268 | $12.75 \pm 0.36$ | $7.09 \pm 0.02$ |
| (3) | Perfect | -2.4 | 0.26 | -0.408 | 220 | $10.11 \pm 0.25$ | $7.09 \pm 0.02$ |
| (4) | Perfect | -1.75 | -0.36 | 0.85 | 119 | $13.20 \pm 0.36$ | $6.58 \pm 0.02$ |
| (5) | Perfect | 0.8 | 0 | 0.2 | 118 | $10.30 \pm 0.27$ | $7.00 \pm 0.02$ |
| (2) | 0.1 mm | -0.6 | -0.36 | -0.408 | 268 | $12.75 \pm 0.35$ | $7.09 \pm 0.02$ |
| (3) | 0.1 mm | -2.4 | 0.26 | -0.408 | 220 | $10.11 \pm 0.25$ | $7.09 \pm 0.02$ |
| (4) | 0.1 mm | -1.75 | -0.36 | 0.85 | 119 | $13.21 \pm 0.36$ | $6.59 \pm 0.02$ |
| (5) | 0.1 mm | 0.8 | 0 | 0.2 | 118 | $10.30 \pm 0.27$ | $7.00 \pm 0.02$ |
| (2) | 0.2 mm | -0.6 | -0.36 | -0.408 | 268 | $12.76 \pm 0.35$ | $7.09 \pm 0.02$ |
| (3) | 0.2 mm | -2.4 | 0.26 | -0.408 | 220 | $10.11 \pm 0.25$ | $7.09 \pm 0.02$ |
| (4) | 0.2 mm | -1.75 | -0.36 | 0.85 | 119 | $13.21 \pm 0.36$ | $6.59 \pm 0.02$ |
| (5) | 0.2 mm | 0.8 | 0 | 0.2 | 118 | $10.29 \pm 0.27$ | $7.00 \pm 0.02$ |
| (2) | 1 mm | -0.6 | -0.36 | -0.408 | 268 | $12.79 \pm 0.35$ | $7.09 \pm 0.02$ |
| (3) | 1 mm | -2.4 | 0.26 | -0.408 | 220 | $10.09 \pm 0.26$ | $7.09 \pm 0.02$ |
| (4) | 1 mm | -1.75 | -0.36 | 0.85 | 119 | $13.24 \pm 0.36$ | $6.59 \pm 0.02$ |
| (5) | 1 mm | 0.8 | 0 | 0.2 | 118 | $10.24 \pm 0.25$ | $7.00 \pm 0.02$ |
| (2) | 2 mm | -0.6 | -0.36 | -0.408 | 268 | $12.81 \pm 0.35$ | $7.09 \pm 0.02$ |
| (3) | 2 mm | -2.4 | 0.26 | -0.408 | 220 | $10.06 \pm 0.25$ | $7.09 \pm 0.02$ |
| (4) | 2 mm | -1.75 | -0.36 | 0.85 | 119 | $13.30 \pm 0.36$ | $6.58 \pm 0.02$ |
| (5) | 2 mm | 0.8 | 0 | 0.2 | 118 | $10.19 \pm 0.25$ | $7.00 \pm 0.02$ |

As it can be seen in Fig. 6.4, all areas of interest that are attributed to shielded HEU have been correctly reconstructed using the muon disappearance algorithm. This in turn confirms them as high-$Z$ materials. F.P.1 for muon scattering tomography is caused by a large block of aluminium. This false positive has has also been reconstructed when using muon disappearance tomography (F.P.3). This represents a limitation of this technique to aid in differentiating blocks of aluminium from shielded HEU. Similar to the empty clutter scenarios, the false positives reconstructed using muon scattering

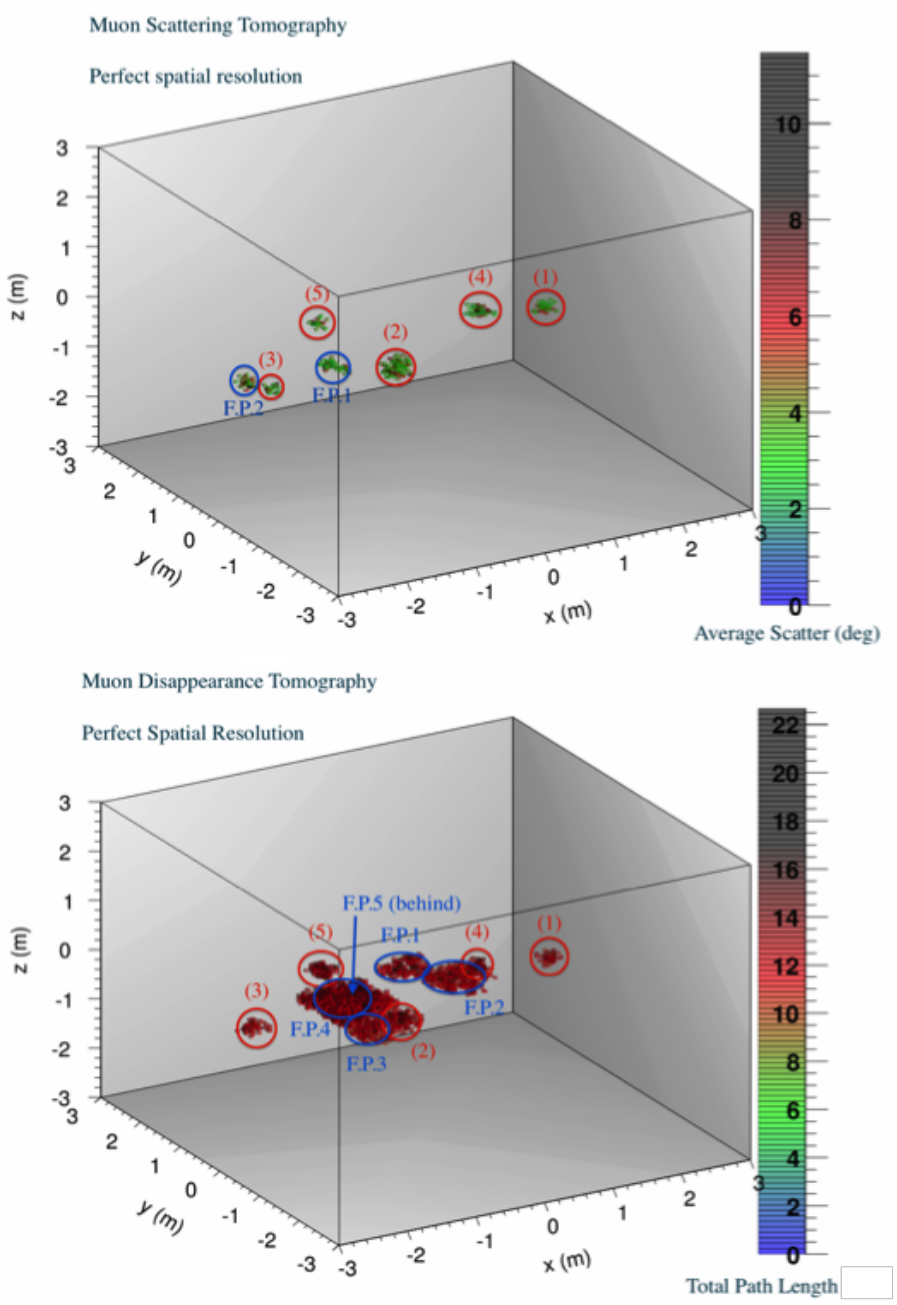


Fig. 6.4 *Image reconstruction of Fig. 6.1 using muon scattering tomography (top) and muon disappearance tomography (bottom). Displayed are all voxels identified under perfect resolution. Red circles represent shielded HEU that have been identified. Blue circles represent false positives attributed to the clutter or cargo.*

tomography (F.P.2), which are attributed to volumes just inside the walls of the cargo container, have not been reconstructed using the muon disappearance algorithm. This again reiterates the success of the muon disappearance algorithm in being able to correctly remove these volumes. The same results are observed for all resolutions whereby: all threat materials identified using muon scattering tomography are confirmed by the muon disappearance algorithm.

The false positive caused by aluminium in muon scattering tomography (F.P.1) is reconstructed for all other resolutions, for both muon scattering tomography and muon disappearance algorithm. Table 6.13 gives the average total path length observed per voxel and the minimum reconstruction parameters of this false positive for each resolution tested. There are a number of other false positives reconstructed by the muon disappearance algorithm in the $z$-planes analysed (F.P.1, F.P.2, F.P.4, F.P.5). These false positives are caused by the other blocks of clutter listed in Table 6.1. However, since they were not originally identified by muon scattering tomography, they can be ignored and assumed to be some type of clutter that has been built up.

There is the build up of a false negative for muon scattering tomography at 0.1 mm, 0.2 mm, 1 mm and 2 mm resolutions. This false negative is identified when using muon disappearance tomography. However, since this volume is not identified using muon scattering tomography it is assumed to be some erroneous clutter.

Table 6.13 List of false positives identified with the muon disappearance algorithm, that have been identified as 'areas of interest' from muon scattering tomography.

| Type | Resolution | Section | $R$ | $V$ | $M$ | Avg Total Path Length (cm) | $x$ (m) | $y$ (m) | $z$ (m) |
|---|---|---|---|---|---|---|---|---|---|
| False Positive | Perfect | 2 | 15 | 45 | 1.4 | $13.66 \pm 0.09$ | -1.55 | -0.56 | 0.412 |
| False Positive | 0.1 mm | 2 | 15 | 45 | 1.4 | $13.70 \pm 0.09$ | -1.55 | -0.56 | 0.412 |
| False Positive | 0.2 mm | 2 | 15 | 45 | 1.4 | $13.97 \pm 0.09$ | -1.55 | -0.56 | 0.412 |
| False Positive | 1 mm | 2 | 15 | 45 | 1.4 | $13.64 \pm 0.09$ | -1.55 | -0.56 | 0.412 |
| False Positive | 2 mm | 2 | 15 | 45 | 1.4 | $13.71 \pm 0.09$ | -1.55 | -0.56 | 0.412 |
| The cause of all these false positives is a block of aluminium of dimensions $101.9 \times 101.9 \times 50$ cm. | | | | | | | | | |

### Analysis for all Twenty Configurations

The analysis applied to the single configuration has also been applied to the other nineteen configurations, whereby the muon disappearance algorithm is used to analyse the 'areas of interest' identified with muon scattering tomography. Similar to Table 6.12,

Appendix C gives an example table of data for one of these twenty configurations. These tables show the position and average total path length per voxel of each of the threats materials identified by applying the muon disappearance algorithm. The primary use of the muon disappearance algorithm was to attempt to reduce the number of false positives observed with muon scattering tomography. Optimum parameters have been given in Table 5.4, which display the parameters required to detect all shielded HEU within each configuration, with the lowest false positive rate. From section 6.3, the total amount of false positives that have been observed when using muon scattering tomography with the analysis algorithm for each resolution, is given in Table 6.9. In addition to these false positives there is also the build-up of multiple false positives located just inside the walls of the cargo container. These are due to muons that have scattered within the cargo container walls. The muon disappearance algorithm has already been shown to be very efficient in removing these volumes as false positives. Therefore when considering the capability of the muon disappearance algorithm, results are only discussed for those false positives that are due to clutter. The false positives due to the walls of the cargo container, were found to be removed 100% of the time with the muon disappearance algorithm.

Table 6.14 lists all the false positives due to clutter found using muon scattering tomography, with parameters optimised for each resolution. It also displays whether these false positives are removed by the muon disappearance algorithm, and the minimum parameters that would be required for them to be removed. As it can be seen the muon disappearance algorithm is unable to remove any of the false positives observed using muon scattering tomography. Most of these false positives are caused by large blocks of aluminium and an increase in the parameters to the point where these blocks would no longer be observed, would result in multiple threat materials also being lost. This presents a limitation of muon disappearance tomography to drastically enhance muon scattering tomography techniques through removal of ‘areas of interest’ attributed to clutter within the cargo. Despite this, the removal of ‘areas of interest’ associated with the walls of the container has been found to be efficient, which demonstrates a success of this new type of algorithm.

Table 6.14 False positives observed using muon scattering tomography.

| Resolution | Configuration | Section | $R$ | $V$ | $M$ | Avg Scattering Angle (degrees) | $x$ | $y$ | $z$ | Cause | Present in Disappearance | $R$ | $V$ | $M$ | Avg Path Length |
|---|---|---|---|---|---|---|---|---|---|---|---|---|---|---|---|
| Perfect | 2 | 4 | 4 | 20 | 1.5 | $4.84 \pm 0.09$ | 2.1 | -0.56 | 0.708 | Block of aluminium size $101.9 \times 101.9 \times 50$ cm | Yes | 13 | 39 | 1.3 | $10.57 \pm 0.15$ |
| Perfect | 13 | 2 | 3 | 20 | 1.3 | $3.53 \pm 0.06$ | 0 | 0 | 0.512 | Aluminium sphere with 55 cm radius | Yes | 15 | 36 | 1.4 | $15.52 \pm 0.28$ |
| Perfect | 15 | 2 | 3 | 20 | 1.3 | $3.56 \pm 0.17$ | -1.55 | -0.56 | 0.412 | Block of aluminium size $101.9 \times 101.9 \times 50$ cm | Yes | 15 | 45 | 1.4 | $13.66 \pm 0.09$ |
| Perfect | 23 | 3 | 3 | 22 | 1.3 | $4.47 \pm 0.04$ | -0.8 | -0.26 | -0.608 | Block of gravel size $101.9 \times 101.9 \times 80$ cm | Yes | 13 | 35 | 1.3 | $13.13 \pm 0.20$ |
| Perfect | 23 | 3 | 3 | 25 | 1.3 | $5.05 \pm 0.08$ | -0.8 | 0.56 | -0.5 | Block of gravel size $101.9 \times 101.9 \times 80$ cm | Yes | 13 | 45 | 1.3 | $13.28 \pm 0.06$ |
| Perfect | 24 | 4 | 4 | 17 | 1.5 | $4.99 \pm 0.19$ | 2.1 | -0.56 | -0.608 | Block of aluminium size $101.9 \times 101.9 \times 50$ cm | Yes | 13 | 31 | 1.3 | $11.11 \pm 0.20$ |
| Perfect | 25 | 2 | 3 | 21 | 1.3 | $4.04 \pm 0.14$ | -1.55 | -0.56 | 0.412 | Block of aluminium size $101.9 \times 101.9 \times 50$ cm | Yes | 15 | 45 | 1.4 | $14.47 \pm 0.14$ |
| Perfect | 27 | 4 | 4 | 19 | 1.5 | $5.17 \pm 0.11$ | 2.1 | -0.56 | -0.608 | Block of aluminium size $101.9 \times 101.9 \times 50$ cm | Yes | 13 | 31 | 1.3 | $11.64 \pm 0.25$ |
| 0.1 mm | 2 | 4 | 4 | 20 | 1.5 | $4.79 \pm 0.11$ | 2.1 | -0.56 | 0.708 | Block of aluminium size $101.9 \times 101.9 \times 50$ cm | Yes | 13 | 39 | 1.3 | $10.48 \pm 0.17$ |
| 0.1 mm | 12 | 2 | 3 | 16 | 1.3 | $3.09 \pm 0.05$ | -1.55 | -0.56 | 0.512 | Block of aluminium size $101.9 \times 101.9 \times 50$ cm | Yes | 15 | 40 | 1.4 | $14.85 \pm 0.07$ |
| 0.1 mm | 13 | 2 | 3 | 19 | 1.3 | $3.66 \pm 0.07$ | 0 | 0 | 0.512 | Aluminium sphere with 55 cm radius | Yes | 15 | 36 | 1.4 | $15.26 \pm 0.24$ |
| 0.1 mm | 15 | 2 | 3 | 19 | 1.3 | $3.36 \pm 0.08$ | -1.55 | -0.56 | 0.412 | Block of aluminium size $101.9 \times 101.9 \times 50$ cm | Yes | 15 | 45 | 1.4 | $13.70 \pm 0.09$ |
| 0.1 mm | 19 | 2 | 3 | 16 | 1.3 | $3.47 \pm 0.06$ | 0 | 0 | 0.512 | Aluminium sphere with 55 cm radius | Yes | 15 | 39 | 1.4 | $16.67 \pm 0.26$ |
| 0.1 mm | 21 | 3 | 3 | 25 | 1.3 | $4.66 \pm 0.32$ | -2.1 | 0.56 | -0.608 | Block of aluminium size $101.9 \times 101.9 \times 50$ cm | Yes | 13 | 45 | 1.3 | $12.02 \pm 0.05$ |
| 0.1 mm | 23 | 2 | 3 | 17 | 1.3 | $3.78 \pm 0.08$ | 0 | 0 | 0.512 | Aluminium sphere with 55 cm radius | Yes | 15 | 45 | 1.4 | $14.18 \pm 0.22$ |
| 0.1 mm | 23 | 3 | 3 | 22 | 1.3 | $4.51 \pm 0.06$ | -0.8 | -0.26 | -0.608 | Block of gravel $101.9 \times 101.9 \times 80$ cm | Yes | 13 | 35 | 1.3 | $13.06 \pm 0.19$ |
| 0.1 mm | 23 | 3 | 3 | 25 | 1.3 | $5.04 \pm 0.08$ | -0.8 | 0.56 | -0.5 | Block of gravel $101.9 \times 101.9 \times 80$ cm | Yes | 13 | 45 | 1.3 | $13.28 \pm 0.06$ |
| 0.1 mm | 25 | 2 | 3 | 18 | 1.3 | $3.67 \pm 0.19$ | -1.55 | -0.56 | 0.412 | Block of aluminium size $101.9 \times 101.9 \times 50$ cm | Yes | 15 | 45 | 1.4 | $14.48 \pm 0.14$ |
| 0.1 mm | 27 | 4 | 4 | 16 | 1.5 | $5.39 \pm 0.14$ | 2.1 | -0.56 | -0.608 | Block of aluminium size $101.9 \times 101.9 \times 50$ cm | Yes | 13 | 31 | 1.3 | $11.63 \pm 0.25$ |
| 0.2 mm | 2 | 4 | 4 | 18 | 1.5 | $4.57 \pm 0.10$ | 2.1 | -0.56 | 0.708 | Block of aluminium size $101.9 \times 101.9 \times 50$ cm | Yes | 13 | 39 | 1.3 | $10.46 \pm 0.15$ |
| 0.2 mm | 12 | 2 | 3 | 16 | 1.3 | $3.22 \pm 0.13$ | -1.55 | -0.56 | 0.512 | Block of aluminium size $101.9 \times 101.9 \times 50$ cm | Yes | 15 | 40 | 1.4 | $14.86 \pm 0.07$ |
| 0.2 mm | 13 | 2 | 3 | 20 | 1.3 | $3.86 \pm 0.09$ | 0 | 0 | 0.512 | Aluminium sphere with 55 cm radius | Yes | 15 | 36 | 1.4 | $15.53 \pm 0.28$ |
| 0.2 mm | 15 | 2 | 3 | 17 | 1.3 | $3.58 \pm 0.14$ | -1.55 | -0.56 | 0.412 | Block of aluminium size $101.9 \times 101.9 \times 50$ cm | Yes | 15 | 45 | 1.4 | $13.97 \pm 0.09$ |
| 0.2 mm | 19 | 2 | 3 | 16 | 1.3 | $3.36 \pm 0.05$ | 0 | 0 | 0.512 | Aluminium sphere with 55 cm radius | Yes | 15 | 39 | 1.4 | $16.68 \pm 0.27$ |
| 0.2 mm | 21 | 3 | 3 | 22 | 1.3 | $4.91 \pm 0.62$ | -2.1 | 0.56 | -0.608 | Block of aluminium size $101.9 \times 101.9 \times 50$ cm | Yes | 13 | 45 | 1.3 | $11.99 \pm 0.05$ |
| 0.2 mm | 23 | 2 | 3 | 17 | 1.3 | $3.85 \pm 0.11$ | 0 | 0 | 0.512 | Aluminium sphere with 55 cm radius | Yes | 15 | 45 | 1.4 | $14.170 \pm 0.21$ |
| 0.2 mm | 23 | 3 | 3 | 22 | 1.3 | $4.65 \pm 0.06$ | -0.8 | -0.26 | -0.608 | Block of gravel $101.9 \times 101.9 \times 80$ cm | Yes | 13 | 35 | 1.3 | $13.08 \pm 0.19$ |

| | | | | | | | | | | | | | | | |
|---|---|---|---|---|---|---|---|---|---|---|---|---|---|---|---|
| 0.2 mm | 23 | 3 | 3 | 23 | 1.3 | 4.62 ± 0.04 | -0.8 | 0.56 | -0.5 | Block of gravel 101.9 × 101.9 × 80 cm | Yes | 13 | 45 | 1.3 | 13.31 ± 0.06 |
| 0.2 mm | 25 | 2 | 3 | 18 | 1.3 | 3.65 ± 0.20 | -1.55 | -0.56 | 0.412 | Block of aluminium size 101.9 × 101.9 × 50 cm | Yes | 15 | 45 | 1.4 | 14.48 ± 0.14 |
| 0.2 mm | 27 | 4 | 4 | 15 | 1.5 | 6.37 ± 0.51 | 2.1 | -0.56 | -0.608 | Block of aluminium size 101.9 × 101.9 × 50 cm | Yes | 13 | 31 | 1.3 | 11.62 ± 0.25 |
| 1 mm | 2 | 4 | 4 | 14 | 1.5 | 5.36 ± 0.10 | 2.1 | -0.56 | 0.708 | Block of aluminium size 101.9 × 101.9 × 50 cm | Yes | 13 | 39 | 1.3 | 10.38 ± 0.29 |
| 1 mm | 2 | 4 | 4 | 14 | 1.5 | 5.08 ± 0.02 | 0 | -0.56 | -0.858 | Block of aluminium size 101.9 × 101.9 × 34 cm | Yes | 13 | 32 | 1.3 | 11.24 ± 0.14 |
| 1 mm | 12 | 2 | 3 | 13 | 1.3 | 3.30 ± 0.09 | -1.55 | -0.56 | 0.512 | Block of aluminium size 101.9 × 101.9 × 50 cm | Yes | 15 | 40 | 1.4 | 14.92 ± 0.07 |
| 1 mm | 13 | 2 | 3 | 20 | 1.3 | 3.67 ± 0.06 | 0 | 0 | 0.512 | Aluminium sphere with 55 cm radius | Yes | 15 | 36 | 1.4 | 15.45 ± 0.21 |
| 1 mm | 14 | 3 | 3 | 24 | 1.3 | 4.92 ± 0.05 | -2.1 | 0.56 | -0.608 | Block of aluminium size 101.9 × 101.9 × 50 cm | Yes | 13 | 45 | 1.3 | 12.58 ± 0.04 |
| 1 mm | 15 | 2 | 3 | 17 | 1.3 | 3.65 ± 0.21 | -1.55 | -0.56 | 0.412 | Block of aluminium size 101.9 × 101.9 × 50 cm | Yes | 15 | 45 | 1.4 | 13.64 ± 0.09 |
| 1 mm | 19 | 2 | 3 | 16 | 1.3 | 3.58 ± 0.06 | 0 | 0 | 0.512 | Aluminium sphere with 55 cm radius | Yes | 15 | 39 | 1.4 | 16.91 ± 0.27 |
| 1 mm | 20 | 4 | 4 | 17 | 1.5 | 5.65 ± 0.31 | 2.1 | -0.56 | -0.608 | Block of aluminium size 101.9 × 101.9 × 50 cm | Yes | 13 | 31 | 1.3 | 12.56 ± 0.20 |
| 1 mm | 21 | 4 | 4 | 16 | 1.5 | 5.55 ± 0.76 | -2.1 | 0.56 | -0.608 | Block of aluminium size 101.9 × 101.9 × 50 cm | Yes | 13 | 45 | 1.3 | 11.89 ± 0.05 |
| 1 mm | 23 | 2 | 3 | 19 | 1.3 | 3.99 ± 0.13 | 0 | 0 | 0.512 | Aluminium sphere with 55 cm radius | Yes | 15 | 45 | 1.4 | 14.25 ± 0.18 |
| 1 mm | 23 | 3 | 3 | 24 | 1.3 | 4.65 ± 0.08 | -0.8 | -0.26 | -0.608 | Block of gravel size 101.9 × 101.9 × 80 cm | Yes | 13 | 35 | 1.3 | 12.92 ± 0.22 |
| 1 mm | 25 | 2 | 3 | 18 | 1.3 | 3.38 ± 0.09 | -1.55 | -0.56 | 0.412 | Block of aluminium size 101.9 × 101.9 × 50 cm | Yes | 15 | 45 | 1.4 | 14.68 ± 0.15 |
| 1 mm | 27 | 4 | 4 | 15 | 1.5 | 6.05 ± 0.26 | 2.1 | -0.56 | -0.608 | Block of aluminium size 101.9 × 101.9 × 50 cm | Yes | 13 | 31 | 1.3 | 11.60 ± 0.21 |
| 2 mm | 2 | 4 | 4 | 14 | 1.5 | 5.12 ± 0.19 | 2.1 | -0.56 | 0.708 | Block of aluminium size 101.9 × 101.9 × 50 cm | Yes | 13 | 39 | 1.3 | 10.49 ± 0.12 |
| 2 mm | 12 | 2 | 3 | 12 | 1.3 | 3.15 ± 0.22 | -1.55 | -0.56 | 0.512 | Block of aluminium size 101.9 × 101.9 × 50 cm | Yes | 15 | 39 | 1.4 | 14.97 ± 0.07 |
| 2 mm | 13 | 2 | 3 | 16 | 1.3 | 3.99 ± 0.15 | 0 | 0 | 0.512 | Aluminium sphere with 55 cm radius | Yes | 15 | 36 | 1.4 | 15.45 ± 0.19 |
| 2 mm | 13 | 2 | 3 | 12 | 1.3 | 3.45 ± 0.18 | -1.55 | -0.56 | 0.512 | Block of concrete size 101.9 × 101.9 × 80 cm | Yes | 15 | 26 | 1.4 | 15.45 ± 0.21 |
| 2 mm | 14 | 3 | 3 | 16 | 1.3 | 5.00 ± 0.17 | -2.1 | 0.56 | -0.608 | Block of aluminium size 101.9 × 101.9 × 50 cm | Yes | 13 | 45 | 1.3 | 12.42 ± 0.04 |
| 2 mm | 15 | 2 | 3 | 17 | 1.3 | 4.65 ± 0.20 | -1.55 | -0.56 | 0.412 | Block of aluminium size 101.9 × 101.9 × 50 cm | Yes | 15 | 45 | 1.4 | 13.71 ± 0.09 |
| 2 mm | 19 | 2 | 3 | 16 | 1.3 | 3.82 ± 0.14 | 0 | 0 | 0.512 | Aluminium sphere with 55 cm radius | Yes | 15 | 39 | 1.4 | 16.36 ± 0.23 |
| 2 mm | 20 | 4 | 4 | 13 | 1.5 | 5.45 ± 0.19 | 2.1 | -0.56 | -0.608 | Block of aluminium size 101.9 × 101.9 × 50 cm | Yes | 13 | 29 | 1.3 | 12.23 ± 0.20 |
| 2 mm | 21 | 4 | 4 | 15 | 1.5 | 5.77 ± 0.78 | -2.1 | -0.56 | -0.608 | Block of aluminium size 101.9 × 101.9 × 50 cm | Yes | 13 | 45 | 1.3 | 11.86 ± 0.05 |
| 2 mm | 23 | 2 | 3 | 18 | 1.3 | 4.11 ± 0.07 | 0 | 0 | 0.512 | Aluminium sphere with 55 cm radius | Yes | 15 | 45 | 1.4 | 14.10 ± 0.15 |
| 2 mm | 24 | 4 | 4 | 13 | 1.5 | 7.56 ± 0.90 | 0 | -0.56 | -0.858 | Block of aluminium size 101.9 × 101.9 × 50 cm | Yes | 13 | 32 | 1.3 | 11.73 ± 0.29 |
| 2 mm | 24 | 4 | 4 | 13 | 1.5 | 6.14 ± 0.03 | 2.1 | -0.56 | -0.608 | Block of aluminium size 101.9 × 101.9 × 50 cm | Yes | 13 | 32 | 1.3 | 11.84 ± 0.27 |
| 2 mm | 25 | 2 | 3 | 15 | 1.3 | 3.78 ± 0.24 | -1.55 | -0.56 | 0.412 | Block of aluminium size 101.9 × 101.9 × 50 cm | Yes | 15 | 45 | 1.4 | 14.75 ± 0.16 |

## 6.3 Shielded HEU Placed within Medium-*Z* Clutter

### 6.3.1 Results using Muon Scattering Tomography

#### Analysis for a Single Configuration

The capability of muon scattering tomography was applied to detecting shielded HEU in cargo containers filled with medium-*Z* clutter. This clutter generally consists of different sized blocks of aluminium, weathering steel, stainless steel and iron. Twenty different types of setup have been simulated. This section will discuss in detail one of these configurations. A schematic of the scenario is displayed in Fig 6.1. A list of the clutter is given in Table 6.1. Fig. 6.5 displays the capability of muon scattering tomography to detect shielded HEU in the scenario described, for all resolutions tested (perfect, 0.1 mm, 0.2 mm, 1 mm, 2 mm). The parameters have been calculated as optimum for the detection of shielded HEU in low-*Z* clutter scenarios for each resolution. These parameters are listed in Table 6.8. As can been seen in Fig. 6.5 muon scattering tomography with the analysis algorithm struggles to detect shielded HEU when housed with medium-*Z* clutter. For all resolutions there are a number of false positives and false negatives identified. A list of these false positives and false negatives is given in Table 6.15.

Analysis into low-*Z* clutter scenarios have demonstrated the inability of muon scattering tomography to distinguish blocks of aluminium from threat materials. Given blocks of the same dimensions, it is reasonable to expect that all blocks with a density higher than aluminium will be reconstructed as threats by muon scattering tomography. From Table 6.15, for each resolution, all blocks with densities higher than aluminium (weathering steel, stainless steel, iron) have been identified as false positives. However, unlike for low-*Z* clutter scenarios, blocks of clutter made of aluminium have not been misclassified as high-*Z* volumes. The analysis algorithm compares the average scattering in each voxel to the plane average. As the density of the blocks in each plane increases, so will the average total scattering angle of the plane. This can be seen through comparing the average scattering angle of each 20 cm plane where the threats are located for low-*Z* clutter scenarios (Table 6.3) and medium-*Z* clutter scenarios (Table 6.16). An increase in the average scattering angle of the plane that voxels are compared to will result in fewer voxels being above the criteria required for detection to be made. This in turn will result in lower density materials not having enough voxels above the criteria for

detection to be made. In addition to the false positives caused by clutter, there is again multiple false positives that occur just inside the cargo container walls. These are due to muons that scatter within the container walls. It can be seen that as resolution decreases the number of false positives detected increases. This is due to the reduction in parameters required for a volume to be identified as high-$Z$ material. This reduction is required so that shielded HEU are detected.

The cause of false negatives is the same as for blocks of aluminium not being identified as threats. The average scattering angle observed for each voxel with a threat material, does not significantly vary for low-$Z$ clutter and medium-$Z$ clutter scenarios. However since the plane average does increase, this results in the number of voxels with an average scattering angle greater than the plane average (times some factor) to be below that required for detection to be made. Secondly the reconstructed ratio is much lower for threat materials in this scenario than compared to its low-$Z$ clutter counterpart. As fewer muons that have interacted with the threat are reconstructed within the threat, the positive identification of these volumes as possible high-$Z$ materials will reduce. A $4^{th}$ false negative (F.N.4) occurs as resolution decreases. The decrease in resolution reduces the accurate reconstruction of a muon track, therefore the reconstructed muon scattering point can end up outside where the threat is located. This in turn prevents the criteria for detection to be made given in Table 6.8, from being met.

The build-up of false positives and false negatives demonstrates a limitation of muon scattering tomography, when applied to medium-$Z$ clutter scenarios. A reduction in parameters so that all nuclear materials are detected has not been considered. Such a reduction will cause the detection of multiple false positives in low-$Z$ clutter scenarios, thus making the algorithm no longer effective for this type of scenario.

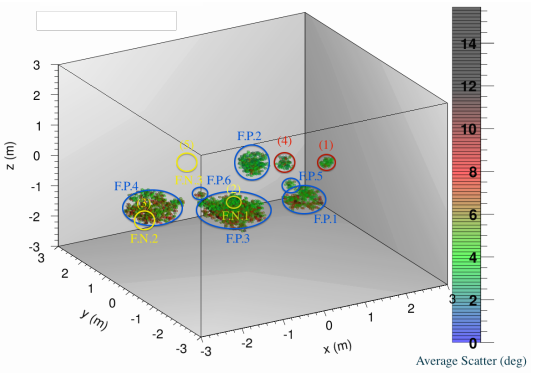


(a) *Perfect spatial resolution.*

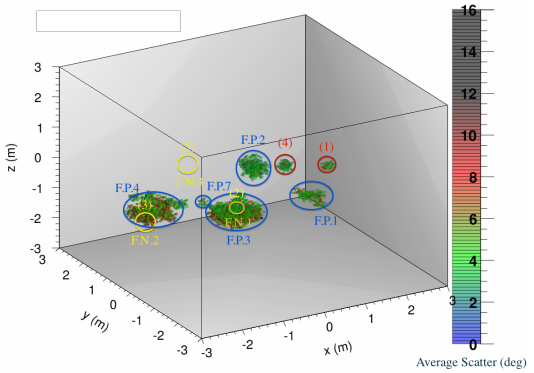


(b) *0.1 mm spatial resolution.*

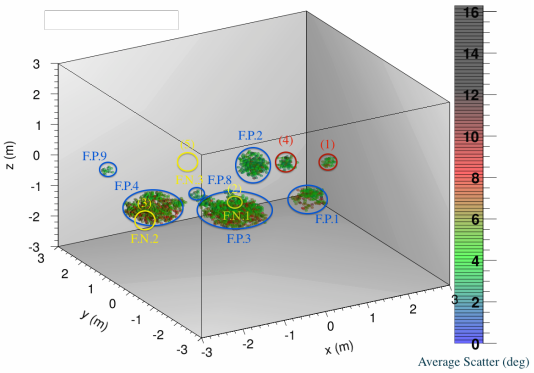


(c) *0.2 mm spatial resolution.*

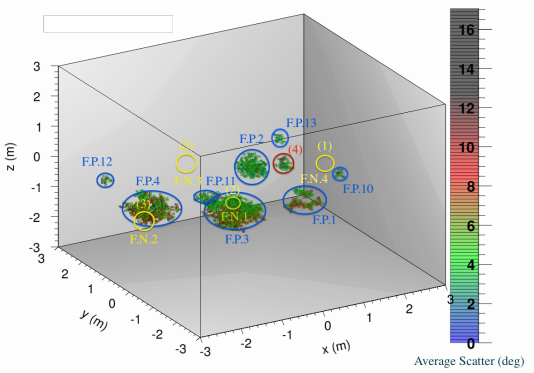


(d) *1 mm spatial resolution.*

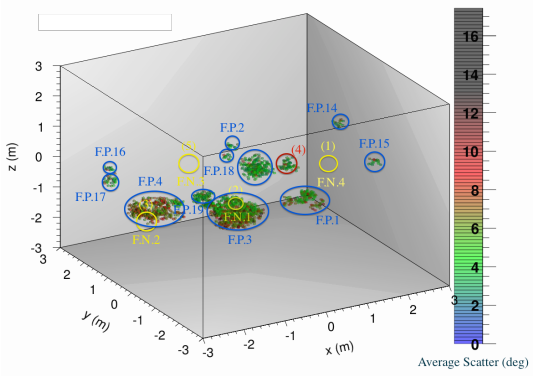


(e) *2 mm spatial resolution.*

Fig. 6.5 *Image reconstruction of Fig. 6.1 using muon scattering tomography for the medium-Z clutter scenario given in Fig. 6.1. Displayed are perfect resolution (top left), 0.1 mm resolution (top right), 0.2 mm resolution (middle left), 1 mm resolution (middle right) and 2 mm resolution (bottom). Red circles represent shielded HEU that have been identified. Blue circles represent false positives attributed to the clutter or cargo. Yellow circles represent volumes where shielded HEU was located, but not identified.*

Table 6.15 False positives and false negatives observed in the medium-$Z$ clutter scenario, for the different resolutions using parameters optimised for each resolution. The parameters are given in Table 6.8.

| Type | Figure I.D | Resolution | Section | $R$ | $V$ | $M$ | Avg Scattering Angle per Voxel (Perfect) | Avg Scattering Angle per Voxel (0.1 mm) | Avg Scattering Angle per Voxel (0.2 mm) | Avg Scattering Angle per Voxel (1 mm) | Avg Scattering Angle per Voxel (2 mm) | $x$ (m) | $y$ (m) | $z$ (m) | Cause |
|---|---|---|---|---|---|---|---|---|---|---|---|---|---|---|---|
| False Positive | F.P.1 | All | 3 | 3 | 27, 28, 27, 23, 25 | 1.3 | $4.91 \pm 0.19$ | $4.67 \pm 0.09$ | $5.22 \pm 0.22$ | $4.82 \pm 0.16$ | $4.83 \pm 0.07$ | 0.8 | -0.56 | -0.608 | Block of iron with dimensions 101.9 × 101.9 × 25 cm |
| False Positive | F.P.2 | All | 2 | 3 | 24, 23, 22, 22, 21 | 1.3 | $3.77 \pm 0.03$ | $3.80 \pm 0.04$ | $4.00 \pm 0.04$ | $4.48 \pm 0.05$ | $4.95 \pm 0.07$ | 0 | 0 | 0.512 | Sphere of inner radius 16 cm and outer radius 35 cm of weathering steel |
| False Positive | F.P.3 | All | 3 | 3 | 28, 28, 26, 34, 26 | 1.3 | $4.45 \pm 0.05$ | $4.65 \pm 0.10$ | $4.59 \pm 0.08$ | $4.57 \pm 0.05$ | $4.84 \pm 0.06$ | -0.8 | -0.56 | -0.608 | Hollow block of iron with outer length 100 × 100 × 50 cm and inner 33 × 33 × 33 cm |
| False Positive | F.P.4 | All | 3 | 3 | 22, 22, 23, 22, 22 | 1.3 | $4.55 \pm 0.03$ | $4.95 \pm 0.05$ | $4.36 \pm 0.04$ | $4.97 \pm 0.07$ | $5.13 \pm 0.08$ | -2.1 | 0.56 | -0.608 | Hollow block of stainless steel with outer length 100 × 100 × 50 cm and inner 33 × 33 × 33 cm |
| All other false positives for all resolutions (F.P.5 - F.P.18) are volumes that have been built up close to or inside the cargo container walls. | | | | | | | | | | | | | | | |
| False Negative | F.N.1 | All | 3 | 3 | 21, 21, 20, 19, 19 | 1.3 | $2.96 \pm 0.20$ | $3.01 \pm 0.28$ | $3.04 \pm 0.24$ | $3.59 \pm 0.34$ | $3.63 \pm 0.31$ | -0.6 | -0.36 | -0.408 | Not detected |
| False Negative | F.N.2 | All | 3 | 3 | 21, 21, 21, 21, 21 | 1.3 | $2.56 \pm 0.26$ | $2.64 \pm 0.24$ | $2.62 \pm 0.29$ | $2.68 \pm 0.36$ | $3.29 \pm 0.35$ | -2.4 | 0.26 | -0.408 | Not detected |
| False Negative | F.N.3 | All | 1 | 3 | 15, 15, 14, 13, 12 | 1.5 | $2.78 \pm 0.30$ | $2.83 \pm 0.32$ | $3.00 \pm 0.30$ | $3.47 \pm 0.29$ | $3.40 \pm 0.29$ | -1.75 | -0.36 | 0.85 | Not detected |
| False Negative | F.N.4 | 1 mm, 2 mm | 3 | 3 | 18, 17 | 1.3 | - | - | - | $2.97 \pm 0.29$ | $3.22 \pm 0.34$ | 2.1 | 0.56 | -0.408 | Not detected |

Table 6.16 Position, average scattering angle per voxel and reconstructed ratio for each of the threats materials in the medium-$Z$ clutter scenario given in Fig. 6.1.

| Resolution | $x$ (m) | $y$ (m) | $z$ (m) | Muons Detected | Muons Correctly Reconstructed | Average Scattering Angle of Threat (degrees) | Average Scattering Angle of Plane (degrees) | Reconstructed Ratio |
|---|---|---|---|---|---|---|---|---|
| Perfect | 2.1 | 0.56 | -0.408 | 3882 | 213 | $2.97 \pm 0.22$ | $2.33 \pm 0.01$ | 0.055 |
| Perfect | -0.6 | -0.36 | -0.408 | 3900 | 203 | $2.97 \pm 0.20$ | $2.33 \pm 0.01$ | 0.052 |
| Perfect | -2.4 | 0.26 | -0.408 | 3432 | 198 | $2.56 \pm 0.26$ | $2.33 \pm 0.01$ | 0.058 |
| Perfect | -1.75 | -0.36 | 0.85 | 2266 | 144 | $2.78 \pm 0.30$ | $1.57 \pm 0.01$ | 0.064 |
| Perfect | 0.8 | 0 | 0.2 | 2443 | 214 | $3.35 \pm 0.29$ | $1.84 \pm 0.01$ | 0.088 |
| 0.1 mm | 2.1 | 0.56 | -0.408 | 3882 | 221 | $2.85 \pm 0.25$ | $2.34 \pm 0.01$ | 0.057 |
| 0.1 mm | -0.6 | -0.36 | -0.408 | 3900 | 208 | $3.01 \pm 0.28$ | $2.34 \pm 0.01$ | 0.053 |
| 0.1 mm | -2.4 | 0.26 | -0.408 | 3432 | 190 | $2.64 \pm 0.24$ | $2.34 \pm 0.01$ | 0.055 |
| 0.1 mm | -1.75 | -0.36 | 0.85 | 2266 | 138 | $2.83 \pm 0.32$ | $1.59 \pm 0.01$ | 0.061 |
| 0.1 mm | 0.8 | 0 | 0.2 | 2443 | 228 | $3.15 \pm 0.26$ | $1.85 \pm 0.01$ | 0.093 |
| 0.2 mm | 2.1 | 0.56 | -0.408 | 3882 | 215 | $2.91 \pm 0.27$ | $2.35 \pm 0.01$ | 0.055 |
| 0.2 mm | -0.6 | -0.36 | -0.408 | 3900 | 106 | $3.04 \pm 0.24$ | $2.35 \pm 0.01$ | 0.027 |
| 0.2 mm | -2.4 | 0.26 | -0.408 | 3432 | 192 | $2.62 \pm 0.29$ | $2.35 \pm 0.01$ | 0.056 |
| 0.2 mm | -1.75 | -0.36 | 0.85 | 2266 | 125 | $3.00 \pm 0.30$ | $1.62 \pm 0.01$ | 0.055 |
| 0.2 mm | 0.8 | 0 | 0.2 | 2443 | 223 | $3.27 \pm 0.28$ | $1.86 \pm 0.01$ | 0.091 |
| 1 mm | 2.1 | 0.56 | -0.408 | 3882 | 218 | $2.97 \pm 0.29$ | $2.49 \pm 0.01$ | 0.056 |
| 1 mm | -0.6 | -0.36 | -0.408 | 3900 | 182 | $3.59 \pm 0.34$ | $2.49 \pm 0.01$ | 0.047 |
| 1 mm | -2.4 | 0.26 | -0.408 | 3432 | 172 | $2.68 \pm 0.36$ | $2.49 \pm 0.01$ | 0.050 |
| 1 mm | -1.75 | -0.36 | 0.85 | 2266 | 95 | $3.47 \pm 0.29$ | $1.79 \pm 0.01$ | 0.042 |
| 1 mm | 0.8 | 0 | 0.2 | 2443 | 181 | $3.48 \pm 0.36$ | $1.94 \pm 0.01$ | 0.074 |
| 2 mm | 2.1 | 0.56 | -0.408 | 3882 | 190 | $3.22 \pm 0.34$ | $2.67 \pm 0.01$ | 0.049 |
| 2 mm | -0.6 | -0.36 | -0.408 | 3900 | 185 | $3.63 \pm 0.31$ | $2.67 \pm 0.01$ | 0.047 |
| 2 mm | -2.4 | 0.26 | -0.408 | 3432 | 154 | $3.29 \pm 0.35$ | $2.67 \pm 0.01$ | 0.045 |
| 2 mm | -1.75 | -0.36 | 0.85 | 2266 | 107 | $3.40 \pm 0.29$ | $1.92 \pm 0.01$ | 0.047 |
| 2 mm | 0.8 | 0 | 0.2 | 2443 | 155 | $4.06 \pm 0.38$ | $2.03 \pm 0.01$ | 0.063 |

### Analysis for all Twenty Configurations

Similar to Table 6.16, Appendix D gives an example table of data for one of these twenty configurations. These tables show the position, average scattering angle per voxel and reconstructed ratio for each of the threats materials. Table 6.17 describes the total amount of false positive (f.pos) and false negatives (f.neg) observed for all twenty configurations with different resolutions when applying the set of parameters given in Table 6.8. These parameters were calculated as being optimum for each resolution for the detection of shielded HEU in low-$Z$ clutter scenarios. There are at maximum 5 false negatives per each individual configuration. For some configurations more than one false positive or false negative has been observed. Since four of the configurations had no threat materials located within them, total false positive rates are taken from all twenty configurations conducted, whereas false negatives rates are taken from sixteen configurations conducted. The percentage of configurations observed to have a false positive or false negative is also given.

Table 6.17 False positives and negative rates for the different resolutions in the medium-$Z$ clutter scenarios, using parameters described in Table 6.8.

| Resolution | Total f.pos | % of configurations with f.pos | Total f.neg | % of configurations with f.neg |
|---|---|---|---|---|
| Perfect | 81 | 100% | 21/80 | 81.25% |
| 0.1 mm | 81 | 100% | 23/80 | 81.25% |
| 0.2 mm | 80 | 100% | 24/80 | 81.25% |
| 1.0 mm | 76 | 100% | 26/80 | 87.5% |
| 2.0 mm | 68 | 100% | 27/80 | 87.5% |

As it can be seen all configurations result in the build-up of at least one false positive. This is expected when we consider the results for the low-$Z$ clutter scenarios. Since the analysis algorithm applied to low-$Z$ clutter scenarios fails to differentiate blocks of aluminium, then it will also be unable to remove blocks of higher density materials. For medium-$Z$ clutter scenarios, the different materials used as clutter are aluminium, stainless steel, weathering steel and iron. Most blocks of iron, weathering steel or stainless steel in each configuration are reconstructed by the analysis algorithm. Due to the increase in each plane's average scattering angle per voxel, not all blocks of aluminium within each configuration are reconstructed. The number of false positives

decreases with resolution. This is again due to the decrease in resolution preventing the accurate reconstruction of a muon track. This in turn causes the muon scattering point to be reconstructed outside the volume where the clutter is located, thus causing the volume to be below the criteria required for a positive detection to be made. In addition to these false positives, there are also multiple additional voxels built up close to the cargo container walls.

A large percentage of configurations observe at least one false negative. The number of false negatives increases as resolution decreases. The is due to the same reason as for a decrease in false positives. The increase in false negatives when compared to the low-$Z$ clutter scenarios is due to the increase in average plane scatter and the reduction in the number of correct reconstructions (reconstructed ratio). Table 6.18 displays the minimum parameters required to detect all shielded HEU. The reduction in parameters required for positive detection to be made, results in the build-up of many more false positives due to clutter for all configurations, in addition to multiple voxels in volumes where no threats are located. The effect of this displays a limitation of muon scattering tomography to detect shielded HEU in medium-$Z$ clutter environments.

Table 6.18 New conditions optimised for each resolution to be applied to the systems where shielded HEU is placed in a cargo container with low-$Z$ clutter.

| Resolution | Section 1 | | | Section 2 | | | Section 3 | | | Section 4 | | |
|---|---|---|---|---|---|---|---|---|---|---|---|---|
| | $R$ | $V$ | $M$ | $R$ | $V$ | $M$ | $R$ | $V$ | $M$ | $R$ | $V$ | $M$ |
| Perfect | 3 | 14 | 1.4 | 3 | 10 | 1.2 | 3 | 22 | 1.1 | 4 | 12 | 1.2 |
| 0.1 mm | 3 | 11 | 1.4 | 3 | 10 | 1.2 | 3 | 19 | 1.1 | 4 | 11 | 1.2 |
| 0.2 mm | 3 | 10 | 1.4 | 3 | 10 | 1.2 | 3 | 19 | 1.1 | 4 | 11 | 1.2 |
| 1 mm | 3 | 8 | 1.4 | 3 | 8 | 1.2 | 3 | 13 | 1.4 | 4 | 11 | 1.2 |
| 2 mm | 3 | 9 | 1.1 | 3 | 7 | 1.3 | 3 | 10 | 1.4 | 4 | 15 | 1.4 |

### 6.3.2 Results using Muon Scattering and Muon Disappearance Tomography

#### Analysis for a Single Configuration

Fig. 6.6 displays the 'areas of interest' identified using muon scattering tomography (top) and the volumes identified by the muon disappearance algorithm (bottom) when

analysing the $z$-slices where the 'areas of interest' are located. The configuration tested is that shown in Fig. 6.1. As it can be seen the two threat materials identified when using muon scattering tomography, have been missed when using muon disappearance tomography. This is a major concern as it not only fails to enhance muon scattering tomography, but actually decreases detection capabilities. All false positives that are attributed to clutter in muon scattering tomography (F.P.1, F.P.2, F.P.3, F.P.4) have also been reconstructed by the muon disappearance algorithm (F.P.1, F.P.2, F.P.3, F.P.4). There is also the build-up of a $5^{th}$ false positive from the muon disappearance algorithm (F.P.5). This false positive is located in the volume between F.P.3 and F.P.4 and is due to muons that have disappeared in each of these clutter items. However, since it is not identified as an 'area of interest' with muon scattering tomography it can be ignored. The groups of reconstructed voxels that represent the items of clutter accurately reflect the actual object size of the false positive. Similar to the low-$Z$ clutter scenarios, all false positives that are attributed to the walls of the cargo container have been removed by the muon disappearance algorithm.

**Analysis for all Twenty Configurations**

The analysis described for the single configuration was applied to all other fifteen configurations for shielded HEU in containers housing medium-$Z$ clutter and four configurations with just medium-$Z$ clutter. Appendix E gives an example table of data for one of the twenty medium-$Z$ clutter configurations. These tables show the position and average total path length per voxel of each of threats identified by the muon disappearance algorithm. As with the analysis discussed for the single configuration, no false positives that are attributed to clutter are removed by the muon disappearance algorithm. The majority of these false positives are caused by blocks of stainless steel, weathering steel or iron. There are multiple instances where shielded HEU identified by muon scattering tomography, are missed by the muon disappearance algorithm. These results demonstrate the inability of the muon disappearance tomography algorithm to enhance traditional muon tomography methods for medium-$Z$ clutter scenarios. Since some shielded threat materials identified by muon scattering tomography are not confirmed by the muon disappearance algorithm, it actually reduces the effectiveness of muon scattering tomography techniques for this type of scenario. As with the low-$Z$ clutter scenarios, 100% of false positives that are caused by muons scattered in the cargo container walls have been removed.

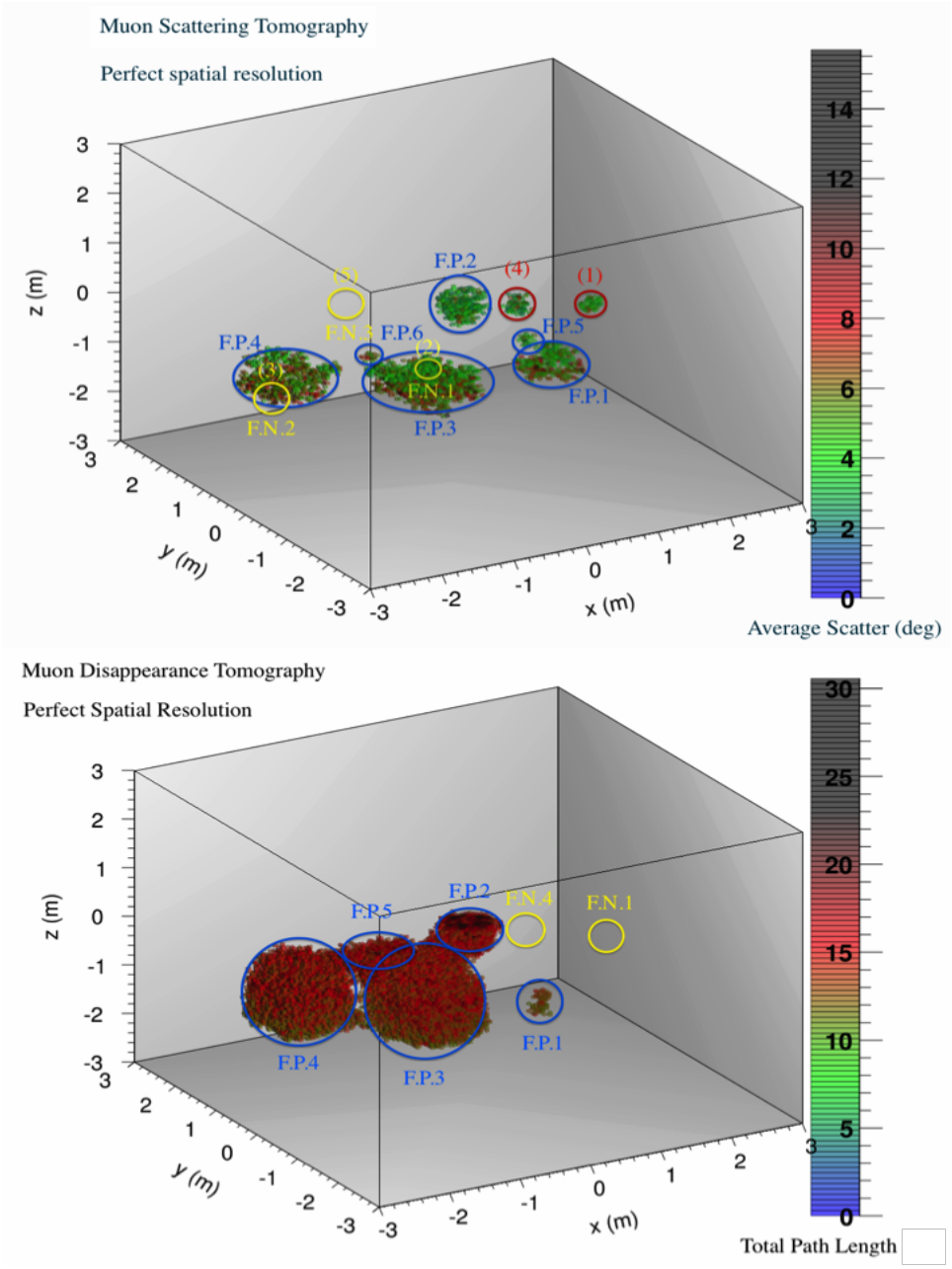


Fig. 6.6 *Image reconstruction of Fig. 6.1 using the muon scattering tomography (top) and the muon disappearance algorithm (bottom). Displayed are all voxels identified under perfect resolution. Red circles represent shielded HEU that have been identified. Blue circles represent false positives attributed to the clutter or cargo. Yellow circle represent volumes where shielded HEU was located, but not identified.*

## 6.4 Summary

The efficiency to detect shielded HEU amongst different clutter scenarios using muon scattering tomography and the muon disappearance algorithm have been evaluated. Both low-$Z$ and medium-$Z$ clutter scenarios have been tested. For each scenario, twenty different clutter configurations were run. Sixteen of the twenty configurations, attempted to detect shielded HEU hidden amongst the clutter, whereas four had no shielded HEU placed within them. Systems that solely used muon scattering tomography with the analysis algorithm described in section 5.2.2, have been shown to be efficient in detecting shielded HEU in amongst low-$Z$ clutter scenarios. Parameters tuned for each resolution display a low false negative build-up. The concern with this system is the build-up of false positives in over 50% of the configurations. These false positives are mainly large blocks of aluminium, therefore any secondary process that could account for these blocks will greatly enhance detection capabilities. However, the removal of other low-$Z$ clutter items demonstrates the success of the algorithm to remove materials such as concrete, sand, carbon, polyethylene and gravel. Other false positives that are located close to the walls of the cargo container are also reconstructed. These volumes represent muons that have undergone scatters in the walls of the cargo container. The addition of the muon disappearance algorithm does not act to remove any false positives that are due to clutter, but does act to remove false positives caused by the cargo container walls. This therefore will enhance overall detection capabilities for shielded HEU in low-$Z$ clutter environments. It has been confirmed that techniques which solely use muon disappearance tomography are unable to clearly detect shielded HEU with a low false positive rate.

For the scenarios discussed in this thesis that involve medium-$Z$ clutter, muon scattering tomography has shown to be inefficient in detecting shielded HEU with a low enough false negative and false positive rate. The addition of the muon disappearance algorithm does not remove any of the false positives identified with muon scattering tomography but instead acts to remove some of the threats that have been identified. This acts to reduce detection efficiency. Therefore it is concluded that both techniques, whether used in conjunction or on their own, struggle to detect shielded HEU in medium-$Z$ clutter scenarios.

# Chapter 7

# Material Segregation using Cosmic-Ray Neutrons

In this chapter a discussion about the feasibility of using cosmic-ray neutrons to detect shielded HEU is given. The concept behind this process is discussed in section 7.1. Section 7.2 displays the validity of using GEANT4.9.6-p02 when applied to neutron interactions with matter. The multiple physical processes that occur when neutrons stop in different density materials have been investigated using GEANT4.9.6-p02 with the 'Shielding 2.0' physics list. A discussion of the secondaries produced for different materials then concludes this section. Section 7.3 analyses the total amount of excess neutrons and $\gamma$-rays produced when cosmic-ray neutrons interact with different materials. Under idealised conditions of 100% detector coverage and efficiencies a discussion is made into whether, through counting these excess neutrons and $\gamma$-rays, we can differentiate between materials. The chapter is concluded in section 7.4, with a study into whether cosmic-ray neutrons can be used to detect shielded HEU in an empty lorry scenario. Section 7.5 summarises the results presented.

## 7.1 Concept

As mentioned in section 2.4.3, cosmic-ray neutrons are produced when primary cosmic rays undergo interactions in the Earths atmosphere. After muons, neutrons represent the most abundant particle produced by cosmic-ray interactions that reach the surface. Due to the wide energy range in which cosmic-ray neutrons span, there is always the possibility that these neutrons will interact with the nucleus of the target they are passing through, resulting in the production of excess neutrons and $\gamma$-rays via fission (for

nuclear material) or spallation (for other material). Detection is established through measuring the gross count rate of neutrons and $\gamma$-rays over a defined time interval. The count rate from background neutrons and $\gamma$-rays will remain roughly the same over time. Upon the introduction of shielded HEU (or similar) gross count rates are again taken over the same time interval. Fissionable materials such as HEU will produce many more excess neutrons and $\gamma$-rays via fission then non-fissionable materials do via spallation. High-$Z$ materials, such as the shielding components will produce excess neutrons and $\gamma$-rays via spallation. This process is more likely to occur in high-$Z$ materials then low-$Z$ materials [41]. Through measuring a sufficiently elevated rate above the background, detection of SNM can be established. This has the advantage over active interrogation methods of no interrogation source, hence there will be no harm to people or materials. Simulations run in this chapter have used GEANT4.9.6-p02 with the 'Shielding 2.0' physics list [97, 98]. All cosmic-ray neutrons have been generated using CRY [49]. A full description of CRY is given in section 7.2.1. As with cosmic-ray muon techniques, exposure times of 5 minutes are tested.

## 7.2 GEANT4 Simulations on Differentiating Between Different Density Materials

The validity of GEANT4.9.6-p02 to accurately represent neutron interactions with matter and subsequent secondary production, has been tested through measuring the neutron multiplicity observed when neutrons interact with $^{235}$U and $^{238}$U. Simulations involved propagating 500,000 neutrons of monochromatic energy through 1 cm $\times$ 1 cm $\times$ 1 cm blocks of both uranium isotopes. Energies chosen were 0.025 eV, 1 MeV, 1.5 MeV, 2 MeV, 2.5 MeV, 3 MeV, 3.5 MeV, 4 MeV, 4.5 MeV, 5 MeV, 7.5 MeV, 10 MeV, 12.5 MeV and 15 MeV. Detectors were placed all around the volume to be inspected, with all neutrons recorded. Multiplicities measured for these two isotopes over the range of neutron energies tested, along with values obtained from literature [110–115] are given in Fig. 7.1. These results show good agreement and confirm the accuracy of GEANT4.9.6-p02 with 'Shielding 2.0' physics list.

### 7.2.1 Simulation Parameters

Before conducting realistic scenarios, simulations were run to show the ability to differentiate materials using cosmic-ray neutrons. Characteristic signatures that are emit-

ted for each material have been measured. Cosmic-ray neutrons were generated using CRY [49], with their full range of energies and angular distributions. Their angular distributions were then ignored and instead all cosmic-ray neutrons were given a direction of vertically straight down. Simulations have been run in GEANT4.9.6-p02 [97, 98], which involved propagating 500,000 cosmic-ray neutrons, with a vertical direction, through several 10 cm $\times$ 10 cm $\times$ 10 cm blocks of different materials. This was done to study the energy distribution of secondary particles with adequate statistics. The materials tested were water, iron, lead, $^{235}$U and $^{238}$U. Both $^{235}$U and $^{238}$U were tested as they emit differing numbers of neutrons and $\gamma$-rays that may act as a marker for the detection of shielded HEU. Detectors were placed fully surrounding the target. They are set to be 100% efficient and detect any neutrons or $\gamma$-rays produced within the simulation.

The cosmic-ray neutron spectrum for all simulations was generated using CRY (Cosmic-ray shower library). CRY is a software package that creates cosmic-ray particles (muons, $\gamma$-rays, neutrons, protons, electrons and pions) at different elevations above sea-level (0 m, 2100 m, 11300 m). Energy spectra can be produced for all or just one of the secondary particles. These spectra are generated on a specified surface area up to 300 m $\times$ 300 m, with their positions on this 'plane' also being recorded. The time of arrival and zenith angle of the particles are also recorded [49]. Fig. 7.2 shows the CRY generated neutron spectrum at sea level and at latitude 51.1295° (the latitude of Dover), in addition to a number of experimental measurements and other parameterisations for comparison [57–59]. The spectrum generated using CRY displays a decreased neutron rate at lower energies when compared to the spectra taken from literature. At higher energies the CRY spectrum agrees well with both experimental data and other parameterisations.

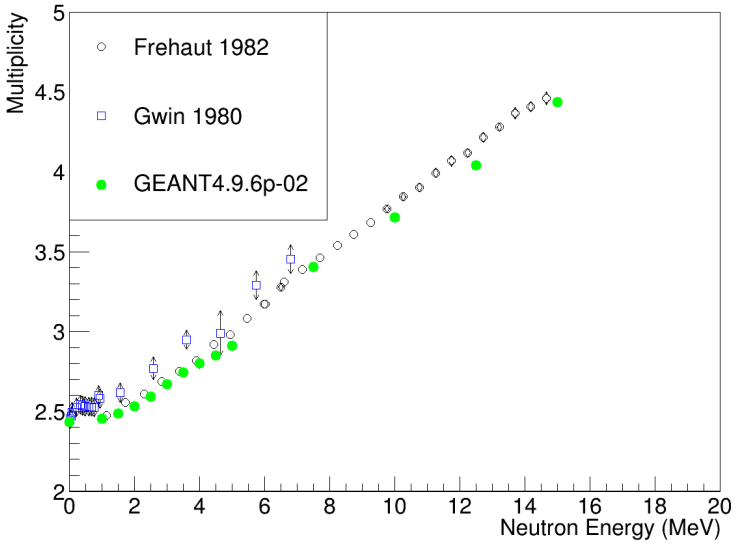


(a) $^{235}U$ *neutron multiplicity.*

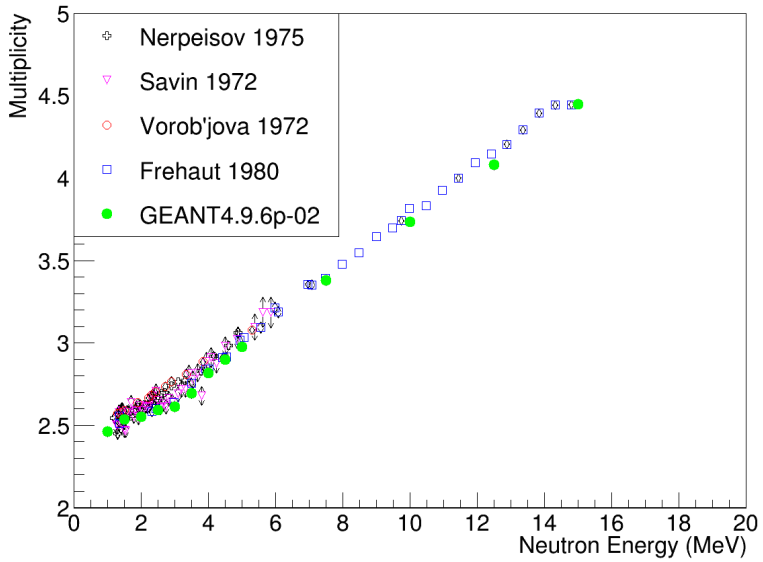


(b) $^{238}U$ *neutron multiplicity.*

Fig. 7.1 *Neutron multiplicity observed for* $^{235}U$ *(top) and* $^{238}U$ *(bottom) over a range of energies using GEANT4.9.6-p02 with the 'Shielding 2.0' physics list when compared to literature values [110–115].*

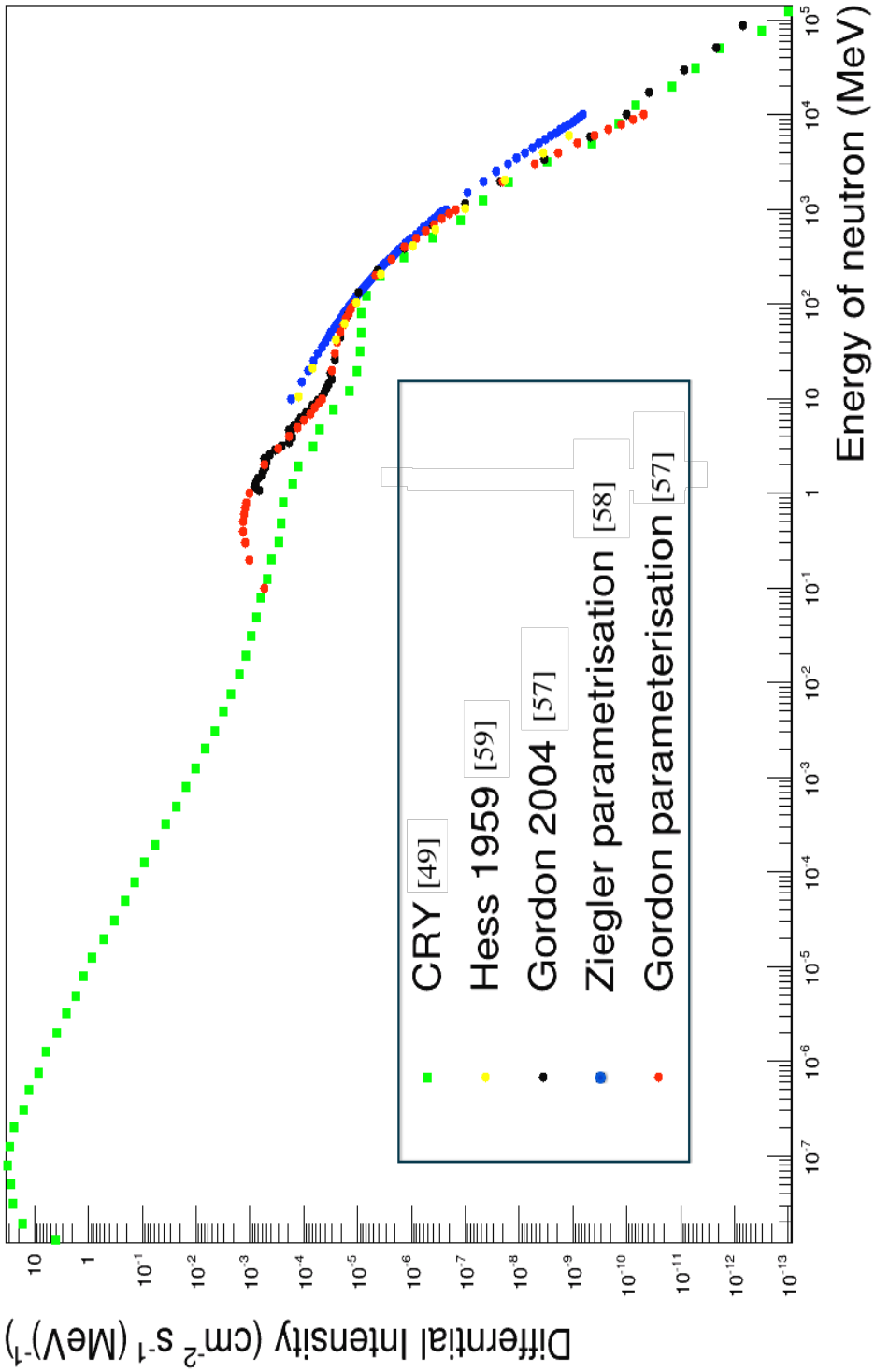


Fig. 7.2 *CRY generated neutron spectrum at sea level together with experimentally determined spectra and other parameterisations [49, 57–59].*

### 7.2.2 Gamma-ray and Neutron Spectra

Secondary neutrons and $\gamma$-rays produced when cosmic-ray neutrons interact with target materials have been analysed. Neutron and $\gamma$-ray energy spectra for this study are displayed in Fig. 7.3. Table 7.1 displays a number of the $\gamma$-ray peaks emitted upon neutron interaction with the target material, along with their cause and GEANT4 process. The dominant process of neutron and $\gamma$-ray production occurs when neutrons undergo inelastic scattering within the target material. During this interaction a neutron will transfer some of its kinetic energy to the nucleus, causing the nucleus to go to an excited state. This will cause the incoming neutron to lose speed and change direction. Since part of the neutron kinetic energy is used to place the nucleus in an excited state, the total kinetic energy of the outgoing neutron and nucleus is less than the kinetic energy of the original incoming neutron. Relaxation of the nucleus to the ground state occurs through the emission of $\gamma$-rays. Secondary processes that produce $\gamma$-rays involve the capture of a neutron by the nucleus of a material. This process is mitigated by the 'nCapture' process in GEANT4. It results in the nucleus rearranging its internal structure and being left over in an excited state. De-excitation occurs via the emission of $\gamma$-rays.

For nuclear materials, fission can occur when neutrons interact with the target nuclei, thus creating additional neutrons and $\gamma$-rays. After neutron inelastic scattering it is the $2^{nd}$ most dominant source of neutron production that occurs within nuclear materials. Upon undergoing fission many of the daughter products undergo radioactive decay in timescales ranging from seconds to years. This again adds an additional source of secondaries. Once a neutron interacts with the target, the target itself becomes a particle within the simulation. This means for $^{235}$U and $^{238}$U once a neutron has interacted with it, they can both start to undergo radioactive decay through to lead. This process takes millennia to occur. Two examples of secondary $\gamma$-rays produced by the radioactive decay of $^{235}$U and $^{238}$U are given in Table 7.1. For $^{235}$U the 2.614 MeV line, and $^{238}$U the 2.2 MeV line observed in the $\gamma$-ray spectra, are caused by $\gamma$-rays emitted as part of the $^{236}$U and $^{238}$U decay chains respectively.

As displayed in Fig. 7.3 given a high resolution detector, large detector area and adequate statistics, the detection of different materials through measuring their $\gamma$-ray spectra is apparent. Unfortunately for the applications discussed in this thesis, whereby the detection of shielded HEU occurs under short timescales with low resolution plastic

scintillators and $^{3}$He neutron detectors, such conditions are not available. Instead detection of shielded HEU has to be made via measuring the gross count rate of neutrons or $\gamma$-rays overtime and comparing this rate to the background count rate. Only if the count rate is sufficiently above the background can detection be determined. The following section will discuss the capability of differentiating between materials using the number of neutrons and $\gamma$-rays detected. Finally the ability to detect shielded HEU in realistic empty lorry scenarios, through measuring the gross count rate of neutrons and $\gamma$-rays over time is presented.

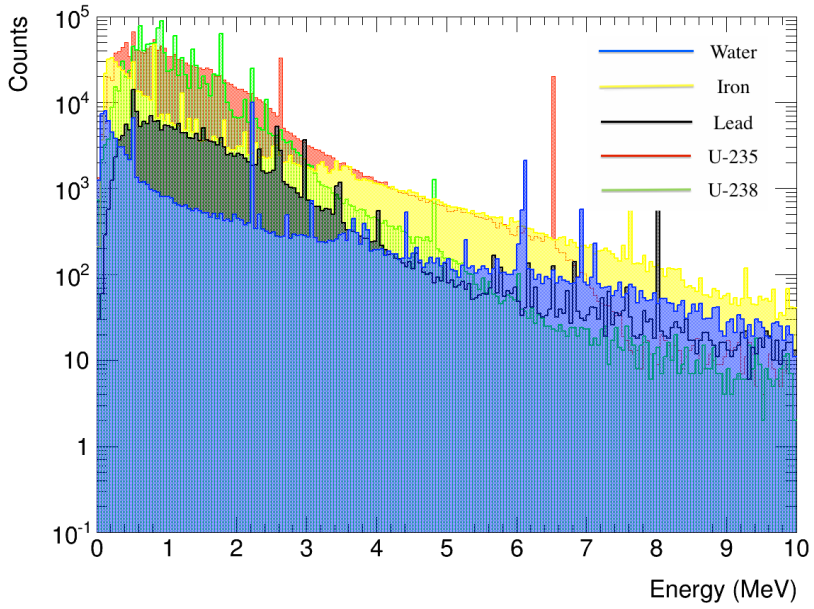


(a) *Secondary γ-ray spectrum.*

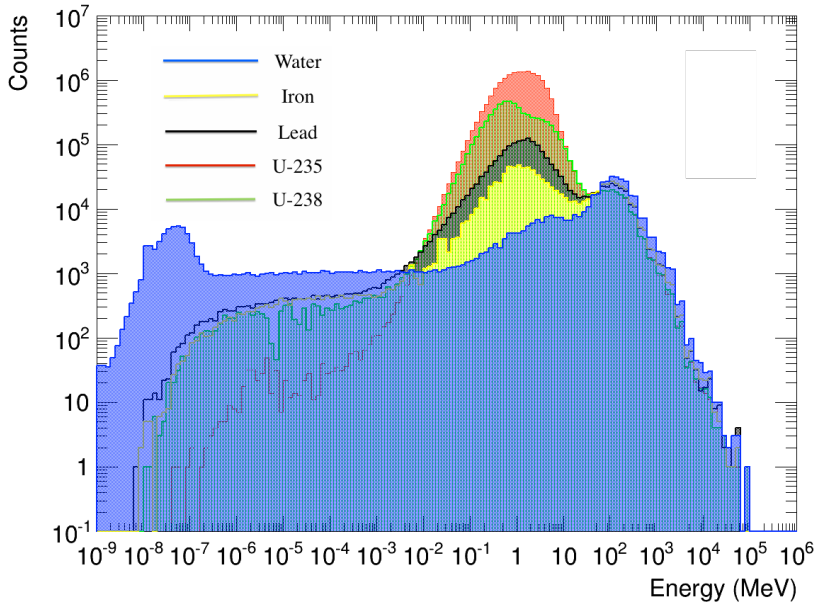


(b) *Secondary neutron spectrum.*

Fig. 7.3 *Secondary γ-ray (top) and neutron (bottom) energy spectra. The results are for 500,000 cosmic-ray neutrons propagated vertically into 10 cm × 10 cm × 10 cm cubes of water (blue), iron (yellow), lead (black),* $^{235}U$ *(red) and* $^{238}U$ *(green).*

Table 7.1 A selection of some of the $\gamma$-ray peaks observed for cosmic-ray neutron interactions with different materials.

| Material | Energy (MeV) | Description | GEANT4 Process |
|---|---|---|---|
| Water | 2.22 | Neutron is absorbed by a proton, which forms deuteron with the release of a $\gamma$-ray of 2.22 MeV in seconds. | nCapture |
| Water | 6.13 | $^{16}$O is activated by high-energy neutrons to produce $^{16}$N, which decays back to oxygen with a half-life of 7.1 seconds and emits a $\gamma$-ray of 6.13 MeV. | NeutronInelastic |
| Water | 6.91 | $^{16}$O is activated by high-energy neutrons to produce $^{16}$N, which decays back to oxygen with a half-life of 7.1 seconds and emits a $\gamma$-ray of 6.91 MeV. | NeutronInelastic |
| Water | 7.12 | $^{16}$O is activated by high-energy neutrons to produce $^{16}$N, which decays back to oxygen with a half-life of 7.1 seconds and emits a $\gamma$-ray of 7.12 MeV. | NeutronInelastic |
| Iron | 7.65 | Neutron is absorbed by a $^{56}$Fe, which forms $^{57}$Fe with the release of a $\gamma$-ray of energy 7.65 MeV in seconds. | nCapture |
| Lead | 2.62 | Neutron interacts with $^{56}$Fe causing the $^{56}$Fe to be left over in an excited state. Relaxation back to the ground state occurs within seconds via the emission of a $\gamma$-ray of 2.62 MeV. | NeutronInelastic |
| Lead | 2.98 | Neutron interacts with $^{56}$Fe causing the $^{56}$Fe to be left over in an excited state. Relaxation back to the ground state occurs within seconds via the emission of a $\gamma$-ray of 2.98 MeV. | NeutronInelastic |
| Lead | 8.04 | Neutron interacts with $^{56}$Fe causing the $^{56}$Fe to be left over in an excited state. Relaxation back to the ground state occurs within seconds via the emission of a $\gamma$-ray of 8.04 MeV. | NeutronInelastic |
| $^{235}$U | 2.614 | Produced as a result of the $^{236}$U decay chain, which takes places over thousands of years. Once the chain reaches $^{208}$Pb it releases a $\gamma$-ray of 2.614 MeV to get to the ground state. | RadioactiveDecay |
| $^{235}$U | 6.545 | A neutron is absorbed by a $^{235}$U nucleus resulting in the production of $^{236}$U in an excited state. Within seconds $^{236}$U will release a $\gamma$-ray of energy 6.545 MeV to get back to the ground state. | nCapture |
| $^{238}$U | 2.2 | Produced by the radioactive decay or $^{214}$Po. Part of the $^{238}$U decay chain, which takes places over thousands of years. | RadioactiveDecay |
| $^{238}$U | 4.81 | A neutron is absorbed by a $^{238}$U nucleus resulting in the production of $^{239}$U in an excited state. Within seconds $^{239}$U will release a $\gamma$-ray of energy 4.81 MeV to get back to the ground state. | nCapture |
| All | 0.511 | Produced when $e$- and $e$+ collide and annihilate resulting in the production of two 0.511 keV $\gamma$-rays. | Annihilation |

## 7.3 Material Segregation using Cosmic-Ray Neutrons

### 7.3.1 Material Segregation for a Single Block Scenario

Cosmic-ray neutrons are generated over a 10 m $\times$ 10 m surface area and implemented so that their true distribution of energies and zenith angles at sea level are represented. These neutrons are interfaced with GEANT4.9.6-p02 and propagated through the inspected volume displayed in Fig. 7.4 (not to scale). The targets to be inspected are blocks of different sizes. These are 10 cm $\times$ 10 cm $\times$ 10 cm and 50 cm $\times$ 50 cm $\times$ 50 cm blocks of low density (water, polyethylene, concrete), medium density (iron) and high density (lead, $^{238}$U) materials. Detectors are placed completely around the system so that all neutrons and $\gamma$-rays are detected. These detectors are assumed to be 100% efficient. The total amount of excess neutrons and $\gamma$-rays that are produced in a 5 minute exposure time are recorded. This is done to determine whether different density materials can be distinguished from one another. Table 7.2 gives the total number of excess neutrons and $\gamma$-rays that are produced, along with their uncertainties. It is assumed that there are no background neutrons or $\gamma$-rays detected. The error given is that calculated on the mean.

Table 7.2 Total amount of excess neutron and $\gamma$-ray observed when propagating 850,000 cosmic-ray neutrons, implemented with their true distribution of energies and zenith angles at sea level, through each one block configuration tested. Detector coverages and efficiencies are 100%. It is assumed that there are no background neutrons or $\gamma$-rays.

| | 10 cm $\times$ 10 cm $\times$ 10 cm blocks | | 50 cm $\times$ 50 cm $\times$ 50 cm blocks | |
|---|---|---|---|---|
| Material | Neutrons Detected | $\gamma$-rays Detected | Neutrons Detected | $\gamma$-rays Detected |
| Water | $15.9 \pm 0.5$ | $26.3 \pm 0.7$ | $995 \pm 4$ | $2875 \pm 7$ |
| Polyethylene | $12.3 \pm 0.5$ | $21.3 \pm 0.6$ | $1210 \pm 4$ | $2600 \pm 7$ |
| Concrete | $29.2 \pm 0.7$ | $47.6 \pm 0.9$ | $2170 \pm 6$ | $3885 \pm 8$ |
| Iron | $144.8 \pm 1.6$ | $150.1 \pm 1.6$ | $9890 \pm 13$ | $4980 \pm 9$ |
| Lead | $330.1 \pm 2.3$ | $80.8 \pm 1.2$ | $23505 \pm 20$ | $3760 \pm 8$ |
| $^{238}$U | $1200 \pm 5$ | $325.4 \pm 2.4$ | $67850 \pm 34$ | $13380 \pm 15$ |

For either sized block, as density increases so does the number of excess neutrons emitted. A sufficiently elevated rate of neutrons over other density materials is observed for $^{238}$U. This increased rate is due to fission events. Sufficient levels of neutrons are also observed for medium and high-density materials (iron, lead, $^{238}$U), that separate them

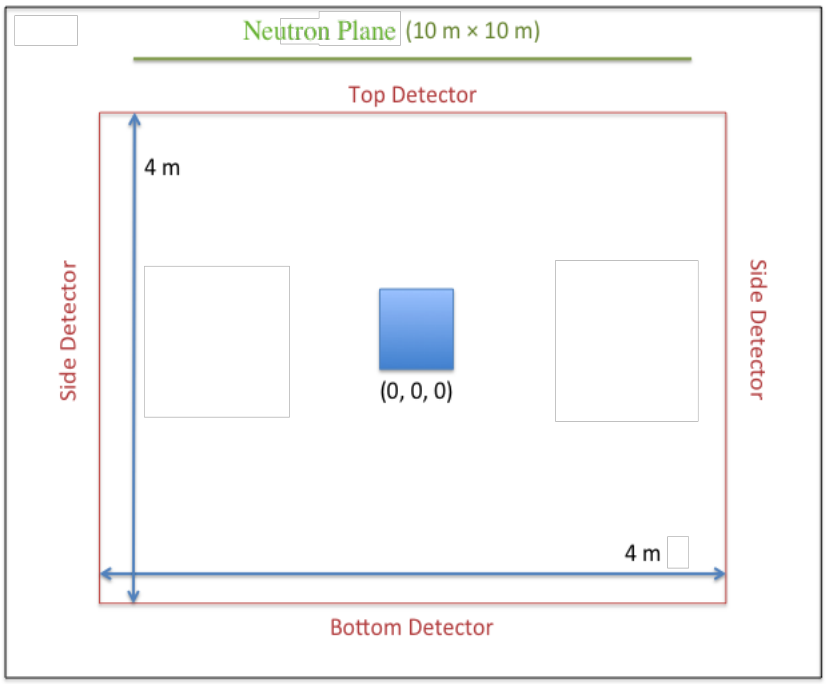


Fig. 7.4 *Standard set-up for the cosmic-ray neutron inspection volume system (not to scale).*

from low density materials (water, polyethylene, concrete). In a shielding scenario both nuclear and high-$Z$ material, or nuclear and medium-$Z$ materials will be used in tandem with one another. This acts to increase the total number of neutrons being produced over low-$Z$ materials (of the same size) and hence this signal should become even clearer. In general as density increases so does the number of excess $\gamma$-rays observed.

In a 5 minute exposure time there are $\approx$ 850,000 cosmic-ray neutrons generated over a 10 m $\times$ 10 m surface area. If these neutrons are evenly distributed there would be 2125 cosmic-ray neutrons over a 0.5 m $\times$ 0.5 m surface area and 85 cosmic-ray neutrons over a 0.1 m $\times$ 0.1 m surface area. These numbers represent a minimum amount of cosmic-ray neutrons one would expect to interact with 50 cm $\times$ 50 cm $\times$ 50 cm and 10 cm $\times$ 10 cm $\times$ 10 cm targets respectively. On average 4300 $\pm$ 65 cosmic-ray neutrons will interact with 50 cm $\times$ 50 cm $\times$ 50 cm sized targets in a 5 minute exposure time. This is significantly more than for 10 cm $\times$ 10 cm $\times$ 10 cm sized targets, where only 175 $\pm$ 15 will interact over the same time length. The increased number of interactions result in more neutrons and $\gamma$-rays being produced for all different materials. As shown

in Table 7.2 this again allows low-density and medium/high-density materials to be differentiated from one another.

An interesting feature observed is the number of additional $\gamma$-rays detected for iron over lead, for both 10 cm $\times$ 10 cm $\times$ 10 cm and 50 cm $\times$ 50 cm $\times$ 50 cm sized blocks. This increased amount is due to the self-shielding effects of lead. More $\gamma$-rays are produced in total through neutron interactions with lead. However, due to the higher density of lead, more $\gamma$-rays are reabsorbed by the target and therefore fewer are available for detection. If we consider a 1 MeV $\gamma$-ray generated at the centre of a block of size 10 cm $\times$ 10 cm $\times$ 10 cm, this $\gamma$-ray is required to travel at least 5 cm to exit the material. The intensity of $\gamma$-rays exiting a material is given by:

$$I = I_0 e^{-\mu x} \tag{7.1}$$

where $I$ is the intensity of $\gamma$-rays exiting, $I_0$ is the initial intensity, $\mu$ is the mass attenuation coefficient in units cm$^2$/g and $x$ is the depth of material in units g/cm$^2$. For $\gamma$-rays of energy 1 MeV passing out of 5 cm of iron or lead, Eq. (7.1) gives the fraction escaping as 9.45% for iron and 1.77% for lead. Therefore even though more $\gamma$-rays are produced when neutrons interact with lead, much fewer escape the target to be available for detection. Therefore even though more $\gamma$-rays are produced when neutrons interact with lead, much fewer escape the target to be available for detection. This feature may cause concerns when attempting to detect shielded HEU through observing an elevated $\gamma$-ray rate, in medium-$Z$ clutter scenarios.

From Table 7.2 it is evident large amounts of nuclear materials produce more neutrons or $\gamma$-rays, which distinguishes them from low-density clutter materials. Due to the results observed, further investigation into this area is made, which accounts for both detector capabilities, more complex geometries and the background. These results are discussed in section 7.3.2.

### 7.3.2 Lorry Scenario

The ability to detect shielded HEU in realistic empty cargo containers has been investigated using GEANT4.9.6-p02 with the 'Shielding 2.0' physics list. Three different types of cargo configuration were run: one where the cargo container was empty with no shielded HEU; one where the cargo container was empty except for HEU shielded

by iron; one where the cargo was empty except for HEU shielded by lead. So that adequate statistics were gathered, each type of configuration was simulated for 50 million cosmic-ray neutrons. Results have been scaled down to 850,000 neutrons, which represents a 5 minute exposure time are presented. We have used 20% enriched uranium (20% $^{235}$U and 80% $^{238}$U) with 7 cm lead shielding or 11 cm iron shielding. This amount of shielding is used as it is enough to attenuate the characteristic 1.001 MeV $\gamma$-ray line, so passive detection could not be made within 5 minutes at 3 standard deviation level. Around the volume to be inspected we placed four PVT $\gamma$-ray detectors (size 180 cm $\times$ 35 cm) and eight $^{3}$He neutron detectors (radius 2 cm and length 55 cm) in the same set-up as that used currently at ports. The efficiency for of $^{3}$He detectors for thermal neutrons is 77% [41]. For the applications discussed in this chapter the efficiency of neutron detectors for all energies was calculated as $\approx$ 1.3%. The efficiency was calculated through propagating 50 million cosmic-ray neutrons through the inspected volume setup described in Fig. 7.5 (but with no lorry). For $\gamma$-rays of all energies detector efficiency is equal to $\approx$ 67%. This efficiency was calculated via propagating $\gamma$-rays produced via radioactive decay of $^{238}$U and $^{232}$Th through 180 cm $\times$ 35 cm $\times$ 6 cm at random angles. A $\gamma$-ray was considered detected if interaction with the $\gamma$-ray detector yielded an electron. An example GEANT4 schematic is displayed in Fig. 7.5. The background level for neutrons and $\gamma$-rays have been calculated using GEANT4. A description of how this background level is ascertained is given in section 4.4.5. There are on average 41.1 $\pm$ 0.8 background neutrons and 300,170 $\pm$ 430 background $\gamma$-rays detected by the current set-up for a 5 minute exposure time.

The total amount of neutrons and $\gamma$-rays detected for each type of configuration is given in Table 7.3. As it can be seen from Table 7.3, for 5 minute exposure times with realistic detector coverage and efficiency, an elevated rate of neutrons is not observed for the configurations where shielded HEU is present. This indicates that under these conditions shielded HEU would struggle to be detected. For $\gamma$-rays there is a slight increase in the number observed when shielded HEU is present. However, this level is not sufficiently above the number of $\gamma$-rays observed when no HEU is present, for definitive detection to be made. An elevated rate is not observed due to the low detector coverage and the low number of neutrons that interact with the target. For HEU shielded by iron, on average 925 $\pm$ 5 neutrons pass through with the target. For HEU shielded by lead on average 520 $\pm$ 3 neutrons pass through with the target. This number includes both cosmic-ray neutrons and neutrons produced when cosmic-ray neutrons undergo inter-

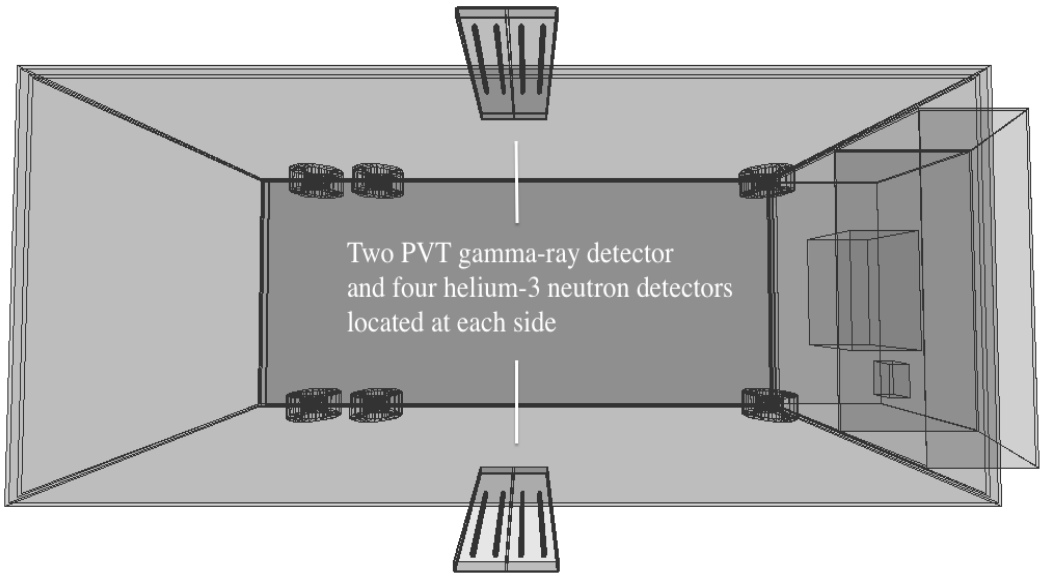


Fig. 7.5 *GEANT4 schematic of the inspected volume. Two PVT $\gamma$-ray detectors and four $^3$He neutron detectors are located at the sides of the lorry to be inspected.*

actions with the components of the lorry. Roughly a thousand times this many neutrons pass through the cargo container and components of the lorry. It is the neutrons and $\gamma$-rays produced from interactions with the components of the lorry, which primarily constitute those neutrons and $\gamma$-rays that are detected. The inability to detect shielded HEU in empty cargo containers means more complex configurations have not been considered.

If it is assumed that by doubling the detector area given in Table 7.3 twice as many secondaries will be detected, a basic estimation can be made to determine the amount of detector coverage required to detect shielded HEU at the 5 sigma level. This coverage is calculated assuming neutron and $\gamma$-ray detector efficiencies given in this thesis. Fig. 7.6 displays the amount of neutron or $\gamma$-ray detector coverage required to get a certain sigma level of detection for HEU shielded by iron or lead. From Fig. 7.6, $\approx$ 13 m$^2$ neutron detector coverage is required to identity HEU shielded by lead, $\approx$ 22 m$^2$ neutron detector coverage is required to identity HEU shielded by iron, $\approx$ 215 m$^2$ $\gamma$-ray detector coverage is required to identity HEU shielded by lead and $\approx$ 240 m$^2$ $\gamma$-ray detector coverage is required to identity HEU shielded by iron.

Table 7.4 displays the average amount of neutrons and $\gamma$-rays observed for 100% de-

tector coverage and efficiency. From Table 7.4 it is clearly evident that given a large enough detector coverage, HEU shielded by either iron or lead, can be discriminated from when there is no HEU present.

Table 7.3 Average neutron and $\gamma$-ray counts observed when propagating 50 million cosmic-ray neutrons through each configuration tested, where HEU is placed in a cargo container. Results have been scaled down to 850,000 neutrons as this represents a 5 minute exposure time. Realistic detector coverage and efficiencies have been used.

| Detector | No Threat | Iron Shielding | Lead Shielding |
|---|---|---|---|
| $^3$He 1 | $14.2 \pm 0.5$ | $15.1 \pm 0.5$ | $14.7 \pm 0.5$ |
| $^3$He 2 | $17.0 \pm 0.5$ | $17.1 \pm 0.5$ | $16.5 \pm 0.5$ |
| $^3$He 3 | $15.4 \pm 0.5$ | $15.4 \pm 0.5$ | $15.5 \pm 0.5$ |
| $^3$He 4 | $17.3 \pm 0.5$ | $18.0 \pm 0.6$ | $17.9 \pm 0.6$ |
| $^3$He 5 | $14.9 \pm 0.5$ | $14.7 \pm 0.5$ | $15.4 \pm 0.5$ |
| $^3$He 6 | $16.4 \pm 0.5$ | $17.5 \pm 0.5$ | $17.5 \pm 0.5$ |
| $^3$He 7 | $15.5 \pm 0.5$ | $15.5 \pm 0.5$ | $15.6 \pm 0.5$ |
| $^3$He 8 | $17.8 \pm 0.6$ | $16.4 \pm 0.5$ | $17.0 \pm 0.5$ |
| **Total Neutron** | $\mathbf{128.5 \pm 1.5}$ | $\mathbf{129.7 \pm 1.5}$ | $\mathbf{130.1 \pm 1.5}$ |
| PVT 1 | $73{,}680 \pm 35$ | $73{,}700 \pm 35$ | $73{,}700 \pm 35$ |
| PVT 2 | $77{,}855 \pm 35$ | $77{,}870 \pm 35$ | $77{,}895 \pm 35$ |
| PVT 3 | $74{,}550 \pm 35$ | $74{,}540 \pm 35$ | $74{,}550 \pm 35$ |
| PVT 4 | $80{,}915 \pm 35$ | $80{,}950 \pm 35$ | $80{,}925 \pm 35$ |
| **Total $\gamma$-ray** | $\mathbf{307{,}000 \pm 70}$ | $\mathbf{307{,}060 \pm 70}$ | $\mathbf{307{,}070 \pm 70}$ |

Table 7.4 Average neutron and $\gamma$-ray counts observed when propagating 50 million cosmic-ray neutrons through each configuration tested, where HEU is placed in a cargo container. Results have been scaled down to 850,000 neutrons as this represents a 5 minute exposure time. 100% detector coverage and efficiency is assumed.

| Detector | No Threat | Iron Shielding | Lead Shielding |
|---|---|---|---|
| Neutron Detector | $23{,}392{,}100 \pm 630$ | $23{,}445{,}000 \pm 630$ | $23{,}450{,}300 \pm 630$ |
| $\gamma$-ray Detector | $37{,}570{,}200 \pm 800$ | $37{,}585{,}400 \pm 800$ | $37{,}581{,}300 \pm 800$ |

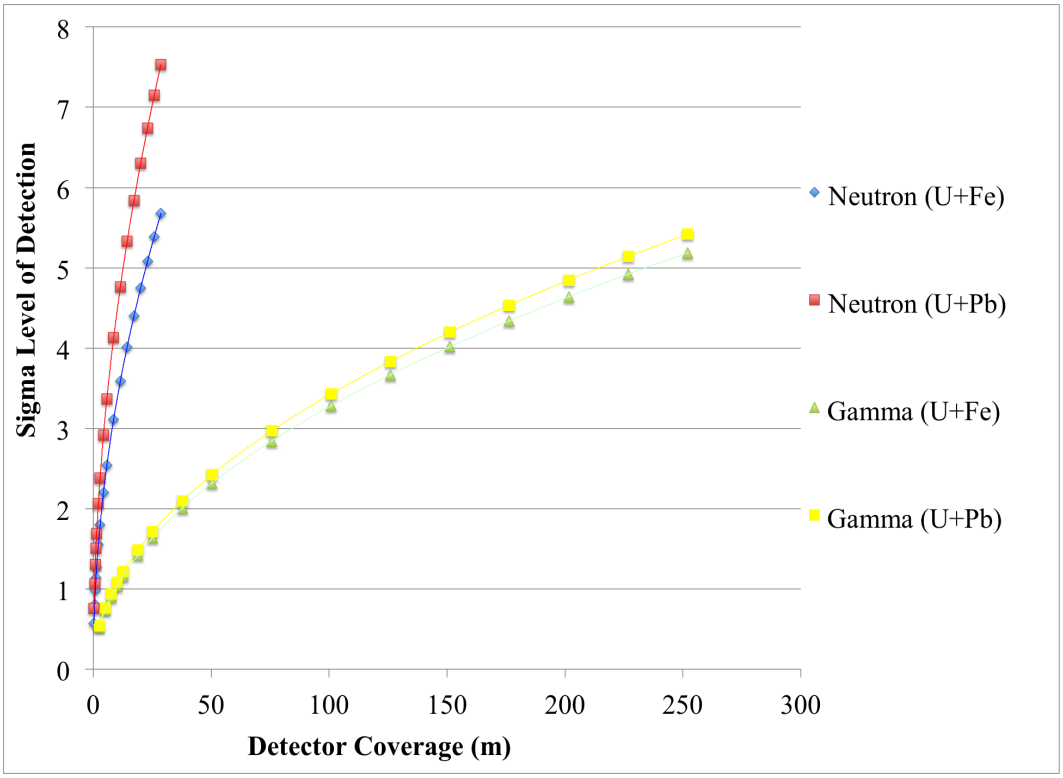


Fig. 7.6 *The amount of neutron or γ-ray detector coverage required to observe HEU shielded by iron or lead when placed in a empty cargo container. The detectors used have realistic efficiencies and the detector coverage m. For γ-rays of all energies detector efficiency is equal to ≈ 67%. The efficiency of neutron detectors for all energies was calculated as ≈ 1.3%.*

## 7.4 Summary

This section has discussed the capability of cosmic-ray neutrons to detect shielded HEU. Simulations were run that propagated 500,000 cosmic-ray neutrons into different materials. Neutron and $\gamma$-ray spectra have been analysed. These spectra demonstrate that given a large detector area with high efficiency, signatures unique to nuclear materials can be measured. For the applications discussed in this thesis, detector coverage is required to be similar to the realistic coverage currently in use at ports. This involves placing four plastic scintillators and eight pressurised $^{3}$He tubes around the inspected target. Current detection techniques rely on measuring the gross count rate of neutrons and $\gamma$-rays over time. If a sufficiently elevated rate above the background level is observed, then it may indicate the presence of nuclear material.

Simulations have been run that show for simple geometries with 5 minute exposure times, when given a large enough detector area and efficiency, different density materials can be distinguished from one another when measuring the excess neutrons or $\gamma$-rays produced. Upon the introduction of more realistic settings, whereby shielded HEU is placed within an empty cargo container, this technique struggles to detect shielded HEU under realistic detector conditions. Either extremely large detector coverages with realistic detector efficiencies or the use of 100% detector coverage and efficiency are required to allow the detection of shielded HEU.

# Chapter 8

# Conclusions

Current passive techniques have been shown to struggle to detect shielded nuclear material, in particular shielded HEU [25]. Cosmic-ray muons are a relatively new application towards aiding the detection of nuclear materials, particularly shielded HEU. The use of cosmic-ray muons has the advantage over active interrogation methods of being naturally occurring and therefore do not irradiate the cargo. Many groups have investigated the use of cosmic-ray muons for this application [2, 3, 83, 88, 90]. Studies focus on the advancement of analysis algorithms and the experimental testing of algorithms that are being developed. Most algorithms that use cosmic-ray muons focus on the multiple Coulomb scattering they undergo in materials. The average amount of scattering a muon undergoes is dependent on the $Z$ of a material. High-$Z$ materials such as HEU and its possible shielding components cause muons to scatter more than low-$Z$ materials. Therefore through calculating the average scattering of multiple muons that pass through an inspected volume, different materials can be identified.

This thesis has presented the development of two new types of algorithm that aim to enhance muon scattering tomography. In Chapter 5 we presented the development of a new density based clustering algorithm that utilises multiple Coulomb scattering. The algorithm splits the inspected volume into sections. Each section is analysed using a set of parameters optimised to that section. An advantage of this type of approach is that it accounts for the energy losses that occur as a muon passes through an inspected volume. This new analysis algorithm has shown promise in being able to detect shielded HEU when placed in empty cargo containers. This new algorithm has also shown to be able to efficiently detect shielded HEU in low-$Z$ clutter scenarios by removing clutter made of materials such as sand, concrete, gravel, carbon and polyethylene. The main

issue with the analysis algorithm is the inability to remove large blocks of aluminium or materials with densities greater than this. Secondly there are a number of false positives built up, which are due to the walls of the cargo container.

In addition to scattering, muons lose energy and can stop within a target material. We have developed an analysis algorithm based on muon disappearances within the inspected volume, to help enhance more traditional muon scattering tomography methods. Chapter 4 presented the initial concept of using muons that stop within an inspected volume. Initial tests of simple scenarios demonstrate the capability of this algorithm to distinguish different sized blocks of different density materials. Upon testing this algorithm in more realistic settings (empty cargo containers) this type of algorithm is shown to be able to detect shielded HEU, but also results in the build up of multiple false positives associated with the container itself. For this reason it is primarily used as a secondary analysis algorithm, to help enhance muon scattering tomography methods. The addition of the muon disappearance algorithm to muon scattering tomography has been shown to enhance muon scattering tomography through efficiently removing the false positives caused by muons that scatter within the cargo container walls.

Upon stopping in a material, negative muons can be captured, resulting in the production of excess neutrons and $\gamma$-rays. Chapter 4 presented a study of the feasibility of using these secondaries to detect different materials, under realistic detector and timing conditions. It is found that given a high enough detector resolution and area, these secondaries can be used to detect different density materials. However, under realistic detector coverage and efficiencies, these techniques become unfeasible.

Chapter 7 presented a study where cosmic-ray neutrons are used to detect shielded HEU. The time frame for our tests is 5 minutes. It has been determined that under realistic detector efficiencies and coverages these cosmic-ray neutrons offer no additional support when attempting to detected shielded HEU.

# References


[1] K. N. Borozdin, G. E. Hogan, C. Morris, W. C. Priedhorsky, A. Saunders, L. J. Schultz, and M. E. Teasdale, "Surveillance: Radiographic imaging with cosmic-ray muons," *Nature*, vol. 422, no. 6929, pp. 277–277, 2003.

[2] W. C. Priedhorsky, K. N. Borozdin, G. E. Hogan, C. Morris, A. Saunders, L. J. Schultz, and M. E. Teasdale, "Detection of high-Z objects using multiple scattering of cosmic ray muons," *Review of Scientific Instruments*, vol. 74, no. 10, pp. 4294–4297, 2003.

[3] L. J. Schultz, *Cosmic ray muon radiography*. PhD thesis, Portland State University, 2003.

[4] L. J. Schultz, K. N. Borozdin, J. J. Gomez, G. E. Hogan, J. McGill, C. Morris, W. Priedhorsky, A. Saunders, and M. Teasdale, "Image reconstruction and material Z discrimination via cosmic ray muon radiography," *Nuclear Instruments and Methods in Physics Research Section A: Accelerators, Spectrometers, Detectors and Associated Equipment*, vol. 519, no. 3, pp. 687–694, 2004.

[5] L. J. Schultz, G. S. Blanpied, K. N. Borozdin, A. M. Fraser, N. W. Hengartner, A. V. Klimenko, C. L. Morris, C. Oram, and M. J. Sossong, "Statistical reconstruction for cosmic ray muon tomography," *IEEE Transactions on Image Processing*, vol. 16, no. 8, pp. 1985–1993, 2007.

[6] R. T. Kouzes, E. R. Siciliano, J. H. Ely, P. E. Keller, and R. J. McConn, "Passive Neutron Detection at Borders," tech. rep., Pacific Northwest National Laboratory (PNNL), Richland, WA (US), 2008.

[7] R. Kouzes, J. Ely, B. Milbrath, J. Schweppe, E. Siciliano, and D. Stromswold, "Spectroscopic and non-spectroscopic radiation portal applications to border security," in *Nuclear Science Symposium Conference Record, 2005 IEEE*, vol. 1, pp. 321–325, IEEE, 2005.

[8] R. T. Kouzes, E. R. Siciliano, J. H. Ely, P. E. Keller, and R. J. McConn, "Passive neutron detection for interdiction of nuclear material at borders," *Nuclear Instruments and Methods in Physics Research A*, vol. 584, pp. 383–400, Jan. 2008.

[9] R. T. Kouzes, J. H. Ely, A. Seifert, E. R. Siciliano, D. R. Weier, L. K. Windsor, M. L. Woodring, J. Borgardt, E. Buckley, E. Flumerfelt, *et al.*, "Cosmic-ray-induced ship-effect neutron measurements and implications for cargo scanning at

borders," *Nuclear Instruments and Methods in Physics Research Section A: Accelerators, Spectrometers, Detectors and Associated Equipment*, vol. 587, no. 1, pp. 89–100, 2008.

[10] J. Ely, R. Kouzes, J. Schweppe, E. Siciliano, D. Strachan, and D. Weier, "The use of energy windowing to discriminate SNM from NORM in radiation portal monitors," *Nuclear Instruments and Methods in Physics Research A*, vol. 560, pp. 373–387, May 2006.

[11] N. Ensslin, "Principles of Neutron Coincidence Counting," *Passive Nondestructive Assay of Nuclear Materials*, vol. 550, 1991.

[12] C. A. L. Presti, D. R. Weier, R. T. Kouzes, and J. E. Schweppe, "Baseline suppression of vehicle portal monitor gamma count profiles: A characterization study," *Nuclear Instruments and Methods in Physics Research Section A: Accelerators, Spectrometers, Detectors and Associated Equipment*, vol. 562, no. 1, pp. 281–297, 2006.

[13] http://www.ortec-online.com.

[14] T. Gosnell, J. Hall, C. Jam, D. Knapp, Z. Koenig, S. Luke, B. Pohl, A. Schach von Wittenau, and J. Wolford, "Gamma-ray identification of nuclear weapons materials," tech. rep., Lawrence Livermore National Lab., Livermore, CA (US), 1997.

[15] G. Fiorentini, M. Lissia, and F. Mantovani, "Geo-neutrinos and earth's interior," *Physics Reports*, vol. 453, no. 5, pp. 117–172, 2007.

[16] T. Gozani, "Fission signatures for nuclear material detection," *IEEE Transactions on Nuclear Science*, vol. 56, no. 3, pp. 736–741, 2009.

[17] D. Langner, J. Stewart, M. Pickrell, M. Krick, N. Ensslin, and W. Harker, "Application Guide to Neutron Multiplicity Counting," tech. rep., Los Alamos National Laboratory, Los Alamos, NM, 1998.

[18] T. E. Valentine, "Evaluation of prompt fission gamma rays for use in simulating nuclear safeguard measurements," *Annals of Nuclear Energy*, vol. 28, no. 3, pp. 191–201, 2001.

[19] V. Verbinski, H. Weber, and R. Sund, "Prompt Gamma Rays from U-235 (n, f), Pu-239 (n, f), and Spontaneous Fission of Cf-252," *Physical Review C*, vol. 7, no. 3, pp. 1173–1185, 1973.

[20] D. Slaughter, M. Accatino, A. Bernstein, J. Candy, A. Dougan, *et al.*, *Detection of special nuclear material in cargo containers using neutron interrogation*. Lawrence Livermore National Laboratory, 2003.

[21] J. Caldwell, E. Dowdy, and G. M. Worth, "Prompt and delayed neutron yields from low-energy photofission of Th-232, U-235, U-238 and Pu-239," in *Physics and chemistry of fission*, 1973.

[22] D. Chichester and E. Seabury, "Using Electronic Neutron Generators in Active Interrogation to Detect Shielded Fissionable Material," *IEEE Transactions on Nuclear Science*, vol. 56, no. 2, pp. 441–447, 2009.

[23] R. C. Runkle, D. L. Chichester, and S. J. Thompson, "Rattling nucleons: New developments in active interrogation of special nuclear material," *Nuclear Instruments and Methods in Physics Research Section A: Accelerators, Spectrometers, Detectors and Associated Equipment*, vol. 663, no. 1, pp. 75–95, 2012.

[24] J. L. Jones, "Active, Non-Intrusive Inspection Technologies for Homeland Defense," tech. rep., Idaho National Laboratory (INL), 2003.

[25] J. Medalia, *Detection of nuclear weapons and materials: science, technologies, observations*. DIANE Publishing, 2010.

[26] K. A. Jordan and T. Gozani, "Pulsed neutron differential die away analysis for detection of nuclear materials," *Nuclear Instruments and Methods in Physics Research Section B: Beam Interactions with Materials and Atoms*, vol. 261, no. 1, pp. 365–368, 2007.

[27] K. A. Jordan and T. Gozani, "Detection of U-235 in hydrogenous cargo with Differential Die-Away Analysis and optimized neutron detectors," *Nuclear Instruments and Methods in Physics Research Section A: Accelerators, Spectrometers, Detectors and Associated Equipment*, vol. 579, no. 1, pp. 388–390, 2007.

[28] T. J. Shaw, D. A. Strellis, J. Stevenson, D. Keeley, and T. Gozani, "Fissile material detection by differential die away analysis," in *Application of Accelerators in Research and Industry: Twentieth International Conference*, vol. 1099, pp. 633–637, 2009.

[29] P. Kerr, M. Rowland, D. Dietrich, W. Stoeffl, B. Wheeler, L. Nakae, D. Howard, C. Hagmann, J. Newby, and R. Porter, "Active detection of small quantities of shielded highly-enriched uranium using low-dose 60-kev neutron interrogation," *Nuclear Instruments and Methods in Physics Research Section B: Beam Interactions with Materials and Atoms*, vol. 261, no. 1, pp. 347–350, 2007.

[30] D. Dietrich, C. Hagmann, P. Kerr, L. Nakae, M. Rowland, N. Snyderman, W. Stoeffl, and R. Hamm, "A kinematically beamed, low energy pulsed neutron source for active interrogation," *Nuclear Instruments and Methods in Physics Research Section B: Beam Interactions with Materials and Atoms*, vol. 241, no. 1, pp. 826–830, 2005.

[31] A. Danagoulian, W. Bertozzi, C. Hicks, A. V. Klimenko, S. E. Korbly, R. J. Ledoux, and C. M. Wilson, "Prompt neutrons from photofission and its use in homeland security applications," in *Technologies for Homeland Security (HST), 2010 IEEE International Conference on*, pp. 379–384, IEEE, 2010.

[32] B. Micklich, D. Smith, T. Massey, C. Fink, and D. Ingram, "FIGARO: detecting nuclear materials using high-energy gamma-rays," *Nuclear Instruments and Methods in Physics Research Section A: Accelerators, Spectrometers, Detectors and Associated Equipment*, vol. 505, no. 1, pp. 466–469, 2003.

[33] B. J. Micklich and D. L. Smith, "Nuclear materials detection using high-energy gamma-rays," *Nuclear Instruments and Methods in Physics Research Section B: Beam Interactions with Materials and Atoms*, vol. 241, no. 1, pp. 782–786, 2005.

[34] A. Dulloo, F. Ruddy, T. Congedo, J. Seidel, and M. McIlwain, "Experimental verification of modeling results for a PGNAA system for nondestructive assay of RCRA metals in drums," *Applied Radiation and Isotopes*, vol. 53, no. 4, pp. 499–505, 2000.

[35] J. L. Jones, W. Y. Yoon, K. J. Haskell, D. R. Norman, J. Hoggan, C. Moss, C. Goulding, C. Hollas, W. Myers, and E. Franco, "Photofission-based, nuclear material detection: technology demonstration," *INL Report*, pp. 02–01406, 2002.

[36] J. Jones, W. Yoon, K. Haskell, D. Norman, J. Zabriskie, J. Sterbentz, S. Watson, J. Johnson, B. Bennett, R. Watson, *et al.*, "Pulsed Photonuclear Assessment (PPA) Technique: CY 04 Year-end Progress Report," tech. rep., Idaho National Laboratory (INL), 2005.

[37] J. L. Jones, B. W. Blackburn, D. R. Norman, S. M. Watson, K. J. Haskell, J. T. Johnson, A. W. Hunt, F. Harmon, and C. Moss, "Status of the prototype Pulsed Photonuclear Assessment (PPA) inspection system," *Nuclear Instruments and Methods in Physics Research Section A: Accelerators, Spectrometers, Detectors and Associated Equipment*, vol. 579, no. 1, pp. 353–356, 2007.

[38] J. Hall, S. Asztalos, P. Biltoft, J. Church, M.-A. Descalle, T. Luu, D. Manatt, G. Mauger, E. Norman, D. Petersen, *et al.*, "The Nuclear Car Wash: Neutron interrogation of cargo containers to detect hidden SNM," *Nuclear Instruments and Methods in Physics Research Section B: Beam Interactions with Materials and Atoms*, vol. 261, no. 1, pp. 337–340, 2007.

[39] http://chemwiki.ucdavis.edu/Physical_Chemistry/Nuclear_Chemistry/Nuclear_Stability_and_Magic_Numbers.

[40] S. Kenneth and E. Richard, *Fundamentals of nuclear science and engineering*. Marcel Dekker, Inc, New York, 2002.

[41] K. S. Krane, *Introductory nuclear physics*. John Wiley and Sons Inc., New York, NY, 1987.

[42] E. Helder, J. Vink, C. Bassa, A. Bamba, J. Bleeker, S. Funk, P. Ghavamian, K. J. van der Heyden, F. Verbunt, and R. Yamazaki, "Measuring the cosmic-ray acceleration efficiency of a supernova remnant," *Science*, vol. 325, no. 5941, pp. 719–722, 2009.

[43] M. Bustamante, P. Jez, J. Monroy Montañez, G. Carrillo Montoya, G. Romeo, F. Padilla Cabal, J. Duarte Chavez, U. Saldaña-Salazar, M. Pino Rozas, M. Velasquez, *et al.*, "High-energy cosmic-ray acceleration," 2010.

[44] M. M. Shapiro, "The Primary Cosmic Radiation," tech. rep., DTIC Document, 1963.

[45] J. Beringer, J. Arguin, R. Barnett, K. Copic, O. Dahl, D. Groom, C. Lin, J. Lys, H. Murayama, C. Wohl, *et al.*, "Review of particle physics," *Physical Review D*, vol. 86, no. 1, 2012.

[46] http://neutronm.bartol.udel.edu/catch/cr2.html.

[47] B. C. Rastin, "An accurate measurement of the sea-level muon spectrum within the range 4 to 3000 GeV/c," *Journal of Physics G: Nuclear Physics*, vol. 10, no. 11, pp. 1609–1628, 1984.

[48] O. Allkofer, K. Carstensen, and W. Dau, "The absolute cosmic ray muon spectrum at sea level," *Physics Letters B*, vol. 36, no. 4, pp. 425–427, 1971.

[49] C. Hagmann, D. Lange, and D. Wright, "Monte Carlo simulation of proton-induced cosmic-ray cascades in the atmosphere," *Lawrence Livermore National Laboratory*, 2007.

[50] V. A. Kudryavtsev, "Muon simulations for LBNE using MUSIC and MUSUN," *LBNE-doc-5833 (April 2012)*, pp. 1–19, 2012.

[51] De Pascale, MP and Morselli, A and Picozza, P and Golden, RL and Grimani, C and Kimbell, BL and Stephens, SA and Stochaj, SJ and Webber, WR and Basini, G and others, "Absolute spectrum and charge ratio of cosmic ray muons in the energy region from 0.2 GeV to 100 GeV at 600 m above sea level," *Journal of Geophysical Research: Space Physics (1978–2012)*, vol. 98, no. A3, pp. 3501–3507, 1993.

[52] Ayre, CA and Baxendale, JM and Hume, CJ and Nandi, BC and Thompson, MG and Whalley, MR, "Precise measurement of the vertical muon spectrum in the range 20-500 GeV/c," *Journal of Physics G: Nuclear Physics*, vol. 1, no. 5, p. 584, 1975.

[53] Kremer, J and Boezio, M and Ambriola, ML ea and Barbiellini, G and Bartalucci, S and Bellotti, R and Bergström, D and Bravar, U and Cafagna, F and Carlson, P and others, "Measurements of ground-level muons at two geomagnetic locations," *Physical Review Letters*, vol. 83, no. 21, p. 4241, 1999.

[54] Haino, Sadakazu and Sanuki, T and Abe, K and Anraku, K and Asaoka, Y and Fuke, H and Imori, M and Itasaki, A and Maeno, T and Makida, Y and others, "Measurements of primary and atmospheric cosmic-ray spectra with the BESS-TeV spectrometer," *Physics Letters B*, vol. 594, no. 1, pp. 35–46, 2004.

[55] Achard, Pablo and Adriani, O and Aguilar-Benitez, M and Van Den Akker, M and Alcaraz, J and Alemanni, G and Allaby, J and Aloisio, A and Alviggi, MG and Anderhub, H and others, "Measurement of the atmospheric muon spectrum from 20 to 3000 GeV," *Physics Letters B*, vol. 598, no. 1, pp. 15–32, 2004.

[56] H. Jokisch, K. Carstensen, W. Dau, H. Meyer, and O. Allkofer, "Cosmic ray muon spectrum up to 1-TeV at 75-degrees zenith angle," *Physical Review*, vol. 19, pp. 1368–1372, 1979.

[57] M. Gordon, P. Goldhagen, K. Rodbell, T. Zabel, H. Tang, J. Clem, and P. Bailey, "Measurement of the flux and energy spectrum of cosmic-ray induced neutrons on the ground," *IEEE Transactions on Nuclear Science*, vol. 51, no. 6, pp. 3427–3434, 2004.

[58] J. F. Ziegler, "Terrestrial cosmic rays," *IBM journal of research and development*, vol. 40, no. 1, pp. 19–39, 1996.

[59] W. N. Hess, H. W. Patterson, R. Wallace, and E. L. Chupp, "Cosmic-ray neutron energy spectrum," *Physical Review*, vol. 116, no. 2, pp. 445–457, 1959.

[60] P. H. Barrett, L. M. Bollinger, G. Cocconi, Y. Eisenberg, and K. Greisen, "Interpretation of Cosmic-Ray Measurements Far Underground," *Review of Modern Physics*, vol. 24, pp. 133–178, 1952.

[61] H. Bethe, "Zur Theorie des Durchgangs schneller Korpuskularstrahlen durch Materie," *Annalen der Physik*, vol. 397, pp. 325–400, 1930.

[62] H. A. Bethe, "Molière's Theory of Multiple Scattering," *Physical Review*, vol. 89, pp. 1256–1266, 1953.

[63] G. R. Lynch and O. I. Dahl, "Approximations to multiple Coulomb scattering," *Nuclear Instruments and Methods in Physics Research Section B: Beam Interactions with Materials and Atoms*, vol. 58, no. 1, pp. 6 – 10, 1991.

[64] V. E. Oberacker, A. Sait Umar, and F. F. Karpeshin, "Prompt muon induced fission: A Sensitive probe for nuclear energy dissipation and fission dynamics," 2004.

[65] D. Measday, "The nuclear physics of muon capture," *Physics Reports*, vol. 354, no. 4–5, pp. 243 – 409, 2001.

[66] P. David, J. Hartfiel, H. Janszen, T. Mayer-Kuckuk, R. Mutius, C. Petitjean, H. Reist, S. Polikanov, J. Konijn, C. Laat, A. Taal, T. Krogulski, T. Johansson, G. Tibell, and J. d'Achard van Enschut, "The study of prompt and delayed muon induced fission," *Zeitschrift für Physik A Atomic Nuclei*, vol. 328, no. 1, pp. 37–47, 1987.

[67] B. Macdonald, J. A. Diaz, S. N. Kaplan, and R. V. Pyle, "Neutrons from negative-muon capture," *Physical Review*, vol. 139, no. 5B, p. B1253, 1965.

[68] P. Singer, "Emission of particles following muon capture in intermediate and heavy nuclei," in *Nuclear Physics*, pp. 39–87, Springer, 1974.

[69] W. Wilcke, M. Johnson, W. Schröder, J. Huizenga, and D. Perry, "Neutron emission from actinide muonic atoms," *Physical Review C*, vol. 18, no. 3, p. 1452, 1978.

[70] S. N. Kaplan, B. J. Moyer, and R. V. Pyle, "Neutron Emission Following μ-Meson Capture in Silver and Lead," *Physical Review*, vol. 112, no. 3, pp. 968–978, 1958.

[71] http://www.world-nuclear.org/info/Nuclear-Fuel-Cycle/Introduction/Physics-of-Nuclear-Energy/.

[72] V. Pronyaev, S. Simakov, and B. Marcinkevicius, "209 bi (n, f) and nat pb (n, f) cross sections as a new reference and extension of the 235 u, 238 u and 239 pu (n, f) standards up to 1 gev," tech. rep., NA, 2015.

[73] T. Ethvignot, M. Devlin, H. Duarte, T. Granier, R. Haight, B. Morillon, R. Nelson, J. O'Donnell, and D. Rochman, "Neutron multiplicity in the fission of u 238 and u 235 with neutrons up to 200 mev," *Physical review letters*, vol. 94, no. 5, p. 052701, 2005.

[74] E. George, "Cosmic Rays Measure Overburden of Tunnel," *Commonwealth Engineer*, vol. July 1, no. 1955, pp. 455–457, 1955.

[75] L. Alvarez, J. Anderson, F. El Bedwei, J. Burkhard, A. Fakhry, A. Girgis, A. Goneid, F. Hassan, D. Iverson, G. Lynch, Z. Miligy, A. Moussa, M. Sharkawi, and L. Yazolino, "Search for Hidden Chambers in the Pyramids," *Science*, vol. 167, pp. 832–839, 1970.

[76] S. Minato, "Feasibility of Cosmic-Ray Radiography: A Case Study of a Temple Gate as a Testpiece," *Materials Evaluation*, vol. 46, pp. 1468–1470, 1988.

[77] K. Nagamine, "Geo-tomographic Observation of Inner-structure of Volcano with Cosmic-ray Muons," *Journal of Geography*, vol. 104, no. 7, pp. 998–1007, 1995.

[78] K. Nagamine, M. Iwasaki, K. Shimomura, and K. Ishida, "Method of probing inner-structure of geophysical substance with the horizontal cosmic-ray muons and possible application to volcanic eruption prediction," *Nuclear Instruments and Methods in Physics Research Section A: Accelerators, Spectrometers, Detectors and Associated Equipment*, vol. 356, no. 2–3, pp. 585 – 595, 1995.

[79] H. Tanaka, K. Nagamine, N. Kawamura, S. Nakamura, K. Ishida, and K. Shimomura, "Development of the cosmic-ray muon detection system for probing internal-structure of a volcano," *Hyperfine interactions*, vol. 138, no. 1-4, pp. 521–526, 2001.

[80] H. K. M. Tanaka, H. Taira, T. Uchida, M. Tanaka, M. Takeo, T. Ohminato, Y. Aoki, R. Nishitama, D. Shoji, and H. Tsuiji, "Three-dimensional computational axial tomography scan of a volcano with cosmic ray muon radiography," *Journal of Geophysical Research: Solid Earth*, vol. 115, no. 12, 2010.

[81] P. Noli, "The MU-RAY project: volcano radiography with cosmic-ray muons," in *EGU General Assembly Conference Abstracts*, vol. 15 of *EGU General Assembly Conference Abstracts*, p. 2866, Apr. 2013.

[82] Dempster, Arthur P and Laird, Nan M and Rubin, Donald B, "Maximum likelihood from incomplete data via the EM algorithm," *Journal of the royal statistical society. Series B (methodological)*, pp. 1–38, 1977.

[83] Blackwell, TB and Kudryavtsev, VA, "Simulation Study into the Identification of Nuclear Materials in Cargo Containers Using Cosmic Rays," *Journal of Instrumentation*, vol. 10, no. 04, p. T04003, 2015.

[84] Blackwell, TB and Kudryavtsev, VA, "Development of a 3D muon disappearance algorithm for muon scattering tomography," *Journal of Instrumentation*, vol. 10, no. 05, p. T05006, 2015.

[85] M. S. Mitra, P. Sarkar, and V. Kudryavtsev, "Empirical expressions for angular deviation of muons transmitted through slabs of iron, lead and uranium," *Nuclear Instruments and Methods in Physics Research Section A: Accelerators, Spectrometers, Detectors and Associated Equipment*, vol. 604, no. 3, pp. 684–693, 2009.

[86] C. Morris, C. Alexander, J. Bacon, K. Borozdin, D. Clark, R. Chartrand, C. Espinoza, A. Fraser, M. Galassi, J. Green, *et al.*, "Tomographic Imaging with Cosmic Ray Muons," *Science and Global Security*, vol. 16, no. 1-2, pp. 37–53, 2008.

[87] K. Gnanvo, B. Benson, W. Bittner, F. Costa, L. Grasso, M. Hohlmann, J. Locke, S. Martoiu, H. Muller, M. Staib, *et al.*, "Detection and imaging of high-Z materials with a muon tomography station using GEM detectors," in *Nuclear Science Symposium Conference Record (NSS/MIC), 2010 IEEE*, pp. 552–559, IEEE, 2010.

[88] K. Gnanvo, P. Ford, J. Helsby, R. Hoch, D. Mitra, and M. Hohlmann, "Performance expectations for a tomography system using cosmic ray muons and micro pattern gas detectors for the detection of nuclear contraband," in *Nuclear Science Symposium Conference Record, 2008. NSS'08. IEEE*, pp. 1278–1284, IEEE, 2008.

[89] M. Hohlmann, P. Ford, K. Gnanvo, J. Helsby, D. Pena, R. Hoch, and D. Mitra, "GEANT4 Simulation of a Cosmic Ray Muon Tomography System With Micro-Pattern Gas Detectors for the Detection of High-Materials," *IEEE Transactions on Nuclear Science*, vol. 56, no. 3, pp. 1356–1363, 2009.

[90] P. Baesso, D. Cussans, C. Thomay, J. Velthuis, J. Burns, C. Steer, and S. Quillin, "A high resolution resistive plate chamber tracking system developed for cosmic ray muon tomography," *Journal of Instrumentation*, vol. 8, no. 8, pp. 1–14, 2013.

[91] Thomay, C and Velthuis, JJ and Baesso, P and Cussans, D and Morris, PAW and Steer, C and Burns, J and Quillin, S and Stapleton, M, "A binned clustering algorithm to detect high-Z material using cosmic muons," *Journal of Instrumentation*, vol. 8, no. 10, p. P10013, 2013.

[92] BURNS, Jonathan and Quillin, Steve and Stapleton, Matthew and Steer, Chris, "Muon Scattering Tomography using Drift Chamber Detectors," in *Proceedings of Technology and Instrumentation in Particle Physics 2014 (TIPP2014). 2-6 June 2014. Amsterdam, the Netherlands. Online at http://pos. sissa. it/cgi-bin/reader/conf. cgi? confid= 213, id. 291*, vol. 1, p. 291, 2014.

[93] Baesso, P and Cussans, D and Thomay, C and Velthuis, J, "Toward a RPC-based muon tomography system for cargo containers.," *Journal of Instrumentation*, vol. 9, no. 10, p. C10041, 2014.

[94] Clarkson, Anthony and Hamilton, David J and Hoek, Matthias and Ireland, David G and Johnstone, John R and Kaiser, Ralf and Keri, Tibor and Lumsden, Scott and Mahon, David F and McKinnon, Bryan and others, "Characterising encapsulated nuclear waste using cosmic-ray muon tomography," *Journal of Instrumentation*, vol. 10, no. 03, p. P03020, 2015.

[95] Clarkson, Anthony and Hamilton, David J and Hoek, Matthias and Ireland, David G and Johnstone, JR and Kaiser, Ralf and Keri, Tibor and Lumsden, Scott and Mahon, David F and McKinnon, Bryan and others, "GEANT4 simulation of a scintillating-fibre tracker for the cosmic-ray muon tomography of legacy nuclear waste containers," *Nuclear Instruments and Methods in Physics Research Section A: Accelerators, Spectrometers, Detectors and Associated Equipment*, vol. 746, pp. 64–73, 2014.

[96] http://www.slac.stanford.edu/comp/physics/geant4/slac_physics_lists/shielding/shielding.html.

[97] S. Agostinelli, J. Allison, K. a. Amako, J. Apostolakis, H. Araujo, P. Arce, M. Asai, D. Axen, S. Banerjee, G. Barrand, *et al.*, "GEANT4—A simulation toolkit," *Nuclear instruments and methods in physics research section A: Accelerators, Spectrometers, Detectors and Associated Equipment*, vol. 506, no. 3, pp. 250–303, 2003.

[98] J. Allison, K. Amako, J. Apostolakis, H. Araujo, P. A. Dubois, M. Asai, G. Barrand, R. Capra, S. Chauvie, R. Chytracek, *et al.*, "GEANT4 developments and applications," *IEEE Transactions on Nuclear Science*, vol. 53, no. 1, pp. 270–278, 2006.

[99] T. K. Gaisser, *Cosmic Rays and Partcle Physics*. Cambridge University Press, 1991.

[100] G. Mengyun, "Muon simulation at the Daya Bay site," *Lawrence Berkeley National Laboratory*, 2011.

[101] D. Sunday, "Distance between Lines and Segments with their Closest Point of Approach [Online]," 2006.

[102] I. Bobodyanov, "On the multiplicity of neutrons produced by μ-capture," in *International Cosmic Ray Conference*, 1970.

[103] T. Yamazaki, K. Nagamine, S. Nagamiya, O. Hashimoto, K. Sugimoto, K. Nakai, and S. Kobayashi, "Negative Muon Spin Rotation," *Physica Scripta*, vol. 11, no. 3-4, p. 133, 1975.

[104] H. Anderson, C. Hargrove, E. Hincks, J. McAndrew, R. McKee, R. Barton, and D. Kessler, "Precise measurement of the muonic x rays in the lead isotopes," *Physical Review*, vol. 187, no. 4, p. 1565, 1969.

[105] F. Hartmann, T. Von Egidy, R. Bergmann, M. Kleber, H.-J. Pfeiffer, K. Springer, and H. Daniel, "Measurement of the muonic x-ray cascade in metallic iron," *Physical Review Letters*, vol. 37, no. 6, p. 331, 1976.

[106] R. Coté, W. Prestwich, A. Gaigalas, S. Raboy, C. Trail, R. Carrigan Jr, P. Gupta, R. Sutton, M. Suzuki, and A. Thompson, "Distribution of charge in th 232 and u 238 determined by measurements on muonic x rays," *Physical Review*, vol. 179, no. 4, p. 1134, 1969.

[107] A. C. Kak and M. Slaney, *Principles of computerized tomographic imaging*. Society for Industrial and Applied Mathematics, 2001.

[108] D. Hamby and A. Tynybekov, "Uranium, thorium, and potassium in soils along the shore of lake issyk-kyol in the kyrghyz republic," *Environmental Monitoring and Assessment*, vol. 73, no. 2, pp. 101–108, 2002.

[109] S. Fetter, V. A. Frolov, M. Miller, R. Mozley, O. F. Prilutsky, S. N. Rodionov, and R. Z. Sagdeev, "Detecting Nuclear Warheads," *Science and Global Security*, vol. 1, pp. 225–302, 1990.

[110] J. Frehaut, M. Soleilhac, and G. Mosinski, "Measurement of the average number of prompt neutrons emitted in the fission of Pu-240 and U-235 induced by neutrons of energy between 1.5 to 15 MeV.," *Private Communication*, 1980.

[111] J. Frehaut, R. Bois, and A. Bertin, "Measurement of prompt ν-bar and prompt e-gamma in the fission of Th-232, U-235 and Np-237 induced by neutrons in the energy range between 1 and 15 MeV.," in *Conference on Nuclear Data for Science and Technology, Antwerp*, 1982.

[112] R. Gwin, R. Spencer, R. Ingle, J. Todd, and H. Weaver, "Measurement of the average number of prompt neutrons emitted per fission of U-235 relative to Cf-252 for the energy region 500 eV to 10 MeV," tech. rep., Oak Ridge National Lab., TN (USA), 1980.

[113] B. Nurpeisov, K. E. Volodin, V. G. Nesterov, L. I. Prokhorova, G. N. Smirenkin, and Y. M. Turchin, "Dependence of ν-bar on Neutron Energies up to 5 MeV for U-233, U-238, and Pu-239," *Atomnaya Energiya*, vol. 39, no. 3, p. 199, 1975.

[114] M. V. Savin, Y. Khokhlov, I. N. Paramonova, and V. A. Chirkin, "Energy Dependence of nu for Fast-Neutron Fission of 238-U," *Atomnaya Energiya*, vol. 32, p. 408, 1972.

[115] *The Definition of ν-Energy Dependence For U-238, Pu-240 and Pu-241 by Analysis of Fission Energy Balance*, 1974.

# Appendix A

# Clutter Description for all Configurations Tested

Given are tables which describe the different types of clutter placed within all cargo containers for both low-$Z$ and medium-$Z$ clutter scenarios. They have the same format as Table 6.1.

Table A.1 Description of the different types of clutter placed within the cargo container for Run 1. Both low-$Z$ and medium-$Z$ clutter configurations are described.

| Material (low-$Z$) | Material (medium-$Z$) | Description | $x$ (m) | $y$ (m) | $z$ (m) |
|---|---|---|---|---|---|
| Aluminium | Weathering Steel | Solid block of dimensions 101.9 cm × 101.9 cm × 25 cm | 0 | -0.56 | -0.858 |
| Aluminium | Weathering Steel | Solid block of dimensions 101.9 cm × 101.9 cm × 50 cm | 2.1 | -0.56 | -0.608 |
| Polyethylene | Aluminium | Solid block of dimensions 101.9 cm × 101.9 cm × 25 cm | -2.1 | -0.56 | 0.512 |
| Polyethylene | Aluminium | Hollow sphere of outer radius 35 cm and inner radius 16 cm | -2.1 | 0.56 | 0.512 |
| Polyethylene | Weathering Steel | Hollow sphere of outer radius 35 cm and inner radius 12 cm | 2.1 | 0.56 | -0.608 |
| Carbon | Iron | Solid block of dimensions 101.9 cm × 101.9 cm × 50 cm | -2.1 | 0.56 | -0.608 |
| Polyethylene | Aluminium | Solid block of dimensions 101.9 cm × 101.9 cm × 25 cm | 0 | -0.56 | 0.512 |
| Carbon | Aluminium | Solid block of dimensions 101.9 cm × 101.9 cm × 50 cm | 0 | 0.56 | 0.512 |

Table A.2 Description of the different types of clutter placed within the cargo container for Run 2. Both low-$Z$ and medium-$Z$ clutter configurations are described.

| Material (low-$Z$) | Material (medium-$Z$) | Description | $x$ (m) | $y$ (m) | $z$ (m) |
|---|---|---|---|---|---|
| Aluminium | Iron | Solid block of dimensions 101.9 cm × 101.9 cm × 25 cm | 0 | -0.56 | -0.858 |
| Aluminium | Aluminium | Solid block of dimensions 101.9 cm × 101.9 cm × 25 cm | 2.1 | -0.56 | -0.708 |
| Polyethylene | Aluminium | Solid block of dimensions 101.9 cm × 101.9 cm × 25 cm | -2.1 | -0.56 | 0.612 |
| Polyethylene | Weathering Steel | Hollow sphere of outer radius 35 cm and inner radius 16 cm | -2.1 | 0.56 | 0.512 |
| Polyethylene | Aluminium | Hollow sphere of outer radius 35 cm and inner radius 12 cm | 2.1 | 0.56 | -0.608 |
| Carbon | Iron | Solid block of dimensions 101.9 cm × 101.9 cm × 25 cm | -2.1 | 0.56 | -0.608 |
| Polyethylene | Aluminium | Solid block of dimensions 101.9 cm × 101.9 cm × 50 cm | 0 | -0.56 | 0.512 |
| Carbon | Stainless Steel | Solid block of dimensions 101.9 cm × 101.9 cm × 25 cm | 0 | 0.56 | 0.512 |

Table A.3 Description of the different types of clutter placed within the cargo container for Run 3. Both low-$Z$ and medium-$Z$ clutter configurations are described.

| Material (low-$Z$) | Material (medium-$Z$) | Description | $x$ (m) | $y$ (m) | $z$ (m) |
|---|---|---|---|---|---|
| Aluminium | Aluminium | Solid block of dimensions 101.9 cm × 101.9 cm × 25 cm | 0 | -0.56 | -0.858 |
| Aluminium | Stainless Steel | Solid block of dimensions 101.9 cm × 101.9 cm × 25 cm | 2.1 | -0.56 | -0.608 |
| Polyethylene | Aluminium | Solid block of dimensions 101.9 cm × 101.9 cm × 50 cm | -2.1 | -0.56 | 0.712 |
| Polyethylene | Weathering Steel | Hollow sphere of outer radius 35 cm and inner radius 16 cm | -2.1 | -0.56 | 0.512 |
| Polyethylene | Stainless Steel | Hollow sphere of outer radius 35 cm and inner radius 12 cm | 2.1 | 0.56 | -0.608 |
| Carbon | Aluminium | Solid block of dimensions 101.9 cm × 101.9 cm × 50 cm | -2.1 | 0.56 | -0.608 |
| Polyethylene | Iron | Solid block of dimensions 101.9 cm × 101.9 cm × 25 cm | 0 | -0.56 | 0.512 |
| Carbon | Aluminium | Solid block of dimensions 101.9 cm × 101.9 cm × 50 cm | 0 | 0.56 | 0.512 |

Table A.4 Description of the different types of clutter placed within the cargo container for Run 11. Both low-$Z$ and medium-$Z$ clutter configurations are described.

| Material (low-$Z$) | Material (medium-$Z$) | Description | $x$ (m) | $y$ (m) | $z$ (m) |
|---|---|---|---|---|---|
| Gravel | Stainless Steel | Solid block of dimensions 101.9 cm × 101.9 cm × 25 cm | 0 | -0.56 | -0.858 |
| Concrete | Aluminium | Solid block of dimensions 101.9 cm × 101.9 cm × 50 cm | 2.1 | -0.56 | -0.608 |
| Sand | Iron | Solid block of dimensions 101.9 cm × 101.9 cm × 25 cm | -2.1 | -0.56 | 0.512 |
| Gravel | Aluminium | Hollow sphere of outer radius 35 cm and inner radius 16 cm | -2.1 | 0.56 | 0.512 |
| Sand | Weathering Steel | Hollow sphere of outer radius 35 cm and inner radius 12 cm | 2.1 | 0.56 | -0.608 |
| Aluminium | Aluminium | Solid block of dimensions 101.9 cm × 101.9 cm × 50 cm | -2.1 | 0.56 | -0.608 |
| Carbon | Iron | Solid block of dimensions 101.9 cm × 101.9 cm × 25 cm | 0 | -0.56 | 0.512 |
| Polyethylene | Stainless Steel | Solid block of dimensions 101.9 cm × 101.9 cm × 50 cm | 0 | 0.56 | 0.512 |

Table A.5 Description of the different types of clutter placed within the cargo container for Run 12. Both low-$Z$ and medium-$Z$ clutter configurations are described.

| Material (low-$Z$) | Material (medium-$Z$) | Description | $x$ (m) | $y$ (m) | $z$ (m) |
|---|---|---|---|---|---|
| Sand | Iron | Solid block of dimensions 101.9 cm × 101.9 cm × 25 cm | 2.1 | 0.56 | -0.608 |
| Sand | Stainless Steel | Solid block of dimensions 101.9 cm × 101.9 cm × 50 cm | -0.8 | -0.56 | -0.608 |
| Gravel | Aluminium | Solid block of dimensions 101.9 cm × 101.9 cm × 25 cm | -2.1 | 0.56 | -0.608 |
| Polyethylene | Aluminium | Hollow sphere of outer radius 35 cm and inner radius 16 cm | 0 | 0 | 0.512 |
| Carbon | Weathering Steel | Hollow sphere of outer radius 35 cm and inner radius 12 cm | 0.8 | 0.56 | -0.608 |
| Gravel | Stainless Steel | Solid block of dimensions 101.9 cm × 101.9 cm × 25 cm | 0.8 | -0.56 | -0.608 |
| Carbon | Aluminium | Hollow block of outer dimensions 101.9 cm × 101.9 cm × 70 cm and inner dimensions 33 cm × 33 cm × 33 cm | -0.8 | 0.56 | -0.5 |
| Aluminium | Aluminium | Solid block of dimensions 101.9 cm × 101.9 cm × 50 cm | -1.55 | -0.56 | 0.512 |
| Sand | Iron | Hollow block of outer dimensions 101.9 cm × 101.9 cm × 50 cm and inner dimensions 33 cm × 33 cm × 33 cm | 2.1 | -0.56 | -0.5 |

Table A.6 Description of the different types of clutter placed within the cargo container for Run 13. Both low-$Z$ and medium-$Z$ clutter configurations are described.

| Material (low-$Z$) | Material (medium-$Z$) | Description | $x$ (m) | $y$ (m) | $z$ (m) |
|---|---|---|---|---|---|
| Polyethylene | Iron | Solid block of dimensions 101.9 cm × 101.9 cm × 25 cm | 2.1 | 0.56 | -0.608 |
| Gravel | Weathering Steel | Solid block of dimensions 101.9 cm × 101.9 cm × 50 cm | -0.8 | -0.56 | -0.608 |
| Carbon | Aluminium | Solid block of dimensions 101.9 cm × 101.9 cm × 25 cm | -2.1 | 0.56 | -0.608 |
| Aluminium | Iron | Hollow sphere of outer radius 35 cm and inner radius 16 cm | 0 | 0 | 0.512 |
| Sand | Stainless Steel | Hollow sphere of outer radius 35 cm and inner radius 12 cm | 0.8 | 0.56 | -0.608 |
| Carbon | Stainless Steel | Solid block of dimensions 101.9 cm × 101.9 cm × 25 cm | 0.8 | -0.56 | -0.608 |
| Gravel | Aluminium | Hollow block of outer dimensions 101.9 cm × 101.9 cm × 70 cm and inner dimensions 33 cm × 33 cm × 33 cm | -0.8 | 0.56 | -0.5 |
| Concrete | Aluminium | Solid block of dimensions 101.9 cm × 101.9 cm × 50 cm | -1.55 | -0.56 | 0.512 |
| Polyethylene | Stainless Steel | Hollow block of outer dimensions 101.9 cm × 101.9 cm × 50 cm and inner dimensions 33 cm × 33 cm × 33 cm | 2.1 | -0.56 | -0.5 |

Table A.7 Description of the different types of clutter placed within the cargo container for Run 14. Both low-$Z$ and medium-$Z$ clutter configurations are described.

| Material (low-$Z$) | Material (medium-$Z$) | Description | $x$ (m) | $y$ (m) | $z$ (m) |
|---|---|---|---|---|---|
| Gravel | Weathering Steel | Solid block of dimensions 101.9 cm × 101.9 cm × 25 cm | 0 | -0.56 | -0.858 |
| Concrete | Iron | Solid block of dimensions 101.9 cm × 101.9 cm × 25 cm | 2.1 | -0.56 | -0.708 |
| Sand | Aluminium | Solid block of dimensions 101.9 cm × 101.9 cm × 25 cm | -2.1 | -0.56 | 0.612 |
| Gravel | Iron | Hollow sphere of outer radius 35 cm and inner radius 16 cm | -2.1 | 0.56 | 0.512 |
| Sand | Aluminium | Hollow sphere of outer radius 35 cm and inner radius 12 cm | 2.1 | 0.56 | -0.608 |
| Aluminium | Stainless Steel | Solid block of dimensions 101.9 cm × 101.9 cm × 25 cm | -2.1 | 0.56 | -0.608 |
| Carbon | Stainless Steel | Solid block of dimensions 101.9 cm × 101.9 cm × 50 cm | 0 | -0.56 | 0.512 |
| Polyethylene | Aluminium | Solid block of dimensions 101.9 cm × 101.9 cm × 25 cm | 0 | 0.56 | 0.512 |

Table A.8 Description of the different types of clutter placed within the cargo container for Run 15. Both low-$Z$ and medium-$Z$ clutter configurations are described.

| Material (low-$Z$) | Material (medium-$Z$) | Description | $x$ (m) | $y$ (m) | $z$ (m) |
|---|---|---|---|---|---|
| Aluminium | Aluminium | Solid block of dimensions 101.9 cm × 101.9 cm × 50 cm | -1.55 | -0.56 | 0.412 |
| Polyethylene | Weathering Steel | Hollow sphere of outer radius 35 cm and inner radius 16 cm | 0 | 0 | 0.512 |
| Air | Sand | Solid block of dimensions 101.9 cm × 101.9 cm × 90 cm | 2.1 | -0.56 | -0.5 |
| Sand | Aluminium | Hollow block of outer dimensions 101.9 cm × 101.9 cm × 101.9 cm and inner dimensions 33 cm × 33 cm × 33 cm | 2.1 | 0.56 | -0.608 |
| Sand | Iron | Hollow block of outer dimensions 101.9 cm × 101.9 cm × 50.5 cm and inner dimensions 33 cm × 33 cm × 33 cm | -0.8 | -0.56 | -0.608 |
| Gravel | Stainless Steel | Hollow block of outer dimensions 101.9 cm × 101.9 cm × 101.9 cm and inner dimensions 33 cm × 33 cm × 33 cm | -2.1 | 0.56 | -0.608 |
| Carbon | Aluminium | Hollow sphere of outer radius 35 cm and inner radius 12 cm | 0.8 | 0.56 | -0.608 |
| Gravel | Iron | Solid block of dimensions 101.9 cm × 101.9 cm × 25 cm | 0.8 | -0.56 | -0.608 |
| Carbon | Aluminium | Solid block of dimensions 100 cm × 100 cm × 70 cm | -0.8 | 0.56 | -0.608 |

Table A.9 Description of the different types of clutter placed within the cargo container for Run 16. Both low-$Z$ and medium-$Z$ clutter configurations are described.

| Material (low-$Z$) | Material (medium-$Z$) | Description | $x$ (m) | $y$ (m) | $z$ (m) |
|---|---|---|---|---|---|
| Concrete | Iron | Solid block of dimensions 101.9 cm × 101.9 cm × 50 cm | -1.55 | -0.56 | 0.412 |
| Aluminium | Aluminium | Hollow sphere of outer radius 35 cm and inner radius 16 cm | 0 | 0 | 0.512 |
| Polyethylene | Iron | Solid block of dimensions 101.9 cm × 101.9 cm × 90 cm | 2.1 | -0.56 | -0.5 |
| Polyethylene | Stainless Steel | Hollow block of outer dimensions 101.9 cm × 101.9 cm × 101.9 cm and inner dimensions 33 cm × 33 cm × 33 cm | 2.1 | 0.56 | -0.608 |
| Gravel | Stainless Steel | Hollow block of outer dimensions 101.9 cm × 101.9 cm × 50.5 cm and inner dimensions 33 cm × 33 cm × 33 cm | -0.8 | -0.56 | -0.608 |
| Carbon | Weathering Steel | Hollow block of outer dimensions 101.9 cm × 101.9 cm × 101.9 cm and inner dimensions 33 cm × 33 cm × 33 cm | -2.1 | 0.56 | -0.608 |
| Sand | Aluminium | Hollow sphere of outer radius 35 cm and inner radius 12 cm | 0.8 | 0.56 | -0.608 |
| Carbon | Iron | Solid block of dimensions 101.9 cm × 101.9 cm × 25 cm | 0.8 | -0.56 | -0.608 |
| Carbon | Aluminium | Solid block of dimensions 100 cm × 100 cm × 70 cm | -0.8 | 0.56 | -0.608 |

Table A.10 Description of the different types of clutter placed within the cargo container for Run 17. Both low-$Z$ and medium-$Z$ clutter configurations are described.

| Material (low-$Z$) | Material (medium-$Z$) | Description | $x$ (m) | $y$ (m) | $z$ (m) |
|---|---|---|---|---|---|
| Gravel | Iron | Solid block of dimensions 101.9 cm × 101.9 cm × 25 cm | 0 | -0.56 | -0.858 |
| Concrete | Aluminium | Solid block of dimensions 101.9 cm × 101.9 cm × 25 cm | 2.1 | -0.56 | -0.608 |
| Sand | Aluminium | Solid block of dimensions 101.9 cm × 101.9 cm × 50 cm | -2.1 | -0.56 | 0.712 |
| Gravel | Stainless Steel | Hollow sphere of outer radius 35 cm and inner radius 16 cm | -2.1 | -0.56 | 0.512 |
| Sand | Weathering Steel | Hollow sphere of outer radius 35 cm and inner radius 12 cm | 2.1 | 0.56 | -0.608 |
| Aluminium | Aluminium | Solid block of dimensions 101.9 cm × 101.9 cm × 50 cm | -2.1 | 0.56 | -0.608 |
| Carbon | Aluminium | Solid block of dimensions 101.9 cm × 101.9 cm × 25 cm | 0 | -0.56 | 0.512 |
| Polyethylene | Aluminium | Solid block of dimensions 101.9 cm × 101.9 cm × 50 cm | 0 | 0.56 | 0.512 |

Table A.11 Description of the different types of clutter placed within the cargo container for Run 18. Both low-$Z$ and medium-$Z$ clutter configurations are described.

| Material (low-$Z$) | Material (medium-$Z$) | Description | $x$ (m) | $y$ (m) | $z$ (m) |
|---|---|---|---|---|---|
| Sand | Iron | Hollow block of outer dimensions 101.9 cm × 101.9 cm × 101.9 cm and inner dimensions 33 cm × 33 cm × 33 cm | 2.1 | 0.56 | -0.608 |
| Sand | Weathering Steel | Hollow block of outer dimensions 101.9 cm × 101.9 cm × 50.5 cm and inner dimensions 33 cm × 33 cm × 33 cm | -0.8 | -0.56 | -0.608 |
| Polyethylene | Gravel | Hollow block of outer dimensions 101.9 cm × 101.9 cm × 80.5 cm and inner dimensions 33 cm × 33 cm × 33 cm | -2.1 | 0.56 | -0.608 |
| Polyethylene | Aluminium | Hollow sphere of outer radius 35 cm and inner radius 16 cm | 0 | 0 | 0.512 |
| Carbon | Iron | Hollow sphere of outer radius 35 cm and inner radius 12 cm | 0.8 | 0.56 | -0.608 |
| Gravel | Stainless Steel | Solid block of dimensions 101.9 cm × 101.9 cm × 25 cm | 0.8 | -0.56 | -0.608 |
| Carbon | Iron | Hollow block of outer dimensions 101.9 cm × 101.9 cm × 50 cm and inner dimensions 29 cm × 29 cm × 29 cm | -0.8 | 0.56 | -0.5 |
| Carbon | Stainless Steel | Hollow block of outer dimensions 101.9 cm × 101.9 cm × 50 cm and inner dimensions 29 cm × 29 cm × 29 cm | -1.55 | -0.56 | 0.412 |
| Sand | Iron | Solid block of dimensions 101.9 cm × 101.9 cm × 20 cm | 2,1 | -0.56 | -0.5 |

Table A.12 Description of the different types of clutter placed within the cargo container for Run 19. Both low-$Z$ and medium-$Z$ clutter configurations are described.

| Material (low-$Z$) | Material (medium-$Z$) | Description | $x$ (m) | $y$ (m) | $z$ (m) |
|---|---|---|---|---|---|
| Polyethylene | Weathering Steel | Hollow block of outer dimensions 101.9 cm × 101.9 cm × 101.9 cm and inner dimensions 33 cm × 33 cm × 33 cm | 2.1 | 0.56 | -0.608 |
| Gravel | Stainless Steel | Hollow block of outer dimensions 101.9 cm × 101.9 cm × 50.5 cm and inner dimensions 33 cm × 33 cm × 33 cm | -0.8 | -0.56 | -0.608 |
| Carbon | Iron | Hollow block of outer dimensions 101.9 cm × 101.9 cm × 80.5 cm and inner dimensions 33 cm × 33 cm × 33 cm | -2.1 | 0.56 | -0.608 |
| Aluminium | Aluminium | Hollow sphere of outer radius 35 cm and inner radius 16 cm | 0 | 0 | 0.512 |
| Sand | Aluminium | Hollow sphere of outer radius 35 cm and inner radius 12 cm | 0.8 | 0.56 | -0.608 |
| Carbon | Aluminium | Solid block of dimensions 101.9 cm × 101.9 cm × 25 cm | 0.8 | -0.56 | -0.608 |
| Gravel | Iron | Hollow block of outer dimensions 101.9 cm × 101.9 cm × 50 cm and inner dimensions 29 cm × 29 cm × 29 cm | -0.8 | 0.56 | -0.5 |
| Concrete | Stainless Steel | Hollow block of outer dimensions 101.9 cm × 101.9 cm × 50 cm and inner dimensions 29 cm × 29 cm × 29 cm | -1.55 | -0.56 | 0.412 |
| Polyethylene | Weathering Steel | Solid block of dimensions 101.9 cm × 101.9 cm × 20 cm | 2,1 | -0.56 | -0.5 |

Table A.13 Description of the different types of clutter placed within the cargo container for Run 20. Both low-$Z$ and medium-$Z$ clutter configurations are described.

| Material (low-$Z$) | Material (medium-$Z$) | Description | $x$ (m) | $y$ (m) | $z$ (m) |
|---|---|---|---|---|---|
| Aluminium | Stainless Steel | Solid block of dimensions 101.9 cm × 101.9 cm × 25 cm | 0 | -0.56 | -0.658 |
| Aluminium | Aluminium | Solid block of dimensions 101.9 cm × 101.9 cm × 50 cm | 2.1 | -0.56 | -0.608 |
| Polyethylene | Aluminium | Solid block of dimensions 101.9 cm × 101.9 cm × 50 cm | -2.1 | -0.56 | 0.512 |
| Polyethylene | Iron | Hollow sphere of outer radius 35 cm and inner radius 16 cm | -2.1 | 0.56 | 0.512 |
| Polyethylene | Weathering Steel | Hollow sphere of outer radius 35 cm and inner radius 12 cm | 2.1 | 0.56 | -0.608 |
| Carbon | Aluminium | Solid block of dimensions 101.9 cm × 101.9 cm × 50 cm | -2.1 | 0.56 | -0.608 |
| Polyethylene | Stainless Steel | Solid block of dimensions 101.9 cm × 101.9 cm × 25 cm | 0 | -0.56 | 0.512 |
| Carbon | Gravel | Solid block of dimensions 101.9 cm × 101.9 cm × 50 cm | 0 | 0.56 | 0.512 |

Table A.14 Description of the different types of clutter placed within the cargo container for Run 21. Both low-$Z$ and medium-$Z$ clutter configurations are described.

| Material (low-$Z$) | Material (medium-$Z$) | Description | $x$ (m) | $y$ (m) | $z$ (m) |
|---|---|---|---|---|---|
| Gravel | Stainless Steel | Solid block of dimensions 101.9 cm × 101.9 cm × 25 cm | 0 | -0.56 | -0.658 |
| Concrete | Iron | Solid block of dimensions 101.9 cm × 101.9 cm × 50 cm | 2.1 | -0.56 | -0.608 |
| Sand | Weathering Steel | Solid block of dimensions 101.9 cm × 101.9 cm × 50 cm | -2.1 | -0.56 | 0.512 |
| Gravel | Aluminium | Hollow sphere of outer radius 35 cm and inner radius 16 cm | -2.1 | 0.56 | 0.512 |
| Sand | Aluminium | Hollow sphere of outer radius 35 cm and inner radius 12 cm | 2.1 | 0.56 | -0.608 |
| Aluminium | Iron | Solid block of dimensions 101.9 cm × 101.9 cm × 50 cm | -2.1 | 0.56 | -0.608 |
| Carbon | Sand | Solid block of dimensions 101.9 cm × 101.9 cm × 25 cm | 0 | -0.56 | 0.512 |
| Polyethylene | Aluminium | Solid block of dimensions 101.9 cm × 101.9 cm × 50 cm | 0 | 0.56 | 0.512 |

Table A.15 Description of the different types of clutter placed within the cargo container for Run 22. Both low-$Z$ and medium-$Z$ clutter configurations are described.

| Material (low-$Z$) | Material (medium-$Z$) | Description | $x$ (m) | $y$ (m) | $z$ (m) |
|---|---|---|---|---|---|
| Sand | Iron | Solid block of dimensions 101.9 cm × 101.9 cm × 20 cm | 2.1 | 0.56 | -0.608 |
| Sand | Stainless Steel | Solid block of dimensions 101.9 cm × 101.9 cm × 20 cm | -0.8 | -0.56 | -0.608 |
| Gravel | Iron | Solid block of dimensions 101.9 cm × 101.9 cm × 15 cm | -2.1 | 0.56 | -0.608 |
| Polyethylene | Aluminium | Hollow sphere of outer radius 35 cm and inner radius 16 cm | 0 | 0 | 0.512 |
| Carbon | Gravel | Hollow sphere of outer radius 35 cm and inner radius 12 cm | 0.8 | 0.56 | -0.608 |
| Gravel | Stainless Steel | Hollow block of outer dimensions 101.9 cm × 101.9 cm × 70 cm and inner dimensions 33 cm × 33 cm × 33 cm | 0.8 | -0.56 | -0.608 |
| Carbon | Iron | Hollow block of outer dimensions 101.9 cm × 101.9 cm × 70 cm and inner dimensions 33 cm × 33 cm × 33 cm | -0.8 | 0.56 | -0.5 |
| Carbon | Iron | Solid block of dimensions 101.9 cm × 101.9 cm × 10 cm | -1.55 | -0.56 | 0.662 |
| Sand | Aluminium | Hollow block of outer dimensions 101.9 cm × 101.9 cm × 50 cm and inner dimensions 33 cm × 33 cm × 33 cm | 2.1 | -0.56 | -0.5 |

Table A.16 Description of the different types of clutter placed within the cargo container for Run 23. Both low-$Z$ and medium-$Z$ clutter configurations are described.

| Material (low-$Z$) | Material (medium-$Z$) | Description | $x$ (m) | $y$ (m) | $z$ (m) |
|---|---|---|---|---|---|
| Polyethylene | Aluminium | Solid block of dimensions 101.9 cm × 101.9 cm × 20 cm | 2.1 | 0.56 | -0.608 |
| Gravel | Iron | Solid block of dimensions 101.9 cm × 101.9 cm × 20 cm | -0.8 | -0.56 | -0.608 |
| Carbon | Stainless Steel | Solid block of dimensions 101.9 cm × 101.9 cm × 15 cm | -2.1 | 0.56 | -0.608 |
| Aluminium | Weathering Steel | Hollow sphere of outer radius 35 cm and inner radius 16 cm | 0 | 0 | 0.512 |
| Weathering Steel | Sand | Hollow sphere of outer radius 35 cm and inner radius 12 cm | 0.8 | 0.56 | -0.608 |
| Carbon | Iron | Hollow block of outer dimensions 101.9 cm × 101.9 cm × 70 cm and inner dimensions 33 cm × 33 cm × 33 cm | 0.8 | -0.56 | -0.608 |
| Gravel | Iron | Hollow block of outer dimensions 101.9 cm × 101.9 cm × 70 cm and inner dimensions 33 cm × 33 cm × 33 cm | -0.8 | 0.56 | -0.5 |
| Concrete | Gravel | Solid block of dimensions 101.9 cm × 101.9 cm × 10 cm | -1.55 | -0.56 | 0.662 |
| Polyethylene | Sand | Hollow block of outer dimensions 101.9 cm × 101.9 cm × 50 cm and inner dimensions 33 cm × 33 cm × 33 cm | 2.1 | -0.56 | -0.5 |

Table A.17 Description of the different types of clutter placed within the cargo container for Run 24. Both low-$Z$ and medium-$Z$ clutter configurations are described.

| Material (low-$Z$) | Material (medium-$Z$) | Description | $x$ (m) | $y$ (m) | $z$ (m) |
|---|---|---|---|---|---|
| Aluminium | Iron | Solid block of dimensions 101.9 cm × 101.9 cm × 25 cm | 0 | -0.56 | -0.858 |
| Aluminium | Aluminium | Solid block of dimensions 101.9 cm × 101.9 cm × 50 cm | 2.1 | -0.56 | -0.608 |
| Polyethylene | Aluminium | Solid block of dimensions 101.9 cm × 101.9 cm × 25 cm | -2.1 | -0.56 | 0.512 |
| Polyethylene | Iron | Hollow sphere of outer radius 35 cm and inner radius 16 cm | -2.1 | 0.56 | 0.512 |
| Polyethylene | Stainless Steel | Hollow sphere of outer radius 35 cm and inner radius 12 cm | 2.1 | 0.56 | -0.608 |
| Carbon | Aluminium | Solid block of dimensions 101.9 cm × 101.9 cm × 50 cm | -2.1 | 0.56 | -0.608 |
| Polyethylene | Aluminium | Solid block of dimensions 101.9 cm × 101.9 cm × 25 cm | 0 | -0.56 | 0.512 |
| Aluminium | Aluminium | Solid block of dimensions 101.9 cm × 101.9 cm × 50 cm | 0 | 0.56 | 0.512 |

Table A.18 Description of the different types of clutter placed within the cargo container for Run 25. Both low-$Z$ and medium-$Z$ clutter configurations are described.

| Material (low-$Z$) | Material (medium-$Z$) | Description | $x$ (m) | $y$ (m) | $z$ (m) |
|---|---|---|---|---|---|
| Sand | Iron | Solid block of dimensions 101.9 cm × 101.9 cm × 25 cm | 0 | -0.56 | -0.858 |
| Concrete | Aluminium | Solid block of dimensions 101.9 cm × 101.9 cm × 50 cm | 2.1 | -0.56 | -0.608 |
| Carbon | Stainless Steel | Solid block of dimensions 101.9 cm × 101.9 cm × 25 cm | -2.1 | -0.56 | 0.512 |
| Polyethylene | Iron | Hollow sphere of outer radius 35 cm and inner radius 16 cm | -2.1 | 0.56 | 0.512 |
| Sand | Aluminium | Hollow sphere of outer radius 35 cm and inner radius 12 cm | 2.1 | 0.56 | -0.608 |
| Polyethylene | Stainless Steel | Solid block of dimensions 101.9 cm × 101.9 cm × 50 cm | -2.1 | 0.56 | -0.608 |
| Polyethylene | Iron | Solid block of dimensions 101.9 cm × 101.9 cm × 25 cm | 0 | -0.56 | 0.512 |
| Aluminium | Weathering Steel | Solid block of dimensions 101.9 cm × 101.9 cm × 50 cm | 0 | 0.56 | 0.512 |

Table A.19 Description of the different types of clutter placed within the cargo container for Run 27. Both low-$Z$ and medium-$Z$ clutter configurations are described.

| Material (low-$Z$) | Material (medium-$Z$) | Description | $x$ (m) | $y$ (m) | $z$ (m) |
|---|---|---|---|---|---|
| Aluminium | Weathering Steel | Solid block of dimensions 101.9 cm × 101.9 cm × 25 cm | 0 | -0.56 | -0.658 |
| Aluminium | Iron | Solid block of dimensions 101.9 cm × 101.9 cm × 50 cm | 2.1 | -0.56 | -0.608 |
| Polyethylene | Aluminium | Solid block of dimensions 101.9 cm × 101.9 cm × 50 cm | -2.1 | -0.56 | 0.512 |
| Polyethylene | Aluminium | Hollow sphere of outer radius 35 cm and inner radius 16 cm | -2.1 | 0.56 | 0.512 |
| Sand | Aluminium | Hollow sphere of outer radius 35 cm and inner radius 12 cm | 2.1 | 0.56 | -0.608 |
| Aluminium | Iron | Solid block of dimensions 101.9 cm × 101.9 cm × 50 cm | -2.1 | 0.56 | -0.608 |
| Carbon | Sand | Solid block of dimensions 101.9 cm × 101.9 cm × 25 cm | 0 | -0.56 | 0.512 |
| Polyethylene | Aluminium | Solid block of dimensions 101.9 cm × 101.9 cm × 50 cm | 0 | 0.56 | 0.512 |

Table A.20 Description of the different types of clutter placed within the cargo container for Run 28. Both low-$Z$ and medium-$Z$ clutter configurations are described.

| Material (low-$Z$) | Material (medium-$Z$) | Description | $x$ (m) | $y$ (m) | $z$ (m) |
|---|---|---|---|---|---|
| Sand | Iron | Solid block of dimensions 101.9 cm × 101.9 cm × 20 cm | 2.1 | 0.56 | -0.608 |
| Sand | Iron | Solid block of dimensions 101.9 cm × 101.9 cm × 20 cm | -0.8 | -0.56 | -0.608 |
| Gravel | Weathering Steel | Solid block of dimensions 101.9 cm × 101.9 cm × 15 cm | -2.1 | 0.56 | -0.608 |
| Polyethylene | Aluminium | Hollow sphere of outer radius 35 cm and inner radius 16 cm | 0 | 0 | 0.512 |
| Carbon | Iron | Hollow sphere of outer radius 35 cm and inner radius 12 cm | 0.8 | 0.56 | -0.608 |
| Gravel | Stainless Steel | Hollow block of outer dimensions 101.9 cm × 101.9 cm × 70 cm and inner dimensions 33 cm × 33 cm × 33 cm | 0.8 | -0.56 | -0.608 |
| Carbon | Iron | Hollow block of outer dimensions 101.9 cm × 101.9 cm × 70 cm and inner dimensions 33 cm × 33 cm × 33 cm | -0.8 | 0.56 | -0.5 |
| Carbon | Iron | Solid block of dimensions 101.9 cm × 101.9 cm × 10 cm | -1.55 | -0.56 | 0.662 |
| Sand | Weathering Steel | Hollow block of outer dimensions 101.9 cm × 101.9 cm × 50 cm and inner dimensions 33 cm × 33 cm × 33 cm | 2.1 | -0.56 | -0.5 |

# Appendix B

# Scattering within Low-$Z$ Clutter

Given is a table of data for one of the twenty simulations conducted for when 5 shielded HEU threats were placed randomly in a cargo container filled with low-$Z$ clutter. The position of each of the threat materials, their average scattering angle per voxel, the average scattering angle of the plane the threat is located in and the reconstructed ratio, is given. The clutter consists of eleven wooden crates of size 1.1 m $\times$ 1.1 m $\times$ 1.1 m placed in the cargo container. For low-$Z$ clutter configurations the crates are filled with various sized blocks of aluminium, carbon, polystyrene, gravel, sand and air. The crates are at most stacked two crates high and placed in random locations.

Table B.1 Position, average scattering angle per voxel and reconstructed ratio for each of the threats materials. Also given is the average scatter per voxel of the plane the threat material is located within.

| Resolution | $x$ (m) | $y$ (m) | $z$ (m) | Muons Detected | Muons Correctly Reconstructed | Average Scattering Angle of Threat (degrees) | Average Scattering Angle of Plane (degrees) | Reconstructed Ratio |
|---|---|---|---|---|---|---|---|---|
| Perfect | -2.1 | -0.56 | -0.608 | 3941 | 740 | $3.00 \pm 0.14$ | $2.31 \pm 0.01$ | 0.188 |
| Perfect | -2.1 | 0.56 | 0.512 | 4036 | 486 | $2.29 \pm 0.21$ | $1.60 \pm 0.01$ | 0.120 |
| Perfect | 2.1 | 0 | 0.512 | 4367 | 439 | $2.30 \pm 0.23$ | $1.60 \pm 0.01$ | 0.101 |
| Perfect | 0 | -0.56 | -0.608 | 2333 | 474 | $4.17 \pm 0.21$ | $2.31 \pm 0.01$ | 0.203 |
| Perfect | 2.1 | 0.56 | -0.608 | 2180 | 474 | $3.64 \pm 0.21$ | $2.31 \pm 0.01$ | 0.217 |
| 0.1 mm | -2.1 | -0.56 | -0.608 | 3941 | 735 | $3.00 \pm 0.14$ | $2.31 \pm 0.01$ | 0.187 |
| 0.1 mm | -2.1 | 0.56 | 0.512 | 4036 | 478 | $2.31 \pm 0.21$ | $1.61 \pm 0.01$ | 0.118 |
| 0.1 mm | 2.1 | 0 | 0.512 | 4367 | 418 | $2.35 \pm 0.24$ | $1.61 \pm 0.01$ | 0.096 |
| 0.1 mm | 0 | -0.56 | -0.608 | 2333 | 469 | $4.19 \pm 0.21$ | $2.31 \pm 0.01$ | 0.201 |
| 0.1 mm | 2.1 | 0.56 | -0.608 | 2180 | 475 | $3.65 \pm 0.21$ | $2.31 \pm 0.01$ | 0.218 |
| 0.2 mm | -2.1 | -0.56 | -0.608 | 3941 | 739 | $3.04 \pm 0.14$ | $2.33 \pm 0.01$ | 0.188 |
| 0.2 mm | -2.1 | 0.56 | 0.512 | 4036 | 467 | $2.33 \pm 0.21$ | $1.62 \pm 0.01$ | 0.116 |
| 0.2 mm | 2.1 | 0 | 0.512 | 4367 | 419 | $2.39 \pm 0.24$ | $1.62 \pm 0.01$ | 0.096 |
| 0.2 mm | 0 | -0.56 | -0.608 | 2333 | 470 | $4.17 \pm 0.21$ | $2.33 \pm 0.01$ | 0.201 |
| 0.2 mm | 2.1 | 0.56 | -0.608 | 2180 | 460 | $3.74 \pm 0.22$ | $2.33 \pm 0.01$ | 0.211 |
| 1 mm | -2.1 | -0.56 | -0.608 | 3941 | 637 | $3.35 \pm 0.16$ | $2.47 \pm 0.01$ | 0.162 |
| 1 mm | -2.1 | 0.56 | 0.512 | 4036 | 409 | $2.51 \pm 0.24$ | $1.73 \pm 0.01$ | 0.101 |
| 1 mm | 2.1 | 0 | 0.512 | 4367 | 414 | $2.50 \pm 0.24$ | $1.73 \pm 0.01$ | 0.095 |
| 1 mm | 0 | -0.56 | -0.608 | 2333 | 420 | $4.45 \pm 0.24$ | $2.47 \pm 0.01$ | 0.180 |
| 1 mm | 2.1 | 0.56 | -0.608 | 2180 | 417 | $4.06 \pm 0.24$ | $2.47 \pm 0.01$ | 0.191 |
| 2 mm | -2.1 | -0.56 | -0.608 | 3941 | 540 | $3.60 \pm 0.19$ | $2.64 \pm 0.01$ | 0.137 |
| 2 mm | -2.1 | 0.56 | 0.512 | 4036 | 347 | $2.84 \pm 0.29$ | $1.80 \pm 0.01$ | 0.086 |
| 2 mm | 2.1 | 0 | 0.512 | 4367 | 397 | $2.73 \pm 0.25$ | $1.84 \pm 0.01$ | 0.091 |
| 2 mm | 0 | -0.56 | -0.608 | 2333 | 384 | $4.84 \pm 0.26$ | $2.64 \pm 0.01$ | 0.165 |
| 2 mm | 2.1 | 0.56 | -0.608 | 2180 | 347 | $4.64 \pm 0.29$ | $2.64 \pm 0.01$ | 0.159 |

# Appendix C

# Muon Disappearances within Low-$Z$ Clutter

Given is a table of data for one of the twenty simulations conducted for when 5 shielded HEU threats were placed randomly in a cargo container filled with low-$Z$ clutter. The position of each of the threat materials, their average total path length angle per voxel and the average total path length of the plane the threat is located in, is given. The clutter consists of eleven wooden crates of size 1.1 m $\times$ 1.1 m $\times$ 1.1 m placed in the cargo container. For low-$Z$ clutter configurations the crates are filled with various sized blocks of aluminium, carbon, polystyrene, gravel, sand and air. The crates are at most stacked two crates high and placed in random locations.

Table C.1 Position and average total path length per voxel of each of the threats materials identified by applying muon disappearance tomography, to the 'areas of interest' obtained using the muon scattering algorithm.

| Target I.D | Resolution | $x$ (m) | $y$ (m) | $z$ (m) | Muons Disappearances (Target) | Average Total Path Length | Average Total Path Length of Plane |
|---|---|---|---|---|---|---|---|
| (1) | Perfect | -0.9 | 0.46 | -0.7 | 274 | $11.81 \pm 0.40$ | $6.86 \pm 0.02$ |
| (2) | Perfect | 0.7 | -0.66 | -0.708 | 203 | $11.42 \pm 0.42$ | $6.86 \pm 0.02$ |
| (3) | Perfect | 2 | -0.66 | -0.7 | 264 | $10.51 \pm 0.36$ | $6.86 \pm 0.02$ |
| (4) | Perfect | -1.45 | 0.36 | 0.312 | 120 | $12.15 \pm 0.54$ | $6.94 \pm 0.02$ |
| (5) | Perfect | -1.55 | -0.56 | 0.2 1 | 31 | $12.81 \pm 0.38$ | $6.97 \pm 0.02$ |
| (1) | 0.1 mm | -0.9 | 0.46 | -0.7 | 274 | $11.80 \pm 0.40$ | $6.86 \pm 0.02$ |
| (2) | 0.1 mm | 0.7 | -0.66 | -0.708 | 203 | $11.42 \pm 0.42$ | $6.86 \pm 0.02$ |
| (3) | 0.1 mm | 2 | -0.66 | -0.7 | 264 | $10.51 \pm 0.36$ | $6.86 \pm 0.02$ |
| (4) | 0.1 mm | -1.45 | 0.36 | 0.312 | 120 | $12.16 \pm 0.54$ | $6.94 \pm 0.02$ |
| (5) | 0.1 mm | -1.55 | -0.56 | 0.2 | 131 | $12.81 \pm 0.38$ | $6.97 \pm 0.02$ |
| (1) | 0.2 mm | -0.9 | 0.46 | -0.7 | 274 | $11.79 \pm 0.40$ | $6.86 \pm 0.02$ |
| (2) | 0.2 mm | 0.7 | -0.66 | -0.708 | 203 | $11.42 \pm 0.42$ | $6.86 \pm 0.02$ |
| (3) | 0.2 mm | 2 | -0.66 | -0.7 | 264 | $10.51 \pm 0.36$ | $6.86 \pm 0.02$ |
| (4) | 0.2 mm | -1.45 | 0.36 | 0.312 | 120 | $12.16 \pm 0.54$ | $6.94 \pm 0.02$ |
| (5) | 0.2 mm | -1.55 | -0.56 | 0.2 | 131 | $12.81 \pm 0.38$ | $6.97 \pm 0.02$ |
| (1) | 1 mm | -0.9 | 0.46 | -0.7 | 274 | $11.72 \pm 0.38$ | $6.86 \pm 0.02$ |
| (2) | 1 mm | 0.7 | -0.66 | -0.708 | 203 | $11.41 \pm 0.41$ | $6.86 \pm 0.02$ |
| (3) | 1 mm | 2 | -0.66 | -0.7 | 264 | $10.49 \pm 0.37$ | $6.86 \pm 0.02$ |
| (4) | 1 mm | -1.45 | 0.36 | 0.312 | 120 | $12.18 \pm 0.54$ | $6.94 \pm 0.02$ |
| (5) | 1 mm | -1.55 | -0.56 | 0.2 | 131 | $12.81 \pm 0.40$ | $6.97 \pm 0.02$ |
| (1) | 2 mm | -0.9 | 0.46 | -0.7 | 274 | $11.64 \pm 0.36$ | $6.86 \pm 0.02$ |
| (2) | 2 mm | 0.7 | -0.66 | -0.708 | 203 | $11.38 \pm 0.39$ | $6.86 \pm 0.02$ |
| (3) | 2 mm | 2 | -0.66 | -0.7 | 264 | $10.46 \pm 0.35$ | $6.86 \pm 0.02$ |
| (4) | 2 mm | -1.45 | 0.36 | 0.312 | 120 | $12.20 \pm 0.52$ | $6.93 \pm 0.02$ |
| (5) | 2 mm | -1.55 | -0.56 | 0.2 | 131 | $12.80 \pm 0.39$ | $6.97 \pm 0.02$ |

# Appendix D

# Scattering within Medium-$Z$ Clutter

Given is a table of data for one of the twenty simulations conducted for when 5 shielded HEU threats were placed randomly in a cargo container filled with medium-$Z$ clutter. The position of each of the threat materials, their average scattering angle per voxel, the average scattering angle of the plane the threat is located in and the reconstructed ratio, is given. The clutter consists of eleven wooden crates of size 1.1 m $\times$ 1.1 m $\times$ 1.1 m placed in the cargo container. For medium-$Z$ clutter configurations the crates are filled with various sized blocks of aluminium, weathering steel, stainless steel and iron. The crates are at most stacked two crates high and placed in random locations.

Table D.1 Position, average scattering angle per voxel and reconstructed ratio for each of the threats materials. Also given is the average scatter per voxel of the plane the threat material is located within.

| Resolution | $x$ (m) | $y$ (m) | $z$ (m) | Muons Detected | Muons Correctly Reconstructed | Average Scattering Angle of Threat (degrees) | Average Scattering Angle of Plane (degrees) | Reconstructed Ratio |
|---|---|---|---|---|---|---|---|---|
| Perfect | -2.1 | -0.56 | -0.608 | 3681 | 154 | $3.61 \pm 0.32$ | $3.23 \pm 0.01$ | 0.042 |
| Perfect | -2.1 | 0.56 | 0.512 | 3928 | 117 | $2.15 \pm 0.43$ | $2.23 \pm 0.01$ | 0.030 |
| Perfect | 2.1 | 0 | 0.512 | 4394 | 156 | $2.48 \pm 0.32$ | $2.48 \pm 0.01$ | 0.036 |
| Perfect | 0 | -0.56 | -0.608 | 2110 | 262 | $3.71 \pm 0.19$ | $3.70 \pm 0.01$ | 0.124 |
| Perfect | 2.1 | 0.56 | -0.608 | 1903 | 291 | $4.54 \pm 0.17$ | $4.50 \pm 0.01$ | 0.153 |
| 0.1 mm | -2.1 | -0.56 | -0.608 | 3681 | 148 | $3.78 \pm 0.34$ | $3.36 \pm 0.01$ | 0.040 |
| 0.1 mm | -2.1 | 0.56 | 0.512 | 3928 | 112 | $2.22 \pm 0.45$ | $2.30 \pm 0.01$ | 0.029 |
| 0.1 mm | 2.1 | 0 | 0.512 | 4394 | 159 | $2.39 \pm 0.31$ | $2.39 \pm 0.01$ | 0.036 |
| 0.1 mm | 0 | -0.56 | -0.608 | 2110 | 256 | $3.75 \pm 0.20$ | $3.76 \pm 0.01$ | 0.121 |
| 0.1 mm | 2.1 | 0.56 | -0.608 | 1903 | 279 | $4.66 \pm 0.18$ | $4.61 \pm 0.01$ | 0.147 |
| 0.2 mm | -2.1 | -0.56 | -0.608 | 3681 | 150 | $3.64 \pm 0.33$ | $3.21 \pm 0.01$ | 0.041 |
| 0.2 mm | -2.1 | 0.56 | 0.512 | 3928 | 108 | $2.25 \pm 0.46$ | $2.34 \pm 0.01$ | 0.027 |
| 0.2 mm | 2.1 | 0 | 0.512 | 4394 | 151 | $2.48 \pm 0.33$ | $2.48 \pm 0.01$ | 0.034 |
| 0.2 mm | 0 | -0.56 | -0.608 | 2110 | 250 | $3.81 \pm 0.20$ | $3.88 \pm 0.01$ | 0.118 |
| 0.2 mm | 2.1 | 0.56 | -0.608 | 1903 | 285 | $4.64 \pm 0.18$ | $4.53 \pm 0.01$ | 0.150 |
| 1 mm | -2.1 | -0.56 | -0.608 | 3681 | 137 | $3.79 \pm 0.36$ | $3.49 \pm 0.01$ | 0.037 |
| 1 mm | -2.1 | 0.56 | 0.512 | 3928 | 101 | $2.45 \pm 0.50$ | $2.49 \pm 0.01$ | 0.026 |
| 1 mm | 2.1 | 0 | 0.512 | 4394 | 135 | $2.85 \pm 0.37$ | $2.85 \pm 0.01$ | 0.031 |
| 1 mm | 0 | -0.56 | -0.608 | 2110 | 226 | $4.06 \pm 0.22$ | $4.20 \pm 0.01$ | 0.107 |
| 1 mm | 2.1 | 0.56 | -0.608 | 1903 | 264 | $4.74 \pm 0.19$ | $4.60 \pm 0.01$ | 0.139 |
| 2 mm | -2.1 | -0.56 | -0.608 | 3681 | 129 | $4.11 \pm 0.39$ | $3.70 \pm 0.01$ | 0.035 |
| 2 mm | -2.1 | 0.56 | 0.512 | 3928 | 82 | $2.86 \pm 0.61$ | $3.11 \pm 0.01$ | 0.021 |
| 2 mm | 2.1 | 0 | 0.512 | 4394 | 125 | $2.94 \pm 0.40$ | $2.94 \pm 0.01$ | 0.028 |
| 2 mm | 0 | -0.56 | -0.608 | 2110 | 205 | $4.43 \pm 0.24$ | $4.55 \pm 0.01$ | 0.097 |
| 2 mm | 2.1 | 0.56 | -0.608 | 1903 | 232 | $5.18 \pm 0.22$ | $5.14 \pm 0.01$ | 0.122 |

# Appendix E

# Muon Disappearances within Medium-$Z$ Clutter

Given is a table of data for one of the twenty simulations conducted for when 5 shielded HEU threats were placed randomly in a cargo container filled with medium-$Z$ clutter. The position of each of the threat materials, their average total path length angle per voxel and the average total path length of the plane the threat is located in, is given. The clutter consists of eleven wooden crates of size 1.1 m $\times$ 1.1 m $\times$ 1.1 m placed in the cargo container. For medium-$Z$ clutter configurations the crates are filled with various sized blocks of aluminium, weathering steel, stainless steel and iron. The crates are at most stacked two crates high and placed in random locations.

Table E.1 Position and average total path length per voxel of each of the threats materials identified by applying muon disappearance tomography, to the 'areas of interest' obtained using the muon scattering algorithm.

| Target I.D | Resolution | $x$ (m) | $y$ (m) | $z$ (m) | Muons Disappearances (Target) | Average Total Path Length | Average Total Path Length of Plane |
|---|---|---|---|---|---|---|---|
| (1) | Perfect | -2.1 | -0.56 | -0.608 | 245 | $12.33 \pm 0.40$ | $6.68 \pm 0.02$ |
| (2) | Perfect | -2.1 | 0.56 | 0.512 | 269 | $18.17 \pm 0.51$ | $7.17 \pm 0.03$ |
| (3) | Perfect | 2.1 | 0 | 0.512 | 267 | $11.53 \pm 0.46$ | $7.17 \pm 0.03$ |
| (4) | Perfect | 0 | -0.56 | -0.608 | 97 | $14.47 \pm 0.52$ | $6.68 \pm 0.02$ |
| (5) | Perfect | 2.1 | 0.56 | -0.608 | 126 | $17.88 \pm 0.34$ | $6.68 \pm 0.02$ |
| (1) | 0.1 mm | -2.1 | -0.56 | -0.608 | 245 | $12.33 \pm 0.40$ | $6.68 \pm 0.02$ |
| (2) | 0.1 mm | -2.1 | 0.56 | 0.512 | 269 | $18.17 \pm 0.51$ | $7.17 \pm 0.03$ |
| (3) | 0.1 mm | 2.1 | 0 | 0.512 | 267 | $11.53 \pm 0.46$ | $7.17 \pm 0.03$ |
| (4) | 0.1 mm | 0 | -0.56 | -0.608 | 97 | $14.47 \pm 0.52$ | $6.68 \pm 0.02$ |
| (5) | 0.1 mm | 2.1 | 0.56 | -0.608 | 126 | $17.89 \pm 0.35$ | $6.68 \pm 0.02$ |
| (1) | 0.2 mm | -2.1 | -0.56 | -0.608 | 245 | $12.32 \pm 0.40$ | $6.68 \pm 0.02$ |
| (2) | 0.2 mm | -2.1 | 0.56 | 0.512 | 269 | $18.17 \pm 0.51$ | $7.17 \pm 0.03$ |
| (3) | 0.2 mm | 2.1 | 0 | 0.512 | 267 | $11.53 \pm 0.46$ | $7.17 \pm 0.03$ |
| (4) | 0.2 mm | 0 | -0.56 | -0.608 | 97 | $14.47 \pm 0.52$ | $6.68 \pm 0.02$ |
| (5) | 0.2 mm | 2.1 | 0.56 | -0.608 | 126 | $17.89 \pm 0.35$ | $6.68 \pm 0.02$ |
| (1) | 1 mm | -2.1 | -0.56 | -0.608 | 245 | $12.31 \pm 0.39$ | $6.68 \pm 0.02$ |
| (2) | 1 mm | -2.1 | 0.56 | 0.512 | 269 | $18.21 \pm 0.49$ | $7.17 \pm 0.03$ |
| (3) | 1 mm | 2.1 | 0 | 0.512 | 267 | $11.57 \pm 0.46$ | $7.17 \pm 0.03$ |
| (4) | 1 mm | 0 | -0.56 | -0.608 | 97 | $14.45 \pm 0.53$ | $6.68 \pm 0.02$ |
| (5) | 1 mm | 2.1 | 0.56 | -0.608 | 126 | $17.91 \pm 0.35$ | $6.68 \pm 0.02$ |
| (1) | 2 mm | -2.1 | -0.56 | -0.608 | 245 | $12.25 \pm 0.38$ | $6.68 \pm 0.02$ |
| (2) | 2 mm | -2.1 | 0.56 | 0.512 | 269 | $18.20 \pm 0.48$ | $7.17 \pm 0.03$ |
| (3) | 2 mm | 2.1 | 0 | 0.512 | 267 | $11.58 \pm 0.45$ | $7.17 \pm 0.03$ |
| (4) | 2 mm | 0 | -0.56 | -0.608 | 97 | $14.45 \pm 0.53$ | $6.68 \pm 0.02$ |
| (5) | 2 mm | 2.1 | 0.56 | -0.608 | 126 | $17.90 \pm 0.38$ | $6.68 \pm 0.02$ |